Carlos Miguel
Marques do Rosário

Processos de condução eletrónica em células de memória ReRAM do tipo VCM com óxidos metálicos

Electronic conduction processes in VCM-type metal-oxide ReRAM cells

Carlos Miguel
Marques do Rosário

Processos de condução eletrónica em células de memória ReRAM do tipo VCM com óxidos metálicos

Electronic conduction processes in VCM-type metal-oxide ReRAM cells

Dissertação apresentada à Universidade de Aveiro para cumprimento dos requisitos necessários à obtenção do grau de Doutor em Engenharia Física, realizada sob a orientação científica do Professor Doutor Nikolai Andreevitch Sobolev, Professor Associado do Departamento de Física da Universidade de Aveiro e co-orientação do Professor Doutor Rainer Waser, Professor Catedrático da Faculdade de Engenharia Electrotécnica e de Tecnologias de Informação da Universidade Técnica da Renânia-Vestfália (RWTH Aachen).

Apoio financeiro da FCT através da bolsa de doutoramento PD/BD/105917/2014 (Programa Doutoral DAEPHYS).

O trabalho foi desenvolvido no âmbito do projecto i3N, UID/CTM/50025/2013, UIDB/50025/2020 & UIDP/50025/2020, financiado por fundos nacionais através da FCT/MEC.

Apoio financeiro do CRUP em parceria com a DAAD através da Ação Integrada Luso-Alemã A-14/17.

Financial support from the DFG through the Collaborative Research Centre SFB 917 “Nanoswitches”.

I dedicate this work to my mother,
Maria Gabriela.

o júri / the jury

presidente / president

Prof. Doutor Aníbal Manuel de Oliveira Duarte Monteiro
Professor Catedrático da Universidade de Aveiro

vogais / examiners committee

Prof.ª Doutora Regina Dittmann
Professora da Universidade de RWTH Aachen

Prof. Doutor Luís Manuel Cadillon Martins Costa
Professor Associado com Agregação da Universidade de Aveiro

Prof. Doutor Henrique Leonel Gomes
Professor Associado da Universidade de Coimbra

Doutora Asal Kiazadeh
Investigadora da Universidade Nova de Lisboa

Prof. Doutor Nikolai Andreevitch Sobolev (Orientador)
Professor Associado da Universidade de Aveiro

acknowledgements

I feel the need to thank many people, without whom my work would not have been possible. First, I wish to express my gratitude to my supervisor Professor Nikolai Sobolev for all the support, guidance, shared experience and opportunities given to me, not only during my PhD but since 2012. I also want to express my gratitude to my co-supervisor Professor Rainer Waser for giving me the opportunity to work in his group in Aachen/Jülich, providing me with one of the best, most challenging and most rewarding professional and personal experiences of my life. A very special thank you to Dr. Dirk Wouters for supervising my work in Aachen, for always being interested in my results and motivating me to pursue solutions whenever I encountered obstacles.

I wish to thank Professor Valeri Afanas'ev from KU Leuven and Professor Carlo Ricciardi from the Polytechnic University of Turin for agreeing to review my thesis and for writing a report for my European Doctorate.

I thank the Physics Department of the University of Aveiro and the I3N for the institutional and financial support. Likewise, I must thank all the institutional support from the IWE 2 at RWTH Aachen University and from PGI-7 at Forschungszentrum Jülich, especially to Dr. Ulrich Böttger, Martina Heins and Maria Garcia.

I must thank Alexander Schönhals for most of the sample fabrication, for sharing his fabrication methods and discussing of the experimental results. I would like to thank Bo Thöner and Professor Matthias Wuttig from the I. Institute of Physics (IA) in Aachen for the low temperature transport measurements. Their interest in the work was invaluable for both the experiments and the discussion of the results. A special thank you to Bo Thöner for his availability and for the always constructive and critical comments in our many discussions. I wish to thank Dr. Stephan Menzel for his incisive comments and overall discussion of the work. I wish to thank Dr. Alexander Meledin and Professor Joachim Mayer from the Central Facility for Electron Microscopy in Aachen for the STEM measurements, and Dr. Nuno Barradas and Professor Eduardo Alves from Campus Tecnológico e Nuclear in Sacavém for the RBS measurements. I thank Thomas Heisig, Dr. Christoph Bäumer and Professor Regina Dittmann for the XPS measurements and Felix Hensling for the help with the sputtering tool in Jülich. I thank Andreas Kindsmüller for the help in sputtering and the analysis of the XPS results. I would like to thank Marco Moors and Maria Glößfor the LC-AFM measurements. I thank Stephan Aussen for the XRR measurements in Jülich. I thank Professor António Cunha for the UV-Vis absorption spectroscopy measurements. I wish to thank Dr. Susanne Hoffmann-Eifert for the enthusiastic discussions whenever I was in Jülich, and Dr. Vikas Rana for the access to the electrical measurement setups in PGI-7.

I would like to acknowledge all the technical support at the different locations where I worked. From the Aachen site, thank you Daliborka Erdoglija for the preparation of the samples in the clean room, Petra Grewe for the XRD and XRR measurements, and Dagmar Leisten for sawing the samples. From Jülich, I must thank René Borowksi, Marcel Gerst, Stephan Massberg, Jochen Freidrich and Georg Pickartz for all the help with the cryostat, in setting up the measurement tools and with sputtering. From Aveiro, I would like to thank Ivo Mateus and Miguel Rocha for the assistance in the mechanical workshop, and David Furtado for the help in setting up the new earthing system in the magnetic resonance lab.

The great atmosphere at IWE 2 was something that I valued deeply and which had a really positive impact on everyday work at the Institute. Therefore, I would like to thank all the colleagues at the Institute in Aachen. A special thank you to Marcel and Tyler, for being the best office mates, for the support in the hard times and for "drooping the snoot" like no others. Another special thank you to Jonathan, for the many Aachen-Jülich commutes in good company and for the 1000+ hours of discussions of what is Mott and what is not(t). Thank you Andi, Daniel and Sebastian for the "classy jazzy" moments. Thank you fellow DSA Helden for integrating a foreign fisherman and lutenist in your party. Thank you Tyler, Moritz, Carsten, Jan and fellow supporters for "going the right way" out. Thank you Anne and Toto for always lightening the mood. Thank you, Camilla, for the German lessons and the challenging Adventskalender. Thank you Andrea, for being the Luigi to my Mario. Thank you Thomas, for the kindness and for the photos. Also, a word of gratitude to all the colleagues at PGI-7 in Jülich for the comradeship.

I would also like to extend my thanks to my lab colleagues in Aveiro for the good times at the lab. I thank Bruno for the company and for sharing the struggles and difficulties, especially in the last two years. I want to thank Jaime for working with me during his third year project and his master thesis, and for his critical assessment of the experimental results. Thank you, Nuno, for always lightening the mood with a good joke. I also thank Andrey and João for the help in the lab. I would like to thank all my colleagues turned good friends that have accompanied me during my years at the University of Aveiro. Thank you all for the companionship, numerous discussions during lunch breaks, occasional snack grabbing and for all the fun moments we shared. I also wish to thank Professor Teresa Monteiro for encouraging me to complete this long endeavour.

To my family and extended family, thank you for supporting me through all the hardships and for encouraging me to go further. Thank you to my friends of old, Amaral, André, Barros, Bernardo, Maria, Pedro and Sarnadas. To Denis for being my brother away from home. To Olívia, Lino and Mariana for always receiving me with a big smile. To Cristina for the support and the advice. To my father José Rui for inciting my scientific curiosity and for (lately) feeding me with his veggies and to my sister Bárbara for feeding my artistic side. Lastly, I am very grateful to Maria for the constant encouragement, for believing in me when I failed to and especially for being herself.

Muito obrigado e bem hajam! Vielen Dank!

Palavras-chave

Transporte elétrico, *resistive switching*, ReRAM, filamentos condutores, TaO_x, metal desordenado

Resumo

Novas aplicações, tais como computação neuromórfica, e as limitações da tecnologia de semicondutores atual exigem uma revolução nos dispositivos eletrónicos. Sendo uma peça chave para um novo paradigma da eletrónica, a memória ReRAM (*redox-based resistive switching random access memory*) tem sido alvo de muita investigação e desenvolvimento. O Ta_2O_5 é um dos materiais mais populares para usar em dispositivos ReRAM, permitindo alta durabilidade e velocidades de comutação elevadas. As ReRAM com Ta_2O_5 baseiam-se na mudança não volátil da resistência elétrica através da modulação da quantidade de oxigénio em filamentos condutores, como é descrito no mecanismo de alteração de valência (*valence change mechanism*). No entanto, a estrutura dos filamentos e a sua composição química exata, são ainda alvo de intenso debate, limitando o desenvolvimento de melhores receitas de fabricação de dispositivos. Os dois modelos atuais na literatura consideram filamentos compostos por lacunas de oxigénio e filamentos com Ta metálico. Este trabalho procura resolver esta disputa ao reportar um estudo detalhado do transporte elétrico através de filamentos condutores em dispositivos ReRAM de Ta_2O_5. Paralelamente, foi estudado em detalhe o transporte elétrico e a estrutura de filmes finos de TaO_x subestequiométrico, depositados de forma a emular o material dos filamentos.

Foi encontrada uma forte correlação entre os mecanismos de transporte nos filamentos condutores dentro dos dispositivos ReRAM de Ta_2O_5 e nos filmes finos de TaO_x com $x \sim 1$. Isto estabelece uma ligação clara entre as propriedades físicas dos materiais que compõem tanto os filamentos como os filmes finos de TaO_x. A análise estrutural efetuada nos filmes de TaO_x revela a presença de aglomerados de Ta. Por outro lado, o transporte elétrico em filmes finos de Ta é dominado pelos mesmos mecanismos de condução observados nos filmes de TaO_x com $x \sim 1$, para a maior parte da gama de temperatura de 2 K a 300 K. Ambos os casos partilham ainda uma concentração de portadores da ordem de 10^{22} cm^{-3} e uma magnetoresistência positiva associada a anti-localização fraca para $T < 30$ K. Portanto, é concluído que o transporte em filmes de TaO_x com $x \sim 1$ é dominado por uma cadeia de percolação de aglomerados de Ta embutidos numa matriz isoladora de Ta_2O_5. Estes aglomerados exibem um comportamento típico de metais desordenados, para os quais a condução é dominada por correções quânticas ao transporte de Boltzmann.

Em conclusão, o transporte elétrico em filamentos condutores dentro de dispositivos ReRAM baseados em Ta_2O_5 é dominado pela percolação de aglomerados de Ta, o que corrobora observações independentes de Ta metálico nos filamentos. Assim, este trabalho suporta o modelo baseado no filamento metálico de Ta.

Keywords Electrical transport, resistive switching, ReRAM, conductive filaments, TaO_x, disordered metal

Abstract

New applications, such as neuromorphic computing, and the limitations of current semiconductor technologies demand a revolution in electronic devices. As one of the key enablers of a new electronics paradigm, redox-based resistive switching random access memory (ReRAM) has been the focus of much research and development. Among the ReRAM research community, Ta_2O_5 has emerged as one of the most popular materials, for enabling high endurance and high switching speed. Ta_2O_5-based ReRAM rely on the non-volatile change of the resistance via the modulation of the oxygen content in conductive filaments, as it is described in the valence change mechanism. However, the filaments' structure and exact composition are currently under intense debate, which hinders the development of better device design rules. The two current models in the literature consider filaments composed of oxygen vacancies and those containing metallic Ta. This work attempts to solve this dispute by reporting a detailed study of the electrical transport through the conductive filaments inside Ta_2O_5-based ReRAM. In parallel, the electrical transport and structure of substoichiometric TaO_x thin films, grown to try and match the material of the filaments, was studied in detail. A strong correlation between the transport mechanisms in the conductive filaments inside the Ta_2O_5 ReRAM and in the TaO_x thin films with $x \sim 1$ was found. This clearly links the physical properties of the materials composing the filaments and the substoichiometric TaO_x thin films. Structural analysis performed on the TaO_x films reveals the presence of Ta clusters inside the films. Moreover, the electrical transport of metallic Ta films shows the same transport mechanism as TaO_x with $x \sim 1$, for most of the measured temperature range, from 2 K to 300 K. Beyond the transport mechanisms, both cases share a carrier concentration on the order of 10^{22} cm^{-3} and a positive magnetoresistance associated with weak antilocalization at $T < 30$ K. Therefore, it is concluded that the transport in the TaO_x films with $x \sim 1$ is dominated by a percolation chain of Ta clusters embedded in an insulating Ta_2O_5 matrix. These clusters exhibit disordered metal-like behaviour, where quantum corrections to the Boltzmann transport dominate the conduction.

In conclusion, the electrical transport in the conductive filaments inside Ta_2O_5-based ReRAM devices is determined by percolation through Ta clusters, which is in line with independent observations of metallic Ta in the filaments. This work strongly supports the metallic Ta filament model.

"It is good to have an end to journey towards;
but it is the journey that matters, in the end"

— Ursula K. Le Guin,
The Left Hand of Darkness

Contents

List of Figures

List of Tables

Acronyms

8W Eightwise.

AE Active Electrode.

AFM Atomic force microscopy.

AI Artificial Intelligence.

BE Bottom Electrode.

C8W Counter-eightwise.

CBA Crossbar array.

CC Current Compliance.

CMOS Complementary Metal-Oxide-Semiconductor.

CPU Central Processing Unit.

CRS Complementary Resistive Switching.

CS Complementary Switching.

DC Direct current.

DRAM Dynamic Random Access Memory.

ECM Electrochemical Mechanism.

EDX Energy dispersive X-ray spectroscopy.

EF Electroforming.

ERDA Elastic recoil detection analysis.

ESH Efros-Shklovskii hopping.

FeRAM Ferroelectric Random Access Memory.

GI-XRD Grazing incidence X-ray diffraction.

HAADF High angle annular dark field.

HLN Hikami-Larkin-Nagaoka.

HRS High Resistance State.

HRTEM High Resolution Transmission Electron Microscopy.

LC-AFM Local conductivity atomic force microscopy.

LRS Low Resistance State.

MIM Metal-Insulator-Metal.

MR Magnetoresistance.

MRAM Magnetoresistive Random Access Memory.

NNH Nearest-neighbour hopping.

OE Ohmic Electrode.

PBL Phase breaking length.

PCM Phase-Change Memory.

QSE Quantum-size effects.

RAM Random Access Memory.

RBS Rutherford backscattering spectrometry.

ReRAM Redox-based Resistive Random Access Memory.

RF Radiofrequency.

RS Resistive Switching.

RTN Random telegraph noise.

SCLC Space-Charge Limited Current.

SCM Storage Class Memory.

STDP Spike-timing-dependent-plasticity.

STEM Scanning transmission electron microscopy.

STT Spin-transfer torque.

TCM Thermochemical Mechanism.

TCR Temperature coefficient of the resistance.

TE Top Electrode.

TEM Transmission Electron Microscopy.

UV Ultraviolet.

VCM Valence Change Mechanism.

vdP Van der Pauw.

VRH Variable Range Hopping.

WAL Weak antilocalization.

WL Weak localization.

XPS X-ray photoelectron spectroscopy.

XRD X-ray diffraction.

XRR X-ray reflectivity.

Introduction

The technological advancements of the last decades in the field of electronics revolutionized the world as we conceive it today. The youngest generations can hardly imagine living without computers, smartphones and touchscreens. Ubiquitous to all these applications is the transfer of huge amounts of data between the different components of each individual tech product or between each other. Every time, everywhere. Moreover, the increasing demand for artificial intelligence, machine learning and other data-centric applications will soon make the total energy consumption reach the total amount of electrical energy produced in the world. The situation will soon be unsustainable. In order to continue this trend of technological development, it is then absolutely crucial to change the paradigm and invest in new technologies with a higher energy efficiency.

The largely advertised end of Moore's law catalysed the research on emerging technologies that could overcome the limitations of the current semiconductor memories based on the complementary metal-oxide-semiconductor (CMOS) fabrication process. However, the persistence and inertia of CMOS technology is maintaining the new technologies' emerging status. Initially pointed out to surpass the CMOS-based memories, such as dynamic random access memory (DRAM) and Flash, these emerging technologies have been kept at research level or relegated to niche applications. Realizing the potential of emerging memories to bridge the gap between the fast, volatile DRAM and the slow, non-volatile Flash, researchers developed the concept of Storage Class Memory and started to advocate the emerging technologies for this purpose.

On the other hand, the devices underlying these emerging memories are now understood as examples of memristive systems. These are named after the memristor, a passive fundamental circuit element theoretically proposed in the 1970s. The response of such memristive systems/devices closely resembles the biochemical behaviour of synapses between neurons. This characteristic promoted the idea of achieving neuromorphic computing at the hardware level, in stark contrast with software-based artificial intelligence (AI), most common nowadays. The paradigm shift from software-based AI to hardware-based AI is extremely relevant in terms of energy efficiency, taking advantage of the efficient architecture of the brain when compared to software-based AI in brain-like computing applications.

One of the top contenders in the emerging memory category is the redox-based resistive random access memory (ReRAM). The technology relies on the non-volatile change of the resistance of a metal-insulator-metal structure upon application of an electric field, a phenomenon known as resistive switching. The switching is most commonly triggered by redox reactions that create a filamentary path inside the oxide with a higher conductivity. The localized disruption and restoration of this filament enables the change in resistance.

Asymmetric structures with transition metal oxides and two different metal electrodes, in which one of these is more affine to oxygen, normally lead to the so-called valence change

mechanism (VCM) type of resistive switching. The vast majority of the cases involve the formation of oxygen-deficient conductive filaments. A particularly popular insulator material for VCM-based resistive switching is Ta_2O_5, as it holds the record for highest endurance and highest switching speed devices among transition metal oxides. Research on VCM-specific systems led to many important conclusions. The key role of the movement of oxygen species inside the oxide enabled by both local heating and electric field acceleration, and the consequent changes of the valence states of the metal cations in the oxide are examples of such conclusions. There is, however, no consensus in the exact nature of the filaments: are they composed of an oxygen deficient oxide phase, such as a suboxide, or is there a precipitation of metallic phases? Most device models assume the existence of oxygen vacancies in the oxide phase and all the other physical properties (such as electrical transport) are explained by these defects. Despite this theory, electron microscopy and spectromicroscopy studies indicate the occurrence of metallic particles inside the oxide layer of resistive switching devices. The work reported in this thesis aimed at unravelling this question through a thorough electrical transport study of conductive filaments in Ta_2O_5-based ReRAM devices. The chosen approach focused not only on studying the transport in the filaments inside Ta_2O_5-based resistive switching devices, but also on producing and studying TaO_x in thin film form that could mirror the material of the filament. After having achieved this, the latter can then be subject to further analytical studies in order to clarify the origin of the transport mechanisms exhibited by the conductive filaments. Therefore, the work is naturally divided in two roads: a "device-oriented road", where operating Ta_2O_5-based resistive switching devices are the focus of the experiments, and a "fundamental physics-oriented road", where the substoichiometric TaO_x thin films are analysed.

This thesis is divided in five main chapters and a final chapter where the main conclusions are summarized and future work is discussed. **Chapter 1** largely extends and supports this introduction. The phenomenon of resistive switching is described, including a brief history of important events in the field, the most relevant physical mechanisms discussed in the literature are presented, and the main applications are introduced. The thesis topic is then properly contextualized in the presented framework. **Chapter 2** reviews the theoretical framework needed for the analysis of the transport experiments carried out in this work. This chapter also includes a general overview of the Ta-O material system, with an introduction of some specific material phases that are relevant for the discussion. **Chapter 3** introduces and briefly describes the experimental techniques used in the course of the reported work. Emphasis is naturally given to the main techniques employed, while auxiliary techniques are mostly given a very brief definition. The original contribution of this thesis is then presented in the two following chapters. **Chapter 4** focuses firstly on the resistive switching obtained in the $Ta/Ta_2O_5/Pt$ ReRAM devices under study, and later characterizes the electrical transport in the different resistance states. The focus then switches slightly to the other road, where the electrical transport data for the TaO_x thin films is presented and compared to the data of the devices. A correlation between the transport mechanisms is clearly observed. Taking advantage of this last point, **Chapter 5** delves deeper into the structure and electrical transport properties of the TaO_x films. This enabled a discussion of the transport mechanisms in light of the microscopic characteristics of the materials involved. The thesis is completed with a summary of the main conclusions and a description of possible future developments.

Fig. 1 shows a schematic diagram that summarizes the research approach reported in this thesis, hopefully making the organization of the thesis clearer.

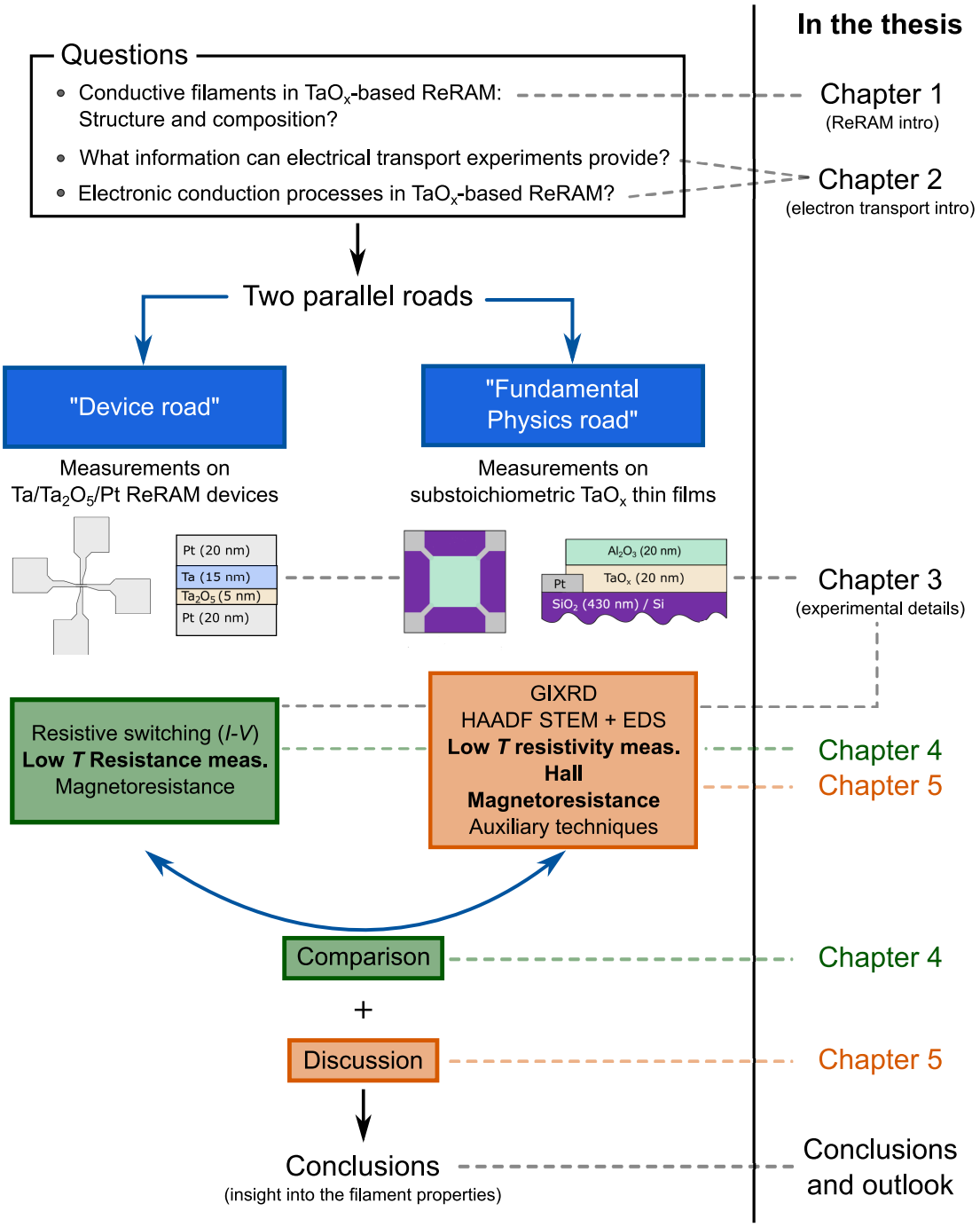

Figure 1: General scheme of the thesis. Starting from the main questions that were targeted, the work was divided in two parallel roads of experimental work. The results of the two paths were compared in order to gain information and attempt to answer the initial questions. On the right side of the scheme, the schematic blocks are mapped to the different thesis chapters. Chapters 4 and 5, containing the main experimental results and discussion, are highlighted in colour to match the colour of the blocks in the scheme.

Chapter 1

Resistive switching and ReRAM

This chapter introduces the physical phenomenon of resistive switching, the related technologies and their most relevant applications. It starts with a definition of resistive switching and the necessary terminology. A brief summary of the most important milestones in the history of resistive switching research are then described, followed by the introduction of the concept of memristor and memristive systems, closely tied with resistive switching. The chapter continues with the introduction of the main redox-based switching mechanisms, of which the valence change mechanism is highlighted. The particular case of TaO_x-based ReRAM devices is then discussed and the experimental work of the thesis is introduced in the presented framework. Finally the main applications of resistive switching devices are introduced.

1.1 Definition and terminology

The phenomenon of resistive switching (RS) consists in the change of the resistance of a material induced by an electrical stimulus through atomic reconfigurations and/or nanoscale redox processes [1, 2]. This term is mostly ascribed to a non-volatile change, in the sense that the resistance is retained if the electrical stimulus is removed. Nevertheless, the change can also be volatile, phenomenon normally termed threshold switching. The simplest and more common case of resistive switching occurs between two different resistance states, a low-resistance state (LRS) and a high-resistance state (HRS). In many systems, multiple states can be achieved and even quasi-analogue behaviour can be obtained, with a very gradual change of the resistance. The operation causing the switching from the HRS to the LRS is termed SET, while the transition from the LRS to the HRS is called RESET. The SET operation is normally controlled by the imposition of a current compliance (CC) that limits the maximum current through the resistive switch.

The RS is distinguished in different types in terms of the relative polarity of the electrical stimulus necessary to induce SET and RESET. Fig. 1.1 shows the typical current-voltage ($I-V$) characteristics that can be observed when the RS elements are subjected to a *quasi-static* voltage sweep. This is the most common way of electrically characterizing the RS, and consists in the successive application of a fixed voltage during a short amount of time for different voltage values. In the most common approach, one measures a full cycle, where the voltage is swept from 0 V to a maximum value, then to a minimum (negative) value crossing 0

V and then finally back to 0 V (or vice-versa). For practical applications, a pulsed operation is preferred, where a single (or multiple) voltage pulse(s) of a specific value is(are) used to switch the resistance. In the case that both SET and RESET can be induced by the same voltage polarity, the RS is said to be unipolar (Fig. 1.1a). If, on the contrary, the SET and RESET occur for different voltage polarities, then the RS is said to be bipolar (Fig. 1.1b). More recently, other kinds of RS have been reported where the overall $I - V$ curves show a more complicated shape. This is the case for complementary resistive switching (CRS) and complementary switching (CS), shown in Fig. 1.1(c) and (d). The small difference in the two names is used here to highlight the origin of the complementary behaviour: as can be seen in Fig. 1.1, the material stack used for both cases is different. The CRS was first proposed to solve the sneak current path problem in crossbar arrays [3] and involves the use of two RS elements stacked anti-serially. On the other hand, the CS allows a similar $I - V$ curve but it can be obtained in a single stack [4, 5], therefore decreasing the number of fabrication steps needed. The CRS and CS can look like volatile switching because of the appearance of a hysteresis at higher voltage and the non-existence of one at low voltage. However, the switching is indeed non-volatile, although the state must be read in a specific way [6].

Unipolar RS is advantageous in terms of the peripheral circuitry involved in integrated systems. However, the differences in the physical mechanisms involved in the RS for redox-based systems make the bipolar RS more reliable and durable, when compared to the unipolar case. This will be highlighted in a following section where the main model mechanisms of redox-based RS are introduced.

1.2 Brief history of resistive switching

The first reports of the RS phenomenon go way back to the 1960s. In 1962, Hickmott showed negative differential resistance in metal-oxide-metal structures for five different oxides, some of which are still the most used RS materials nowadays: SiO, Al_2O_3, Ta_2O_5, ZrO_2 and TiO_2 [7]. In the next two years, Bashara and Nielsen showed reversible voltage-induced resistance change in Au/SiO/Au structures and suggested the use of this device structure as a memory element [8, 9]. In 1964, NiO was also introduced as switching oxide and shown to switch its resistance between 100-200 Ω and 10-20 MΩ with switching times as low as 100 ns [10]. By the end of the 1960s, the term "resistive memory" had already been coined and even analogue memory behaviour had been shown [11]. However, RS memories based on these earlier studies were never developed because of problems in stability and scaling of the devices, but also mainly due to the emergence and consequent explosion of the Si-based memories, which still dominate the memory market nowadays.

By the end of the 1990s, the resistive switching phenomenon reappeared in the literature, sometimes as a side effect in structures for magnetic applications, like magnetoresistive manganites [12]. The research into resistive switching had then a revival in the 1990s. In 2000, a group from IBM Zürich showed important improvements in the resistive memory technology by presenting reproducible non-volatile switching with voltage pulses with time duration shorter than 100 ns [13]. In 2002, the term RRAM, standing for Resistance Random Access Memory, was coined and a 1D1R (1 diode, 1 resistor) structure was proposed [14]. In 2004, a group from Samsung showed the first integration of resistive switching devices with CMOS technology, showing the feasibility of the integration of these devices and showing good prospects in terms of scalability [15]. This work was done with NiO and also coined the

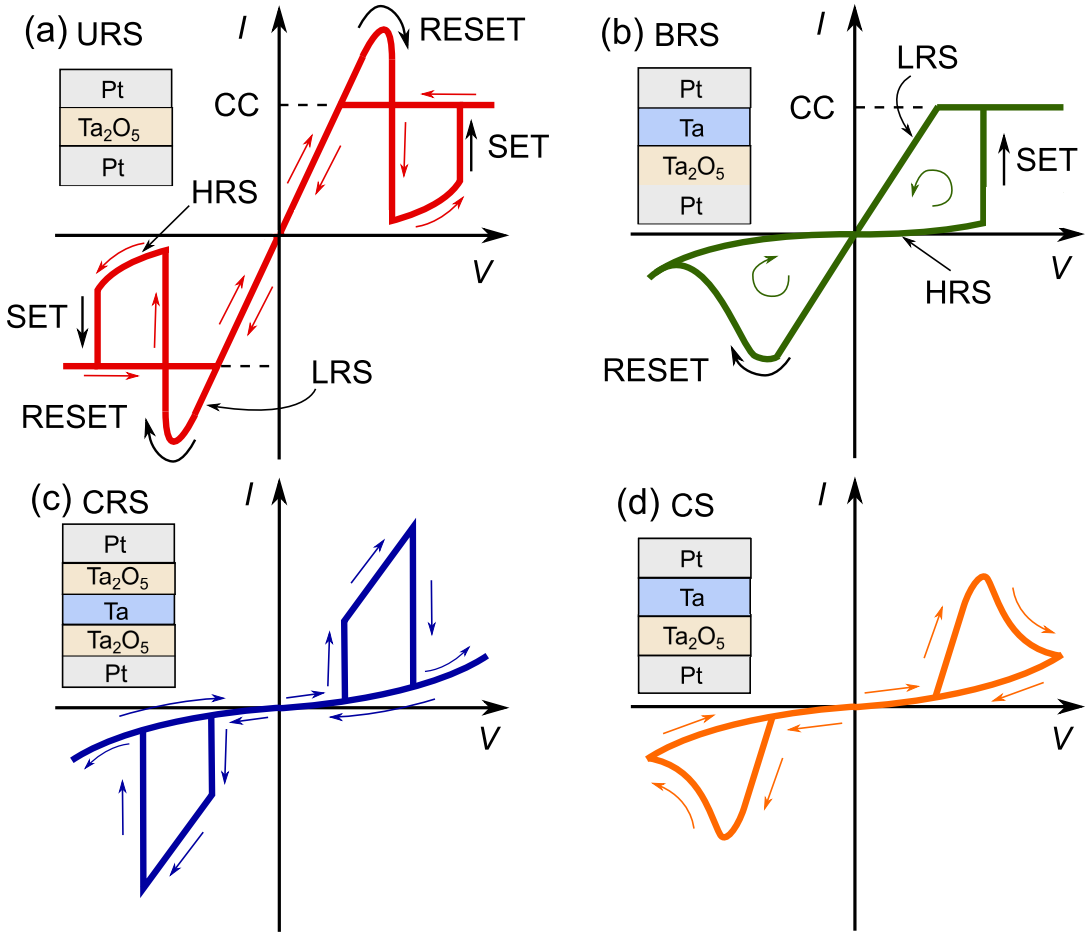

Figure 1.1: Illustration of the different current-voltage ($I-V$) characteristics obtained for the different types of resistive switching: (a) Unipolar resistive switching (URS) (b) Bipolar resistive switching (BRS) (c) Complementary resistive switching (CRS), using two anti-serially connected devices (d) Complementary switching (CS) using only one device. The $I-V$ characteristics are accompanied by typical materials stacks used to obtain the different behaviour in Ta_2O_5-based ReRAM. The BRS with the polarity shown in (b), with a positive SET and negative RESET, is obtained when the voltage is applied to the Ta top electrode, while grounding the Pt electrode. As can be seen, the stacks in (b) and (d) are identical in terms of the employed layers. However, the obtained behaviour can be controlled by tuning the thickness of the Ta layer, as will be discussed in section 1.5.2.

term OxRAM to define transition metal oxide-based RRAM.

An even bigger interest in the field was raised by a paper in 2008 from a group in HP Labs that established a link between the long known resistive switching effect and the memristor [16], a fundamental passive circuit element theoretically predicted by Leon Chua in 1971 [17].

1.3 The memristor and memristive systems

The memristor, acronym for memory resistor, is a fundamental passive circuit element theoretically predicted by Leon Chua in 1971 [17]. Chua analysed the mathematical relations between the four fundamental electric circuit quantities: the voltage v, the current i, the electric charge q and the magnetic flux ϕ. With these four variables it is possible to obtain six different mathematical relations, of which only five were already known: the relation between q and i, the relation between ϕ and v (Faraday's law) and the axiomatic definitions of the resistance (relation between v and i), the capacitor (q and v) and the inductor (ϕ and i), the three known fundamental circuit elements. Chua stated in his paper that from the logical, as well as axiomatic, point of view, it is necessary, for the sake of completeness, to consider a fourth fundamental circuit element that he named memristor. This element is then defined by the relation between ϕ and q and its name stems from its behaviour, which resembles a nonlinear resistor with memory. Fig. 1.2(a) summarizes the representation of the aforementioned quantities, their inter-relations and the four fundamental circuit elements.

The memristor is characterized by a quantity with dimensions of resistance named memristance, defined as:

$$M(q) = \frac{d\phi(q)}{dq}. \tag{1.1}$$

This expression can be transformed considering the other fundamental relations, in order to show a relation between the voltage and the current involving the memristance:

$$\begin{aligned} V &= R\left(q\right) I \\ \dot{q} &= I, \end{aligned} \tag{1.2}$$

where the resistance $R(q)$ represents the memristance M.

The concept of the memristor is purely mathematical and thus, ideal. By the time of its conception, no simple physical device fulfilled all the requirements to be classified as a memristor. However, the concept was further generalized to a class of dynamical systems, called memristive systems, for which some physical devices were immediately associated with: thermistors, the Hodgkin-Huxley membrane circuit model and discharge tubes [19]. The memristive systems are described by:

$$\begin{aligned} \dot{x} &= f\left(x, u, t\right) \\ y &= g\left(x, u, t\right) u, \end{aligned} \tag{1.3}$$

where u and y represent the input and output of a system and x is the state variable. For a current-controlled memristive system, these equations transform into:

$$\begin{aligned} \dot{x} &= f\left(x, I, t\right) \\ V\left(t\right) &= R\left(x, I, t\right) I\left(t\right), \end{aligned} \tag{1.4}$$

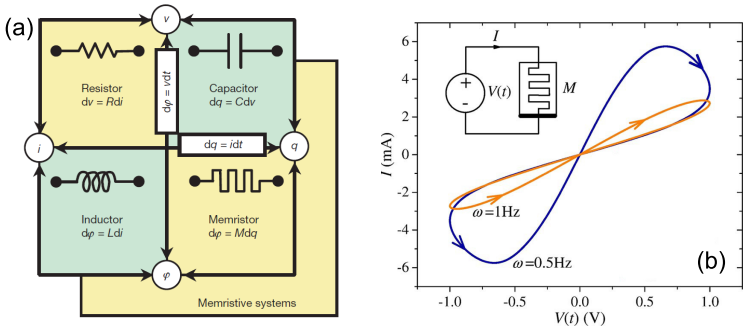

Figure 1.2: (a) Schematic picture of the four fundamental passive circuit elements: the resistor, the capacitor, the inductor and the memristor, according to Leon Chua. (b) Typical pinched hysteresis loop in the $I - V$ characteristic of an ideal memristor response to an AC voltage signal for two different frequencies, 0.5 and 1 Hz. Taken from [16] and adapted from [18], respectively.

A characteristic of these systems is the fact that they exhibit Lissajous figures with hysteresis in the current-voltage ($I - V$) plot, like the ones shown in Fig. 1.2(b). This characteristic fingerprint helped the group at HP Labs to establish the link between the memristor and the already known resistive switching phenomenon [16]. More recently, Chua himself stated that all two-terminal non-volatile memory devices based on resistive switching are memristors, regardless of the device material and physical mechanisms [20]. Despite this, a part of the scientific community is still sceptic regarding this link, especially because of the formal mathematical definition initially given by Chua that does not seem to be directly related to the experimentally reported RS [21]. Some have claimed that the memristor has indeed not been found and may not be even possible [22]. Other groups claim that the fourth element is a different one named transtor, where the link between the magnetic flux and the charge is more evident [23, 24]. Corinto et al. have also clarified that ϕ can be understood as voltage-momentum so that it does not necessarily have to be a magnetic flux [25]. Nevertheless, the popularity of the name memristor led to its almost indiscriminate use in the scientific community. All the different phenomena that induce similar change in the resistance of materials now fit under the denomination "memristive phenomena" and are presented in Fig. 1.3. In this thesis, the term "memristive device" will be used to describe electronic devices that exhibit some kind of memristive phenomena and that can be understood as memristive systems under certain additional conditions. For non-volatile resistive switching devices, the additional conditions are [26]:

1. The state variable x must have a material-dependent component, for example the magnetization (in MRAM), the crystallographic phase (PCM), or the length of a conducting filament formed by an internal redox process (ReRAM);

2. The state variable x must have a lower and upper limit, $x_{\min} < x < x_{\max}$;

3. Since $\dot{x}$ describes the kinetics of the switching process, the function f in $\dot{x} = f(x, I, t)$ must be highly nonlinear due to the voltage-time dilemma [27].

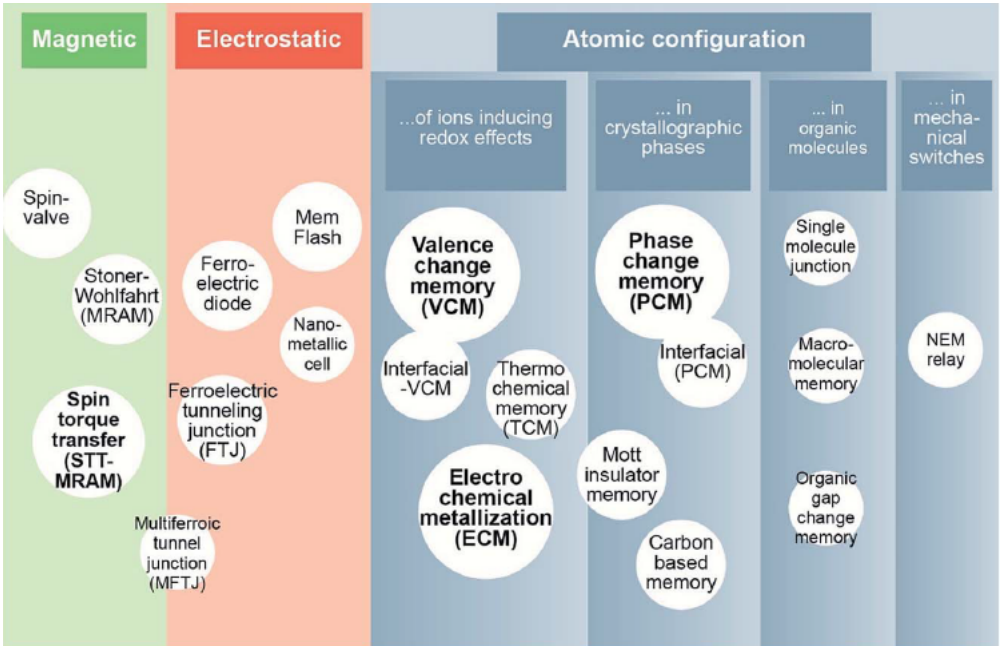

Figure 1.3: Survey of the different types of memristive phenomena. Taken from [26].

1.4 Redox-based resistive switching mechanisms

Most of the research done in RS is based on oxides and higher chalchogenides. In the majority of these systems, reduction-oxidation (redox) reactions play a pivotal role in the RS phenomenon [28]. The systems, either elements, cells or devices that function on this basis are generally termed redox-based resistive switching random access memory (ReRAM), which will be a generic term frequently used throughout this document. However, there are many phenomena that also lead to similar switching in the resistance of materials stacks via very different physical mechanisms. Fig. 1.3 summarizes the majority of phenomena that can be considered. These include magnetic memories such as spin-transfer torque magnetic random access memory (STT-MRAM), ferroelectric memory based on ferroelectric tunnel junctions, as well as phase change memory (PCM). All these emergent memory technologies have been proposed as alternatives to the current memory paradigm. Other interesting phenomena are based on purely electronic effects that include charge trapping- and Mott transition-induced RS [29]. A particular case of charge trapping is the so-called nanometallic resistive switching, where the insulator layer is “doped” with metallic particles [30–32]. Here, the charge trapping induces a metal-insulator transition. The Mott transition is also based on a metal-insulator transition. However, for this case, the transition is induced by electronic correlations that are only possible for a restricted group of materials. Two of the most popular for resistive switching applications are the metal oxides Cr:V_2O_3 and NbO_x [33, 34]. Although very different physics underlies these technologies, the overall result is a change of the electrical resistance of the device. For clarification, the term resistive switching (RS) will be used throughout the text to refer to the redox-based phenomena only.

The RS is normally obtained in metal-insulator-metal (MIM) structures. Metal oxides are the most common choice for the insulator layer. Three major classes of redox-based RS mechanisms were identified [28]: the thermochemical mechanism (TCM), the electrochemical

mechanism (ECM) and the valence change mechanism (VCM). The dominant mechanism is determined by the balance between thermochemical and electrochemical redox reactions [35]. In these mechanisms, the change in resistance is normally ascribed to the formation of conductive filaments in the insulator layer. Although all three redox-based mechanisms are being widely studied, two of them seem more suitable for applications: the ECM and the VCM. The RS associated with these two mechanisms is favoured since it shows lower power consumption and superior reliability compared to the TCM-based RS devices [36]. However, the ECM is much better understood than the VCM due to the more elaborated existing physics-based device models [37].

All the three mechanisms share some common features. Namely, the RS is caused by atomic reconfiguration and redox reactions at the nanoscale. Also, the RS is preceded by an initiation step known as electroforming (EF, or just forming), which redistributes the atoms/ions in the insulator layer and enables the RS. The RS is most of the times filamentary in nature, in that a filament with a higher conductivity is formed in the insulator layer during EF and is the main enabler of the RS process.

1.4.1 TCM - Thermochemical Mechanism

When thermochemical redox reactions dominate the switching, it can be understood through the thermochemical mechanism (TCM). The TCM is based on redox reactions and stoichiometry changes driven by high temperatures achieved via the Joule effect [35]. Due to inhomogeneities in the material it is more probable that these reactions occur very locally, giving rise to the formation of a filament with a higher conductivity. This establishes the LRS. The disruption of the filament and consequent transition to the HRS, is also achieved with local heating of the filament. The RS is thus intrinsically unipolar, because it depends only on the square of the current through the Joule effect. Limiting the maximum current is very important to control the SET transition, especially the dimensions of the filament that is created and to prevent a total breakdown of the oxide that would otherwise ruin the device.

In more detail, the RS is preceded by a thermally induced electroforming process, which corresponds to the first SET transition. As the current is flowing through the insulator, the Joule heating promotes a local increase in the temperature T, according to the equation:

$$\sigma \mathscr{E}^2 = c_V \frac{\partial T}{\partial t} - \nabla \cdot (\kappa \nabla T)\,, \tag{1.5}$$

where σ and κ represent, respectively, the electrical and thermal conductivities of the insulator, c_V is the specific heat of the same material and $\mathscr{E}$ the applied electric field. The last term of the equation represents the heat conduction in the insulator. The electrical conductivity in insulators and semiconductors is generically given as a function of the temperature as

$$\sigma \propto \exp\left(-\frac{E_a}{k_B T}\right), \tag{1.6}$$

where E_a represents the activation energy of the process that promotes the conduction and k_B is the Boltzmann constant. The combination of the processes described by equations (1.5) and (1.6) leads to an uncontrolled increase of the electrical current, which is called thermal runaway. This runaway induces a soft dielectric breakdown, controllable via the CC, that occurs in a filamentary way, as already mentioned. The temperature increase promotes the formation of transition metal oxides with lower valence of the cations through the motion of

oxygen anions out of the heated region. The Ellingham diagram, shown in Fig. 1.4, which represents a plot of the Gibbs free energy of formation of the oxides as a function of the temperature, helps predict the behaviour of the transition metal oxides with the increase in temperature [35]. In TiO_2, for example, Magnéli phases of the type Ti_nO_{2n-1}, which are thermodynamically more stable above a critical temperature, were observed in the conductive filament through high resolution transmission electron microscopy [38].

TCM-type ReRAM cells are normally achieved with symmetrical MIM structures with oxides that show a lower resistivity in reduced states such as ZrO_x, TiO_x, Fe_2O_3, CoO, CuO, NiO, Al_2O_3 and SiO_2 and with inert metallic electrodes such as Pt or Ir. In this mechanism the role of the electrodes is not as significant as for the other two, so in principle almost all metals or electron conductors can be used, except electrochemically active metals, which should give rise to the ECM. The most prominent structure has been the Pt/NiO/Pt stack [2].

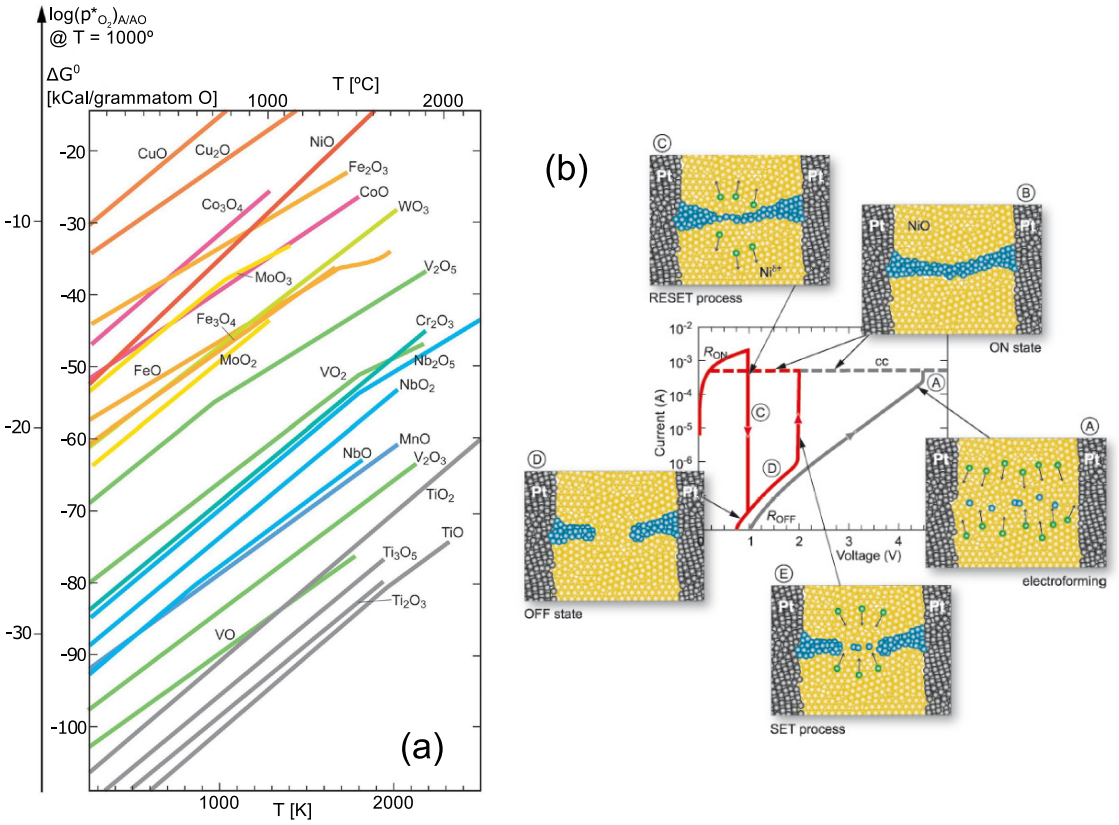

Figure 1.4: (a) Ellingham diagram. Adapted from [35]. (b) Model of the thermochemical mechanism for the prototypical structure Pt/NiO/Pt: in the centre there is a plot of the typical $I-V$ characteristics observed in TCM systems; around the central plot there are schematic depictions of the evolution of the atomic configuration throughout the different stages of the RS process. The green spheres represent the Ni ions, while the blue spheres represent Ni atoms (or at least NiO with lower oxygen content). Adapted from [2].

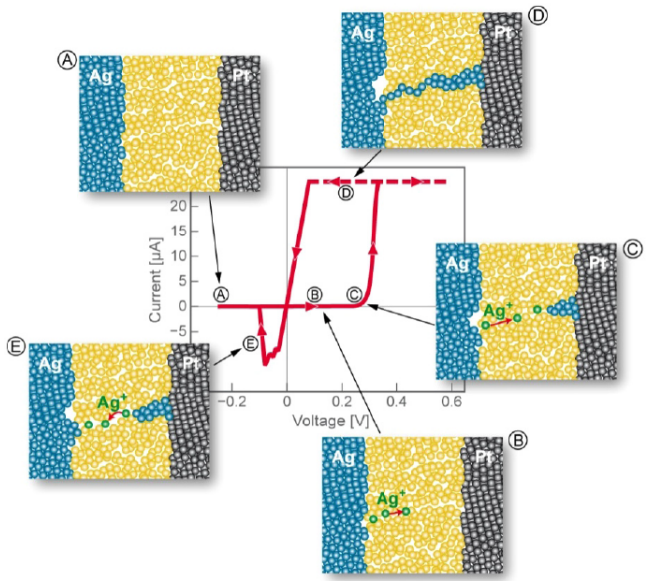

Figure 1.5: Schematic model of the electrochemical mechanism: in the center there is a plot of the typical $I-V$ characteristics observed in ECM systems, here exemplified for a Ag/solid electrolyte/Pt system where the Pt electrode is grounded and Ag is the biased electrode; sketches of the different stages of the RS in ECM systems are depicted around the central graph. The green spheres represent Ag^+ cations, while the blue spheres represent Ag atoms. Taken from [39].

1.4.2 ECM - Electrochemical Mechanism

The electrochemical mechanism (ECM) is proposed to explain the bipolar RS in a MIM structure composed of an electrochemically active electrode, a solid electrolyte as the insulator layer and an electrochemically inert electrode. A solid electrolyte is a good ionic conductor, a material where the ions have a high ionic mobility. In this case, the filament responsible for the RS is metallic and is formed as a result of electrochemical reactions occurring along the structure. While one polarity reconstitutes the filament, leading to the LRS, the opposite polarity induces its dissolution, resulting in the HRS [39]. Fig. 1.5 shows a typical $I-V$ characteristic obtained in ECM systems, as well as schematic depictions of the switching mechanism.

The SET transition is initiated with the anodic dissolution of the electrochemically active metal M_a, described by the reaction

$$M_a \rightarrow M_a^{z+} + ze^-, \tag{1.7}$$

where M_a^{z+} represents the metallic cations in the solid electrolyte and z defines the total charge of the cation. Under the action of the high electric field, the M_a^{z+} ions drift across the solid electrolyte towards the inert electrode. On the surface of the latter electrode, there is the reduction and electro-crystallization of the metal according to the cathodic deposition reaction given by

$$M_a^{z+} + ze^- \rightarrow M_a. \tag{1.8}$$

This last process is electric-field-enhanced and leads to the formation of a metallic filament that grows in the direction of the active electrode, eventually bridging the two electrodes and

leaving the resistive cell in the LRS. This state is maintained until a sufficiently high voltage of the opposite polarity is applied between the electrodes. This induces the dissolution of the filament, which corresponds to the RESET process. The first creation of the filament, during the EF, differs from the subsequent SET operations, usually showing different switching parameters, such as higher voltage. One suggestion is that the EF creates a channel in the electrolyte that later serves as a template for the following filaments [39].

Typical ECM structures use a reactive metal, such as Ag, Cu or Ni, as active electrode, while non-reactive metals such as Pt, Au or Ir are common for the inert electrode. For the insulator layer, either a solid electrolyte or an oxide is needed. Common examples of the former are Ag_2S, amorphous Si, C, GeSe, GeS, (Zn,Cd)S, while popular oxides are SiO_2, ZrO_2, Al_2O_3, Ta_2O_5 and WO_3 [1, 28].

The RS based on the ECM is likely the most mature for large scale industrial implementation. This type of ReRAM is also known as Conductive Bridge RAM (CB-RAM) or Programmable Metallization Cells [39].

1.4.3 VCM - Valence Change Mechanism

Similarly to the ECM, the valence change mechanism (VCM) is based on ion migration. The RS is thus also bipolar, caused by the motion of the charged ions under the electric field. The main ionic species responsible for the RS are the oxygen anions, which induce redox processes [28]. However, it is now understood that also the metal cations can play a role in the switching process [40]. The motion of the oxygen anions is more commonly described by the opposite motion of oxygen vacancies, represented by $V_O^{\bullet\bullet}$, according to the Kröger-Vink notation [41]. The cations most probably occur as interstitials in the oxide [40]. Both oxygen vacancies and cation interstitials can act as mobile donors in the metal oxide [40], thus giving rise to an increased conductivity in the conductive filament. Similarly to the ECM case, also an assymetrical MIM structure is normally required. In this case, a transition metal oxide is sandwiched between an active electrode (AE) and an ohmic electrode (OE), where the AE has a low oxygen affinity and a high work function, and the OE has a high oxygen affinity and a low work function. Examples for AE are Pt, Ir and TiN, whereas for the OE it is common to use metals such as Ta, Hf, W or Ti. It is very common to use the metallic element correspondent to the metal oxide as OE, for example, Hf for a HfO_2 insulator layer and Ta for a Ta_2O_5 layer.

The VCM owes its name to the change of the valence state of the metal cations in metal oxide-based RS. This was directly observed several times through techniques based on X-rays that are sensitive to the local chemical environment, such as X-ray absorption near-edge structure spectroscopy (XANES) [42], or X-ray photoemission electron microscopy (XPEEM), a spectromicroscopy technique [43, 44]. The valence change occurs due to the redistribution of the defects in the insulator layer, such as the oxygen vacancies and the cation interstitials. Direct experimental evidences of the existence of conductive filaments in VCM systems have been obtained via spectromicroscopy [45], atomic force microscopy-related techniques [46, 47] and transmission electron microscopy [48, 49].

Besides the more frequent filamentary-type switching, some VCM systems exhibit a homogeneous change of the resistance along the whole area of the active interface [50]. This area-dependent or interfacial RS is normally obtained in bi-layered structures, for example in devices based on $Sm_{0.7}Ca_{0.3}MnO_3/La_{0.7}Sr_{0.3}MnO_3$ [51], $Pr_{1-x}Ca_xMnO_3/ZrO_2(Y)$ or TaO_x/HfO_x heterostructures [52]. In some cases both filamentary and area-dependent switch-

ing can be observed in the same structure [53, 54]. An additional feature that distinguishes different kinds of VCM systems is the polarity of the bipolar RS, *i.e.* the voltage polarity that induces the SET or RESET transitions. The polarity can be distinguished by the way the RS $I-V$ curve is obtained. Some groups use the designations eightwise (8W) and counter-eightwise (C8W) in relation to the way we hand draw a figure of "8" [26]. Equivalently, one can use the designations "positive-set-negative-reset" and "negative-set-positive-reset", if the voltage is applied to the active electrode and the ohmic electrode is grounded, in the same sense as 8W and C8W, respectively [55]. Coexistence of both 8W and C8W has also been reported several times [53–58]. The more common switching mode, and the one that will be of interest to the discussion of this work, is the filamentary C8W switching. Therefore, this specific mode will be introduced in more detail.

Mechanism for filamentary C8W-switching

The proposed mechanism for the filamentary C8W VCM switching is schematically depicted in Fig. 1.6, along with a typical $I-V$ characteristic obtained in a $Pt/ZrO_x/Zr$ RS cell. As can be seen in the lower right corner of Fig. 1.6, after the EF the cell is composed of two main components: the plug and the disc. The plug is the formed filament, composed of a highly oxygen deficient material, that does not change significantly thereafter. The disc corresponds to the interfacial region between the plug and the active electrode where the switching takes place. As pointed out already, the switching occurs due to the motion of oxygen vacancies in the oxide during the SET and RESET processes, respectively (b) and (d) in Fig. 1.6. The accumulation of oxygen vacancies in the disc leads to the LRS, shown in (c) of Fig. 1.6. Their depletion from the same region leads to the HRS, shown in (a) of Fig. 1.6 [2].

According to this mechanism, the oxygen vacancies play a key role in the RS. The filament that constitutes the plug is rich in oxygen vacancies, which serve as donors in transition metal oxides. A higher concentration of oxygen vacancies leads to a change of the valence states of the transition metal cations, through reduction of the oxide, and consequently to a higher n-type conductivity. This type of conductivity is favoured because for most MO_x oxides, the native donors, $V_O^{\bullet\bullet}$, have shallow energy levels, while the native acceptors, such as V_M'', have energy levels which are deep in the band gap [2]. The oxygen ions move by hopping from site to vacant site within the oxide layer. The hopping is achieved by overcoming an energy barrier ΔG_{hop}. The ionic transport can be mathematically described by the Mott-Gurney law of ion hopping:

$$j_{hop} = 2zecaf \exp\left(-\frac{\Delta G_{\mathrm{hop}}}{k_{\mathrm{B}}T}\right) \sinh\left(\frac{aze}{2k_{\mathrm{B}}T}\mathscr{E}\right), \tag{1.9}$$

where a is the mean hopping distance, f the attempt frequency, z the charge number of the hopping ion, c the ion concentration and $\mathscr{E}$ the electric field. This expression, however, overestimates the ion mobility in very high electric fields, which can probably occur locally during resistive switching. In such cases, an extension of this law is more adequate [59]. The hopping distance varies with the structural order of the oxide and is in the range of atomic distances in crystals [60]. The degree of the structural order of the oxides used in the MIM structures is also an important aspect for the understanding of other processes involved in the RS. The amorphous, polycrystalline or single crystalline character of the oxides should lead to differences in the mechanisms, specially on the diffusion and on the electrical and thermal

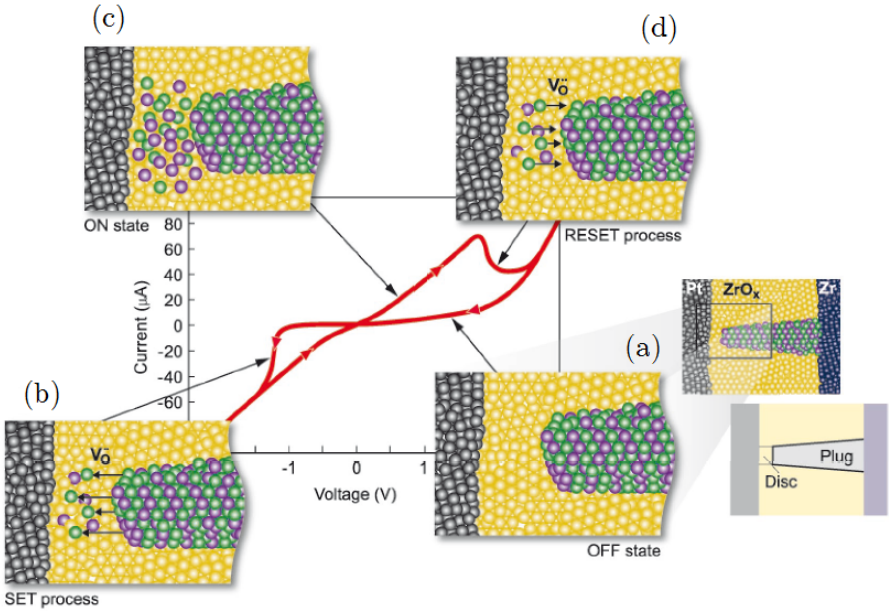

Figure 1.6: Schematics of the proposed mechanism for filamentary C8W VCM switching along with a typical $I-V$ characteristic measured for a $Pt/ZrO_2/Zr$ cell where the AE Pt is biased and Zr, the OE, is grounded. Around the central plot, the different stages of the RS process are schematically depicted. These stages are: (a) HRS (b) SET process (c) LRS (d) RESET process. The green spheres represent the mobile oxygen vacancies and the purple spheres the immobile Zr ions with a lower valence state. The configuration of the cell after EF is also schematically depicted with the plug and disc regions that are the responsible for the RS. Taken from [2].

conductivity [61]. For example, the electromigration of the oxygen vacancies in $SrTiO_3$ single crystals can occur through dislocations [62].

At the AE/oxide interface, there is normally a Schottky barrier due to the high work function of the metal and/or to the higher or lower capacity of the metal to reduce the oxide. The change of the oxygen vacancy concentration in the disc leads to a modulation of the height of the Schottky barrier. A higher concentration of these defects on the interface decreases the barrier height, resulting in the LRS. On the other hand, the HRS is obtained with a lower concentration of the same species of defects at the interface [63]. RS models based on the modulation of this Schottky barrier have enabled very good prediction of the RS behaviour [64, 65].

The VCM is not only an electric field-induced phenomenon, as the temperature also plays a key role in enabling the switching. Simulations of VCM cells with typical materials indicate a drastic increase of the temperature in the plug and in the disc relatively to the remaining cell [27]. This temperature increase strongly affects the mobility of the oxygen vacancies, leading to the highly nonlinear switching kinetics observed for VCM cells. The electric field acceleration is not enough to explain the kinetics data. Both field and temperature accelerations are needed to explain the experimental data. The SET time varies many orders of magnitude as the voltage is increased [27]. Experimentally, temperatures over 1000 K due to Joule heating in the conductive filaments have been measured [66–70].

Electroforming

The electroforming (EF) is also an important first step towards the achievement of VCM-type RS. It enables the creation of oxygen vacancies in the oxide and the formation of the plug that comes in the vicinity of the AE, as was directly observed by conductive atomic force microscopy [53]. The generation of oxygen vacancies can happen simultaneously with the release of oxygen gas, according to the oxygen exchange reaction in the Kröger-Vink notation given by [28]:

$$O_O \rightleftharpoons \frac{1}{2}O_2\,(g) + V_O^{\bullet\bullet} + 2e'. \tag{1.10}$$

This reaction occurs in a localized region at the oxide/OE interface and corresponds to a reduction of the oxide [28]. The release of oxygen gas has actually been observed, with the accumulation of gas bubbles underneath the surface of the MIM structures [62, 71]. Depending on the voltage polarity used during the EF, the device can end up in the LRS or in the HRS, due to the polarity-dependent motion of the oxygen vacancies [72]. The presence of the $V_O^{\bullet\bullet}$ changes the valence state of the neighbouring metal cations of the metal oxide film, giving the name to the mechanism [73].

Additionally, the forming procedure can be facilitated by promoting an oxygen exchange between the oxide layer and the OE. The oxygen is extracted from the oxide and oxidises the OE metal. This reaction introduces oxygen vacancies in the oxide film close to the interface with the OE, which reduces the voltage needed for the EF. This exchange reaction should occur during deposition of the OE on top of the oxide layer [73]. For some cases, the right engineering of the layers' thickness can even avoid the need for the EF, enabling a forming-free device, as shown for $SrTiO_3$ with a Ti OE [57]. This is very relevant for practical applications due to the normally high voltages needed to form the devices, the inherent stochasticity imposed by the EF and the sometimes irreversible degradation caused by the procedure. The EF can also be avoided if the device stack includes a highly oxygen-deficient oxide layer adjacent to the stoichiometric oxide where the RS occurs. The former serves as an oxygen vacancy reservoir, avoiding the need for the defect generation [74]. Other ways to eliminate the need for EF include special annealing procedures, creating impurity doping profiles [57] and decreasing the dimensions of the oxide layer, as shown for HfO_x with a thickness below 2.5 nm [75]. Ion implantation is another useful tool to prepare forming-free devices, either during device fabrication [76] or as a post-fabrication treatment [77].

1.5 The particular case of TaO_x-based ReRAM

1.5.1 From TiO_x to TaO_x

The 2008 paper by Strukov et al. [16] linking the experimentally observed RS phenomenon to the memristor theoretical framework increased the visibility of the research topic. Besides that, the material that was used to produce the RS devices shown in the paper was TiO_2. This, in conjunction with the vast literature on the electronic and crystallographic structures of this material, led to it being considered a prototypical memristive material [61]. However, the rich phase diagram of the Ti-O material system, with multiple intermediate phases, could be responsible for the big variability and low endurance observed in TiO_x-based ReRAM [78, 79]. Therefore, the research on this system has decreased lately. On the other hand, TaO_x-based ReRAM got the focus of the RS community due to the very high endurance

and fast switching speed obtained in such devices. First, Wei et al. from Panasonic showed an endurance of up to 10^9 cycles in $Pt/TaO_x/Pt$ [80]. This record was later surpassed by Yang et al. that reported 1.5×10^{10} cycles [78]. The absolute maximum so far in TaO_x-based devices was achieved by Lee et al. in 2011, with over 10^{12} cycles obtained in bi-layered $Pt/Ta_2O_{5-x}/TaO_{2-x}Pt$ structures [81]. The high endurance of TaO_x-based ReRAM is probably related to its more stable amorphous phase and adaptive lattice rearrangements of the oxygen vacancies when compared to other metal oxides [82]. On the other hand, the TaO_x proved to be not only reliable in terms of switching endurance, but also in terms of operation speed. Torrezan et al. reported sub-nanosecond switching in $Ta/Ta_2O_5/Pt$ devices, with SET and RESET being achieved with pulses as short as 105 and 120 ps, respectively [83]. These high performance characteristics made TaO_x the most popular RS material systems in the research environment. The popularity of TaO_x devices culminated in the world's first mass production of ReRAM-based products implemented by Panasonic in 2013, where TaO_x ReRAM was used as memory in 8-bit microcontroller units for embedded applications [84, 85].

1.5.2 Overview of TaO_x-based ReRAM

TaO_x is thus a highly popular material to be used as the insulator layer in ReRAM devices. Although it is also sometimes used as the solid electrolyte layer in ECM devices [39], most of the times, the switching mechanism involved in TaO_x-based devices is the VCM.

Pt is by far the most used active electrode material [46, 73, 86, 87]. Due to its compatibility with the CMOS fabs, TiN is also used several times [48, 88]. Regarding the ohmic electrode, an oxygen scavenging layer (oxygen exchange layer) is normally the choice. The material chosen for this layer is important in defining the retention properties of the devices. Electrodes such as Ti lead to short retention, as the HRS drifts to the LRS due to the constant movement of oxygen towards the Ti electrode. This occurs because it is thermodynamically more favourable to form TiO_x than TaO_x [88]. A similar behaviour occurs with a Hf electrode [73]. On the other hand, using Ta as the ohmic electrode enables good retention, especially for a sufficiently thick Ta layer [88]. Therefore, the structure $Ta/Ta_2O_5/Pt$ is one of the standard structures for TaO_x-based VCM-type RS. Besides having a determinant effect on controlling the retention properties, the thickness of the Ta electrode can toggle the switching mode in Ta/Ta_2O_5 devices. For a fixed Ta_2O_5 layer thickness of 5 nm, a 15 nm-thick Ta electrode leads to bipolar resistive switching, while a 5 nm-thick Ta layer induces complementary switching [89].

In terms of the switching, the $Ta/Ta_2O_5/Pt$ structure follows the filamentary C8W-VCM mode described in section 1.4.3. The RS proceeds typically between two different resistance states: the LRS and the HRS. In the LRS there is a conductive filament connecting the electrodes. Most of the literature considers the formation of a single conductive filament, which has been observed, for example, via spectromiscroscopy [45]. The diameter of such filaments normally ranges between approximately 10 nm and 100 nm [46, 65, 90]. On the other hand, bilayer structures with two TaO_x layers differing in composition, show multiple filaments in the same device [91]. There are also studies that show different geometries of the conductive region. For example, Skaja et al. clearly report the formation of dendrite-like conductive paths, whose appearance was linked to the presence of an adsorbate layer with moisture and hydrocarbons [44]. But the debate continues, because there is still no consensus on the exact composition and structure of the conductive filaments. Many studies

refer to filaments composed of oxygen vacancies [86, 92–94], whereas others mention filaments consisting of very Ta-rich phases or even metallic Ta phases [46, 91, 95, 96].

1.6 Introduction of the thesis in the presented framework

As it was mentioned, the exact structure and composition of the conductive filaments in Ta_2O_5-based ReRAM devices is not clear. This has obvious implications for the transport properties of the ReRAM devices, therefore there are also different types of conduction mechanisms that have been considered. On the other hand, due to the nanoscale dimensions of the filaments, it proves very challenging to study these objects using conventional methods for composition and structure determination. For these reasons, this work focuses on the electronic transport properties as a tool to gain information on the filaments, more specifically on the conduction mechanisms involved and their composition and structure. The ReRAM structure selected to perform the study was the $Ta/Ta_2O_5/Pt$, for the reasons described earlier.

One thing that is rather accepted by the community is the key role of the movement of oxygen in the oxide layer. Starting from the stoichiometric Ta_2O_5, it is straightforward to admit that the filament will then be composed of some oxygen-deficient phase based on Ta and O. Although there are studies on the electrical transport in substoichiometric TaO_x, these mostly focus on films with $x > 2$ where the conductivity stems from phonon-assisted tunnelling between traps [97–99], or on films where the TaO_x behaves as a Fermi glass with charge carriers hopping between conduction centers identified as neutral oxygen vacancies [79, 100]. These models should, however, fail in the interesting region where TaO_x has low values of x, as it is expected for the material that composes the conductive filaments.

Taking advantage of this link between the material that composes the filament inside the $Ta/Ta_2O_5/Pt$ ReRAM devices and the substoichiometric TaO_x films, the work presented in this thesis aims at experimentally studying the electrical transport properties of these two systems. The work then naturally divides itself in two parallel roads, a "device road", where the transport in the conductive filaments inside Ta_2O_5 ReRAM devices is assessed, and a "fundamental physics road", where the transport in substoichiometric TaO_x thin films is studied. The flexibility in designing the geometry of the latter samples enables the use of other experimental techniques that cannot assess the conductive filaments, such as typical structure characterization techniques. The objective is to verify if the roads intertwine and if there are correlations between the transport in both systems, with the final objective of retrieving relevant information about the conductive filament material and conduction. The preceding Fig. 1 in the introduction schematically shows the above mentioned approach to the experimental work developed in the framework of the thesis and connects the different parts of the work to the different chapters of the text, for an easier navigation.

1.7 Applications of ReRAM

Memristive devices in general, and ReRAM in particular, show excellent prospects for numerous applications. The two biggest drivers of research in this topic are the memory industry and neuromorphic computing. The former was acknowledged early on, while the latter has been pointed out more recently and has evolved to be the main focus of research in the last couple of years.

1.7.1 Memory

The use of RS for the development of a memory technology was put forth in the 1960s [8, 9]. However, technological difficulties and the rapid development of Si-based technologies led to a decrease in interest, until the idea was later revived in the 1990s. Another reason for the recent increase in research in emergent memories like ReRAM is the scaling limitations that the established complementary metal-oxide-semiconductor (CMOS) transistor-based technologies are facing. Moore's law [101], which states that the number of transistors that can be integrated on a chip of fixed area doubles every 12 months (later amended to doubling every 18-24 months), is indeed coming to an end in the near future [102]. This is mostly related to the problems in continuing with the miniaturization of the transistors, which leads to increased heating and high leakage current through the gate oxide. An early sign that Moore's law was in its final stages came with the end of Dennard's scaling rules in around 2004. Up until then, Moore's law ran in conjunction with Dennard's scaling [103], which showed how to keep power consumption of the integrated circuits constant while increasing their density. To maintain the performance of the transistors with further miniaturization (according to Moore's law), it was necessary to limit the power density in the chips [104].

The great majority of the memory devices used nowadays are Dynamic Random Access Memory (DRAM) to act as main memory and NAND-Flash for storage. These are based on the CMOS technology, which means they too are facing the physical limits of miniaturization and related consequences. Therefore, ReRAM, as well as other memristive phenomena-based memory technologies, are promising as substitutes to enable the next generation of memories. Due to the excellent scaling prospects and competitive switching speed and endurance compared to the DRAM technology, it was expected that ReRAM would grow to eventually replace DRAM [21, 105], at least in some applications [106]. However, the still-low reliability [107], limited endurance and operation speed of the ReRAM do not favour the immediate transition from DRAM to ReRAM [21]. On the other hand, the NAND-Flash community solved the problem so far with the exploration of the third spatial dimension, with the advent of the 3D vertical NAND-Flash, which can be envisioned as a stack of layers of NAND-Flash arrays. This disruptive transition enabled a change of focus from the continuing miniaturization of the transistors to the stacking of the arrays [108].

In terms of performance, there is still a big difference between DRAM and NAND-Flash. While the former enables very fast operation speed at a high cost, the latter is very cheap to produce at a loss of operation speed. To bridge this performance/cost gap, a new type of memory was put forth, called Storage Class Memory (SCM). The idea of the SCM is to fill this gap between the fast, volatile DRAM, used for memory and computation, and the slower, non-volatile NAND-Flash, used for storage [109]. Fig. 1.7 illustrates the emergence of the SCM by comparing the main memory technologies in a plot of the access time vs. the cost of a die. This vacant position for a SCM offers a great opportunity for the emergent memory technologies based on resistance change, as these technologies are non-volatile, present operation speed between that of DRAM and NAND-Flash and can, in principle, be cost-effective. Table 1.1 lists the main performance parameters of four of the emergent memories: ReRAM, phase-change memory (PCM), spin-transfer-torque magnetic random access memory (STT-MRAM) and ferroelectric random access memory (FeRAM). The table includes also the values for the two established technologies, DRAM and NAND-Flash. All of the emergent memories can almost reach DRAM in terms of speed and endurance offering at the same time non-volatility, while they operate much faster and endure much more operation cycles than NAND-Flash.

Beyond that, ReRAM offers very high density and simple fabrication (associated with low cost) as the main advantages, while lacking the maturity of PCM and the high endurance and performance of STT-MRAM. As main drawbacks the ReRAM technology still has a low reliability and cycling endurance. On the other hand, PCM demands a higher switching power, STT-MRAM technology faces difficulties in the fabrication of the magnetic tunnel junctions, mainly patterning and etching issues, as well as a back-end-of-the-line thermal budget, and FeRAM also struggles with reliability issues. Therefore, ReRAM is in a good position to fill the role of SCM [110].

Recently, Intel and Micron have partnered in the development of a new technology coined “3D X-Point”, with Intel releasing the first product that fits in the SCM typology, called "Optane", based on this technology [112, 113].

1.7.2 Neuromorphic computing

The need for alternative forms of computing stems from the inefficiency of traditional computing architectures to deal with the big data paradigm we are facing nowadays. The computing architecture has suffered few changes since the initial modern computers and is based on the pioneering work of the mathematician and physicist John von Neumann [118]. According to the traditional von Neumman architecture, the central processing unit (CPU), responsible for processing the data, is physically separated from the memory unit, where both the data and the processing instructions are stored. Therefore, to transfer the data between the CPU and the memory, a communication lane, termed “bus”, is needed. This paradigm is labeled “conventional computing” in Fig. 1.8 where different computing approaches are presented. The problem of using conventional computing for data intensive applications is that the data transfer rate of the bus effectively limits the computing speed and increases the energy cost. This is known as the “von Neumann bottleneck". While this problem has been traditionally solved by optimizing specific characteristics of this architecture or by employing parallel computation, a much more radical and ingenious approach is to redesign the architecture so that the CPU and the memory are no longer separated. This allows for “in-memory” or “stateful logic” computing, as is also shown in Fig. 1.8. For this purpose, devices that can function both as memory and as logic devices for computations are needed. Interestingly enough, the brain computes in a similar fashion but with a totally different architecture. The neurons in the brain establish many connection between themselves and form a neural network, which acts both as memory and processing unit. This establishes the third computing paradigm in Fig. 1.8, known as neuromorphic computing.

So far, brain-like computing has been achieved mainly by software emulation of several brain functionalities by using the established CMOS technology. This approach is largely based on artificial neural networks and machine learning algorithms such as deep learning, which enabled very important steps in the demonstration of the potential of this kind of computing [119]. Examples are IBM’s supercomputer Watson that beat the champions of the American quiz show “Jeopardy!” in 2011 [120, 121] and the Google DeepMind’s AlphaGo computer program that beat the world champion in the strategy game Go in 2016 [122, 123]. These are two very complex tasks for computers. The main issue is that these artificial brains consume much more energy than the natural brain they take as a model. While the brain runs at a power of approximately 20 W, these computers need several tens of kW to MW [119]. It is then clear that new approaches are required to enable energy-efficient brain-like computing. This can be achieved when the neuromorphic computing is achieved at the hardware level.

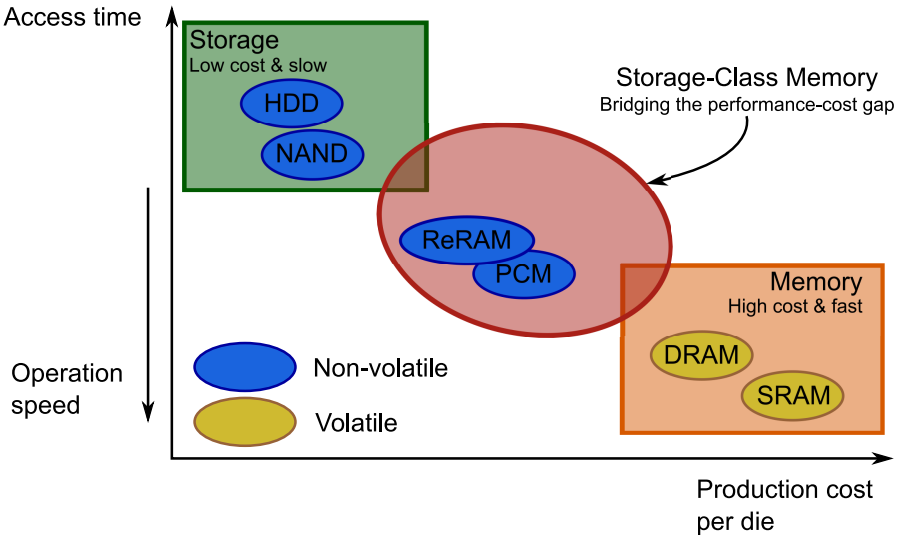

Figure 1.7: Qualitative plot of the access time as a function of the production cost per die for the main memory technologies, illustrating the emergence of the (speed) performance-cost gap and the storage class memory as a new memory class to fill this gap. The emergent memory technologies are naturally positioned in the SCM domain and, therefore, are promising for this application. While the relative positioning of the three groups is the main information of the figure, the relative positioning of the different technologies inside each group is not necessarily meant to be real and accurate. The figure was drawn based on a figure designed by Western Digital and published in *PC Mag* [111].

Table 1.1: Comparison of different emergent memory technologies based on the general device requirements and main performance parameters. The data for the emergent memories was taken from [110], while for DRAM and NAND-Flash the information was taken from [21, 114–117].

Technology	ReRAM	PCM	STT-MRAM	FeRAM	DRAM	NAND-Flash
Cell size	4-12F^2	4-30F^2	6-50F^2	15-34F^2	6F^2	5F^2
Multibit	2	2	1	1	Yes	4
Voltage	< 3 V	< 3 V	< 1.5 V	< 4 V	< 1 V	> 5 V
Read time	< 10 ns	< 10 ns	< 10 ns	< 10 ns	10 ns	10 μs
Write time	< 10 ns	≈ 50 ns	1-10 ns	≈ 30 ns	< 10 ns	100 μs
Write current	10-100 μA	80-200 μA	> 50 μA	< 100 μA	—	—
Retention	10 years	10 years	10 years	10 years	64 ms	10 years
Endurance	$> 10^6 - 10^{12}$	$> 10^9$	$> 10^{15}$	$\approx 10^{10}$	$> 3 \times 10^{16}$	$> 10^5$
ON/OFF ratio	10^{1-4}	10^{1-4}	TMR $= 100 - 200\%$	10^{2-3}	—	—
Write energy	0.1-1 pJ per bit	10 pJ per bit	≈ 0.1 pJ per bit	≈ 0.1 pJ per bit	< 1 pJ per bit	100 pJ per bit

F represents the minimum feature size of the technology.

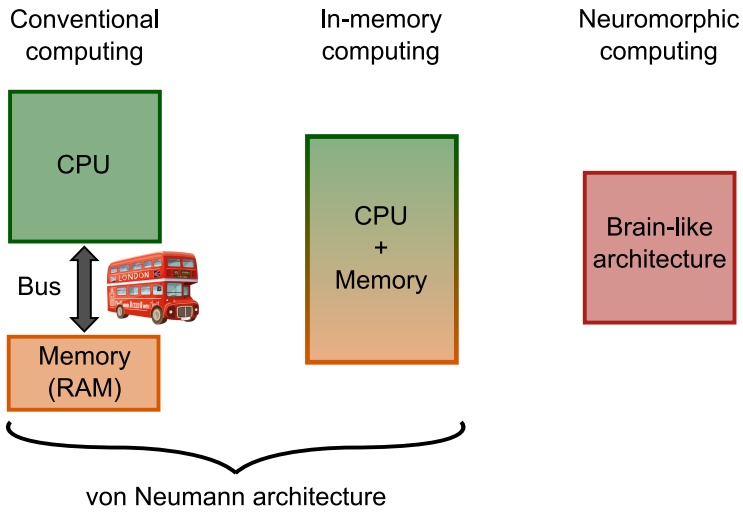

Figure 1.8: Summary of the different kinds of computing mentioned in the text: conventional computing, using the traditional von Neumman architecture, with clearly separated memory and processor (CPU); in-memory computing, also known as stateful logic computing, that utilizes emerging devices that can act both for processing and data storage; neuromorphic computing, where there is no distinction between memory and processing unit, and a new brain-inspired architecture is used, thus avoiding the von Neumann architecture completely.

Neuromorphic computing architectures using memristive devices, such as ReRAM, can revolutionize the brain-like computing paradigm by enabling an energy efficient approach. The relationship between memristive devices and neurons was pointed early on due to the similar behaviour to the Hodgkin-Huxley circuit model of the neuron [19]. Later on it was realized that memristive devices behave very similarly to the biological synapses between neurons [16, 124]. The key feature of the memristive device that allows this comparison is the possibility to tune its resistance values, thus allowing the modification of the synaptic weights between neurons, what in biology is known as synaptic plasticity. It is widely understood that it is this plasticity that enables learning in biological systems [124]. The biological process responsible for this tuning of the weights is known as spike-timing-dependent-plasticity (STDP). STDP can be obtained (or rather emulated) in memristive devices, as shown, for example, in Fig. 1.9(c), which compares fairly well to the STDP measured in biological systems, as shown in Fig. 1.9(b). This allows the development of spiking neural networks, one of the ways to achieve neuromorphic computing.

Ideally, pure analog behaviour of the memristive device, where all the resistance states between two values are available, would be the best choice for artificial synapses. However, in real devices it is much easier to obtain discrete resistance values due to the high variability associated, for example, with the inherent stochasticity of the conductive filament formation [125]. Therefore, neural networks based on crossbar arrays of devices operated in a binary way, with just two discrete resistance states, have also been proposed [126].

This kind of computing is particularly important for data-centric applications such as autonomous vehicles, real-time image recognition and natural language processing [127, 128]. The requirements of ReRAM for neuromorphic computing are less strict in comparison to the application in memory and storage, in terms of operation speed, retention time and device

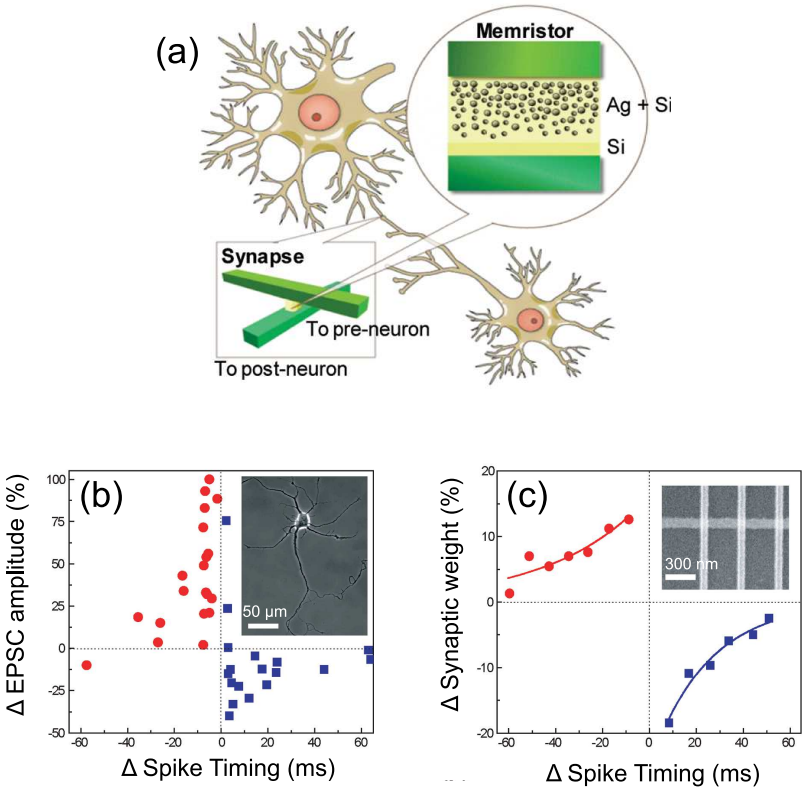

Figure 1.9: (a) Schematic illustration of a synapse between two neurons and of a crosspoint memristive device as a possible artificial synapse. (b) Demonstration of STDP in a memristive device with the change in the synaptic weight as a function of the relative timing of the neuron spikes. (c) Measurement of the excitatory postsynaptic current of rat hippocampal neurons after repetitive correlated spiking as a function of the relative spike timing. Adapted from [124].

density, which can further boost the practical implementation of the ReRAM technology.

1.7.3 Other applications

Besides these two main applications, ReRAM is also being investigated for new applications in logics [86, 129], modular arithmetics [130] and reconfigurable radiofrequency devices [131, 132]. Due to the stochastic nature of the switching, which enables the construction of true random number generators, memristive devices can also be used in security applications [110].

Chapter 2

Theory and other relevant background

This chapter deals with the background information that is essential for the analysis and discussion of the electrical transport data that will be presented in the following chapters. The content includes some important theoretical aspects related to electronic transport and also a general review of the materials of interest to this study. Starting with the semi-classical transport theory for metals based on the Boltzmann equation, the limits of its application are then discussed, and the quantum corrections needed in some limit cases are introduced. For the cases where the Boltzmann formalism is invalid, hopping transport is presented. Afterwards, the transport characteristics of some relevant specific systems are introduced. These systems include granular metals, metal-insulator-metal structures and quantum point contacts. Finally, the Ta-O material system is presented, with important material aspects of the different phases that can be obtained.

2.1 Electron transport

In terms of the electrical properties, materials are normally divided into three categories: metals, semiconductors and insulators. In fact, the last two can be put in the same category and just be called insulators. The physical quantity used to distinguish between the different categories is the electrical conductivity σ. The electrical conductivity appears naturally as the proportionality constant between the current density $\boldsymbol{j}$ and the electric field $\boldsymbol{\mathscr{E}}$:

$$\boldsymbol{j} = \sigma \boldsymbol{\mathscr{E}}. \tag{2.1}$$

For the simple case of single-channel transport, the conductivity is determined by the charge carrier concentration n and the charge carrier mobility μ through:

$$\sigma = e\mu n. \tag{2.2}$$

The conductivity can be substituted by its inverse quantity, known as resistivity $\rho = 1/\sigma$.

There are two criteria to distinguish between metals and insulators [133]. The first is

based on the temperature dependence of the resistivity:

$$\begin{cases} \frac{\partial \rho}{\partial T} < 0 \longrightarrow \text{insulator} \\ \\ \frac{\partial \rho}{\partial T} > 0 \longrightarrow \text{metal.} \end{cases} \tag{2.3}$$

The second criterion is based on the limit of the conductivity when the temperature approaches 0 K:

$$\begin{cases} \lim_{T \to 0\ \mathrm{K}} \sigma(T) = 0 \longrightarrow \text{insulator} \\ \\ \lim_{T \to 0\ \mathrm{K}} \sigma(T) \neq 0 \longrightarrow \text{metal.} \end{cases} \tag{2.4}$$

However, the first criterion is not unambiguous, because there are metals that do exhibit the $\frac{\partial \rho}{\partial T} < 0$ behaviour. These particular metals will be the focus of section 2.1.2.

2.1.1 Boltzmann equation and its limits

The electrical transport in solids is the net result of the driving force of external fields and the dissipative effect of the scattering of charge carriers by phonons and defects. The interplay of these two mechanisms is described by the Boltzmann equation. It assumes a periodic potential in a crystalline solid and thus, that the electrons propagate as Bloch waves. The equation describes how the distribution of carriers in thermal equilibrium changes with these mechanisms [134]. At thermal equilibrium, the distribution of the carriers is defined by the Fermi-Dirac distribution:

$$f_0\left[E\left(\boldsymbol{k}\right)\right] = \frac{1}{\exp\left(\frac{E(\boldsymbol{k})-E_F}{k_\mathrm{B}T}\right)+1}, \tag{2.5}$$

where $E\left(\boldsymbol{k}\right)$ represents the energy for the wave vector $\boldsymbol{k}$ and E_F is the Fermi energy. In the presence of external electric and magnetic fields, $\boldsymbol{\mathscr{E}}$ and $\boldsymbol{B}$, and/or a temperature gradient, the non-equilibrium distribution $f\left(\boldsymbol{r},\boldsymbol{k},t\right)$ is space- and time-dependent and is given by:

$$f\left(\boldsymbol{r}+\boldsymbol{v}dt, \boldsymbol{k}+\frac{\boldsymbol{F}}{\hbar}dt, t+dt\right) = f\left(\boldsymbol{r},\boldsymbol{k},t\right) + \left(\frac{\partial f}{\partial t}\right)_{\mathrm{scatt}} dt, \tag{2.6}$$

where $\boldsymbol{v} = \frac{1}{\hbar}\nabla_{\boldsymbol{k}} E\left(\boldsymbol{k}\right)$ is the group velocity of the Bloch wave, and $\boldsymbol{F} = -q\left(\boldsymbol{\mathscr{E}} + \frac{1}{c}\boldsymbol{v}\times\boldsymbol{B}\right)$ is the electromagnetic force caused by the external electric and magnetic fields. The Boltzmann equation is obtained by performing a Taylor expansion up to the first order of the term on the left side of equation 2.6, leading to:

$$\frac{\partial f}{\partial t} + \boldsymbol{v}\cdot\nabla_{\boldsymbol{r}} f - \frac{e}{\hbar}\left(\boldsymbol{\mathscr{E}} + \frac{1}{c}\boldsymbol{v}\times\boldsymbol{B}\right)\cdot\nabla_{\boldsymbol{k}} f = \left(\frac{\partial f}{\partial t}\right)_{\mathrm{scatt}}. \tag{2.7}$$

The terms on the left side of the Boltzmann equation are called the drift terms and describe the influence of the external fields on the distribution of the charge carriers. The term on the right is the scattering term, which takes into account the different scattering mechanisms. The sources of the scattering are deviations from the strict periodicity in the lattice caused by defects (impurities, vacancies, dislocations, etc.), phonons and other electrons. However, the electron-electron scattering is neglected in most cases, because the probability is much lower

than that of electron-defect or electron-phonon scattering. Still, the Boltzmann equation is a rather complicated one to solve due to the scattering term. Therefore, this term is normally simplified by using the relaxation time approximation/*ansatz*. This approximation assumes that the rate at which f returns to the equilibrium distribution f_0 is proportional to the deviation of f from f_0. This assumption is mathematically described by:

$$\left(\frac{\partial f}{\partial t}\right)_{\text{scatt}} = -\frac{f\left(\boldsymbol{r},\boldsymbol{k},t\right) - f_0\left(\boldsymbol{r},\boldsymbol{k},t\right)}{\tau\left(\boldsymbol{r},\boldsymbol{k}\right)}, \tag{2.8}$$

where $\tau\left(\boldsymbol{r},\boldsymbol{k}\right)$ is the relaxation time for position $\boldsymbol{r}$ and wave vector $\boldsymbol{k}$. For small electron scattering rates and considering that the scattering mechanisms are independent of each other, the relaxation time can be given by:

$$\frac{1}{\tau} = \frac{1}{\tau_{\text{e-def}}} + \frac{1}{\tau_{\text{e-ph}}} + \frac{1}{\tau_{\text{e-e}}}, \tag{2.9}$$

where $\tau_{\text{e-def}}$, $\tau_{\text{e-ph}}$ and $\tau_{\text{e-e}}$ are the relaxation times for the different scattering mechanisms: electron-defect, electron-phonon and electron-electron, respectively. The last term disappears when this last interaction is neglected.

According to the Drude model, the conductivity of a metal is given by:

$$\sigma = \frac{e^2\tau(E_F)}{m^*}n, \tag{2.10}$$

where m^* is the effective mass of the electrons in the metal. With the relaxation time approximation, the resistivity of a metal can then be rewritten into:

$$\rho = \rho_{\text{def}} + \rho_{\text{ph}}\left(T\right) + \rho_{\text{e-e}}\left(T\right) \approx \rho_{\text{def}} + \rho_{\text{ph}}\left(T\right). \tag{2.11}$$

This is known as Matthiesen's rule and was first identified experimentally. In the limit when temperature approaches 0 K, the resistivity tends to ρ_{def}, as the scattering by phonons is largely reduced.

The phonon scattering was theoretically approached by Grüneisen, who obtained the following resistivity component:

$$\rho_{\text{ph}}\left(T\right) = A\left(\frac{T}{\theta_D}\right)^5 \int_0^{\frac{\theta_D}{T}} \frac{x^5}{\left(\mathrm{e}^x - 1\right)\left(1 - \mathrm{e}^{-x}\right)} dx, \tag{2.12}$$

where A is a constant and θ_D is the Debye temperature. This expression is simplified for temperatures far away from θ_D, such that the resistivity simplifies to:

$$\begin{aligned} &\rho = \rho_{\text{def}} + \beta T^5, \;\; T \ll \theta_D \\ &\rho = \alpha T, \;\; T \gg \theta_D, \end{aligned} \tag{2.13}$$

with α and β being constants [135]. The $T \gg \theta_D$ regime gives the "normal" metallic behaviour, *i.e.* a linearly increasing resistivity with increasing temperature.

The Boltzmann equation is very good to describe the resistivity of these "typical" metals. However, for some cases, this formalism loses its validity. One remarkable example of a case where the Boltzmann equation fails to explain the experimental data is the temperature dependence of the resistivity of a variety of metallic alloys as shown extensively by Mooij [136],

which will be described later. He showed that the temperature coefficient of the resistance (TCR), defined as:

$$\mathrm{TCR} = \frac{1}{R}\frac{\mathrm{d}R}{\mathrm{d}T}, \tag{2.14}$$

changed its sign when the alloys reached a certain resistivity value. Alloys with a resistivity below $(100 - 150)$ $\mu\Omega$·cm showed a positive TCR, while the alloys with resistivity above the same range exhibited a negative TCR. This empirical knowledge became known as Mooij rule. In light of the Boltzmann equation, the negative TCR would translate into a scattering mechanism where the respective relaxation time would increase with increasing temperature. Such a scattering mechanism does not seem to exist in metals, therefore the Boltzmann formalism fails to predict this behaviour.

Clearly there must be a way to know if the Boltzmann equation can be applied or not. The key to understand the applicability limit of this equation is directly related to the assumption that the electrons propagate as Bloch waves with the Fermi wave vector k_F and Fermi wavelength $\lambda_F = \frac{2\pi}{k_F}$. The mean free path L_e of the electrons is defined as the distance travelled by the electron between two successive and independent scattering events. The Boltzmann equation is only valid if the mean free path is much longer than the Fermi wavelength. Translating this mathematically, apart from some numerical factors of the order of unity, leads to the relation:

$$k_F \cdot L_e \gg 1. \tag{2.15}$$

The same condition can be derived purely from quantum mechanics by invoking Heisenberg's uncertainty principle: $\Delta k \Delta x \sim 1$. Δk should be much less than k_F, so $\Delta x \gtrsim \frac{1}{k_F}$. The mean free path should be greater than the minimum uncertainty, so we reach $k_F \cdot L_e \gtrsim 1$. Eq. 2.15 is known as the Ioffe-Regel limit or criterion [135]. Based on this criterion it is possible to understand if the Boltzmann equation is valid or not, *i.e*, if it can be applied to the situation under study or not. Namely, three different situations arise:

1. $k_F \cdot L_e < 1$ Strong localization - Boltzmann equation is invalid.
2. $k_F \cdot L_e \gtrsim 1$ Weak localization - Boltzmann equation is valid at high T but quantum corrections are needed at low T.
3. $k_F \cdot L_e \gg 1$ Ordinary metal - Boltzmann equation is valid.

Therefore, an estimation of $k_F \cdot L_e$ is an important thing to consider in the analysis of the experimental results. It can be estimated from experimental values of resistivity and carrier concentration obtained from Hall measurements. The resistivity of a metal can be obtained from Eq. 2.10. Approximating the Fermi surface of the metals to a sphere, the Fermi wave vector is $k_F = \left(3\pi^2 n\right)^{1/3}$, so the Ioffe-Regel parameter returns:

$$k_F \cdot l \sim \left(3\pi^2\right)^{2/3} \frac{\hbar}{e^2}\frac{n^{1/3}}{\rho}. \tag{2.16}$$

For the case no. 2, the Boltzmann equation is valid for high temperatures, but there is the need to consider quantum corrections to the conductivity at low temperatures in order to properly describe the transport. These quantum corrections will be discussed in the next subsection.

2.1.2 Quantum corrections to the conductivity

It is now important to consider the different types of scattering processes possible. There are two types of processes, depending on the kinetic energy of the electron being conserved or not. In elastic scattering processes, both the electron energy and the phase are conserved, while in inelastic scattering processes, the energy is not conserved and the phase of the electron wave is changed stochastically (the electron "forgets" the phase it had prior to the collision). The electron-defect scattering fits in the first group, while the electron-phonon and electron-electron scattering processes fit in the second. There is an additional scattering process, the spin-flip scattering, where the energy might not be conserved and the phase might be lost. The spin-flip scattering only becomes important when the spin-orbit coupling is strong. For both types of processes the respective mean free paths can be associated, being L_e and L_{in}, for elastic and inelastic scattering, respectively.

The phase-breaking length L_ϕ is defined as the spatial distance after which the phase of the electron is changed stochastically. It can be related to the probability of losing the phase memory $1/\tau_\phi$, through the diffusion coefficient D by $L_\phi = \sqrt{D\tau_\phi}$. If there are no spin-flip scattering events: $L_{in} = L_\phi$.

The quantum corrections presuppose that $L_\phi \gg L_e$, *i.e.* that the elastic scattering from static disorder occurs much more frequently than the inelastic processes. Additionally, the transport has to be diffusive.

Weak localization and weak anti-localization

During the diffusive transport, an electron that at $t = 0$ was at the origin, the position $\boldsymbol{r} = \mathbf{0}$, can be later found at the point $\boldsymbol{r}$ with probability $p(\boldsymbol{r}, t)$, given by:

$$p(\boldsymbol{r}, t) = (4\pi Dt)^{-d/2} \exp\left(-\frac{r^2}{4Dt}\right), \text{ with } r^2 = \sum_1^d x_i^2 \text{ and } \int p(\boldsymbol{r}, t)\, d\boldsymbol{r} = 1, \tag{2.17}$$

where d is the dimensionality of the space where the diffusion takes place. Interestingly, the quantum mechanical approach to p differs from the classical approach at the particular point $\boldsymbol{r} = \mathbf{0}$. Considering the wave properties of the electron, there is an increase in the probability of finding the electron at the origin. Fig. 2.1(a) illustrates an electron moving diffusively and returning to the origin through a particular path. For classical diffusion, the probability of the electron propagating on the same path but in the opposite direction is the same. The sum of these two equal probabilities gives the total probability of $1/(4\pi Dt)$. However, in the quantum mechanical interpretation, considering the wave-like character of the electron, the two partial waves that propagate in both directions interfere constructively at the origin and increase the probability by a factor of 2. This happens because the probability is obtained by the square of the sum of the amplitudes of both waves, not by the sum of the squares, as it is calculated in the classical case. For points in space other than the origin, the partial waves are generally incoherent and only their intensities add. The increase in the probability of finding the electron in the origin can be seen in figure 2.1(b). The width of the peak at $\boldsymbol{r} = \mathbf{0}$ is determined by the uncertainty principle. This phenomenon was thought to be a precursor of localization, because the electron tends to remain at a fixed position (the origin), so it is called weak localization [137].

Obviously the constructive interference only happens if the electron remembers its phase, therefore, only when the electron returns to the origin within time $t < \tau_\phi$. The quantum

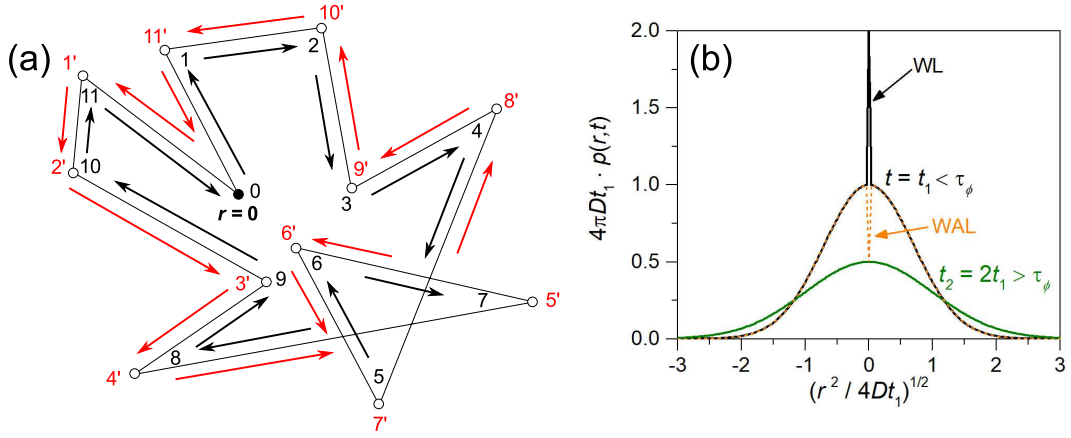

Figure 2.1: (a) Possible closed diffusion path of an electron. The electron propagates the closed path in both directions: $0 \to 1 \to 2 \to ... \to 11 \to 0$ and $0 \to 1' \to 2' \to ... \to 11' \to 0$, indicated by the black and red arrows, respectively. (b) Plot of the probability function given by Eq. 2.17 for two-dimensional diffusion ($d = 2$) at times $t_1 < \tau_\phi$ and $t_2 = 2t_1 > \tau_\phi$. For time t_1 the increase of the probability due to the weak localization (WL) is clearly observed, while for time $2t_1$ the probability at the origin is already the same as in the classical picture. For the case where the spin-orbit coupling is strong, weak antilocalization (WAL) occurs, giving the decreased probability shown in orange.

correction depends on the dimensionality of the transport. The dimensionality is determined by comparing the sample size where the transport takes place to the phase-breaking length, while the dimensionality for diffusion is determined by comparing it to the mean free path. For the different dimensions d, the quantum corrections to the conductivity are [135]:

$$\begin{aligned} d = 3: &\quad \Delta\sigma_{3D} \approx -\text{const.} + \left(\frac{e^2}{\hbar}\right) L_\phi^{-1} \\ d = 2: &\quad \Delta\sigma_{2D} \approx -\left(\frac{e^2}{\hbar}\right) \ln\left(\frac{L_\phi}{L_e}\right) \\ d = 1: &\quad \Delta\sigma_{1D} \approx \text{const.} - \left(\frac{e^2}{\hbar}\right) L_\phi. \end{aligned} \tag{2.18}$$

The temperature dependence of these corrections is linked to the temperature dependence of L_ϕ. Normally, it is considered that $\tau_\phi \propto T^{-p}$, where p is an index that depends on the scattering mechanism and on the dimensionality [138]. The conductivity corrections as a function of temperature then are calculated to be [138]:

$$\begin{aligned} d = 3: &\quad \Delta\sigma_{3D} = \sigma_0 + \frac{e^2}{\hbar\pi^3}\frac{1}{a} T^{p/2} \\ d = 2: &\quad \Delta\sigma_{2D} = \sigma_0 + \frac{p}{2}\frac{e^2}{\hbar\pi^2} \ln\left(\frac{T}{T_0}\right) \\ d = 1: &\quad \Delta\sigma_{1D} = \sigma_0 - \frac{ae^2}{\hbar\pi} T^{-p/2} \end{aligned} \tag{2.19}$$

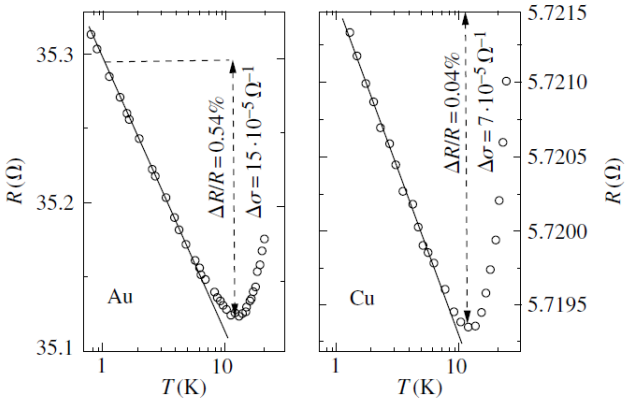

Figure 2.2: Resistance as a function of temperature (on a logarithmic scale) for thin films of Au (left) and Cu (right), evidencing the upturn of the resistance at low temperatures characteristic of weak localization. Taken from [135].

The 2D correction is normally sufficient for thin films, because at the low temperatures, at which the weak localization is normally observed, the thickness of the film is lower than L_ϕ. $\Delta\sigma_{2D} \propto \ln(T)$ is thus the most well known signature of weak localization. This temperature dependence is then used to identify a possible occurrence of this quantum interference effect as it leads to a pronounced increase in the resistivity at low temperature. Fig. 2.2 shows an example of this feature for thin films of Au and Cu below 10 K.

When the spin-orbit coupling is strong, the partial waves are no longer coherent at the origin because of the loss of phase information with spin-flip scattering. The constructive interference ceases to exist. In fact, there is a reduction in the backscattering probability that leads to the exact opposite behaviour of the resistivity, which is named weak anti-localization (WAL).

Another important characteristic of WL and WAL is the effect of the magnetic field. If an electron travels along a loop in a magnetic field B, its wave function Ψ gets an additional phase factor [135]:

$$\Psi \longrightarrow \Psi \exp\left(i\frac{e}{\hbar c}\int \boldsymbol{A}d\boldsymbol{l}\right) = \Psi \exp\left(\pm\frac{i\pi\Phi}{\Phi_0}\right), \tag{2.20}$$

where $\boldsymbol{A}$ represents the vector potential of the magnetic field, defined by $\boldsymbol{B} = \nabla \times \boldsymbol{A}$, $\Phi_0 = \pi\hbar c/e$ is the magnetic flux quantum and Φ is the total magnetic flux. The plus and minus signs represent the two different partial waves, one for each direction of motion along the closed loop. These two partial waves will now have a phase difference at the origin of $\Delta\phi = 2\pi(\Phi/\Phi_0)$ due to the magnetic field, which will break the constructive interference between the two waves at this point. It effectively changes the "strength" of the WL effect by decreasing the probability of finding the electron at the origin. For a certain magnetic field the effect will even be completely destroyed. Therefore, the increase of the resistance associated with WL will disappear with the magnetic field, leading to a negative magnetoresistance (MR). On the contrary, the decrease of the resistance observed in case WAL is taking place will vanish, which translates into a positive MR.

The MR due to WL or WAL was theoretically calculated by Hikami, Larkin and Nagaoka (HLN) [139]. The HLN formalism enables a quantitative fit to the MR data, so the MR

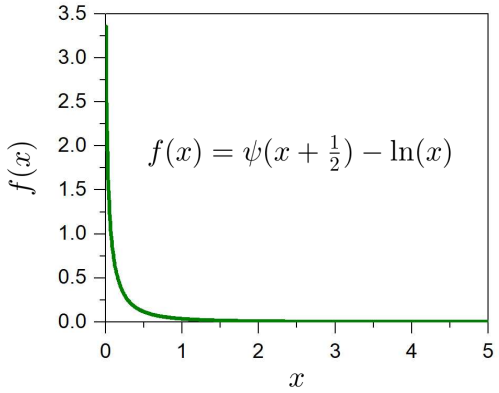

Figure 2.3: Plot of the base function underlying the HLN formula expressed in Eq. 2.21.

measurements can be used as a tool to measure basic solid state properties of materials [138]. According to this formalism, the change in the conductance due to a magnetic field B is given by:

$$\begin{aligned}\Delta G(B) = &-\frac{e^2}{2\pi h}\left[\psi\left(\frac{B_\phi}{B}+\frac{1}{2}\right)-\ln\left(\frac{B_\phi}{B}\right)\right]\\ &-\frac{e^2}{\pi h}\left[\psi\left(\frac{B_{so}+B_e}{B}+\frac{1}{2}\right)-\ln\left(\frac{B_{so}+B_e}{B}\right)\right]\\ &+\frac{3e^2}{2\pi h}\left[\psi\left(\frac{\frac{4}{3}B_{so}+B_\phi}{B}+\frac{1}{2}\right)-\ln\left(\frac{\frac{4}{3}B_{so}+B_\phi}{B}\right)\right],\end{aligned} \tag{2.21}$$

where $B_i = \frac{\hbar}{4eL_i^2}$ are the characteristic fields for the different scattering channels, $i = \phi, so, e$, associated with the respective characteristic lengths L_i: the phase-breaking length L_ϕ, the spin-orbit scattering length L_{so} and the elastic scattering length or mean free path L_e [139, 140]. This original formula can be approximated by a simpler form in the case of small fields. Under this condition, the phase-breaking term clearly dominates, because the associated length is much longer than both the spin-orbit and elastic scattering lengths, and the underlying function decreases with the increase of the argument (see Fig. 2.3). Taking this into consideration, the change in conductance caused by an applied magnetic field B is approximated to [140]:

$$\Delta G(B) = -\frac{\alpha_{2D}e^2}{\pi h}\left[\psi\left(\frac{\hbar}{4eL_\phi^2 B}+\frac{1}{2}\right)-\ln\left(\frac{\hbar}{4eL_\phi^2 B}\right)\right]+bB^2, \tag{2.22}$$

where α_{2D} is a factor included to account for possible contributions from the top and bottom surface of the films and other effects, and b is the quadratic coefficient that includes not only the classical component arising from the cyclotronic MR (b_c), but also the simplified components of the spin-orbit and elastic terms of the HLN model (b_q) [140]. The classical cyclotronic MR term arises from the deviation of the electrons' trajectories due to the Lorentz force in the applied magnetic field. It comes as:

$$b_c = -\mu_{\mathrm{MR}}^2 G_0, \tag{2.23}$$

where μ_{MR} is the MR mobility and G_0 is the zero-field conductance [140]. The MR mobility is related to the Hall mobility μ_H through the magnetoresistance scattering factor, but to take $\mu_{\mathrm{MR}} = \mu_H$ is normally a good approximation [141]. The other components that add to b are the approximated components from the HLN formula that deal with the spin-orbit and elastic scattering. These can be simplified to b_q:

$$b_q = -\frac{e^2}{24\pi h}\left(\frac{1}{B_{so}+B_e}\right)^2 + \frac{3e^2}{48\pi h}\left(\frac{1}{\frac{4}{3}B_{so}+B_\phi}\right)^2. \tag{2.24}$$

In the case where $L_{so} > L_e$, the ΔG arising from this last term is positive. The complete term is then $b = b_c + b_q$ [140].

If, however, the quantum interference occurs in 3D, the change in resistivity is described by: [142]

$$\frac{\Delta\rho}{\rho^2}(B) = \alpha_{3\mathrm{D}}\frac{e^2}{2\pi^2\hbar}\left(\frac{eB}{\hbar}\right)^{\frac{1}{2}}\left[\left(\frac{1}{2}+\beta\right)f_3\left(\frac{B}{B_\phi}\right) - \frac{3}{2}f_3\left(\frac{B}{B_4}\right)\right], \tag{2.25}$$

with

$$\begin{aligned} f_3(h) &= \sum_{n=0}^{+\infty} 2\left[\left(n+1+\frac{1}{h}\right)^{\frac{1}{2}} - \left(n+\frac{1}{h}\right)^{\frac{1}{2}}\right] - \frac{1}{\left(n+\frac{1}{2}+\frac{1}{h}\right)^{\frac{1}{2}}} \\ &\approx \begin{cases} \frac{h^{\frac{3}{2}}}{48}\left(1-\frac{7h^2}{64}+\frac{91h^4}{2048}-\frac{3h^6}{160}\right), & h \le 0.6 \\ 0.6049 - \frac{2}{h^{\frac{1}{2}}} + \frac{2.389}{h} - \frac{2.355}{h^2}, & h \ge 25 \end{cases} \end{aligned}, \tag{2.26}$$

where $\alpha_{3\mathrm{D}}$ is again a fitting parameter. The field B_4 is given by $B_4 = B_\phi + 2B_{\mathrm{SO}}$. The factor β is related to the quenching of the superconducting fluctuations, where $\beta \approx 0$ if $T \gg T_c$, with T_c being the superconducting transition temperature.

Electron-electron interference

Whereas WL and WAL emerge as a consequence of the electron wave interfering with itself, there is an additional effect stemming from the interference of different electron waves. This is known as electron-electron interference or interaction and it also gives rise to a correction to the conductivity. The problem was theoretically assessed by Al'tshuler and Aronov and therefore is also known as Al'tshuler-Aronov effect [143].

In order for the waves of different electrons to interfere, the electrons must be close to one another for a sufficient period of time. When the transport is diffusive, the electrons stay close to one another, as the mean distance between electrons increases more slowly with time than in the ballistic transport regime. Analogously to the weak localization case, where the main factor is the phase-breaking length L_ϕ, for interelectron interference, there is also a phase-breaking length L_{ee} and the respective phase-breaking time τ_{ee}. The phase of an electron with the initial energy E_i as a function of time is described by $\exp(iE_i/\hbar)\,t$. Two electrons with an energy difference of ΔE with the same phase at $t = 0$ will have at time t a phase difference of $\Delta\Phi_{12} = \frac{\Delta E}{\hbar}t$. Therefore, after a time $\hbar/\Delta E$ the phase difference is on the order of unity. The electrons that take part in the diffusive transport are the ones that can reach unoccupied states at temperature T, which have energies in the range:

$$E_F - k_B T \lesssim E \lesssim E_F + k_B T. \tag{2.27}$$

Therefore, the difference in energy of two electrons is $\Delta E \approx k_B T$. This gives an approximation of the phase-breaking time as:

$$\tau_{\text{ee}} \approx \frac{\hbar}{k_B T} \tag{2.28}$$

From this, it is concluded that the lower the temperature, the longer the phase-breaking time, *i.e.* electron-electron interactions are favoured at low temperatures. The phase-breaking length for this interaction can be obtained by:

$$l_{\text{ee}} \approx L_e \sqrt{\frac{\tau_{\text{ee}}}{\tau_e}} \approx \sqrt{\frac{\hbar D}{T}} \tag{2.29}$$

The corrections to the conductivity due to electron-electron interactions have the same form of the ones shown in equation 2.18, with L_ϕ substituted by the phase-breaking length l_{ee}:

$$\begin{aligned} d = 3: &\quad \Delta\sigma_{3\text{D}} \approx -\text{const.} + \left(\frac{e^2}{\hbar}\right) l_{\text{ee}}^{-1} \\ d = 2: &\quad \Delta\sigma_{2\text{D}} \approx -\left(\frac{e^2}{\hbar}\right) \ln\left(\frac{l_{\text{ee}}}{L_e}\right) \\ d = 1: &\quad \Delta\sigma_{1\text{D}} \approx \text{const.} - \left(\frac{e^2}{\hbar}\right) l_{\text{ee}}. \end{aligned} \tag{2.30}$$

Substituting relation 2.29 in equations 2.30, it is possible to get the temperature dependence of the conductivity correction due to electron-electron interactions. For 3D, $\Delta\sigma_{3\text{D}} \propto \sqrt{T}$, while for 2D, $\Delta\sigma_{2\text{D}} \propto \ln T$. The temperature dependence of the 2D case is exactly the same as the one obtained for the weak localization. This becomes problematic in the distinction between the two quantum interference effects. The effect of the magnetic field then becomes particularly important, as it destroys the weak localization, but has a much smaller effect on the electron-electron interaction. Another important method to experimentally identify the occurrence of electron-electron interactions is tunnelling spectroscopy. Through this technique, the density of states is measured, which is sensitive to the occurrence or not of the mentioned interactions.

The corrections to the conductivity can be quantitatively obtained using the Kubo formalism. The corrections are [138]:

$$\begin{aligned} d = 3: &\quad \Delta\sigma_{3\text{D}} = \frac{e^2}{2\pi h} \frac{1.3}{\sqrt{2}} \left(\frac{4}{3} - \frac{3}{2}\tilde{F}_\sigma\right) \sqrt{\frac{T}{D}} \\ d = 2: &\quad \Delta\sigma_{2\text{D}} = \frac{e^2}{2\pi h} \left(2 - \frac{3}{2}\tilde{F}_\sigma\right) \ln\left(T\tau_e\right) \\ d = 1: &\quad \Delta\sigma_{1\text{D}} = -\frac{1}{A}\frac{e^2}{h}\frac{1.3}{\sqrt{2}} \left(4 - \frac{3}{2}\tilde{F}_\sigma\right) \sqrt{\frac{D}{2T}} \end{aligned} \tag{2.31}$$

A is the wire cross-section area in the 1D case. The quantity $\tilde{F}_\sigma$ is given by:

$$\begin{cases} \tilde{F}_\sigma = 8\left(1 + \frac{F}{2}\right)\frac{\ln\left(1+\frac{F}{2}\right)}{F} - 4, & \text{for } d = 2 \\ \\ \tilde{F}_\sigma = -\frac{32}{d}\left(d-2\right)\left[1 + \frac{d}{4}F - \left(1 + \frac{F}{2}\right)^{d/2}\right]F, & \text{for } d \neq 2, \end{cases} \tag{2.32}$$

where F is the Hartree term that quantifies the strength of the screening between electrons.

According to Eqs. 2.31, disordered metals where electron-electron interactions occur should exhibit a $\sigma \propto \sqrt{T}$ behaviour for transport in 3D, if the associated quantum correction is dominating the temperature dependence.

Disordered metals

From the previous sections, it is now clear that disorder can induce very distinctive behaviour in the electrical transport of materials. This condition is verified in a group of metals known as disordered metals, sometimes also called dirty metals. These materials serve as a good playground to observe the effects of disorder on the conductivity, and share some common characteristics among themselves.

As it was already mentioned, J. H. Mooij found a correlation between the resistivity of disordered metals and their TCR (see Eq. 2.14). Mooij published a plot with data for many different metallic alloys (such as NiCr or AlTi) in both bulk and thin film form, which is reproduced in Fig. 2.4 [136]. This led to the so-called Mooij's rule, which states that metallic alloys having a resistivity lower than 100-150 $\mu\Omega$cm usually have a positive TCR, while those with resistivity exceeding 100-150 $\mu\Omega$cm have a negative TCR [135].

The $\sqrt{T}$ dependence of the conductivity is observed in many of these disordered metals. Initially, the community tried to explain this behaviour within the Boltzmann transport theory, but it is clear that the Ioffe-Regel criterion is violated for these systems, inhibiting its use. Later, it was clarified that the observed behaviour had to be related with quantum corrections to the Boltzmann transport. Howson and Greig proposed that the weak localization explains the $\sqrt{T}$ behaviour at high temperatures [144, 145]. According to these authors, the conductivity of the amorphous metallic alloys is given by [146]:

$$\begin{aligned} &\sigma \propto T, \quad T \ll \theta_D \\ &\sigma \propto \sqrt{T}, \quad T \gtrsim \theta_D, \end{aligned} \tag{2.33}$$

with θ_D being the Debye temperature. However, the effect of the electron-electron interference also leads to the same temperature dependence of the conductivity with the $\sqrt{T}$ term. To which the authors mention that this effect appears only at very low temperatures [146]. On the other hand, the WL shows a dependence with a higher power of the temperature, taking the form $T^{p/2}$, where p is greater than 1 and depends on the scattering mechanisms that destroy the phase coherence (thus decreasing the WL effect). If the Coulomb electron-electron scattering dominates in the dirty limit, $p = 3/2$; if the electron-electron scattering occurs in the clean limit, $p = 2$; if, on the other hand, the electron-phonon scattering dominates, $p = 3$ [138].

In summary, for 3D disordered metals, the conductivity corrections are described by [138, 147]:

$$\Delta\sigma_{3\mathrm{D}} = A_{WL}T^{p/2} + A_{e-e}\sqrt{T} \tag{2.34}$$

where the first term is due to the weak localization effect and the second term originates in the electron-electron interactions. A_{WL} and A_{e-e} contain all the factors detailed in Eqs. 2.19 and 2.31.

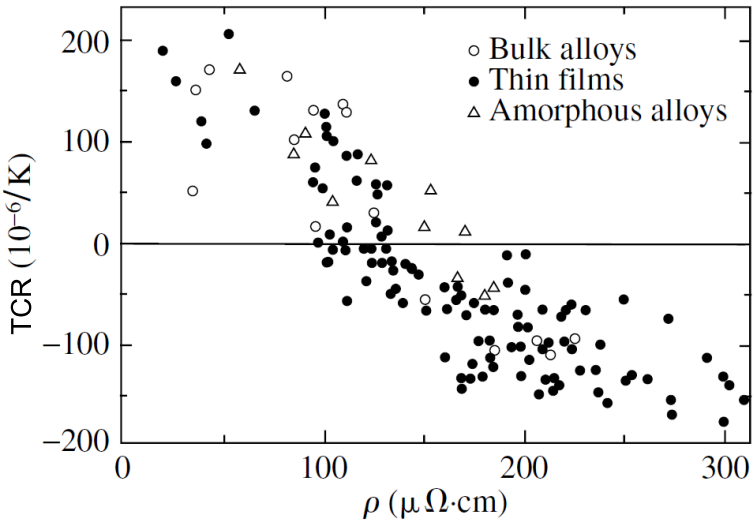

Figure 2.4: Temperature coefficient of the resistance (TCR), here represented with $\overline{\alpha}$ as a function of the resistivity for different disordered metallic alloys, showing a clear correlation between the two quantities. For a resistivity below approximately 150 $\mu\Omega$cm, the TCR is positive, while above this value the TCR is negative. This experimental correlation is called Mooij's rule. The different symbols represent different types of samples, as indicated in the legend of the figure. Adapted from [135].

2.1.3 Hopping transport

In the regime of strong localization, as described in section 2.1.1, the Boltzmann transport equation is not valid. In this regime, the wave function of the states is concentrated in a very small region of space, decaying exponentially outside of this region. This decay of the wave function as $r \to \infty$ can be described by [135]:

$$\psi(r) = f(r) \exp\left(-\frac{r}{\xi}\right), \tag{2.35}$$

where ξ is termed localization radius or localization length. In solids, impurity centres, such as shallow donors and acceptors, are normally described as hydrogen-like centres with a Bohr radius dependent on the effective electron mass m^* and the electric permittivity ε:

$$a_B = \frac{\varepsilon \hbar^2}{m^* e^2}. \tag{2.36}$$

Transport between the localized states is called hopping transport and occurs through carrier hopping from occupied to free states. Hopping transport considers that all the states have different energies, *i.e.*, that two states with the same energy are infinitely spaced from each other. As there is an energy difference, the hopping must be accompanied by emission or absorption of phonons [135]. These processes are rate determining, therefore, the conductivity contains an activation energy E_a and takes the form [148]:

$$\sigma = \sigma_0 \exp\left(-E_a / k_B T\right). \tag{2.37}$$

The conductivity tends to zero at low temperatures, which is a behaviour of insulators, according to criterion 2.4.

The simplest form of hopping occurs via transitions between sites that are closest in space, *i.e.* nearest neighbours. If E_D is the energy of the localized states, the probability that this state is free depends on its energy with respect to the Fermi level, which is proportional to $\exp\left(-|E_F - E_D|/k_BT\right)$. Substituting this exponential term in equation 2.37 leads to the nearest-neighbour hopping (NNH) conductivity:

$$\sigma = \sigma_0 \exp\left(-\frac{|E_F - E_D|}{k_BT}\right). \tag{2.38}$$

If the temperature drops, so that $k_BT \ll |E_F - E_D|$, the number of empty sites among the nearest neighbours is too small, and the NNH freezes out. In this scenario, localized states that are further away in space become increasingly important, as these states should be closer in energy to the Fermi level. The lower the temperature, the longer the hopping distance. Therefore, this kind of hopping is called variable-range hopping (VRH). The expression for the conductivity is different from the one for NNH:

$$\sigma = \sigma_0 \exp\left[-\left(\frac{T_M}{T}\right)^{1/4}\right], \tag{2.39}$$

where T_M represents Mott's temperature, which is inversely proportional to the density of states at E_F and to the cube of the localization length. The pre-factor σ_0 is different from the one in equation 2.38 and is a power function of the temperature, although this is usually neglected [135]. This expression, however, is only valid for 3D transport. The VRH is dependent on the dimensionality of the transport d. The general expression for the conductivity is:

$$\sigma = \sigma_0 \exp\left[-\left(\frac{T_M}{T}\right)^{1/(d+1)}\right]. \tag{2.40}$$

This returns the exponents $\frac{1}{2}$, $\frac{1}{3}$ and $\frac{1}{4}$ for 1D, 2D and 3D transport, respectively.

The density of states in the vicinity of the Fermi level is assumed constant in order to derive the expression for VRH. When electron correlations play an important role, the density of states vanishes at the Fermi level. This is caused by the Coulomb repulsion between electrons, and is called the Coulomb gap. This phenomenon changes the VRH conductivity into the expression:

$$\sigma = \sigma_0 \exp\left[-\left(\frac{T_{\mathrm{ES}}}{T}\right)^{1/2}\right], \tag{2.41}$$

where $T_{\mathrm{ES}} \approx e^2/(\varepsilon a_B)$, with a_B being the Bohr radius. This variant is named Efros-Schklosvkii hopping (ESH) after the physicists that first proposed it. The Coulomb gap plays an important role in the low temperature conductivity of insulator materials [149].

The temperature plays a significant role in hopping. As the temperature decreases from room temperature down to very low temperatures on the order of mK, it is possible to go through all the discussed types of hopping mechanisms. Figure 2.5 illustrates this possibility for a lightly-doped semiconductor, where the Fermi level lies in an impurity band formed by the localized states. Besides the different mathematical expressions, also a schematics of the evolution of the density of states with decreasing temperature is shown.

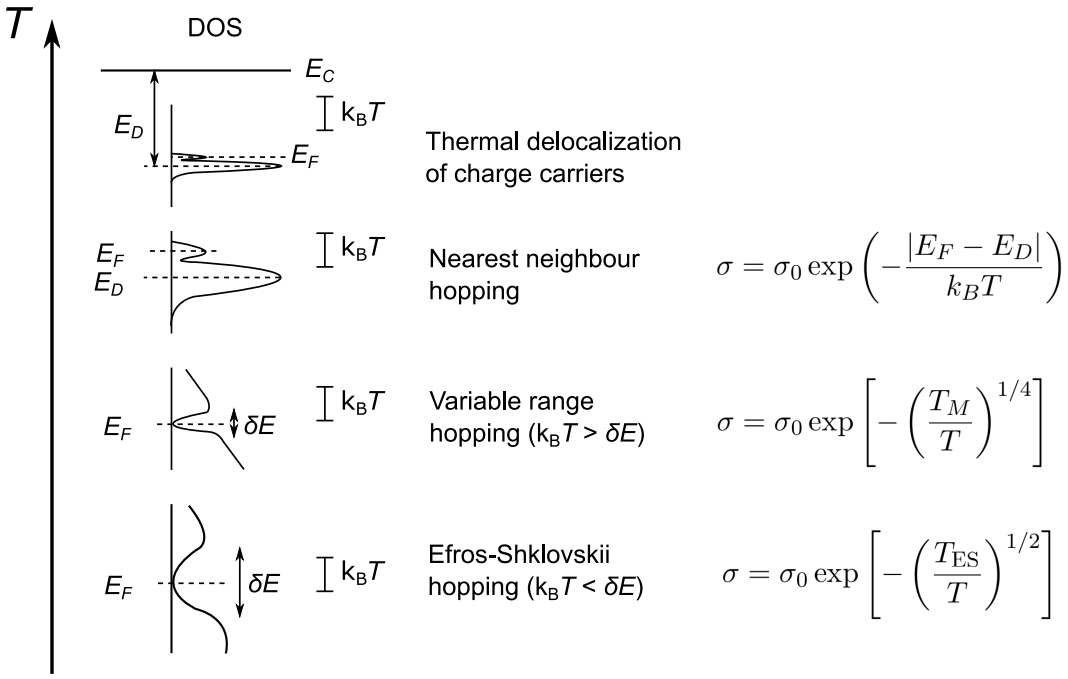

Figure 2.5: Schematics showing the change of hopping transport mechanisms as temperature is decreased for a lightly-doped semiconductor. The small inset plots represent the density of states (DOS) around the Fermi level E_F and are not depicted in the same scale. E_D represents the minimum of the conduction band, k_BT represents the thermal energy at temperature T, δE represents the energy width of the Coulomb gap, while the other symbols retain the same meaning as in the text. Based on a figure from [135].

2.1.4 Granular metals

The different transport mechanisms presented up to this point all consider that the charge carriers are moving in a homogeneous material. When a material is not homogeneous and is rather composed of different phases with different electrical transport properties, a good picture of the electrical transport in the material as a whole can be hard to envision. The task of understanding the transport becomes simplified in the case where there are only two phases with very different conductivity values, however. This is normally the case for a mixture of metallic and insulating phases. Granular metals are arrays of metallic particles (granules) embedded into an insulating matrix. The metallic granules usually range from a few to hundreds of nanometers in size. It is important that the granules are sufficiently large in order to possess a distinct electronic structure, but also small enough to be considered mesoscopic and to exhibit quantization of the electronic levels of the confined electrons. This class of artificial materials enables a tuning of the electronic properties with a control on the nanoscale. On the other hand, it offers a good playground for the study of the effects of disorder on the transport properties [150]. Granular metals are a particular case of a system where a percolation threshold occurs, and therefore some of the results are based on the percolation theory [151].

An example of the evolution of the morphology of a granular metal with the change in concentration of the metal component is shown in Fig. 2.6, where In was deposited on top of Si. The In does not wet the Si, therefore, the In atoms tend to coalesce in the form of individual granules. For a sufficiently high amount of In, the resulting clusters are isolated from each other, as in Fig. 2.6(a). For a higher amount of In, there are almost no isolated clusters and there is a continuous region of metal on the surface of Si, which forms percolation paths for conduction. This highlights that there are two very distinct regimes in granular metals: the insulating regime and the metallic regime. In the former, the granules are isolated from each other leading to an insulating behaviour. In the latter case, there is enough metal to form a percolation of metallic granules or form large regions of metal, thus allowing metallic transport.

The theoretical models devised to understand the transport in granular metals consider metallic granules identical in size and shape, which is radically different from the real granular metals. Nevertheless, the theory still enables accurate predictions. The electron coupling between different granules is described via a tunneling matrix. Within this framework, the key parameter determining most of the physical properties of the array of granules is the average tunnelling conductance G between neighbouring granules [150]. It is useful to consider the dimensionless conductance $g = G/\left(2e^2/\hbar\right)$. This parameter allows an easy distinction between the insulating regime with $g \lesssim 1$ and the metallic regime with $g \gtrsim 1$. A second important parameter is the Coulomb charging energy of a single granule E_C, which is equal to the change in energy of the granule when one electron is removed or added.

Metallic regime

Deep in the metallic regime, with $g \gg 1$, the electrons tunnel easily between granules and the granular metal behaves similarly to a homogeneous metal. Also here, the quantum interference effects described in section 2.1.2 play a decisive role, as normally the metallic granules present sufficient disorder. The electron transport across the granular metal is diffusive, because on a scale larger than the granule size there is always scattering at least at the

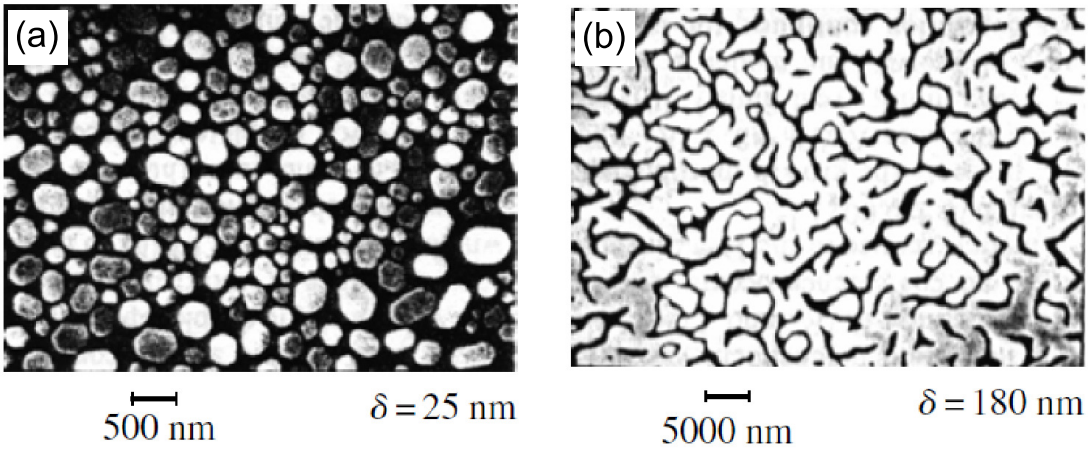

Figure 2.6: Scanning electron microscopy pictures of In deposited on top of Si for different average In film thickness (δ), showing different kinds of coverage of the surface, exemplifying a granular metal in the insulating regime in (a) and in the metallic regime (b). Adapted from [135].

boundary of the granules, even though the intragranular transport can be ballistic. Ballistic transport will not lead to quantum corrections to the conductivity. The effective diffusion coefficient is given by:

$$D_{\text{eff}} = \Gamma a^2, \tag{2.42}$$

where Γ is called the characteristic energy and a is the average size of the granule (for example its diameter for spherical granules). Using the Einstein relation to retrieve the mobility as a function of the diffusion coefficient, the conductivity of the granular metal is:

$$\sigma_0 = 2e^2 N\left(E_F\right) D_{\text{eff}}, \tag{2.43}$$

where $N\left(E_F\right)$ is the density of states at the Fermi level in the region inside the granule. As the conductivity can also be affected by interference effects such as electron-electron interactions, the final conductivity is given by:

$$\sigma = \sigma_0 + \delta\sigma_1 + \delta\sigma_2. \tag{2.44}$$

The correction $\delta\sigma_1$ is caused by the granularity of the system and arises from the Coulomb interaction between electrons at scales smaller than the granule's size. This is possible due to the diminished electronic screening enabled by the granularity of the system, which largely reduces the amount of electrons moving around the granules. This increases the Coulomb interaction between the electrons in the granules. The correction is given by:

$$\frac{\delta\sigma_1}{\sigma_0} = -\frac{1}{2\pi dg} \ln\left[\frac{gE_C}{\max\left(T,\Gamma\right)}\right] \tag{2.45}$$

When the coherent electron motion on scales larger than the grain size a dominates the physics, there is the correction $\delta\sigma_2$:

$$\frac{\delta\sigma_2}{\sigma_0} = \begin{cases} \frac{\alpha}{12\pi^2 g}\sqrt{\frac{T}{\Gamma}}, & d=3 \\ -\frac{1}{4\pi^2 g}\ln\frac{\Gamma}{T}, & d=2 \\ -\frac{\beta}{4\pi g}\sqrt{\frac{\Gamma}{T}}, & d=1 \end{cases} = \begin{cases} \frac{\alpha}{12\pi^2 g}a\sqrt{\frac{T}{D_{\text{eff}}}}, & d=3 \\ -\frac{1}{4\pi^2 g}\ln\frac{\Gamma}{T}, & d=2 \\ -\frac{\beta}{4\pi g a}\sqrt{\frac{D_{\text{eff}}}{T}}, & d=1 \end{cases} \tag{2.46}$$

with d representing here the dimensionality of the array of granules, and $\alpha \approx 1.83$ and $\beta \approx 3.13$ being numerical constants. The expression has the same temperature dependence as in the homogeneous disordered metal case shown in Eq. 2.31. This term dominates the temperature dependence of the conductivity at low temperatures. However, for granular metals the $\sqrt{T}$ dependence has been observed up to room temperature. This is related to the small mean free path of the electrons in granular metals caused by the strong disorder and the higher probability of interaction between electrons in the reduced space of the granule. This enables a stronger effect of the electron-electron interaction on the conductivity relatively to homogeneous disordered metals [152]. Although widely observed and theoretically studied, the ascription of the $\sqrt{T}$ behaviour to the Al'tshuler-Aronov effect is still considered by some authors as not satisfactory [153].

Insulating regime

In the insulating regime, there is a weak coupling between the granules, and no metallic transport is possible. The transport then occurs similarly to the hopping case described in section 2.1.3, with the hopping occurring between neighbouring granules. However, the charged metallic granule induces an electric field in the space between it and another neighbouring granule. This creates an electrostatic energy barrier, also known as Coulomb blockade, that must be overcome in order for the hopping to occur. This results in the resistivity [135]:

$$\rho = \rho_0 \exp\left(\frac{T_0}{T}\right)^{1/2}. \tag{2.47}$$

This situation is very similar to the Efros-Schklovskii hopping case, where there is the appearance of a Coulomb gap (see section 2.1.3). More recent studies point toward a different origin for this $\exp\left(T^{-1/2}\right)$ behaviour [150, 154]. The electrostatic disorder causes fluctuations in the electrostatic energy of the granules and lifts the Coulomb blockade at some of the granules. Then, the transport is not possible between neighbouring granules, but it is in a variable range sense. The electrostatic disorder is most likely caused by charged defects in the insulating matrix. The transport between granules occurs through tunneling via virtual electron levels in a sequence of granules, which is called co-tunneling, which can be elastic and inelastic. Elastic co-tunneling occurs when tunneling in and out of the granule deals with the same intra-granule electron state, while inelastic co-tunneling leaves behind an excited electron-hole pair. Inelastic co-tunneling prevails at higher temperatures and elastic at lower temperatures [154]. The tunneling probability decays exponentially with the distance between the granules, simulating the effect of the exponentially decaying probability between hops with similar energies of the variable range hopping, and thus gives rise to the same temperature dependence of Eq. 2.47.

Metal-insulator transition in granular metals

The transport regime of the granular metal is determined by the metallic fraction x. Fig. 2.7(a) shows the evolution of the resistivity of a granular system with x. The rapid increase of ρ as x decreases indicates the metal-insulator transition. The x value for which this transition occurs is related to the percolation threshold.

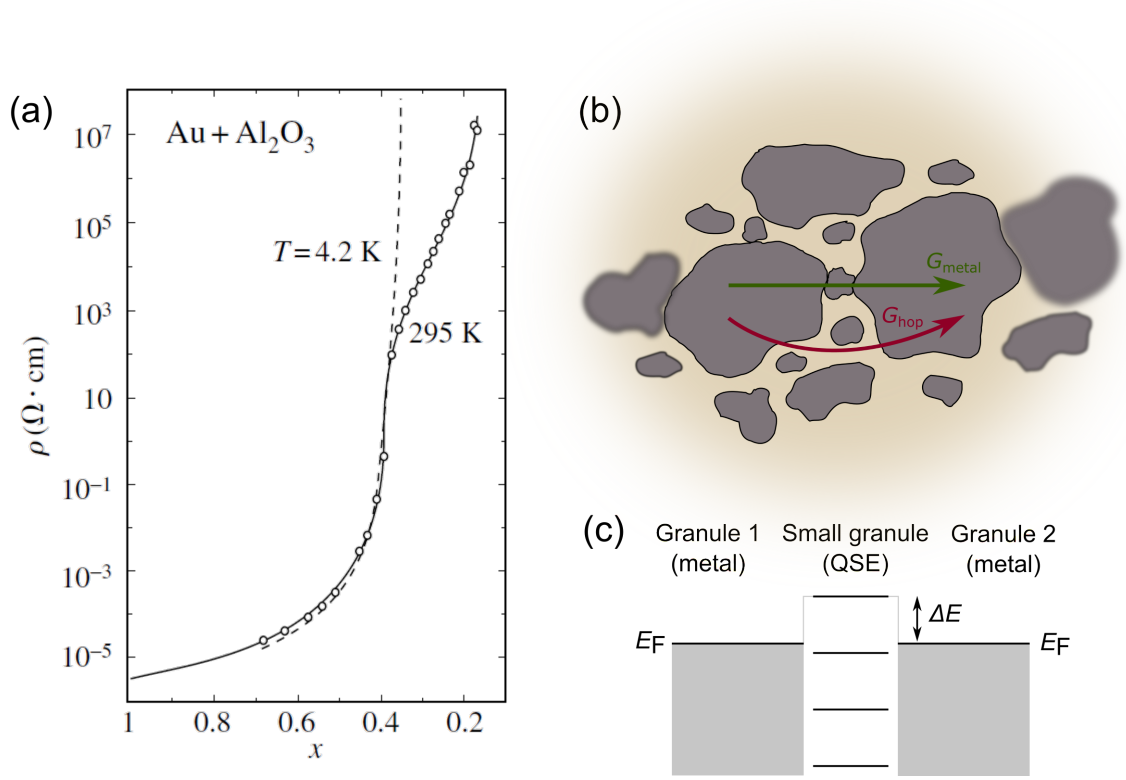

Figure 2.7: (a) Resistivity of a granular metal as a function of the metallic fraction x for the example system Au + Al_2O_3. The solid lines and symbols are obtained at room temperature, while the dashed line shows the data obtained at helium temperature, where a much steeper transition with decreasing x is observed. Adapted from [135]. (b) Scheme of percolating channel in the vicinity of a weak link between larger metallic regions. G_{metal} is the conductance through the percolating cluster of metal granules and G_{hop} corresponds to the hopping conductance over separated granules; (c) Simplified band diagram showing the energy levels splitting owing to QSE in the small granule and energy barrier ΔE for conduction electrons within the constriction.

Close to the percolation threshold, there is another effect that causes a kind of a metal-insulator transition. This is determined by temperature and is due to the emergence of quantum size effects (QSE) [147, 155]. Near the percolation threshold on the metallic side, the chain of metallic granules can have joining points where the contact is minimum. This forms constrictions that act as bottlenecks to the electron transport. A schematic depiction of such a situation is shown in Fig. 2.7(b). The constriction at the contact between granules confines the electron motion and therefore splits the electronic energy levels at the contact. In its turn this

leads to an energy barrier for the electrons. At sufficiently high temperatures, the electrons can overcome the barrier, and metallic conductivity is possible. At lower temperatures, when the electrons cannot be thermally excited above the barrier, the transport occurs via tunnelling, and the metallic conductivity is broken. Hence, a change in the temperature can also induce a metal-insulator transition in granular metals [152].

In Fe-SiO_2 granular metals, the transition from metal to insulator due to QSE occurs at approximately 70 K and leads to a decrease of one order of magnitude of the carrier concentration [147]. In Pd_xC_{1-x} granular metals it was shown that the transition temperature was always roughly the same, independently of the film thickness and metal fraction x [155].

2.2 The Ta-O material system

In order to understand the material dynamics during the resistive switching in the Ta_2O_5-based ReRAM devices it is necessary to introduce the relevant Ta-O material system. This system includes, naturally, the stable oxide Ta_2O_5 as well as other possible substoichiometric TaO_x phases and the metallic Ta phases.

2.2.1 Phase diagram of the Ta-O system

The phase diagram of the Ta-O system is presented in Fig. 2.8, as reported by Garg et al. [156]. Several important things can be understood from the phase diagram. Namely:

1. Only two stable compounds exist: the stoichiometric oxide Ta_2O_5 and a solid solution of Ta and O, *i.e.* Ta(O).

2. From the previous point, it is straightforward to conclude that there are no stable suboxide phases of TaO_x.

3. The Ta metal is able to accommodate a significant amount of oxygen without forming the oxide Ta_2O_5.

In the following subsections, the main phases of the Ta-O material system, Ta metal and Ta_2O_5, will be introduced in more detail. An overview of the more relevant metastable phases will be also presented.

2.2.2 The oxide: Ta_2O_5

The stoichiometric tantalum oxide Ta_2O_5 is an electrical insulator with a band gap of around 4 eV [97], although values up to 5.38 eV have also been reported [157].

Ta_2O_5 has two main crystallographic phases: α-Ta_2O_5 and β-Ta_2O_5, which are also named H-Ta_2O_5 and L-Ta_2O_5, respectively, referring to a high (H) and a low (L) temperature phase. The transformation occurs at a temperature around 1320 °C [156]. The H form has been reported as tetragonal, hexagonal and monoclinic, while the L form has been reported mostly as orthorhombic and sometimes as monoclinic [156]. Most of the structures are very similar and can easily be interchanged by small variations of the ion positions [158] and the exact symmetries of the structures are still unclear. Nowadays, however, the α phase is said to be tetragonal, while the β phase is reported as orthorhombic. A third phase, the metastable δ-Ta_2O_5, with an hexagonal structure, was also reported more recently [158]. However, in

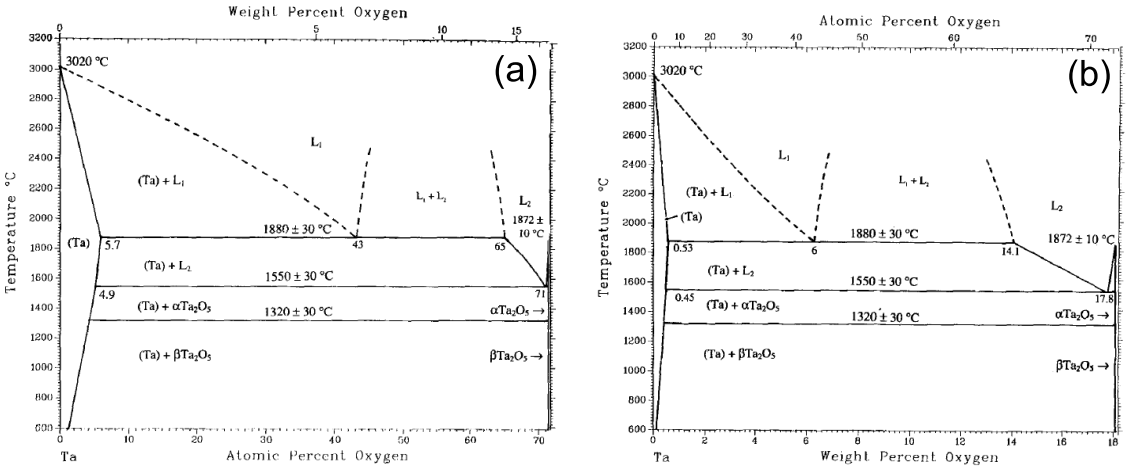

Figure 2.8: Phase diagram of the Ta-O system with: (a) Atomic percent of oxygen on the horizontal axis scale; (b) Weight percent of oxygen on the horizontal axis scale. Taken from [156].

most of the relevant applications, including ReRAM, the Ta_2O_5 is amorphous in nature. This is the normally obtained oxide when the material is deposited at room temperature. The transition from amorphous to the β phase occurs at approximately 650 °C [159].

In terms of optical properties, it is known to have a high dielectric constant of around 25 (measured at high frequency, probably around 1 MHz) and a refractive index between 2.1 and 2.2 (for $\hbar\omega = 2$ eV) [160, 161].

The defect chemistry of β-Ta_2O_5 can be described by the following reactions that show the intrinsic formation of defects [162]:

$$O_O^{\times} \rightleftharpoons V_O^{\bullet\bullet} + 2e' + \frac{1}{2}O_2(g) \tag{2.48}$$

$$O_O^{\times} \rightleftharpoons O_i'' + V_O^{\bullet\bullet} \tag{2.49}$$

$$\text{nil} \rightleftharpoons e' + h^{\bullet}. \tag{2.50}$$

The different species are written using the Kröger-Vink notation [41]. $O_O^{\times}$ represents an oxygen ion in its right place in the β-Ta_2O_5 lattice, with neutral charge relatively to the lattice indicated by $\times$. $V_O^{\bullet\bullet}$ represents a vacancy (V) in the oxygen (O) position of the lattice with two positive charges relatively to the lattice given by the two $\bullet$. O_i'' represents oxygen in an interstitial position (i) with two negative charges indicated by the two $'$. The same rules are used for the electron (e) and hole (h).

The electroneutrality condition for this situation is given by:

$$2\left[O_i''\right] + n = 2\left[V_O^{\bullet\bullet}\right] + p. \tag{2.51}$$

that for the case of low oxygen partial pressure simplifies to

$$n = 2\left[V_O^{\bullet\bullet}\right]. \tag{2.52}$$

The existence of oxygen interstitials is not clear, as there is a lack of experimental proof [163]. However, a recent work by Gries et al. suggests that oxygen interstitials play a major role in the ionic conductivity of β-Ta_2O_5 under oxidizing conditions [164].

2.2.3 The metal: Ta

The tantalum metal occurs naturally in the body-centred cubic (BCC) phase. This phase is called α-Ta and is the thermodynamically stable phase at the ambient conditions. However, when Ta is deposited in the form of a thin film, the most common phase is the metastable β-Ta phase, which has a tetragonal structure.

The origin of the β phase stabilization over the α phase in thin films is still not completely understood [165]. Some works point to the importance of carefully controlling the oxygen content in the atmosphere of the deposition chamber [166, 167]. The α phase is only obtained via sputtering when the oxygen content is low enough. Others point to the importance of the substrate material, as β-Ta seems to be favoured when the growth occurs on amorphous oxide substrates [165, 168], or substrates that easily form surface oxides [168]. Crystalline substrates, such as clean Si(100) or crystalline Mo, induce the formation of α-Ta [165, 169]. The α phase is also promoted by having a seed layer of face-centred cubic (FCC) TaN grown on substrates with native oxides of Ti and Si [170]. These examples show the importance of the initial nucleation of Ta for the final phase of the thin film. Other deposition parameters of the magnetron sputtering process, such as chamber pressure during deposition and temperature, also play an important role [169–171]. The post-growth β- to α-Ta transformation is normally achieved with thermal annealing in vacuum of the as-grown films at temperatures in the range from 400-650 °C [165], or at lower temperatures of 300-400 °C in oxygen-free films in ultra-high vacuum [172].

The bulk phase, α-Ta, has a BCC structure with a lattice constant $a = 3.306$ Å and belongs to the space group $Im\bar{3}m$ [165].

The β-Ta crystallographic structure is quite complex, and only in 2002 it was finally studied in proper single crystals obtained at normal pressure conditions [173]. The structure is tetragonal and belongs to the σ-type Frank-Kasper structures that are also observed in β-U and binary intermetallic compounds. The unit-cell parameters are $a = 10.211$ Å and $c = 5.3064$ Å, while the space group is $P\bar{4}2_1m$.

The two different phases are also easily distinguishable in terms of their electrical properties, namely in terms of resistivity and temperature coefficient of the resistance (TCR). The α-Ta phase has a lower resistivity of approximately $1.5 - 2.5 \times 10^{-7}$ Ωm and a positive TCR of 1500×10^{-6} K^{-1} [171]. On the other hand, the β-Ta phase shows an order of magnitude higher resistivity of around 2×10^{-6} Ωm and a negative TCR of -150×10^{-6} K^{-1} [174].

2.2.4 Metastable suboxide phases

As mentioned in the previous subsection, the phase diagram of the Ta-O material system shows that only two compounds are thermodynamically stable, excluding suboxide phases. These can, nevertheless, occur in conditions of metastability. Garg et al. mentioned that none of the metastable forms have been isolated in pure form and that the reported synthesis methods have poor reproducibility [156]. Still, they found 25 different reported phases. The metastable phases are usually obtained after devitrification and thermal annealing under oxidizing conditions [175–177]. The metastable phases eventually transform into Ta_2O_5 if the

conditions are kept for a longer time and there is enough oxygen in the environment. Recent works report the observation of metastable suboxide phases such as TaO_2, crystallizing in the rutile phase [40], and Ta_2O showing a metallic transport behaviour [175], among other phases, such as $Ta_2O_{2.2}$ and γ-TaO_x, which is supposed to have a composition of $Ta_{12}O$ [176].

Particularly relevant to the resistive switching in Ta_2O_5-based devices is the TaO_2 phase reported by Wedig et al. [40]. The authors claim that TaO_2 forms in the Ta/Ta_2O_5 interface and mediates the ionic movement and consequently the oxidation of Ta, and thus, the switching.

The Ta_2O phase reported by Donaldson et al. is electrically conducting with a room temperature resistivity of approximately $(1.5 - 3.3) \times 10^{-4}$ Ωcm [176]. Hall measurements showed a carrier concentration of $(1.9 - 3.0) \times 10^{20}$ cm^{-3} with a mobility in the range of $62 - 110$ $cm^2V^{-1}s^{-1}$. Optical measurements show transparency in the visible light range for films up to 100 nm-thick and a bandgap between 2.04 and 2.17 eV. These films were deposited by sputtering on a crystalline saphire substrate at temperatures in the range from 600-700 °C and then subjected to a first thermal annealing for a few minutes at 700 °C under $0.5 - 1$ Pa of oxygen gas, followed sometimes by a second annealing in vacuum at the same temperature.

Chapter 3

Experimental techniques

In the first part of the chapter, the main experimental techniques used during the experimental work are described, as well as some auxiliary techniques. The second part of the chapter describes the fabrication process of the investigated samples.

3.1 Fabrication techniques

3.1.1 Sputtering

In materials science, sputtering is defined as the physical vaporization of atoms from the surface of a material by momentum transfer from bombarding energetic atomic-sized particles, which are normally ions accelerated in an electric field. The sputtered atoms can be deposited onto a substrate in a process named sputter deposition, which is normally known by sputtering [178, 179]. Different ways of bombarding the surface of the target (source of atoms) and different conditions lead to different variants of sputter deposition. The most common are known as DC sputtering, radiofrequency (RF) sputtering and ion-beam sputtering. The first two make use of a plasma, a quasi-neutral gas of charged and neutral particles (atoms, molecules, electrons and ions), as the source of the ions for the bombardment, while the third directly uses ions to bombard the target. The sputtered atoms travel from the target to the substrate where there is condensation and deposition.

The plasma is created by applying a sufficiently high electric field between two electrodes in a chamber with adequate gas pressure (after vacuum was made). The gas will breakdown into a plasma discharge, and afterwards inelastic electron-atom collisions sustain the plasma. In DC sputtering, the plasma is created by a DC electric field. The substrate is the anode and the target is the cathode. However, using a DC field becomes problematic when the target is an insulator, because there is accumulation of charge on the surface of the target. To circumvent this problem, RF sputtering employs an alternating current, usually with a frequency of 13.56 MHz, which is applied to the target, while the substrate is grounded. Additionally, a magnetron is commonly employed, enabling a magnetic field underneath the target that limits the movement of the electrons and restrains the plasma to the target region. This increases the sputter rate and impedes the heating of the substrate by the plasma.

Reactive sputtering enables the deposition of thin films of compound materials by sputtering from an elemental target in a partial pressure of a reactive gas. For example, a reactive atmosphere containing O_2 is used while sputtering from a transition metal target to produce

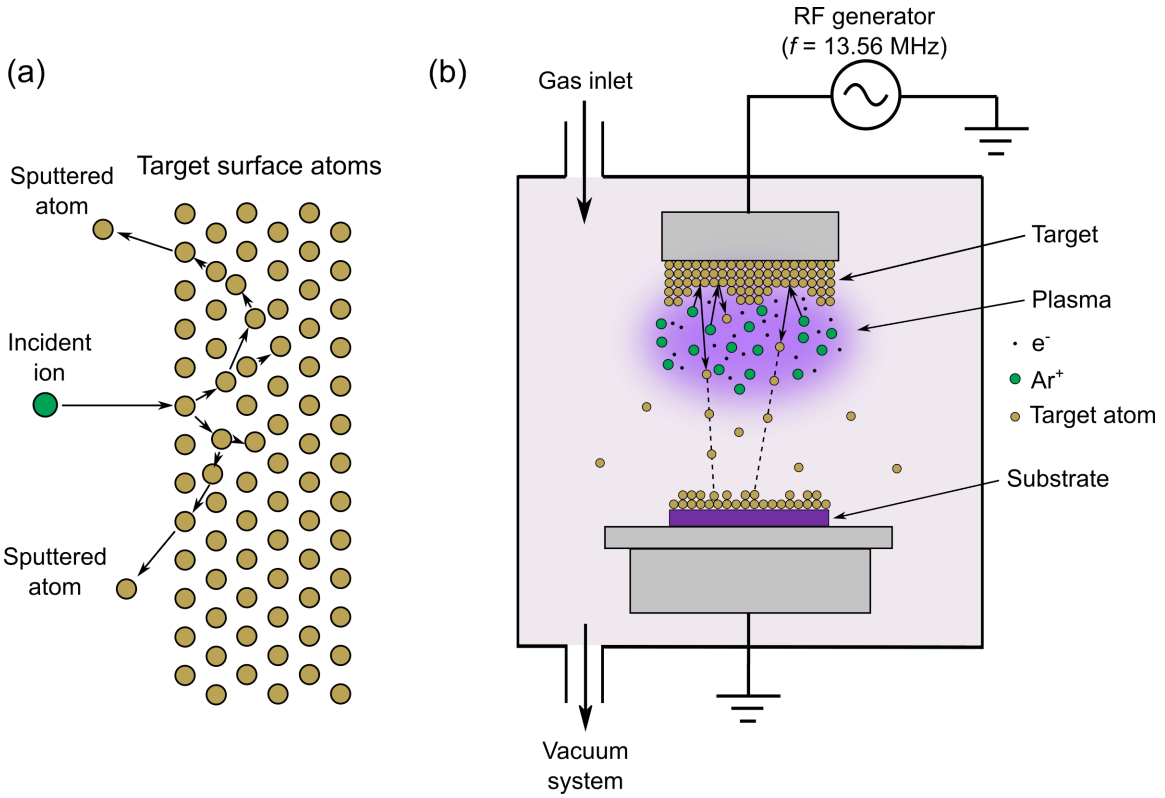

Figure 3.1: (a) Simple schematic depiction of the sputtering of surface atoms by an accelerated incident ion. (b) Simplified schematic representation of the magnetron sputtering process inside a vacuum chamber with Ar gas. The violet region indicates the plasma with Ar^+ ions represented with green dots, the electrons are represented by the small black dots and the yellow dots represent the atoms sputtered from the target (on top) that can be deposited onto the substrate (on the bottom).

the corresponding transition metal oxide, if the right conditions are met. The reaction occurs after the deposition of the target atoms on the film surface, which is exposed to the reactive gas. Therefore, the rate at which the sputtering and deposition occur is an important factor to consider in producing thin films in this way, because it controls the amount of time the freshly-sputtered atoms are exposed to the reactive gas before being covered by other sputtered atoms. A second important factor is the amount of reactive gas molecules existent in the chamber, which is controlled by the partial pressure of the gas.

3.1.2 Photolithography and lift-off

Conventional photolithography uses UV radiation to transfer a pattern from a mask to a photosensitive film with the objective of microfabricating devices and structures. It is, thus, an essential tool in the semiconductor industry [180]. The photosensitive film is called photoresist and is a polymer-based material that changes its solubility in a developer solution after UV exposure. A following development step selectively removes the resist leaving a pattern in the wafer.

There are two different photolithography processes: in the positive process, the resulting

photoresist pattern after development is the same pattern of the mask, while in the negative process the inverted pattern is obtained after development.

A positive lithography process can be condensed into four different stages:

1. Photoresist application into the wafer/substrate
2. Alignment of the mask and the wafer/substrate
3. Exposure of the photoresist to the UV radiation
4. Chemical development of the pattern

In stage 1, the photoresist, which normally comes in the form of a solution, is spin-coated on top of the substrate and is dried in a heating step. Afterwards, in stage 2, the mask must be aligned in respect to the substrate in the exposure system. The alignment is essential when multiple photolithograpy steps are required to obtain the final structure, enabling the correct translation of the desired result. The alignment is normally achieved by designing structures in the mask that enable easy orientation of the substrate in the alignment system. After the alignment, in step 3, the photoresist is exposed to the UV radiation according to the mask pattern. The simplest way to perform the exposure is by bringing the mask and the substrate into contact for exposure. Finally, the substrate is immersed in a chemical developer that removes the unexposed regions of the resist. The final result is the exact transfer of the pattern from the mask into the substrate in the form of a resist layer. For the negative process, two additional stages are needed before the development. After the exposure with the mask the substrate must be heated again and then exposed to the UV radiation without the mask (flood exposure). When the development is then applied, the resist regions that were previously exposed to the UV radiation during the exposure with the mask, are now the ones being removed by the chemical bath.

The transferred pattern can be used for different purposes in microfabrication. The pattern can be used as a mask for wet or dry etching, as a mask for ion implantation or it can be used to selectively deposit thin films. The latter application is called lift-off and is the one used in this work. The material deposited on top of the resist is later washed away during the stripping of the resist, leaving only the regions without the resist covered by the deposited film. For lift-off, the thickness of the film to be deposited must be less than the resist thickness and the deposition process should not exceed 120 °C due to the thermal limitation of the resist. The stripping of the resist is achieved with acetone.

Figure 3.2 depicts a possible negative lithography process followed by lift-off used to deposit a thin film only in certain regions and enable microstructuring of electronic devices.

Experimental conditions for this work

The photolithography system used in this work was the Karl Suss MA6 Mask Aligner. The photoresist was the AZ5214E and the developer was the AZ826MIF. UV radiation with a wavelength of 365 nm was used for the exposure.

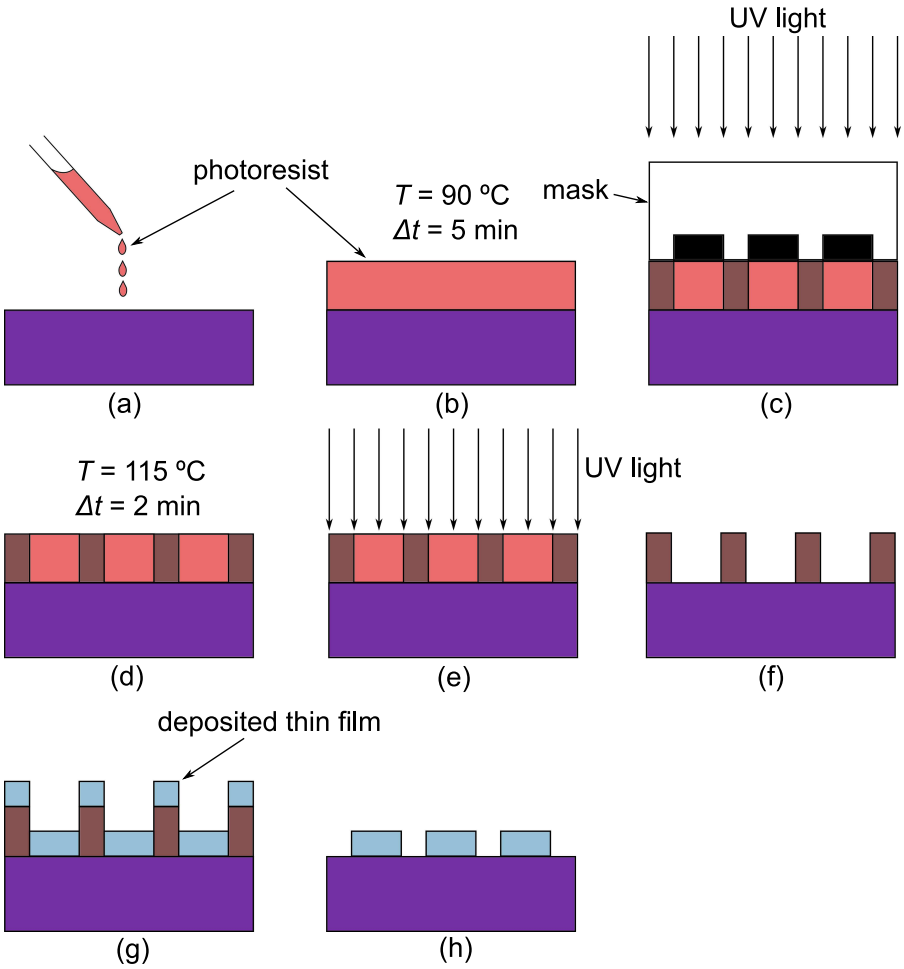

Figure 3.2: Schematic diagram of a negative lithography process used in this work for the fabrication of the samples: (a) the solution with the photoresist (AZ5214E) is spin-coated on top of a previously cleaned substrate at 6000 RPM during 30 s; (b) the photoresist is dried during a heating step at 90 °C for 5 min; (c) After proper alignment of the substrate relatively to the transfer mask, the photoresist and the mask are exposed to UV radiation for 4.5 s, leading to the photochemical change of the exposed regions of the photoresist. (d) The radiation exposure is followed by a second heating step, this time at 115 °C for 2 min; (e) the photoresist is exposed to UV radiation a second time now without the mask for 14.5 s (flood exposure); (f) finally the photoresist is developed in a chemical bath (developer: AZ826MIF) and afterwards cleaned in deionized water, resulting in the inverse pattern of the transfer mask solidly drawn by the photoresist layer; (g) the desired thin film can be deposited on the whole surface of the substrate with the lithographically defined resist pattern; (h) the final step is the lift-off with the stripping of the resist by acetone. The final result shows the deposited film remaining only in the regions that are defined in the transfer mask. In the case of a positive process, the exposure time in (c) is increased to 7 s and steps (d) and (e) are skipped.

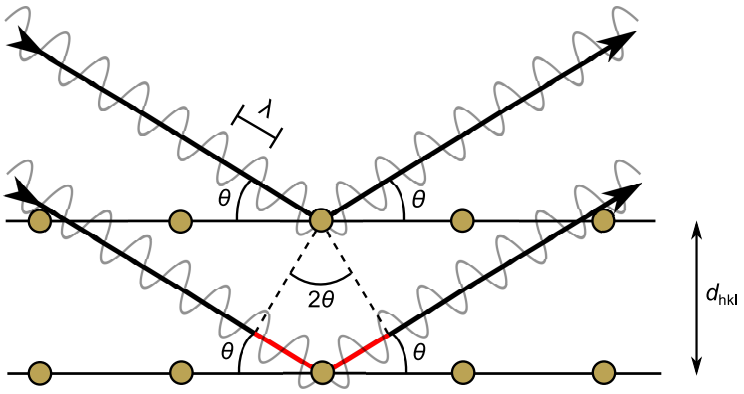

Figure 3.3: Schematic representation of the wave interference of X-rays that leads to Bragg's law. The lines in red indicate the path difference between the two reflected X-ray beams, which must be a multiple of the wavelength of the X-rays in order for constructive interference to occur. This condition is stated as Bragg's law.

3.2 Structural characterization techniques

3.2.1 X-ray diffraction (XRD) and X-ray reflectometry (XRR)

X-ray diffraction

The classical and most used technique for the assessment of the crystal structure of materials is the X-ray diffraction (XRD) [181]. The technique is based on the diffraction of X-rays in crystals that was discovered by Max von Laue in 1912. The diffraction results were explained in a very simple way by W. H. Bragg and his son W. L. Bragg in 1913. While Laue envisaged crystals in terms of a three-dimensional network of rows of atoms, the Braggs thought of crystals as layers or planes of atoms that acted as reflecting planes for the X-rays, analogously to optics. Although not physically correct, the geometrical framework made sense, and the simplicity of the system led to the famous Bragg law:

$$n\lambda = 2d_{hkl}\sin\theta, \tag{3.1}$$

where λ is the wavelength of the X-rays, n is the order of diffraction, d_{hkl} is the lattice plane spacing for (hkl) planes and θ is the angle of incidence (and reflection) relatively to the lattice planes, also known as Bragg's angle. The hkl indices are called Miller indices and represent a set of lattice planes. The expression 3.1 is a condition for constructive interference of the waves scattered by atoms from adjacent (hkl) lattice planes, and can be calculated from the geometrical analysis of the scheme in Fig. 3.3.

Bragg's law enables the identification of the lattice planes of a crystal that produce diffraction in a certain configuration and their inter-planar spacing. This carries information on the lattice parameters, and therefore on the size and shape of the unit cell of the crystal structure. A typical XRD diffraction pattern shows not only the geometry of the diffraction, but also contains information on the intensity of the diffraction spots. For the latter, expression 3.1 does not provide explanation, however. The intensity of the diffraction depends on the atoms where the X-rays scatter, more specifically on the number of electrons, which are the main contributors to the scattering, and also on the position of the atoms in the unit cell. Therefore, this already gives information of the chemical nature of the material. The atomic

scattering factor represents the scattering amplitude of an atom. By summing the atomic scattering factors of all the atoms in the unit cell of the crystal structure, the structure factor F_{hkl} is obtained. The structure factor then modulates the intensity of the diffracted beams.

In practice, the X-ray beams have a finite breadth and are not perfectly parallel. These instrumental factors give rise to a broadening of the diffracted X-ray beams, which translates in a broadening of the diffraction peaks in a diffractogram. But the broadening can also stem from the material under study, and is due to the crystallite size and its state of strain, particularly important for thin films over substrates. The broadening of the X-ray beam due to the crystal size is given by Scherrer equation:

$$\beta = \frac{\lambda}{t \cos\theta}, \tag{3.2}$$

where the broadening β is the width at half the maximum peak intensity and t is the size of the crystallite.

The more common experimental configuration for the measurement of XRD from polycrystalline samples is the Bragg-Brentano symmetrical arrangement. The X-ray source and X-ray detector are positioned so that the incident and reflected beams make equal angles to the specimen surface. For example, the sample is fixed while the source and detector are rotated in opposite sense. It is geometrically identical to fix the source while rotating the sample and the detector with double the angular speed of the sample. In this arrangement, only the d-spacings of the planes that are parallel to the sample surface are measured. Therefore, for a single crystal only one diffraction peak is obtained. For a powder sample, however, due to the random orientation of the crystals, it is possible to obtain many more diffraction peaks. A scheme of the Bragg-Brentano configuration is shown in Fig. 3.4(a).

For a sample with very thin films, the signal from the substrate can become problematic due to the high penetration depth of the X-rays. In light of this, a different configuration is better suited, where the angle of incidence of the X-ray relatively to the sample surface is very small. This configuration decreases the interaction of the X-rays with the substrate and largely increases the interaction length in the thin films. This approach is called grazing incidence X-ray diffraction (GIXRD). Fig. 3.4(b) shows a typical geometrical configuration to measure the GIXRD. The X-ray beam is made very parallel, for example using a mirror, and is incident at a very small angle to the sample surface that is kept constant, while the detector is swept along the arc centred on the sample. The scattering vector $\boldsymbol{Q}$ in the figure indicates the (hkl) planes that are detected for each 2θ angle, which are the ones perpendicular to the scattering vector [182, 183].

X-ray reflectometry

Beyond diffraction, the X-rays can be used to obtain more information on thin films. When considering a sample composed of a thin film on top of a substrate, as depicted in Fig. 3.5(a), the incident X-ray beam can be reflected on the surface of the thin film, can be transmitted through it, or even be absorbed in the thin film or in the substrate bulk. There is, however, a critical angle of incidence, relatively to the surface, below which there is no transmission due to total reflection. The total reflection occurs because, for the majority of materials, the refraction index for X-rays is below 1, the refraction index of air. This angle is normally around 0.1°. The X-rays that are transmitted through the thin film can be again reflected at the film/substrate interface and be transmitted back to the air. This transmitted ray will

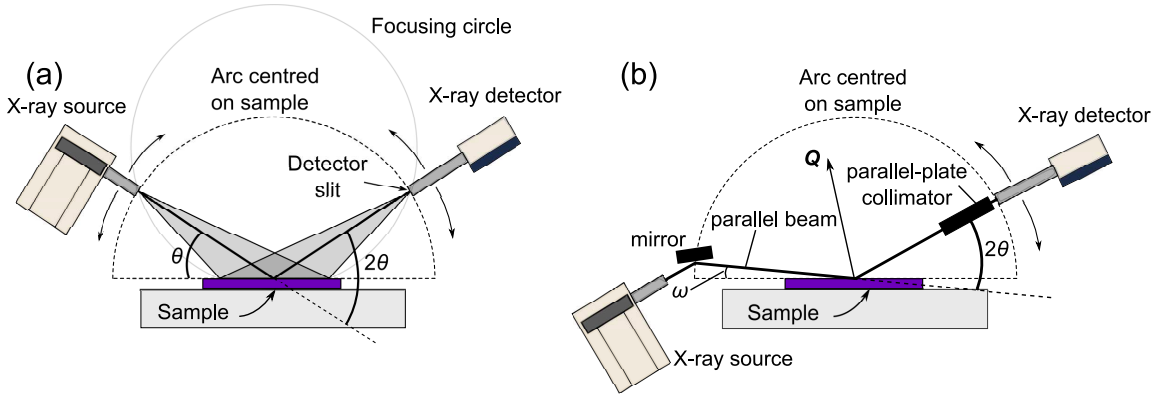

Figure 3.4: Schematic illustrations of two different experimental configurations to measure X-ray diffraction: (a) Bragg-Brentano configuration. (b) Grazing incidence configuration.

interfere with the reflected one, constructively or destructively, depending on the thickness of the thin film. The mathematical treatment of this situation is based on the Fresnel reflection and transmission coefficients as derived in the electromagnetic wave propagation theory. By changing the angle of incidence, successive destructive and constructive interference conditions can be achieved. By measuring the periodicity of the fringes pattern in the reflectivity vs. incident angle plot, such as the one in Fig. 3.5(c), the thickness of the thin film can be retrieved [184].

The critical angle of incidence, below which total reflection is observed, carries information on the density of the thin film material. The complex refractive index is described by a deviation from unity with a real dispersive part δ and an imaginary dissipative part related to absorption β [185]:

$$n = 1 - \delta - i\beta. \tag{3.3}$$

The dissipative part β is usually much smaller than the dispersive part δ, so it normally is neglected, giving $n = 1 - \delta$. The latter term is given by:

$$\delta = \frac{\lambda^2 r_e}{2\pi}\rho_e \tag{3.4}$$

where λ is the wavelength of the incident X-rays, $r_e \approx 2.818 \times 10^{-15}$ m is the classical electron radius and ρ_e the electron density. The electron density can be used to calculate the mass density ρ_m of the material by:

$$\rho_m = \frac{\sum_i x_i A_i}{N_A \sum_i x_i \left(Z_i + f_i\right)}\rho_e, \tag{3.5}$$

with x_i the atomic (or molar) ratio, A_i the atomic mass, Z_i the atomic number and f_i the atomic scattering factor, all for the ith atom, and N_A is Avogadro's number. Using Snell's law for refraction and the knowledge that $\delta \ll 1$, one arrives at the condition for the critical angle θ_c for total reflection:

$$\theta_c \approx \sqrt{2\delta}. \tag{3.6}$$

Therefore, the measurement of the critical angle enables the determination of the density of the thin film.

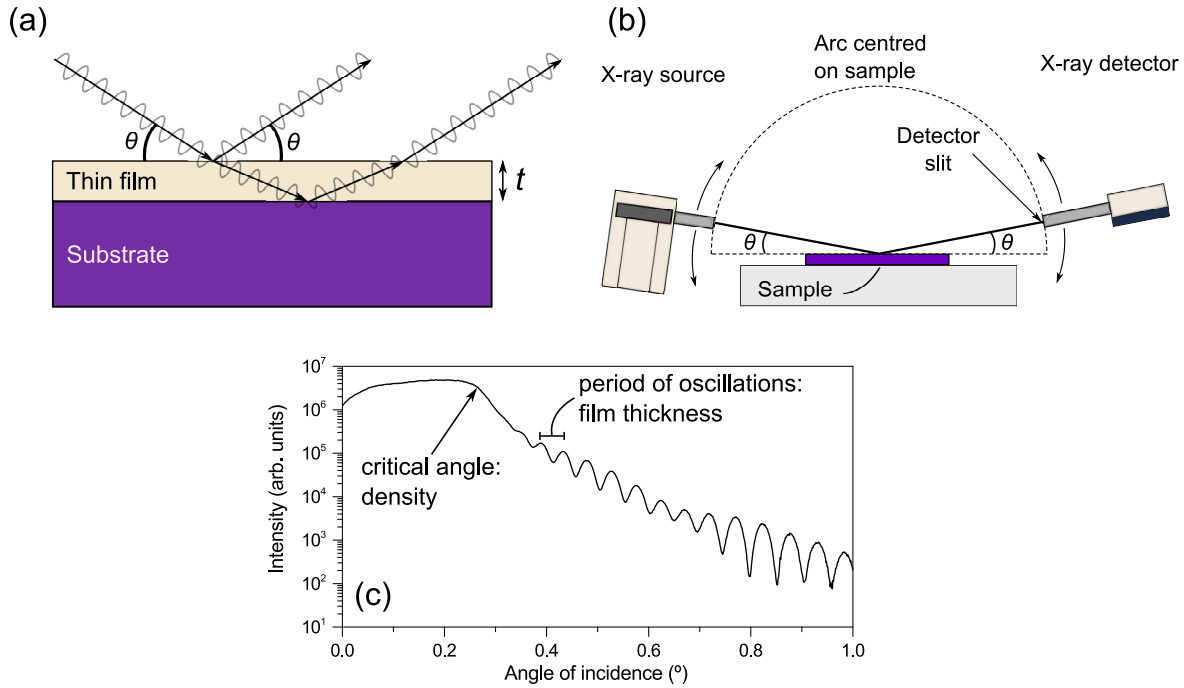

Figure 3.5: (a) Schematic illustration of the X-ray reflection and refraction at the air-film interface, showing the path of the X-rays and the origin of the intereference that gives rise to the fringes in the X-ray reflectometry data. (b) Sketch of the experimental configuration used to measure the X-ray reflectometry. It is symmetrical just like the Bragg-Brentano configuration for XRD measurements, but as it is dealing with very small angles of incidence, takes the necessary instrumentation considerations used in the GIXRD configuration. (c) Example of XRR data, showing how the film density and thickness can be retrieved from the data. The data refers to a 36 nm-thick Pt thin film on top of SiO_2 with a 6 nm-thick Ta adhesion layer.

Experimental conditions for this work
The equipment used for the XRD and XRR measurements was the PANalytical "X'Pert PRO" X-ray diffractometer. The characteristic Cu K_α radiation with $\lambda = 1.5406$ Å was used in all measurements. The analysis of the layers by XRR with the determination of the thickness and film density was performed by fitting the experimental data to a layer model using a commercial software from PANalytical.

3.2.2 Rutherford backscattering spectrometry (RBS)

Ernest Rutherford developed a model of the atom in 1911 based on the experimental observation of backscattering of alpha particles from a gold foil, which was not compatible with the "plum-pudding" model of the atom, put forth in 1904 by J. J. Thomson. Rutherford's experimental setup was later adapted into a technique for the analysis of solids named Rutherford backscattering spectrometry (RBS) [186].

The technique consists in the irradiation of solid materials with accelerated light ions (normally $^4He^+$) and the detection of the backscattered ions due to collisions with the atoms from the material. The energy lost by the backscattered ions gives quantitative information on the chemical composition of the material and the depth profiling of individual elements.

In the Cornell geometry, the incident beam, the exit beam and the sample rotation axis are in the same plane, as illustrated in Fig. 3.6(a). This geometry has the advantage of combining a large scattering angle, which enables a better mass resolution, with the possibility to irradiate the sample in a grazing incidence, which increases the depth resolution.

The determination of the energy of the backscattered ions is based on the classical kinematics of elastic collisions, with conservation of energy and momentum, where the ions are considered hard spheres. The situation is schematically depicted in Fig. 3.6(b). Given an ion with incident energy E_0 and mass M_1, its energy after the elastic collision is given in the laboratory system by:

$$E_1 = KE_0, \tag{3.7}$$

where K is the kinematic factor given by:

$$K = \frac{M_1^2}{(M_1 + M_2)^2}\left[\cos\theta \pm \sqrt{\left(\frac{M_2}{M_1}\right)^2 - \sin^2\theta}\right]^2, \tag{3.8}$$

with θ the scattering angle and M_2 the mass of the target nucleus, considered to be initially at rest. This is enough to determine the elements that compose the sample material. However, this simple classical kinematic approach to the problem does not enable the quantitative analysis of the material composition. For that, the model of the collision has to be enhanced by considering the scattering due to the Coulomb repulsion between the charged ion and the charged nucleus of the atom where the first scatters.

To quantify the number of atoms in the target per unit of cross section area, one needs to know the probability of collision between the incident ion and the atoms of the target. This can be obtained by measuring the total number of detected ions for a certain number of incident ions. The effective scattering section describes the probability of an atom from the target to scatter an ion at an angle θ inside a solid angle $d\Omega$ centred around θ. In a RBS

system, the solid angle of the detector is small, so that the mean scattering section is given by

$$\sigma(\theta) = 4\left(\frac{Z_1 Z_2 e^2}{16\pi\varepsilon_0 E_0}\right)^2 \frac{\left[\sqrt{1-\left(\frac{M_1}{M_2}\sin\theta\right)^2}+\cos\theta\right]^2}{\sin^4\theta\sqrt{1-\left(\frac{M_1}{M_2}\sin\theta\right)^2}} \quad \left(\mathrm{m^2 sr^{-1}}\right), \tag{3.9}$$

with Z_1 and Z_2 the atomic numbers of the incident ion and of the target atom, respectively and ε_0 the electrical permittivity of the vacuum. This formula takes into account the recoil of the target atom due to the Coulomb repulsion. The original formula by Rutherford did not consider this recoil and comes simply as:

$$\sigma(\theta) = \left(\frac{Z_1 Z_2 e^2}{16\pi\varepsilon_0 E_0}\right)^2 \frac{1}{\sin^4\left(\frac{\theta}{2}\right)}. \tag{3.10}$$

The depth profiling is possible due to the inelastic scattering with electrons (electron stopping) and target nuclei (nuclear stopping).

Complementary methods

The sensitivity of RBS for light elements is low, therefore it is often required to combine the technique with other methods such as nuclear reaction analysis (NRA) and/or elastic recoil detection analysis (ERDA). While NRA detects the ions that were inelastically scattered and that took part in nuclear reactions, ERDA detects recoil atoms from the sample after the collision at forward angles (Also shown in Fig. 3.6(a)). Depth profiling is also possible in ERDA due to the same stopping effects mentioned before.

Experimental conditions for this work

RBS measurements were made in the universal chamber, at grazing angle (78° or 80°) and at 45°. ERDA spectra were collected at 24° forward angle. The RBS detector is located at a scattering angle of 160° in the Cornell geometry. Spectra were collected for 2 MeV $^4He^+$. The RBS data were analysed with the IBA DataFurnace NDF v9.6i [187]. Double scattering was calculated with the algorithms given in ref. [188]. Pileup was calculated with the algorithms given in ref. [189].

The TaO_x films used for the RBS measurements had a thickness of approximately 50 nm but were not the same as the ones used in the XRD study due to a special structure used to optimize the oxygen signal from the TaO_x layer in the RBS spectra. A study based on simulations of RBS spectra using the RUMP software [190] revealed that for the materials available in the deposition tools used, the TaO_x layers should be covered with an Au layer. This metallic layer is preferred to the Al_2O_3 used throughout the work, because the oxygen signal stemming from the Al_2O_3 would decrease the sensitivity of the technique to the determination of the oxygen content of the underlying TaO_x layer. The same argument was used against the use of the SiO_2 insulating layer beneath the TaO_x. So, a Si substrate with just the natural oxide on the surface was preferred. The layer structure used for the RBS samples is shown in Fig. 3.6(c), while the simulated RBS spectrum is shown in Fig. 3.6(d).

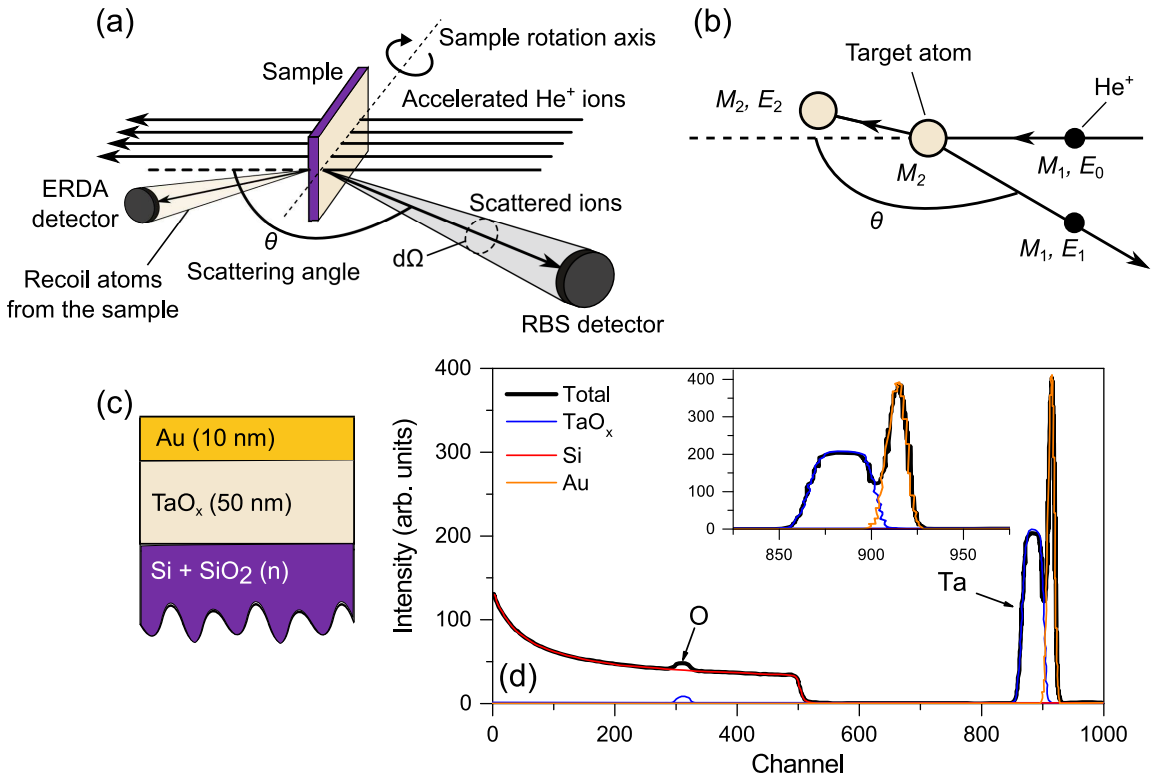

Figure 3.6: (a) Simplified schematic illustration of the RBS configuration in the Cornell geometry. The incident beam, the detected backscattered beam and the sample rotation axis lie in the same plane. The RBS detector is positioned in the backward region, while the ERDA detector is positioned in the forward region relatively to the ion beam incident on the sample. (b) Illustration of the simplified kinematic approach to the backscattering of accelerated ions by atoms of the target (sample), where the ion and the atom are considered hard spheres with mass M_1 and M_2, respectively. (c) Simulation of the RBS signal from a $Au/TaO_x/Si$ stack obtained using the simulation tool RUMP.

3.2.3 Transmission electron microscopy (TEM)

The smallest distance that can be resolved with a microscope is given by

$$\delta = \frac{0.61\lambda}{n \sin \alpha}, \tag{3.11}$$

where λ is the wavelength of the radiation used in the microscope, n is the refractive index of the viewing medium and α is the semi-angle of collection of the magnifying lens. The denominator is known as the numerical aperture of the lens. Therefore, a smaller distance can be resolved if the numerical aperture is increased and/or the wavelength decreased. Transmission electron microscopy takes advantage of the fact that accelerated electrons have a very short wavelength [191]. The wavelength of the electrons is determined by their kinetic energy E_c through:

$$\lambda = \frac{12.2}{\sqrt{E_c(\text{eV})}} \quad (\text{Å}), \tag{3.12}$$

ignoring relativistic effects. This relation means that with a higher accelerating voltage, a higher resolution is achieved, *i.e.* a smaller distance can be resolved.

There are two main phenomena that are used to obtain a source for electrons in an electron microscope: the thermionic emission and the field emission. In analogy with an optical microscope, TEM also needs lenses to magnify and form the image. The lenses of the optical microscope are substituted by magnetic lenses, normally based on the magnetically induced deviation of the electron trajectory. There are different types of lenses in the TEM and they control all the basic operations of the TEM. Either they act to demagnify the source image onto the specimen or they magnify the image (or electron diffraction pattern) from the specimen. Each lens is often accompanied by an aperture that can be inserted above, in, or below the plane of the lens. Its objective is to limit the collection angle of the lens, *i.e.* the electrons that will form the image. The aperture of the objective lens controls the resolution of the image, the image contrast, the depth of field, the depth of focus, among other things. The aperture of the condenser lens can select the electrons that illuminate the sample and thus form a more parallel beam when a smaller aperture is used, at the cost of decreasing the electron current. The apertures are usually circular holes made in refractory metal disks. The placement of the objective aperture also allows to choose between two different types of TEM images that can be acquired, a bright-field image or a dark-field image. For bright-field imaging the aperture is centred on the direct beam, while for dark-field imaging it is centred on a diffracted beam. Another approach to obtain dark-field is to tilt the electron beam incident on the sample so that the diffracted beam is on the optical axis, which reduces the effect of aberrations (greater effect in off-optical axis beams).

The images are formed due to contrast, which is the difference in intensity between two adjacent areas. In TEM, the contrast arises from the scattering of electrons by the sample. There are two distinct types of contrast, the amplitude contrast and the phase contrast. In the amplitude contrast there are two main mechanisms of contrast, the mass-thickness contrast and the diffraction contrast, so that in total there are three main mechanisms of contrast. The mass-thickness contrast is related to the stronger scattering of the electrons by more dense (higher mass of the elements) and thicker samples, which translates into higher scattering angles and gives rise to a darker region in the bright-field image [192]. The diffraction contrast arises from the differing amplitudes of the undiffracted and diffracted beams, which results in different intensity variations in the image formed by the different beams. It is the major

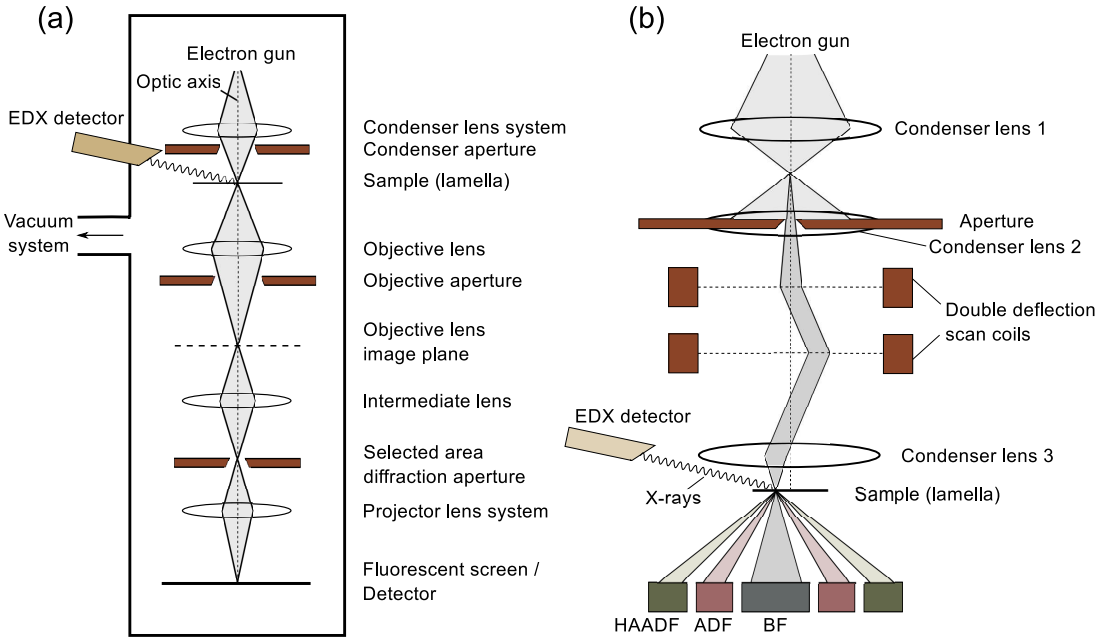

Figure 3.7: (a) Simplified scheme of a TEM with an EDX detector, showing the main components used to form an image of a thin sample. The rays indicated are relative to the image formation and not to the diffraction pattern. (b) Scheme illustrating the image formation in STEM, highlighting the main instrumentation differences relatively to traditional TEM shown in (a). For the specific case of HAADF STEM imaging the signal is collected at the high-angle annular dark field (HAADF) detector and used to produce the image of the sample.

contrast mechanism in crystalline samples. The diffracted beams are used to form dark-field images. Microstructural features like bends, variations in the thickness and crystal defects show strong diffraction contrast. The phase contrast is due to the interference of electrons with different phases and is specially important for high-resolution TEM (HRTEM). The possibility of imaging the atomic structure comes from the dependence of the interference of the electrons on the periodicity of the lattice.

The microscope

The TEM is normally composed by three main parts: the illumination system, the objective lens and stage and the imaging system. A simplified scheme is presented in figure 3.7(a).

The illumination system includes the electron gun and all the lenses that exist prior to the sample, and its function is precisely to illuminate the sample. This system can be operated in the parallel beam mode, used for TEM imaging and diffraction (selected-area), and in the convergent-beam mode, used for scanning TEM (STEM) and auxiliary techniques such as energy dispersive X-ray spectroscopy (EDX or EDS) and electron energy loss spectrometry (EELS). The illumination system operating in the parallel beam mode has at least two condenser lenses that adjust the electron beam to be parallel as it illuminates the sample. With only two condenser lenses, the second condenser lens is underfocused, so that the focus plane is under the sample and the beam is approximately parallel as it hits the sample. By

decreasing the size of the condenser aperture the beam can be made more parallel, at the expense of the electron current. The inclusion of a third condenser lens makes it easier to obtain of a parallel beam at the sample. For operation in the convergent beam mode, the second or the third condenser lens is focused on the sample.

The objective lens and stage are the most important components as it is where the beam-sample interactions occur. Also, the quality of the objective lens defines the quality of the retrieved information as it is responsible for the creation of both the image and the electron diffraction pattern. These can be obtained in the image plane and in the back focal plane of the objective lens, respectively. The stage is used to fix the sample after the focusing has been achieved and the eucentricity set. The eucentric plane is a reference plane for side-entry sample holders where a tilt of the sample along the holder axis does not laterally move a point in the optic axis. This simplifies the acquisition of the images and the diffraction patterns.

After the objective lens the image and diffraction patterns need to be magnified before reaching the screen/detector, which is achieved with the imaging system that contains at least two more lenses: an intermediate lens and a projector lens. If the selected area diffraction pattern is wanted, an aperture, known as selected area aperture, is inserted in the image plane of the objective lens in order to virtually select the area of the sample that is illuminated. If the image is to be acquired, another aperture, known as the objective aperture, is inserted in the back focal plane of the objective lens. The location of this aperture can be changed in order to obtain a bright- or dark-field image.

Finally, the image is formed by transforming the transmitted electron beam into visible light through cathodoluminescence. Traditionally this was performed with a fluorescent screen, but this has evolved into detectors based on semiconductors or scintillator-photomultiplier systems, such as a charge-coupled devices (CCD).

Scanning transmission electron microscopy

Scanning TEM (STEM) is obtained when the incident beam is scanned over the sample, instead of being static and incident on a larger area as in the traditional TEM described [191]. The beam is controlled by scan coils that deflect it into a point in the sample. The signal generated from the transmission of this beam is then displayed in the final image at an equivalent point. STEM uses double deflection scan coils in order to guarantee that the incident beam is always parallel to the optical axis, so that the diffraction is achieved in the same conditions for every scanning point.

In a STEM all the lenses after the objective lens are dispensed, as the detector is placed on a conjugate plane of the back focal plane of the objective lens in the direct beam or a diffracted beam, if a bright- or dark-field image is to be acquired, respectively. But a better solution for dark-field imaging is to use an annular detector that surrounds the bright-field detector, eliminating the need for the detector's displacement. This establishes the annular dark field imaging. If the electrons scattered at higher angles are collected by a detector surrounding the first annular detector, the technique is called high-angle annular dark field (HAADF) STEM. The scattering at higher angles is mostly caused by Rutherford scattering of the electrons at the nucleus of the atoms of the sample. This enables a different contrast mechanism, comparatively to the normal TEM, which is called Z-contrast (Z stands for the atomic number). In this high-angle collection mode, the Z-contrast should superimpose the diffraction contrast from crystalline parts of the sample, which is more prominent for lower angles. The Z-contrast is highly chemically sensitive because the elastic cross section of the

scattering is highly dependent on Z, resulting in a higher signal (brighter image) from heavy elements.

EDX

The interaction of the electrons with matter leads to the generation of different types of signals that can be detected accordingly by auxiliary techniques and give useful information to aid the sample analysis. The accelerated electrons of the beam can induce electron transitions in the atoms, which upon relaxing will emit characteristic X-rays. This characteristic radiation can be collected in a detector in order to retrieve information about the chemical composition of the sample. Combined with the STEM imaging, this allows a chemical mapping of the sample. The technique associated with the detection and analysis of these X-rays is called energy-dispersive X-ray spectroscopy (EDX or EDS).

Experimental conditions for this work
The HAADF STEM imaging combined with EDX spectroscopy mapping was carried out on a FEI Titan ChemiSTEM probe C_s-corrected TEM operated at 200 kV and equipped with a Bruker "Super-X" wide solid angle EDX detector. The microscope is thoroughly described in [193].

3.3 Electrical characterization techniques

3.3.1 Current-Voltage measurements

An important way to characterize the electrical behaviour of an electronic device or electrical circuit is achieved by measuring its current-voltage ($I-V$) characteristic, which depicts the current response of a device/circuit when an electric potential difference (voltage) is applied at its terminals. A simple $I-V$ measurement can immediately distinguish different types of devices, such as resistors, diodes, solar cells or memristive devices. The $I-V$ characterization is, in fact, an essential procedure in the study of the RS. Although memory devices are meant to be operated in a pulsed voltage/current scheme, the $I-V$ characteristics enable the study of the memory operation [2]. Typically, continuous voltage sweeps are used to measure the $I-V$ characteristics, but pulsed sweeps are also common, where the voltage increase or decrease is performed by pulses interleaved by a time interval where no voltage is applied. By analysing the $I-V$ characteristics, the different resistance states can be distinguished and the main RS characteristics can be obtained, namely the SET and RESET voltages, the ohmic or rectifying character of the curves, as well as the resistance in each state. The $I-V$ curves, at least for a certain voltage range, also contain information on the conduction mechanisms involved in the different resistance states.

Experimental conditions for this work
The $I-V$ measurements were carried out using a SourceMeter from Keithley. Different models were used with little relevant changes in their specifications between them for the measurements performed: either 2611A, 6440 or 2440. The measurements were automated via in-house written software, written in LUA (RWTH) or Matlab® (UAveiro). The devices were probed in a suitable probestation equipped with micropositioners, a microscope and

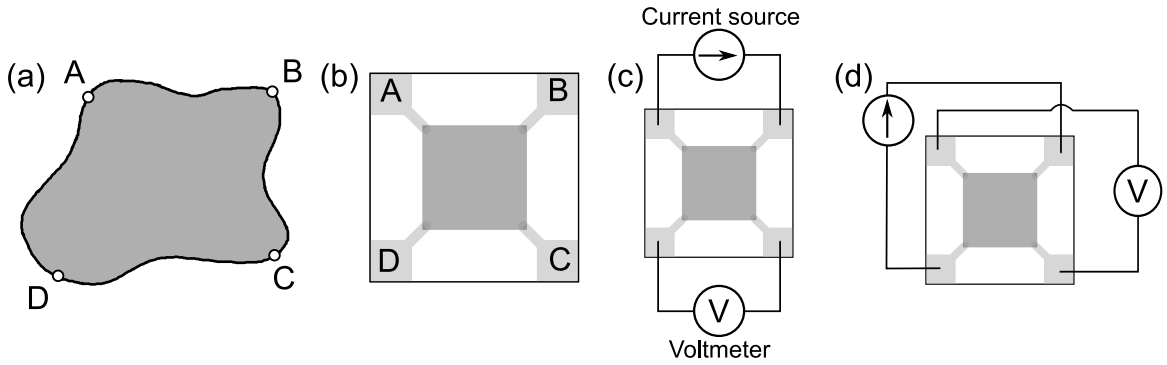

Figure 3.8: (a) Illustration of an arbitrarily shaped sample where 4 electrical contacts A, B, C and D are made to measure the resistivity through the van der Pauw (vdP) method. (b) Illustration of a possible symmetrical vdP configuration, the one used in this work. (c) Schematic of one of the individual measurements required for obtaining the resistivity by the vdP method, where the current is applied between adjacent contacts (A,B) and the voltage is measured between the two remaining contacts (C,D). (d) Schematic of the wiring configuration needed for a Hall measurement using the vdP method, where the current is applied between diagonally opposite contacts (B,D) and the Hall voltage is measured between the two remaining contacts (A,C).

tunsgten needles for electrical contacting (RWTH), or in a in-house-made sample holder with wire-bonding via gold wires (UAveiro). The voltage was swept in a quasi-static (continuous) regime with a sweeping rate of approximately 0.5 V/s.

3.3.2 Resistivity measurements

In a two-point measurement the sample is measured by using two contacts, which serve as both current and voltage probes. While being the most simple measurement method, this configuration leads to a measured resistance that includes not only that of the sample but also the contact resistance and the resistance from the wires/probes that connect the sample to the measurement equipment. This problem can be largely avoided by employing a four-point configuration. Two additional contacts are made, separating the current probes, through which a current is imposed into the sample, from the voltage probes, where the voltage drop in the sample is measured. Due to the normally high input impedance of a voltmeter, the current flowing through the voltage path is very low, greatly decreasing the voltage drops due to the contact and wire resistances.

Typical 4-point methods to measure the resistivity (ρ) of materials include the collinear 4-probe method and the Hall test bar.

The van der Pauw method

An additional method for the measurement of the resistivity was developed by van der Pauw in 1958 [194]. This is now known as the van der Pauw method, and it is particularly useful for the measurement of the resistivity and Hall effect of arbitrarily shaped samples, such as the example illustrated in Fig. 3.8. Applying a current I_{AB} between the contacts A

and B and measuring the potential difference V_{DC} between contacts D and C, the measured resistance is:

$$R_{AB,DC} = \frac{V_{DC}}{I_{AB}}. \tag{3.13}$$

Analagously, we can write

$$R_{AD,BC} = \frac{V_{BC}}{I_{AD}}. \tag{3.14}$$

The van der Pauw method is based on the theorem that there is a relation between these two resistances, expressed as:

$$\exp\left(-\pi\frac{R_{AB,DC}}{R_S}\right) + \exp\left(-\pi\frac{R_{AD,BC}}{R_S}\right) = 1, \tag{3.15}$$

where $R_S = \rho/t$ is the sheet resistance, from which the resistivity can be directly obtained with the knowledge of the thickness t of the sample. This equation has to be solved numerically to obtain R_S. However, if the sample is symmetrical, so that $R_{AB,DC} = R_{AD,BC} = R$, equation (3.15) is simplified, and the sheet resistance can be directly calculated by:

$$R_S = \frac{\pi}{\ln 2}R \approx 4.532R. \tag{3.16}$$

The accuracy of the resistivity determination can be enhanced if the reciprocal values of resistance are also measured, *i.e.* if the current and voltage probes are switched for each of the resistances indicated above. An average of these resistances for each pair of contacts is then calculated:

$$R_h = \frac{R_{AB,DC} + R_{DC,AB}}{2} \text{ and } R_v = \frac{R_{AD,BC} + R_{BC,AD}}{2}, \tag{3.17}$$

which are then introduced in eq. (3.15):

$$\exp\left(-\pi\frac{R_h}{R_S}\right) + \exp\left(-\pi\frac{R_v}{R_S}\right) = 1. \tag{3.18}$$

Further accuracy is obtained when the direction of the current is reversed, leading to a total of 8 resistance measurements. This is important for the case of strong voltage offsets due, for example, to thermoelectric effects. Eq. (3.18) can be solved numerically, *e.g.* with Newton's method, in order to obtain R_S and consequently the resistivity ρ.

The van der Pauw method is based on the assumption of negligibly small contacts located on the sample periphery. Not taking this into consideration largely increases the experimental error and compromises the resistivity value obtained [141]. For this work, a symmetrical square sample with electrical contacts at the 4 vertices was chosen, as depicted in Fig. 3.8(b). The contact configuration to measure the resistivity is shown in Fig. 3.8(c).

3.3.3 Hall and magnetoresistance measurements

Hall measurements are based on the Hall effect and enable the determination of the charge carrier sign, density and mobility [141]. The Hall effect was discovered by Edwin Hall in 1879. It describes the appearance of an electric field when a magnetic field is applied perpendicularly to the current flow in the conductor. The electric field develops perpendicularly to both the current and the magnetic field and is caused by the accumulation of charge carriers on one

of the sides of the sample due to the deflection imposed by the magnetic field. The voltage associated with the produced electric field is called the Hall voltage and, considering that electrons are the only charge carriers, it is given by:

$$V_H = -\frac{tR_H}{BI}, \tag{3.19}$$

with t the film thickness, B the external magnetic field, I the current and R_H the Hall coefficient, which carries the information on the carrier concentration (n):

$$R_H = -\frac{r}{qn}, \tag{3.20}$$

where r is the Hall scattering factor, which is dependent on the scattering mechanism of the charge carriers, but that normally ranges between 1 and 2 at low magnetic fields. Therefore, r is normally taken as unity. However, in some cases, it may be needed to account for the actual value of r [195]. The Hall mobility differs from the conductivity mobility (as defined in eq. (2.2)) and is given by:

$$\mu_H = \frac{|R_H|}{\rho} = \frac{1}{qn\rho}. \tag{3.21}$$

The drift mobility is obtained by dividing the Hall mobility by the Hall scattering factor r.

The Hall effect is normally measured in a bridge-shaped sample. However, the van der Pauw geometry enables an easier approach to measure the Hall effect. The measurement configuration differs from that of the resistivity measurements as the measurement has to be done diagonally. For the symmetric arrangement of Fig. 3.8(b), this means that the voltage is measured betweeen contacts A and C (V_{AC}), while sourcing current through the contacts D and B (I_{DB}), as can be seen in Fig. 3.8(d).

The application of an external magnetic field can also have an effect in the resistivity. The change in resistance induced by a magnetic field is called magnetoresistance (MR) and is calculated by:

$$\mathrm{MR} = \frac{R_B - R_0}{R_0}, \tag{3.22}$$

with R_B being the resistance for an applied magnetic field B and R_0 being the resistance without an applied magnetic field.

3.3.4 Temperature and magnetic field dependence

To further characterize the electrical transport, resistivity, Hall and MR measurements are performed in the temperature range from 1.8 K to 300 K. These measurements play a central role in the study presented in this work, because the transport mechanisms have different temperature fingerprints that are visible through the characteristic temperature dependence of the resistivity, the Hall parameters and the MR. The access to the lowest temperatures is especially relevant and may give useful information regarding the local disorder resulting in quantum interference effects (as presented in chapter 2). These disorder-induced effects, such as weak (anti)localization and electron-electron interactions, are normally only observable at very low temperatures. Recently, this kind of analysis was successfully applied to phase-change materials [196]. In order to have access to the low temperatures, a cryostat is needed.

Experimental conditions for this work

The electrical measurements performed in this work were mainly carried out in two cryostats from Quantum Design, Inc.: the PPMS® and the PPMS® Dynacool™, where PPMS stands for Physical Property Measurement System. The major differences between the two systems are the lowest available temperature and the cooling technology. While the PPMS uses liquid helium to refrigerate down to 2 K, the Dynacool uses a cryogen-free pulse tube cryocooler to reach the lower temperature of 1.8 K. Both cryostats enable the application of a magnetic field of up to 9 T to the samples. The magnetic field is provided by a superconducting coil incorporated inside the cyostats. The magnetic field direction is fixed with respect to the cryostat, but for angular dependence of the magnetic field, a rotating sample stage was available. All samples were wire-bonded with Al wires to establish the electrical contacting inside the cryostats. The temperature was measured directly at the sample holder, minimizing the temperature offset, and it was swept at a maximum rate of 4 K/min. The magnetic field was swept at a maximum sweep rate of 10 mT/s.

For additional measurements, a third cryostat was employed: the TTP4 cryoprobestation from Lake Shore®. This cryostat uses liquid nitrogen to provide a flow of cooled He gas to a metallic sample stage, where a minimum temperature of 80 K is achieved. This enabled *in-situ* electrical contacting via four micropositioners equipped with tungsten needles, making it possible to change the device being measured while in vacuum and at low temperature.

3.4 Auxiliary techniques

3.4.1 X-ray photoelectron spectroscopy (XPS)

The photoelectric effect, famously explained by Albert Einstein in one of his *annus mirabilis* papers of 1905, consists in the ejection of electrons from atoms of a solid through bombardment with photons of sufficient energy. The ejected electrons are then called photoelectrons. There is a minimum energy necessary to produce photoelectrons that is defined by the work function of the solid Φ. This minimum energy is related to a threshold frequency ν_t, which is then given by:

$$h\nu_t = \Phi. \tag{3.23}$$

For photons with a higher frequency, there is an excess of energy that is converted into kinetic energy of the photoelectrons:

$$h\nu = \Phi + \frac{1}{2}m_e v^2, \tag{3.24}$$

where m_e and v are their mass and velocity. Photoelectron spectroscopy (also known as photoemission spectroscopy) makes use of this effect in order to retrieve information of materials' surfaces by the analysis of the ejected photoelectrons' kinetic energy [197]. Compared to the easily ionizable alkali metals, for which ultraviolet radiation was sufficient to eject electrons, normal solid surfaces demand higher energy photons. The X-ray photoelectron spectroscopy (XPS) is a particular kind of photoelectron spectroscopy, where X-rays are used to excite the photoelectrons. XPS can induce the ejection of electrons not only from the valence orbitals but also from the core orbitals of the atoms. Therefore, XPS may be used to retrieve chemical

information of the materials under study, namely the valence state of the cations in transition metal oxides and chemical changes that occur in interfaces.

The photoelectrons are inelastically scattered in the material, which largely reduces their mean free path, and therefore the depth from which these electrons can reach the vacuum. Therefore this technique is only surface sensitive and does not provide information of the bulk of the materials or deep layers buried below the surface. This is particularly important in samples where the surface is prone to be modified by atmospheric exposure.

Experimental conditions for this work

The XPS measurements were carried out in a NanoESCA Photoemission electron microscope from Scienta Omicron GmbH (described in detail in ref. [198]). The machine is equipped with a monochromatic aluminum K_α source with an excitation energy of 1486.6 eV. For obtaining regular, non spatially resolved, photoelectron spectra a single channeltron detector was used.

3.4.2 Local conductivity atomic force microscopy (LC-AFM)

Atomic force microscopy (AFM) is a powerful tool for materials research at the nanoscale. It makes use of a small sharp tip to analyse the surface of materials with a high lateral spatial resolution of the order of nm. The physical principle behind the technique is the force exerted on the small tip by the atoms of the surface. This force is attractive or repulsive depending on the distance between the tip and the surface, and can be qualitatively described by the Lennard-Jones potential. This mechanism allows the mapping of a sample's surface topography.

The AFM is quite versatile, as the tip can be designed to enable measurement of other physical properties of the sample's surface. When the tip is carefully designed in order to be conductive, the microscope can be used for local conductivity AFM (LC-AFM), also known just as conductive AFM (CAFM) [199]. With this technique, when a voltage is applied between the tip and the sample, the current through the sample can be mapped, along with the topography of the surface. For measuring the current, the microscope needs to be operated in contact mode.

The LC-AFM was applied for the first time to analyse the electrical properties of gate oxides in the 1990s [200]. More recently it has been widely used to study the RS phenomenon in oxides [201, 202].

Experimental conditions for this work

The LC-AFM measurements were conducted in a VT-SPM XA microscope from Scienta Omicron GmbH. An ultrananocrystalline diamond (UNCD) cantilever with a tip diameter smaller than 150 nm was employed and a force of 2 nN was used for the contact mode operation of the LC-AFM. The base pressure of the chamber was 10^{-9} mbar.

3.4.3 Optical absorption spectroscopy

Electromagnetic radiation interacts with matter in different ways. When light, a particular case of electromagnetic radiation, shines on the surface of a material, it can be reflected,

transmitted or absorbed. From these different types of light-matter interaction it is possible to obtain valuable information of the materials. In particular, the absorbed light carries information on the electronic properties of the material, namely the energy bandgap and other possible in-gap electronic states [203].

The absorption needs to be measured indirectly, by measuring the transmitted and reflected light. The most common approach limits the experiment to the measurement of the intensity of the transmitted light and to its comparison with the intensity of the incident light. The absorbance A is then given by the Beer-Lambert law:

$$A = \log_{10}\left(\frac{I_0}{I}\right), \tag{3.25}$$

where I_0 is the intensity of the light incident on the sample surface, which is measured without the sample in the beam path, and I is the intensity transmitted through the sample.

Experimental conditions for this work
The absorption spectroscopy measurements were performed in a Shimadzu UV-3600 UV-Vis-NIR spectrophotometer. The subtrate was measured first, so its signal could be subtracted from the data collected for the different samples with the thin films deposited on top of the substrate.

3.5 Sample fabrication details

Radiofrequency (RF) magnetron sputtering was used to deposit all the layers during the fabrication of the samples. All the samples were grown on top of thermally oxidized p-doped (100)-oriented Si substrates with approximately 430 nm of SiO_2. The as-purchased Si substrates (6 ” wafers) were cleaned and afterwards the SiO_2 layer was formed via thermal oxidation. The base pressure of the sputtering chamber was always lower than 10^{-5} mbar and higher than 10^{-7} mbar before the deposition of the layers, and the sputtering was performed at room temperature.

3.5.1 ReRAM devices

The ReRAM devices were fabricated in a crosspoint geometry. This not only allowed the investigation of microdevices, but also enabled remote contacting of the devices without significantly disturbing the active device area. This last point was particularly important for the low temperature measurements performed in the cryostats, where wire bonding to the samples was needed. To allow an easier bonding to the contact pads, these were designed as 300 μm-wide squares. On the other hand, the sample holder for the cryostats demanded a maximum sample size of 1×1 cm. Therefore, a special photolithography mask was produced in order to abide to these conditions. A schematic depiction of the device geometry and layout can be found in Fig. 3.9. UV photolithography and lift-off (as described in section 3.1.2, and more specifically in Fig. 3.2), were used to pattern the devices in the crosspoint geometry with active cell areas of 5×5 μm^2, 10×10 μm^2 and 25×25 μm^2. The fabrication was performed on top of 1” substrates and the devices were distributed evenly in four 1×1 cm^2 samples (Fig. 3.9(c)).

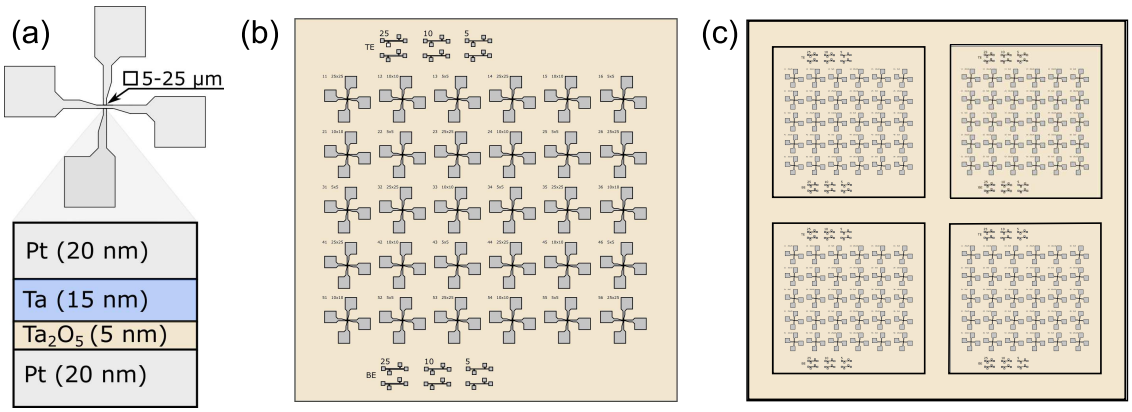

Figure 3.9: (a) Crosspoint geometry used in the fabrication of the Ta_2O_5-based ReRAM devices. (b) Layout of the 1×1 cm^2 samples used in the cryostats, each one with 27 ReRAM devices (3 of the devices were grown without the oxide layer to use as a reference). (c) Layout of the 1×1 inch^2 samples from which the 1×1 cm^2 samples were cut.

The layer stack and thickness of the different layers of the fabricated ReRAM devices were chosen based on a previous optimization process, in order to guarantee the obtention of the desired bipolar counter-eightwise VCM-type switching [89]. The layer stack is composed of 20 nm Pt as a bottom electrode (BE), a 5 nm-thick Ta_2O_5 layer, a Ta layer of 15 nm as top electrode (TE) and a Pt capping layer of 20 nm. This capping layer prevents the oxidation of the Ta TE caused by exposure to the atmosphere. A second series of samples differed in the thickness of the Pt layers, which was increased to 30 nm while maintaining the thickness of the remaining layers. By changing the thickness of Pt, it is possible to tune slightly the series resistance. The metallic layers, Ta and Pt, were sputtered in an inert Ar atmosphere. A Ti or TiO_x adhesion layer of 5 to 15 nm was sputtered prior to the sputtering of the Pt bottom electrodes. The Ta_2O_5 layer was reactively sputtered from a Ta target (99.95 % purity) in a reactive atmosphere composed of a mixture of Ar and O_2. The produced Ta_2O_5 films were all amorphous. A schematic flowchart with the main steps in the fabrication of the Ta_2O_5 crosspoint structures is depicted in Fig. 3.10(a). The main deposition parameters used for the sputtering processes are shown in table 3.1.

3.5.2 Substoichiometric thin films

For the electrical transport measurements, the TaO_x layers were patterned in a van der Pauw structure with 30 nm-thick Pt electrodes using UV lithography and lift-off. The TaO_x layers have been sputtered with a thickness of 20 nm, mainly to keep a similar order of magnitude to the thickness of the oxide layer in the ReRAM devices. To avoid oxidation when exposed to air, the TaO_x films were *in-situ* capped with a 20 nm-thick Al_2O_3 layer, which is a good oxygen diffusion barrier [204]. This layer should not oxidize the TaO_x layer, because Al_2O_3 is a more stable oxide than Ta_2O_5 [82]. Fig. 3.10(b) schematically shows the main fabrication steps used to obtain the van der Pauw TaO_x samples. The layer stack and sample geometry are illustrated in Fig. 3.11. For the composition calibration, XRD and TEM measurements, the samples were sputtered without any patterning and with a thicker TaO_x layer of approximately 50 nm. For the absorption measurements, the TaO_x layers were sputtered on top of sapphire substrates.

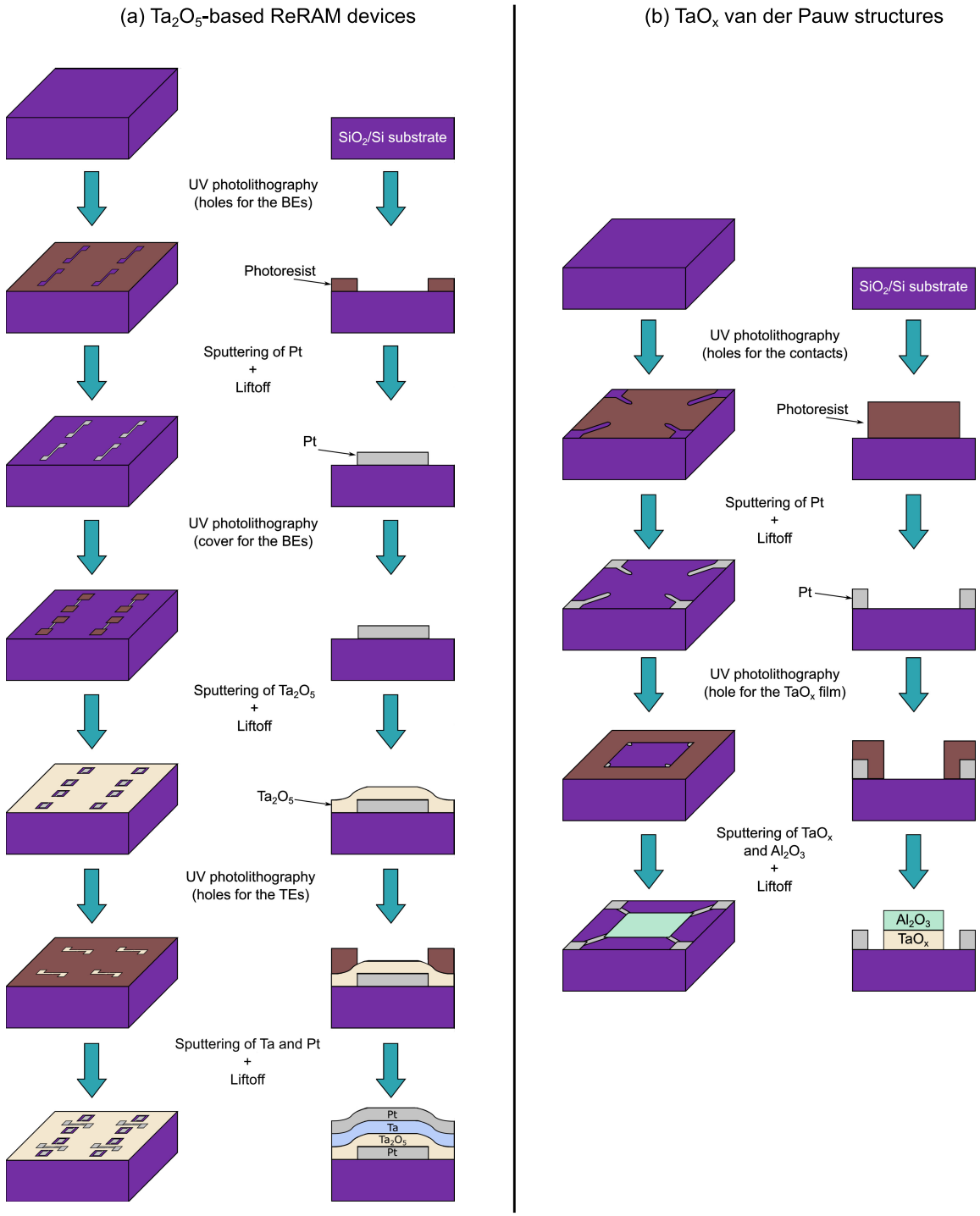

Figure 3.10: Schematic diagram illustrating the main fabrication processes of: (a) the Ta_2O_5-based ReRAM devices; (b) the van der Pauw samples with the TaO_x thin films. The column in the left shows a perspective of the samples' surface in order to schematically show the evolution of the deposited structures, while the column in the right shows the evolution of the layer stacks. BE = bottom electrode and TE = top electrode.

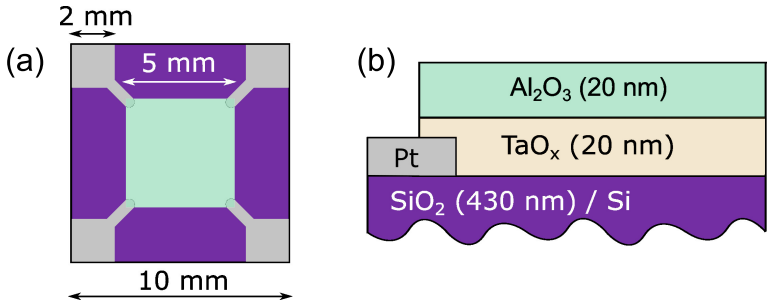

Figure 3.11: (a) Schematic depiction of the van der Pauw structure used to fabricate the TaO_x samples for electrical measurements, with some relevant geometric dimensions. (b) Illustration of the layer stack used in the van der Pauw structures.

Table 3.1: Summary of the reactive magnetron RF sputtering conditions used in the deposition of the different thin films used in this work, which include the metallic layers of Pt and Ta, the substoichiometric TaO_x films, the stoichiometric Ta_2O_5 and Al_2O_3.

Film composition	Power density [W/cm^2]	Ar content[a)] [%]	O_2 content[a)] [%]	Pressure [mbar]	O_2 partial pressure [bar]
Pt	15.79	100	0	0.005	0
Ta	19.74	100	0	0.004	0
TaO_x, $x \sim 1$	29.60	99.98	0.02	0.01	2×10^{-9}
TaO_x, $x \sim 1.3$	17.76	99.98	0.02	0.01	2×10^{-9}
TaO_x, $x \sim 1.5$	9.87	99.96	0.04	0.01	4×10^{-9}
Ta_2O_5	19.74	60	40	0.04	16×10^{-6}
Al_2O_3	9.87	100	0	0.005	0

[a)]Percentage of the gas in the atmosphere inside the sputtering chamber.

The Pt contacts were sputtered in an inert Ar atmosphere. The TaO_x layers were reactively sputtered from a Ta target (99.95 % purity) in a reactive atmosphere composed of a mixture of Ar and O_2 in different proportions. The oxygen content in the TaO_x thin films was tuned by modifying the O_2-to-Ar ratio, the chamber pressure (operating pressure) and the RF power. This influences two main parameters: the oxygen partial pressure and the deposition rate. To allow the needed low oxygen partial pressure, a gas bottle with a mixture of 1% O_2 and 99 % Ar was used to obtain the TaO_x films with the lowest oxygen content. Also the deposition rate should not be too low, as increasing it increases the probability of the reaction of sputtered Ta with the oxygen in the chamber. On the other hand, to guarantee the deposition of the stoichiometric Ta_2O_5, it is important to have a high oxygen partial pressure and a low deposition rate. For comparison of the experimental results obtained for the TaO_x samples, films of Ta and Ta_2O_5 were also sputtered. For the former, no O_2 was introduced in the deposition chamber. Finally, the capping layer of Al_2O_3 was sputtered from a ceramic Al_2O_3 target in Ar atmosphere. The sputtering conditions for the five main compositions used in this work are summarized in table 3.1.

Chapter 4

Correlation between the transport mechanisms in Ta_2O_5-based ReRAM devices and in TaO_x thin films

This chapter deals, in most part, with the electrical properties of the conductive filaments in Ta_2O_5-based ReRAM devices and their relation to the in-plane transport in substoichiometric TaO_x thin films. First, the resistive switching in the Ta/Ta_2O_5/Pt ReRAM devices used throughout the work is characterized. The ReRAM devices with 15 nm-thick Ta top electrodes and 5 nm-thick Ta_2O_5 show the typical bipolar RS of VCM systems. Afterwards, the temperature dependence of the resistance in different resistance states (low and high) of the ReRAM devices is shown. For comparison, the temperature dependence of the resistivity of substoichiometric TaO_x thin films is presented. Finally, a correlation between the transport in the conductive filaments in the devices and the in-plane transport in TaO_x thin films with $x \sim 1$ is highlighted and discussed.

The major results and conclusions presented in this chapter were published in: Carlos M. M. Rosário, et al., *Applied Physics Letters* **112**(21): 213504 (2018). `https://doi.org/10.1063/1.5024504`

4.1 Resistive switching in Ta/Ta_2O_5/Pt ReRAM devices

As previously mentioned in chapter 1, Ta_2O_5 is one of the most popular insulators in MIM structures for ReRAM devices as it enables high endurance and fast switching. To use the advantage of having an oxygen exchange layer in the device stack, a Ta layer was chosen for the top electrode, which also serves as the ohmic electrode. The second electrode was chosen to be Pt, due to its low affinity to oxygen needed for its use as active electrode. The samples fabricated and studied in the framework of this thesis were based on previously optimized fabrication processes, work mainly done by Alexander Schönhals [205]. The balance between the thickness of the Ta and Ta_2O_5 layers defines the polarity mode of the RS obtained. Schönhals et al. showed that for a 5 nm-thick Ta_2O_5 layer, a 15 nm-thick Ta layer provides

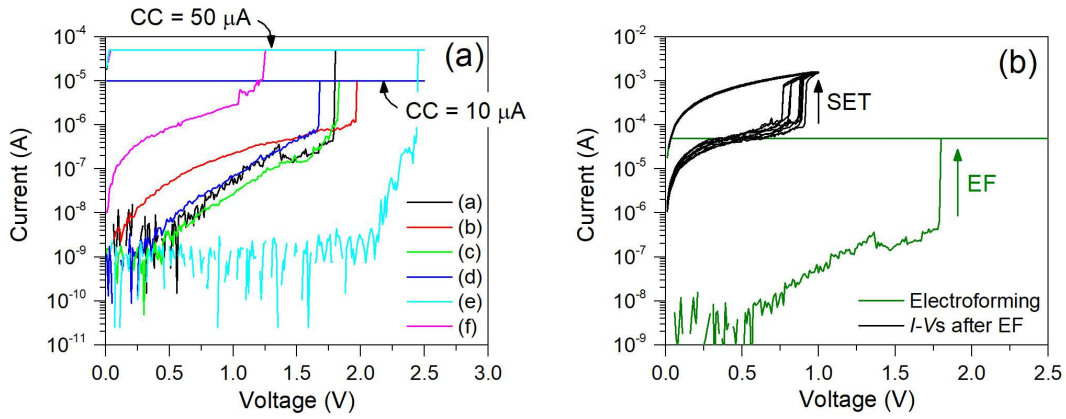

Figure 4.1: (a) Typical quasi-static current-voltage ($I-V$) sweeps obtained during electroforming (EF) of the ReRAM devices, with the current axis on a logarithmic scale. The legend links the EF data to the switching data shown in Fig. 4.2: *e.g.*, (a) corresponds to the device of Fig. 4.2(a). (b) Comparison of the $I-V$ curves during and after electroforming, evidencing the big difference between the resistance in the virgin state and in the HRS.

a bipolar RS, while a 5 nm-thick Ta layer induces complementary switching [89].

4.1.1 Electroforming

Before the RS is observable in the devices, an initial electroforming step is necessary. For the 15 nm-thick Ta devices, the forming is typically achieved at around +2 V. Fig. 4.1 shows some examples of forming $I-V$ curves obtained. The forming voltage shows a dependence on the initial resistance of the device, which varies a few orders of magnitude from device to device. This variability can be due to variations in thickness of the Ta_2O_5 thin film along the sample, or to differences in the size of the oxygen exchange region between Ta and Ta_2O_5, which should be responsible for a decrease in the forming voltage (refer to section 1.4.3). In order to limit the maximum current, a current compliance (CC) of 10 or 50 μA is always used, with no significant differences observed between devices formed with these two different CC values. However, the measurement equipment cannot follow the fast electroforming process, so that the main control of the current is achieved with the series resistance. This series resistance is obtained from the crosspoint electrode lines. It has been shown that the best way to control the maximum current through the ReRAM device is by putting a transistor in series. However, an integrated resistor, such as the one achieved by the lines' series resistance in this case, is a good solution, still better than to rely exclusively on a current compliance from the measurement equipment or on an external series resistor [206]. The current overshoot that exists when the current is not efficiently limited (*i.e.*, on time) is known to affect the filament's size and the subsequent operation of the devices [207–209]. After the electroforming, the typical filamentary C8W VCM-type RS is obtained. As can be seen in Fig. 4.1b, the current in the HRS after forming is several orders of magnitude higher than the initial current in the virgin (pre-forming) state. The voltage needed to induce the SET transition, from LRS to HRS, is also significantly lower than the voltage needed for the electroforming, which can be understood as the first SET.

4.1.2 Bipolar resistive switching

The typical $I-V$ characteristics measured in the $Ta/Ta_2O_5/Pt$ devices are summarized in Fig. 4.2, showing the $I-V$ characteristics measured for six different devices. Fig. 4.2(a)-(d) show four devices where no CC was applied and the current was controlled by the series resistance, either stemming from the line resistance, such as in cases (a)-(c), or from some other internal resistance, as it seems to be the case for (d). Not having a CC normally leads to less variability in the SET voltage, especially when the CC is of the order of 100 μA. Having a CC normally leads to higher resistances in both LRS and HRS. For most of the cases, the devices show a linear $I-V$ characteristic in the LRS, while for the HRS it is always nonlinear. In a few cases, such as the one shown in Fig. 4.2(c), the LRS shows a more nonlinear behaviour, paired with a higher variability in the resistance. The linearity of the LRS indicates an ohmic behaviour and precludes a strong nonlinear effect of contact resistances and other interface effects. There is, thus, no rectifying behaviour dominating the conduction through the ReRAM device in the LRS. This is important for the analysis of the transport data, therefore, the subsequent electrical measurements were mainly based on the devices showing the ohmic behaviour in the LRS.

Besides the nonlinearity, the HRS also exhibits a pronounced asymmetry of the $I-V$ curve, with a lower current (higher resistance) being observed at positive bias in comparison with the same HRS when negatively biased. This is better observed in a $R-V$ plot, where the resistance is plotted as a function of the voltage. It can be clearly seen in Fig. 4.3(a), in the region marked by the red square, that the resistance increases with increasing positive voltage up until the threshold for the SET transition, contrarily to the decrease of the resistance for decreasing negative voltage. This has been explained by a competitive switching process taking place in an 8W fashion, *i.e.* with contrary polarity comparatively to the main RS process. In the 8W switching, the RESET occurs for the same polarity where the SET of the main RS process takes place. The full 8W cycle is sometimes clearly visible, as in the case shown in Fig. 4.3(b), where both switching modes are observable in the same device, after a C8W SET failure up to +1 V in the measurement of the data represented in red led to the observation of the 8W cycle. The 8W RS has been associated with the exchange of oxygen with the Pt active electrode, which can accommodate some oxygen while creating further oxygen vacancies in the conductive filament [55]. The existence of this competitive process limits the RESET of the C8W RS. Similar oxygen exchange with the Pt electrode has also been reported for $SrTiO_3$-based ReRAM cells [210].

4.1.3 "Intrinsinc" resistive switching curve

To obtain an estimate of the real "intrinsic" switching $I-V$ characteristics, the voltage drop over the series resistance can be subtracted. The procedure is based on a paper by Fantini et al. [211], where the authors conclude that the SET transition takes place at a constant voltage. During this time, the applied voltage is still being increased, and the remaining voltage (applied voltage minus the intrinsic SET voltage) drops at the series resistance. Therefore, we can estimate the series resistance by calculating the resistance value necessary to make the SET transition vertical in the $I-V$ plot. Two examples of the intrinsic $I-V$ characteristics obtained by this method are shown in Fig. 4.4, along with the measured data, for the first two cases of Fig. 4.2. Besides the change in the SET voltage, also the RESET voltage changes significantly after the subtraction, relatively to the applied voltage,

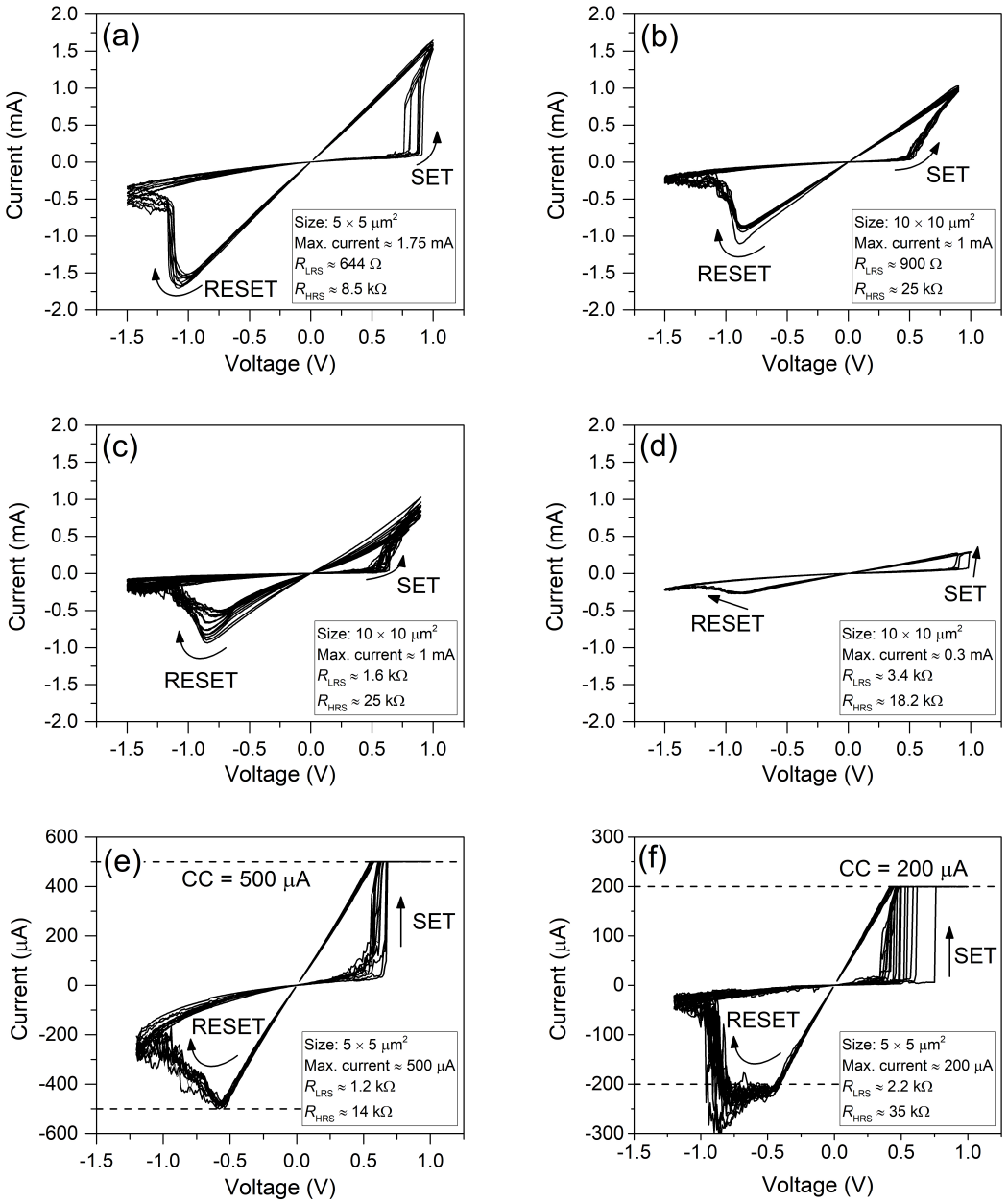

Figure 4.2: Summary of the typical $I - V$ characteristics measured for the $Ta/Ta_2O_5/Pt$ ReRAM devices, along with some characteristics of the RS, the maximum current through the device and the resistance values (measured at $V = 0.1$ V) in the LRS and HRS. Graphs (a) through (d) show 4 different devices where no current compliance was imposed to control the current during SET (current controlled by the series resistance), exhibiting slightly different behaviour, especially in terms of the current values and SET/RESET voltage. Both the voltage and current scales were kept the same between the four graphs in order to enable a better comparison. Graphs (e) and (f) show the typical RS observed with the imposition of a current compliance of 500 μA and 200 μA, respectively. The compliance was only active at positive bias. The dashed line at negative currents is just an indication of the CC value to compare with the maximum RESET current.

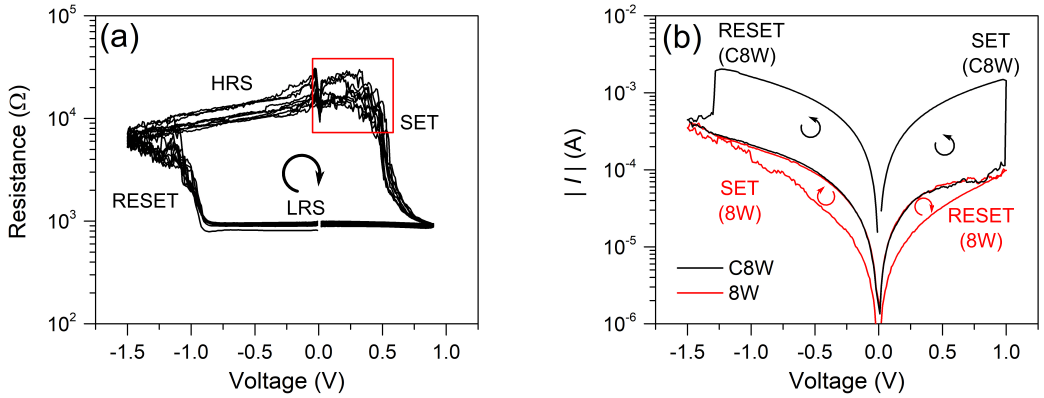

Figure 4.3: (a) Resistance as a function of the voltage for the $I-V$ curves shown previously in Fig. 4.2(b). (b) Example of $I-V$ characteristics evidencing the simultaneous occurrence of counter-eightwise (in black) and eightwise (in red) RS in the same device, which leads to the pronounced asymmetry of the HRS shown in (a).

revealing an almost symmetrical switching curve, with SET and RESET occurring at roughly the same absolute value of the voltage. The voltage for which these transitions occur is known to be around $0.4-0.6$ V for typical VCM systems, independently of the materials used, for relatively slow sweeping rates as used in the *quasi*-static measurements[1] [212]. Even though the origin of this universal voltage is not yet completely clarified, it should be local and/or related to the interface where the switching takes place, because the voltage does not depend on the thickness of the insulating layer [212].

For most of the measured devices, such as the examples shown in Fig. 4.4, the series resistance calculated by using the procedure to obtain the intrinsic $I-V$ curves compares fairly well with the expected series resistance from the electrode lines. Therefore, this further confirms that the lines' resistance is the main origin of the series resistance. Other possible causes for the series resistance, such as internal resistance in the Ta layer due to redistribution of oxygen during the oxygen exchange reaction at the Ta/Ta_2O_5 interface, seem thus to have a negligible effect for the cases shown. The same should not be applicable, however, to the case shown in Fig. 4.2(c), where there should be an additional resistance limiting the current during SET.

On the other hand, the procedure described is equivalent to a measurement performed in a 4-wire configuration, where only the voltage at the ReRAM device terminals is measured, avoiding the voltage dropped at the series resistance.

4.1.4 Cyclability and endurance

Extensive endurance and retention tests were not carried out for these samples. However, the devices can be cycled a lot of times, as can be seen in Fig. 4.5 for two different CC levels, and 100 and 200 μA. These measurements were, however, done using a different apparatus compared to the rest of the measurements. Here, a signal generator and an oscilloscope were used, in order to enable fast sweeping using a triangular wave with a frequency of 100 Hz.

[1] Sweep rates of the order of 1 V/s, for example.

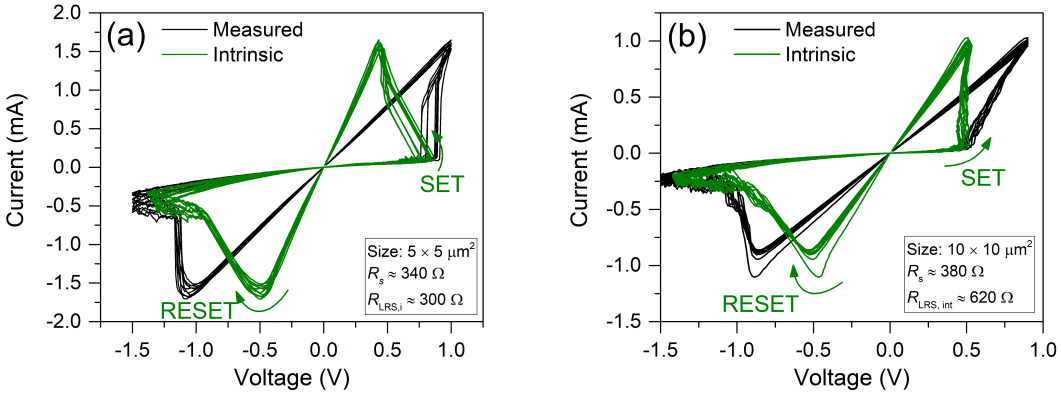

Figure 4.4: Graphs showing the measured $I-V$ characteristics, in black, and the intrinsic $I-V$ characteristics obtained by the procedure mentioned in the text, in green, for two ReRAM devices (shown before in Fig. 4.2(a) and (b), respectively).

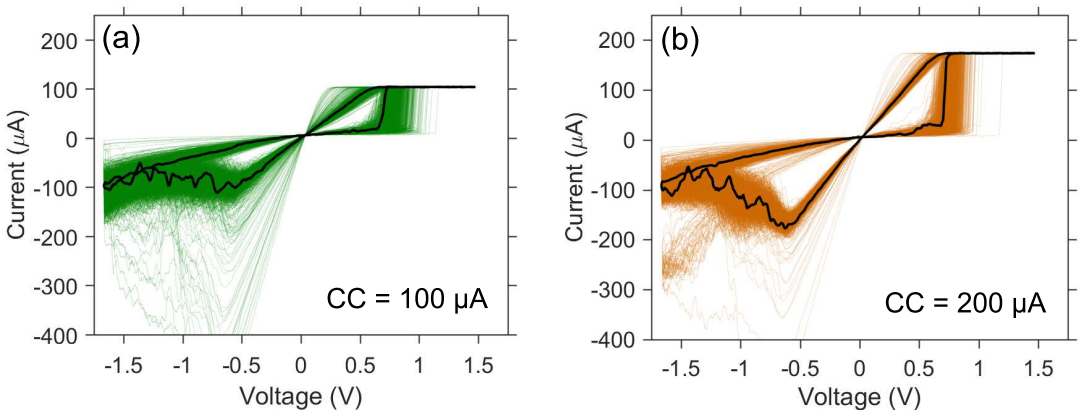

Figure 4.5: $I-V$ characteristics of a $Ta/Ta_2O_5/Pt$ ReRAM device using a "high-frequency" setup showing 1000 cycles. The vast majority of the cycles superimpose each other, with a few outliers. Some current overshoot events are clearly visible but represent less than 1 % of the data. The data is shown for two different current compliance levels: (a) 100 μA and (b) 200 μA. The thick black line represents an example single cycle, in this case the 450th cycle for each data set.

By measuring 100 cycles/s the voltage was swept with a rate of approximately 300 V/s. The plots show approximately 1000 cycles without severe degradation, apart from some events of current overshoot (less than 10 %) that lead to a lower LRS resistance and higher RESET current. The higher frequency of cycling leads to an increase in SET voltage, as it is predicted by the very nonlinear switching kinetics of RS, where a shorter time leads to an increase in the voltage necessary to induce switching [27].

4.2 Temperature dependence of the transport in Ta_2O_5-based ReRAM devices

4.2.1 Low resistance state (LRS)

After at least 10 switching cycles, the devices were set to the LRS, and their resistance was measured as a function of temperature from 300 K down to 2 K in a cryostat. The resistance was measured at a fixed current value in a 4-wire configuration to exclude the series resistance and only probe the Ta/Ta_2O_5 stack. Having ohmic contacts is very important for all the implemented analysis. The $I-V$ data at 300 K already showed that the LRS exhibits a clear linear behaviour, for the majority of the devices. The linearity is an indication of the ohmic nature of the electrical contacts between the conductive filaments (CFs) and the metal electrodes in the LRS. The $I-V$ characteristics also show a linear behaviour in the LRS at the lowest temperature of 2 K and up to the current values that were used for the measurements. An example for the device presented in Fig. 4.2(a) is shown in Fig. 4.6.

The typical temperature dependence of the resistance observed is exemplified by the data for four different devices presented in Fig. 4.9. To enable a better comparison, the data is shown for the four devices that exhibit the RS shown in Fig. 4.2(a)-(d). For all the cases, the resistance decreases with increasing temperature, exhibiting a negative temperature coefficient of resistance (TCR). The temperature dependence is very weak, with the resistance changing by less than 10% from 300 K to 2 K. Also, the resistance is clearly not diverging strongly at low temperatures, evidencing metal-like behaviour. By visual inspection of the data, one can see a slight change of behaviour of the temperature dependence in graphs (a) and (c) at a temperature around 50 K, while in graphs (b) and (d), the resistance seems to follow the same temperature dependence for the whole temperature range.

Fit to conduction mechanisms

In the literature, the main "bulk", non-interfacial-dominated, conduction mechanisms associated with the conductive filaments have been hopping-based processes, such as nearest neighbour hopping (NNH) and Mott's 3D variable range hopping (VRH) [94, 96]. These mechanisms are identified by their characteristic temperature dependences, which were presented in section 2.1.3. By plotting the data in the right set of axes to observe the dependence predicted by these mechanisms, one can graphically assess their suitability to describe the measured data. For the two mechanisms mentioned, the plots that should return a linear behaviour are:

$$\begin{aligned} \text{NNH} &: \ln(1/\rho) \text{ vs. } 1/T \\ \text{3D VRH} &: \ln(1/\rho) \text{ vs. } T^{-1/4}. \end{aligned} \tag{4.1}$$

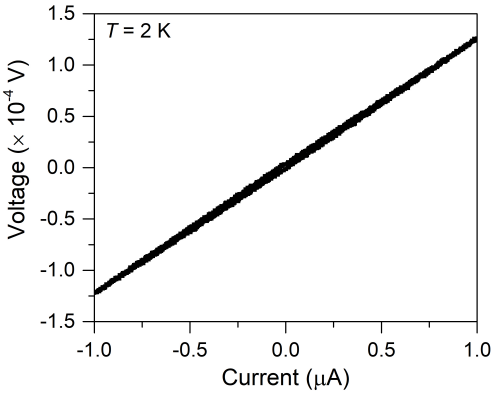

Figure 4.6: $I - V$ characteristic measured at a temperature of 2 K for an example device. A linear behaviour is clearly observed, indicating the ohmic character of the electrical contacts in the device.

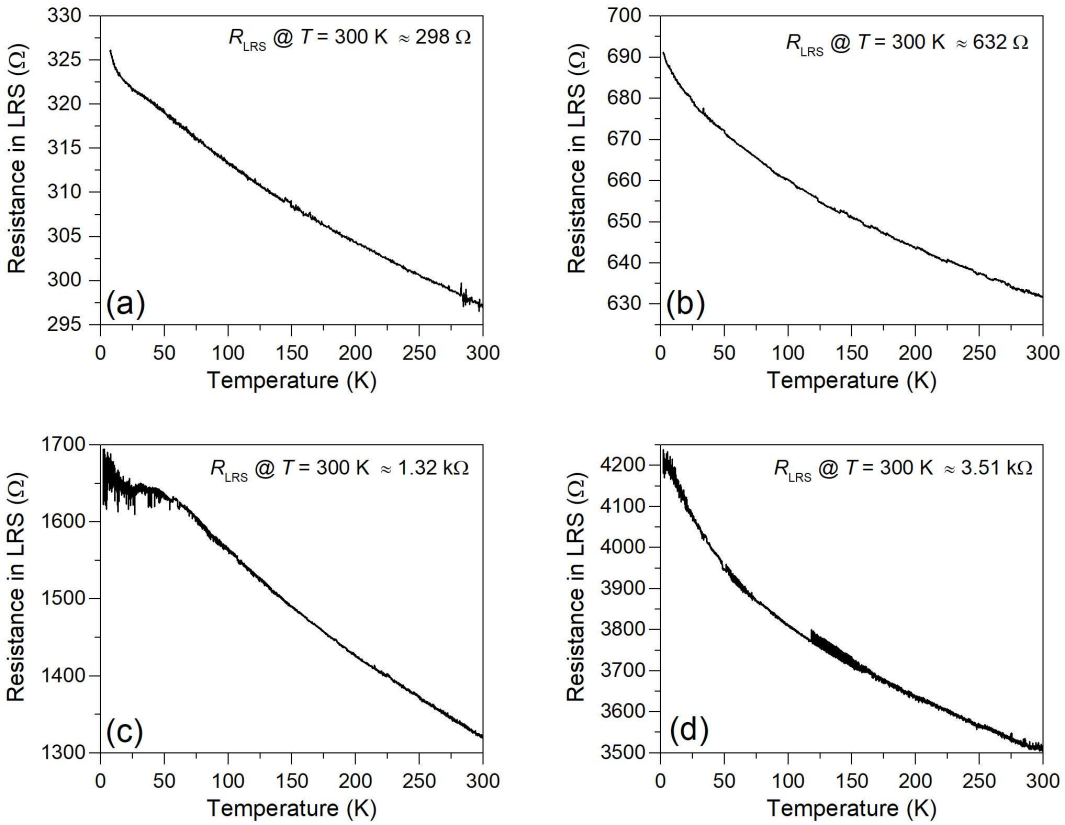

Figure 4.7: Resistance as a function of the temperature for different LRSs, obtained for the four devices whose $I - V$ characteristics are depicted in Fig. 4.2(a)-(d). The graphs are depicted in the same arrangement as before.

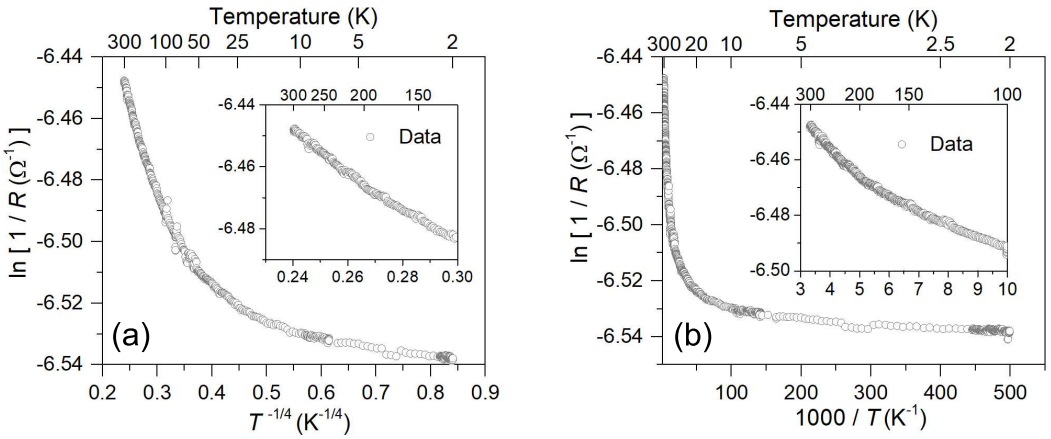

Figure 4.8: Hopping fit tests, with the R vs. T data plotted in the right set of axes for VRH in (a) and for NNH in (b). The insets show in more detail the high temperature region, difficult to observe due to the inverse temperature scale in the x-axis.

Testing these mechanisms does not prove satisfactory, as can be seen in Fig. 4.8 for the data depicted in Fig. 4.7(b). In the VRH plot shown in Fig. 4.8(a), there is just a limited temperature range where the linear behaviour could exist near room temperature and at the lowest temperatures. On the other hand, in the NNH plot presented in 4.8(b), the relationship appears linear also just for a very limited temperature range in the vicinity of 300 K. The obtained activation energy for the NNH fit is approximately 1.1 meV, which seems to be a very small value for this kind of hopping process. Beyond this, the hopping mechanisms lead to unrealistic parameters that are reported in the literature. More specifically, one work assumes hopping distances such as 0.16 nm [96], which are smaller than the reported minimum interatomic distance of 0.19 nm in amorphous Ta_2O_5 [213]. In another case, the distance between oxygen vacancies, considered to be the hopping sites, is 0.3 nm [94], which contradicts the hopping mechanisms involving localized energy levels, as for such a small distance already small energy band should form and lead to a different kind of transport. Therefore, it was concluded that the hopping mechanisms were not suitable to describe the measured transport. This means that different mechanisms for the transport in conductive filaments should be considered.

Going back to the measured temperature dependence of the resistance, for some of the devices, (a) and (c) in Fig. 4.7, a distinctive change in the behaviour of the R vs. T curve is observed at approximately 50 K, as already noted. This divides the R vs. T curve into two regions. In the high-temperature regime, for 50 K $< T <$ 300 K, a very good fit to the data is obtained with a $\sqrt{T}$ dependence of the conductance. In the low-temperature regime, at $T <$ 50 K, an $\exp\left(T^{-1/2}\right)$ dependence gives a good fit for the resistance. The motivation behind the choice of these particular mechanisms and their respective mathematical expressions used in the fitting procedure will be clearly presented in the next chapter. Fig. 4.9(a) shows the results of the fitting procedure with these two expressions, with the linear fits evidenced in the graphs shown in Fig. 4.9(b) and (c). For other devices, as exemplified by the curve in Fig. 4.9(d), the same low temperature regime is less clearly observed. However, the high-temperature regime is maintained until lower temperatures (below 50 K), indicating that, if existent, the transition between the two regions is slightly shifted down on the temperature

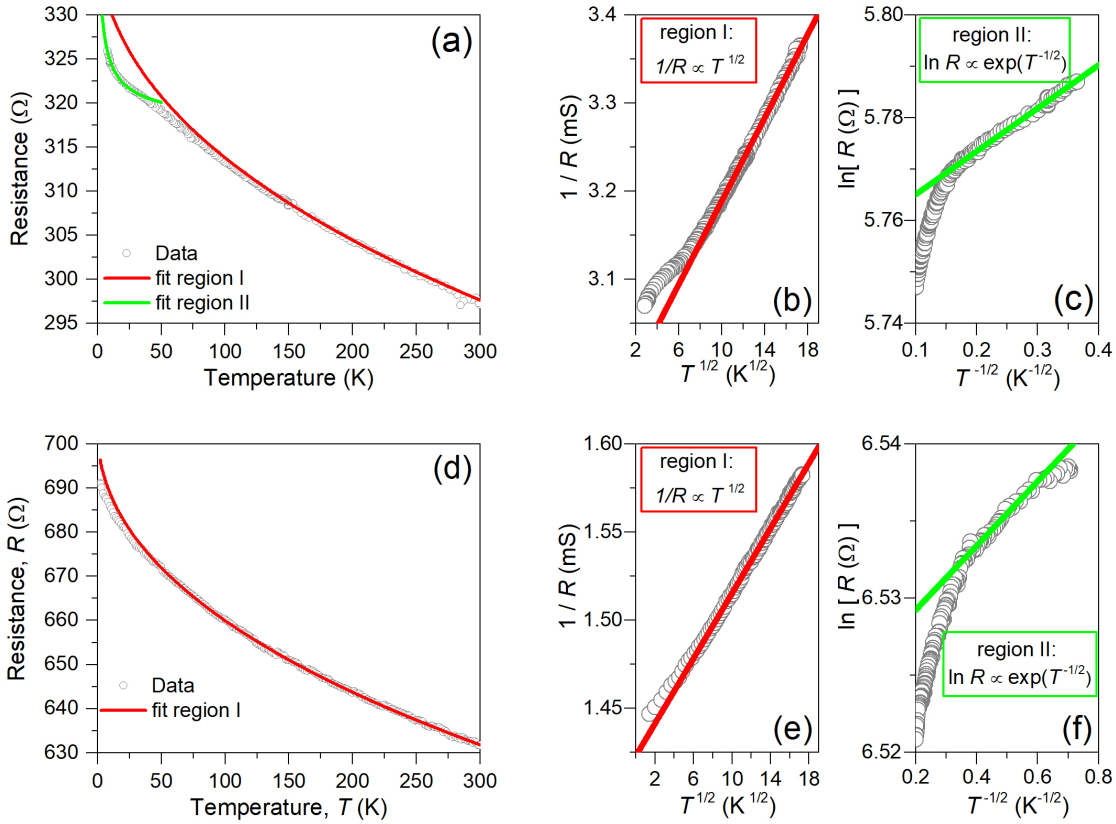

Figure 4.9: (a,b) Resistance as a function of the temperature for two different $Ta/Ta_2O_5/Pt$ devices in the low resistance state. The coloured curves are results of the least squares fitting in two different temperature ranges. The smaller plots on the right show the data in the right set of axes to evidence the linear behaviour and the respective linear fit both for the high- and low-temperature regimes mentioned in the text. The high-temperature regime corresponds to $G = \frac{1}{R} \propto T^{1/2}$, while the low-temperature regime corresponds to $\ln R \propto T^{-1/2}$.

scale.

The data shown so far was measured in the devices with 20 nm-thick Pt electrodes. Measurements were also performed on a second series of devices, with a higher thickness of the Pt electrode of 30 nm. For the same active device area, the increase of the thickness of the Pt layers decreases the series resistance. This allows higher currents through the devices for the same voltage, considering that no CC is used. An example of such devices is shown in Fig. 4.10(a). This particular device shows a temperature dependence of the LRS resistance quite different than the one shown before in Fig. 4.7. As can be seen in Fig. 4.10(b), the TCR is positive, strongly contrasting with the negative TCR observed for the other devices. Interestingly, the positive TCR is also observed for devices in both series that suffered a hard breakdown, which creates a very low resistance state and impedes further RS. This means that the positive value of the TCR is clearly a product of high currents through the conductive filament, and consequent high temperatures achieved via Joule heating. The resistance changes less than 10 % in the whole temperature range. At low temperatures there

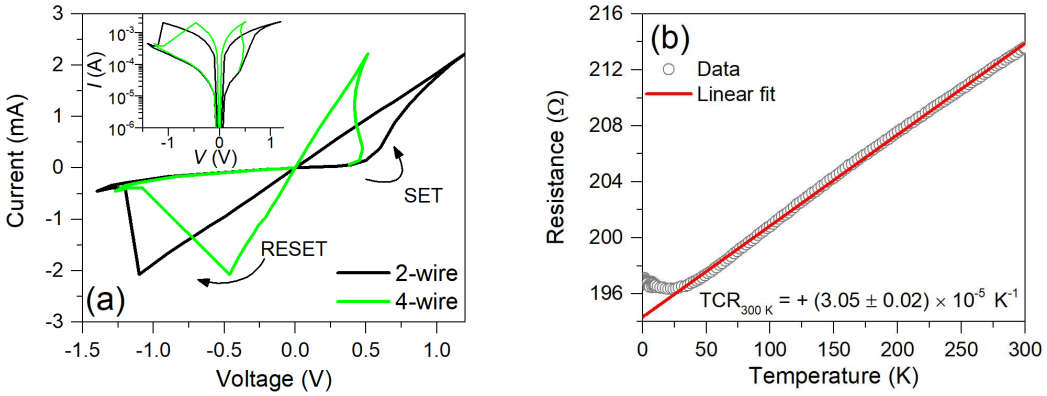

Figure 4.10: (a) Quasi-static current-voltage ($I-V$) characteristics of a device with 30 nm-thick Pt electrodes, and with a series resistance of ca. 300 Ω. The maximum value of the current that passed through the filament was 2.2 mA. The black line shows the measured data, measured in a 2-wire configuration, while the green curve was measured in a 4-wire configuration, thus showing the "intrinsic" switching curve (without the voltage drop over the series resistance). The inset plot shows the data with a logarithmic current scale. (b) Temperature dependence of the resistance in the LRS for the device shown in (a), where a positive TCR is clearly observed.

is again a change of the R vs. T behaviour with an upturn of the resistance, similar to the change observed for the devices with negative TCR.

Parasitic effects

In a two-terminal device like ReRAM, which consists of layered stacks of different materials, it is hard to ascribe the conduction to the desired object of study [214]. Through the measurement in a 4-wire configuration, it is possible to avoid the measurement of the series resistance and only measure the Ta/Ta_2O_5 stack. However, there could still be additional parasitic contributions involved.

In order to know the possible contribution from the vertical conduction in the Ta top electrode, we measured a Ta layer with the same thickness of 15 nm used in the devices, also sputtered on top of a 5 nm-thick Ta_2O_5 layer, in order to keep the same condition as the Ta layers in the measured ReRAM devices. Fig. 4.11(a) shows the resistivity of the Ta layer as a function of the temperature between 2 K and 300 K. A positive TCR is observed for the whole temperature range.

The Pt layers also show a positive TCR, as can be seen in Fig. 4.11(b) for a Pt line as used in the devices For this, small Hall bars with the Pt layers were fabricated on the same wafer where the devices were grown in order to check the Pt resistivity.

Thirdly, a crosspoint structure with no Ta_2O_5 layer was measured. This allows for the stack of Pt/Ta/Pt to be measured in the same configuration as in the fully functional ReRAM devices. The results are shown in Fig. 4.11(c), where also a positive TCR is observed.

Another possible contribution for the temperature dependence of the resistance of the ReRAM devices in the LRS can arise from the interfacial contact resistance. Following Wang et al. [215], the possible contribution from the contact resistance was checked by measuring

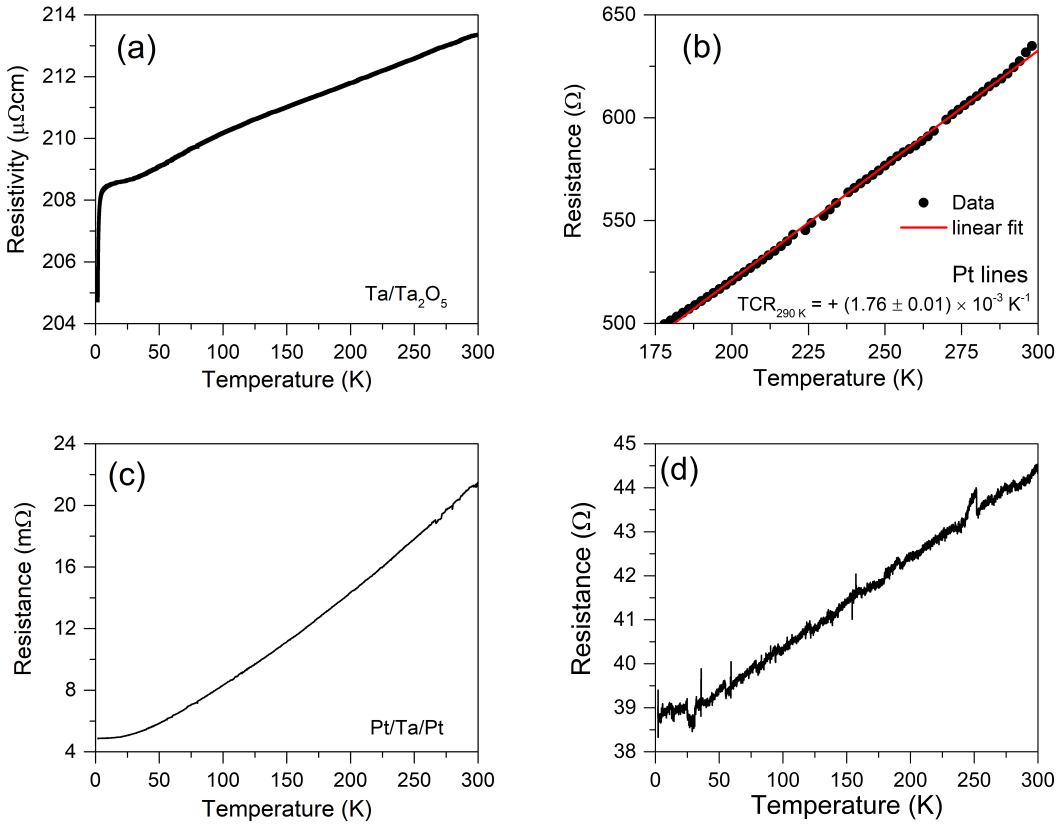

Figure 4.11: Overview of possible parasitic effects in the measurement of the electrical transport in the Ta_2O_5-based ReRAM devices: (a) Resistivity as a function of the temperature for a 15 nm-thick Ta film on top of 5 nm-thick Ta_2O_5, to evidence the transport behaviour of the Ta film in the same conditions as the one in the stack of the ReRAM devices. (b) Resistance as a function of the temperature for a 10 μm-wide Pt line used as metallic line in the crosspoint Ta_2O_5 ReRAM devices studied. (c) Resistance as a function of the temperature for a stack with no Ta_2O_5 layer (Pt/Ta/Pt). (d) Resistance as a function of the temperature for a device after hard breakdown was induced.

a device after breakdown, in order to reduce the contribution from the conduction through the conductive filament. The resistance was also measured in the temperature range from 2 K up to 300 K. As can be seen in Fig. 4.11(e), a positive TCR is measured as well as a very weak temperature dependence.

This analysis makes it clear that the negative TCR measured in most of the devices in the LRS is caused by the transport in conductive filaments in the Ta_2O_5 layer and not by the Ta electrode layer or any contact resistance. However, a positive TCR could be originated in part by the conduction in the Ta top electrode or affected by the contact resistance. This makes the ascription of the positive TCR solely to the conductive filament more complicated.

Magnetoresistance

To study the effect of an externally applied magnetic field in the electrical transport in the LRS, the magnetoresistance was measured for different temperatures and for different directions of the magnetic field relatively to the devices. Fig. 4.12(a) and (b) show the MR for the same device in two different configurations. In Fig. 4.12(a) the magnetic field is applied in parallel to the layer stack of the device, *i.e.* perpendicular to the vertical current flow in the filament. In the case of a pure vertical flow of the current, this would maximize the MR. However, as can be seen in Fig. 4.12(b), there is also a significant MR when the field is perpendicular to the layer stack and thus parallel to the filament. Indeed the value of the MR is almost the same as the one measured in the previous configuration, as can be seen in Fig. 4.12(c). For a different measurement, there is a more pronounced anisotropy of the MR, as can be seen in Fig. 4.12(d). These measurements were performed on the same device but at a different time, with a slightly different resistance $R_{T=2\text{ K},B=0\text{ T}} = 330\ \Omega$, compared to 260 Ω for (a-c). But still, there is no abrupt decrease of the MR as the angle is decreased from 90° to 0°. Similar MR data is obtained for different devices, as shown in Fig. 4.12(d).

The MR decreases rapidly with temperature as can be seen in both Fig. 4.12(a) and (b). After approximately 30 K the change in the resistance is lower than the noise level, therefore, no MR is measurable in the setup used.

The seamlessly low anisotropy of the MR can provide information on the geometry of the current path, and thus, of the filament. As the interaction of the electrons with the magnetic field is highly dependent on the relative direction of the electron's velocity and the magnetic field, the results indicate that the electrons responsible for the measured current probably do not follow a strictly vertical path in the filament. The electron transport could be rather directionally random in space, with significant movement perpendicular to the filament axis, but with a vertical net flow.

4.2.2 High resistance state (HRS)

Besides the LRS, where the study of the transport in the conductive filament was the main goal, also the HRS was measured as a function of the temperature in the same range from 300 K down to 2 K. Fig. 4.13 shows two examples of the temperature dependence of the resistance in the HRS. The resistance was measured at a fixed current of 1 μA. Similarly to the LRS case, also a negative TCR is observed, but the dependence on the temperature is higher. However, when compared to thermally assisted processes such as the ones observed in typical insulators and semiconductors, the observed dependence seems rather weak.

The nonlinearity of the $I-V$ characteristics in the HRS indicates, however, that interfacial

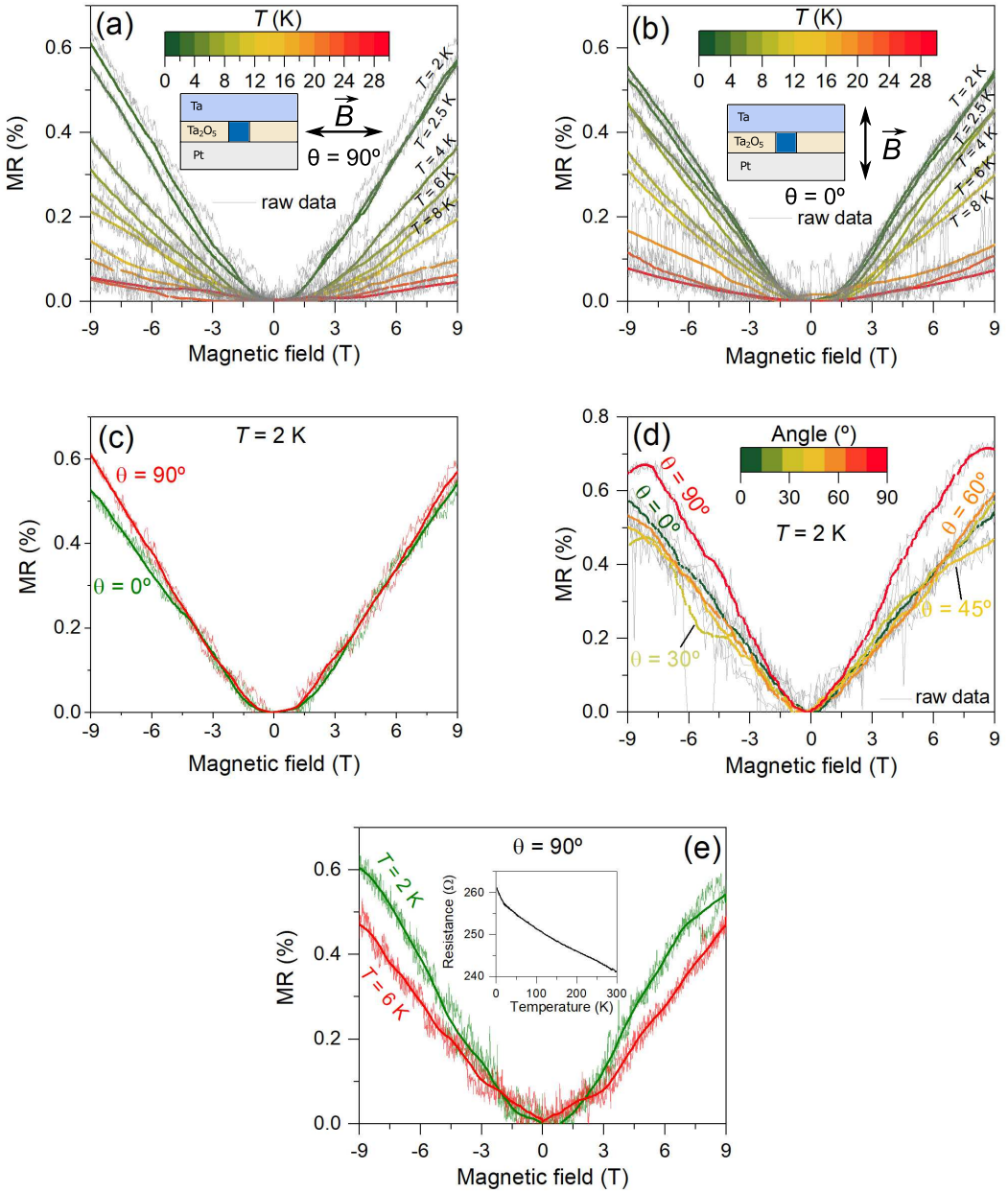

Figure 4.12: (a-b) Magnetoresistance (MR) as a function of the applied magnetic field for a $Ta/Ta_2O_5/Pt$ ReRAM device in the LRS (same device as in Fig. 4.7(a))for different temperatures from 2 K up to 26 K. The magnetic field was applied in parallel to the plane of the layer stack (perpendicular to the vertical current flow in the filament, $\theta = 90°$) in (a), while for (b) the field is perpendicular to the layer stack ($\theta = 0°$). The insets clarify the orientation of the magnetic field (B). The light coloured lines represent the (noisy) raw data, while the coloured lines are a result of smoothing using a Savitsky-Golay filter. (c) Comparison of the MR measured in the two configurations shown in (a) and (b) at $T = 2$ K. (d) MR as a function of the applied magnetic field for different orientations of the magnetic field relatively to the device. (e) MR for a different ReRAM device at $T = 2$ K and $T = 6K$, showing very similar results to the device shown in (a-d). The inset shows the temperature dependence of the resistance for this device.

or other nonlinear $I - V$ effects have a dominant role in limiting the current. Therefore, the temperature dependence of the resistance, measured for a single current value, offers a limited view of the transport processes taking place in the HRS.

Random telegraph noise

The data obtained for the HRS show evidences of random telegraph noise (RTN). At the lowest temperature of 2 K, the device in the HRS for which the R vs. T data of Fig. 4.13(a) was obtained was subject to an applied magnetic field. The change of the resistance in the HRS as a function of the magnetic field is rather small, however a bigger change of the resistance in time was measured, which was not caused by the magnetic field. This can be seen in Fig. 4.13(c). The inset shows the change in resistance with the application of an external magnetic field of the middle branch of the resistance, which gives a MR of approximately 0.02%, and therefore not very significant. However, there are at least 3 distinct resistance levels, with two more frequent, which is a strong experimental evidence of RTN. Another example of RTN behaviour is shown in Fig. 4.13(d), where the data from Fig. 4.13(b) was subtracted by a filtered version of the data that passes only through the points at the main resistance branch. This allows the observation of the RTN effect.

The origin of the RTN is, however, not clear. RTN is commonly observed in ReRAM devices, but its interpretation is based on the physical mechanisms used to understand the switching and conduction in the devices. For example, for HfO_2-based structures, the RTN is related to the activation and deactivation of traps responsible for the charge transport through the oxide according to trap-assisted tunneling [216]. The traps are normally considered to be the oxygen vacancies [217]. RTN can also be caused by atomic hopping in and out of the conductive filament, as discussed in the framework of the Quantum Point Contact model by Degraeve et al. [218].

4.3 Transport in the substoichiometric TaO_x thin films

The substoichiometric TaO_x thin films show an increase of the (room temperature) resistivity with increasing oxygen content. Fig. 4.14(a) displays the three TaO_x films with x = 1, 1.3, 1.5. According to earlier studies, the resistivity is expected to start changing more drastically at around $x \sim 1.5$ [80]. For the films sputtered in order to obtain higher oxygen contents the resistivity ran out of the measurement range of the van der Pauw setup and the used equipment, therefore there is no available data for more oxidized films. The stoichiometric Ta_2O_5 is highly insulating and has a resistivity between 10^5-10^7 Ωm, according to the literature [219].

Fig. 4.14(b) shows the resistivity as a function of temperature for the three different compositions mentioned before. The temperature dependence of the resistivity is qualitatively similar for all compositions shown. The resistivity increases monotonically with decreasing temperature. The dependence is rather weak for most of the temperature range from 300 K down to approximately 50 K, temperature at which it gets stronger. The increase at lower temperatures seems to scale with the oxygen content, because a more pronounced increase is observed for a higher x value. With increasing x the behaviour gets more similar to an insulator according to criterion number 2 (as defined in chapter 2), dealing with the divergence of the resistivity (conductivity tends to 0) as the temperature decreases towards absolute zero. An inspection of the individual curves in Fig. 4.14(c)-(e), where the resistivity is plotted in

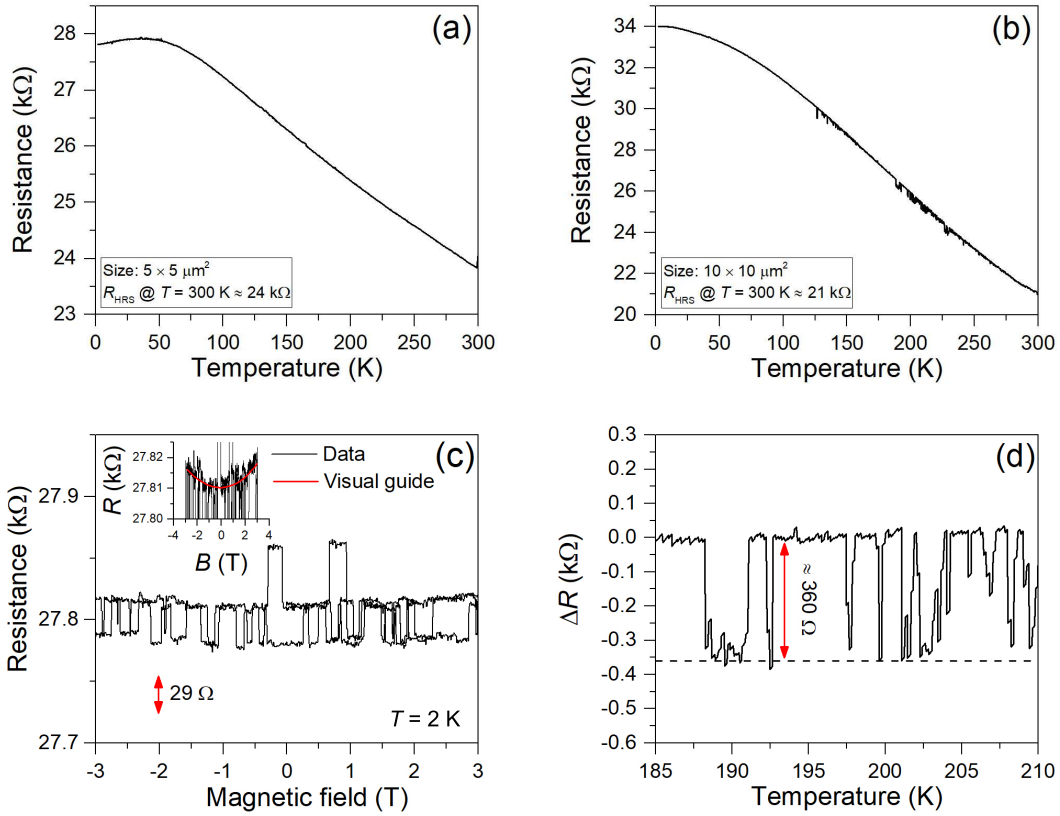

Figure 4.13: (a,b) Resistance as a function of the temperature in the HRS for two different devices, with different active area and with different resistance values. (c) Resistance as a function of the applied magnetic field at $T = 2$ K, evidencing random telegraph noise (RTN) for the device shown in (a). The effect of the noise is greater than the effect of the magnetic field, which can be seen for one of the RTN branches in the inset. The multiple data points for the same magnetic field value are due to the magnetic field sweep used in the measurement, where the field was swept from 0 T up to 3 T, then down to -3 T and finally back up to zero. (d) Change in resistance due to RTN as a function of the temperature for the HRS of the device shown in (b). The change was calculated by subtracting the resistance data shown in (b) from a filtered version of the same data following only the main branch observed , which does not have the noise component.

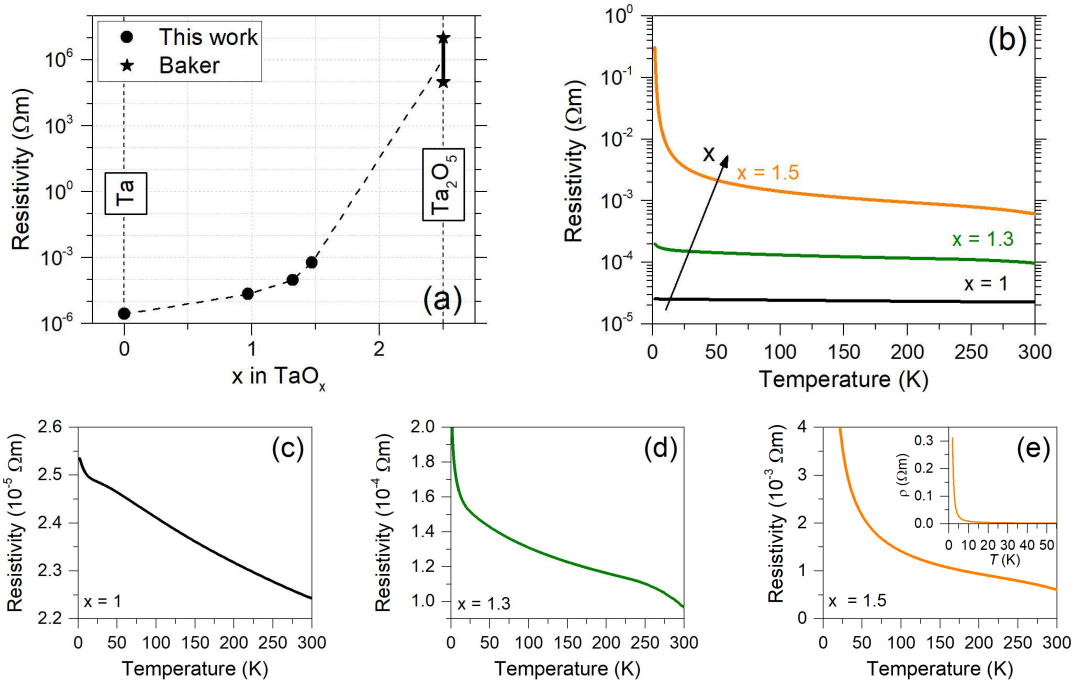

Figure 4.14: (a) Room temperature resistivity as a function of x for the TaO_x films with x = 1, 1.3 and 1.5, a sputtered Ta film and literature values for Ta_2O_5 from Baker [219]. The dashed line connecting the data points is a visual guide for the trend of the resistivity as a function of the composition. (b) Resistivity as a function of temperature for TaO_x films with x = 1, 1.3 and 1.5. The individual data of these films is plotted in (c), (d) and (e), respectively, showing the evolution of the resistivity with temperature with a linear scale for the resistivity.

a linear scale, enables a more detailed look at the data. The resistivity of the film with x = 1 is particularly interesting, because it has a striking resemblance with the temperature dependence of the resistance of the ReRAM devices in the LRS that showed a negative TCR.

4.3.1 Fit to conduction mechanisms

The conduction in TaO_x has been associated with Fermi glass behaviour and VRH [79]. However, for the sputtered TaO_x thin films once again, similarly to the LRS case, hopping mechanisms do not enable a sound fit of the data. As can be seen in Fig. 4.15, the data approaches a linear behaviour in very limited regions.

Following the visible similarities between the temperature dependence of the resistivity of the TaO_x thin film with $x = 1$ and of the resistance in the LRS of the Ta/Ta_2O_5 ReRAM devices, the same approach was attempted. Fig 4.16(a) shows the data along with the results of the least squares fit. Once more, the conductivity follows the $\sqrt{T}$ and $\exp\left(-T^{1/2}\right)$ dependences. It can be observed, however, that in the very low temperature range, below 10 K, a deviation from the $\exp\left(-T^{1/2}\right)$ behaviour occurs for the TaO_x film with $x = 1$, which is not observed for the LRS. The origin of this deviation will be explored further in the next

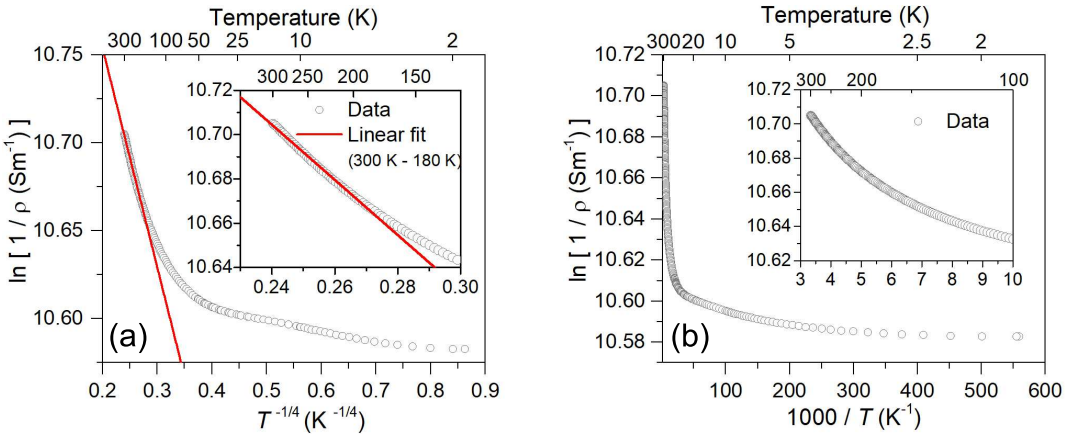

Figure 4.15: (a) Resistivity data for the TaO_x film with $x = 1$ plotted in order to show linearity for the case of Mott's VRH conduction in 3D (similar results for the 1D and 2D versions). (b) Same data as in (a) plotted in the right set of axis to show linear behaviour in the case of temperature activated NNH conduction.

chapter.

The films with $x = 1.3$ and $x = 1.5$, although presenting a higher resistivity and more pronounced increase of the resistivity below 50 K, are also well described by the same mechanisms as the film with $x = 1$, as shown in Fig. 4.16(b) and (c). For the film with $x = 1.3$ there is also a deviation at the lower temperatures from the $\exp\left(T^{-1/2}\right)$ behaviour, just like in the film with $x = 1$. For the film with $x = 1.5$, the low temperature regime seems to hold up to a higher temperature than in the film with $x = 1$.

4.4 Correlations between the transport mechanisms in the conductive filaments and in the TaO_x thin films

The data presented in the previous sections clearly establish a link between the transport mechanisms in the conductive filaments in the $Ta/Ta_2O_5/Pt$ ReRAM devices and in the TaO_x thin films, especially the film with $x = 1$. These correlations are further supported if one plots the reduced activation energy as a function of the temperature. The reduced activation energy was popularized by Zabrodskii [220], and is defined as:

$$w = \frac{d \ln \sigma}{d \ln T} = -\frac{d \ln \rho}{d \ln T}. \tag{4.2}$$

The limiting behaviour as T tends to the absolute zero further informs of the metallic or insulating behaviour of the sample, where divergence to high values indicates an insulator and convergence to zero indicates a metal [221]. The numerical method used to calculate the reduced activation energy from the data is described in detail in appendix B. The calculated reduced activation energies are plotted in Fig. 4.17 for the two ReRAM devices in the LRS of Fig. 4.9 and the TaO_x film with $x = 1$. The different samples show the exact same trend for most of the temperature range of the measurement. The change in the sign of the slope at around 25 K is clearly seen in both the TaO_x film and the LRS represented in red (device A in Fig. 4.17). For the other LRS (device B) the change in the sign of the slope is not visible,

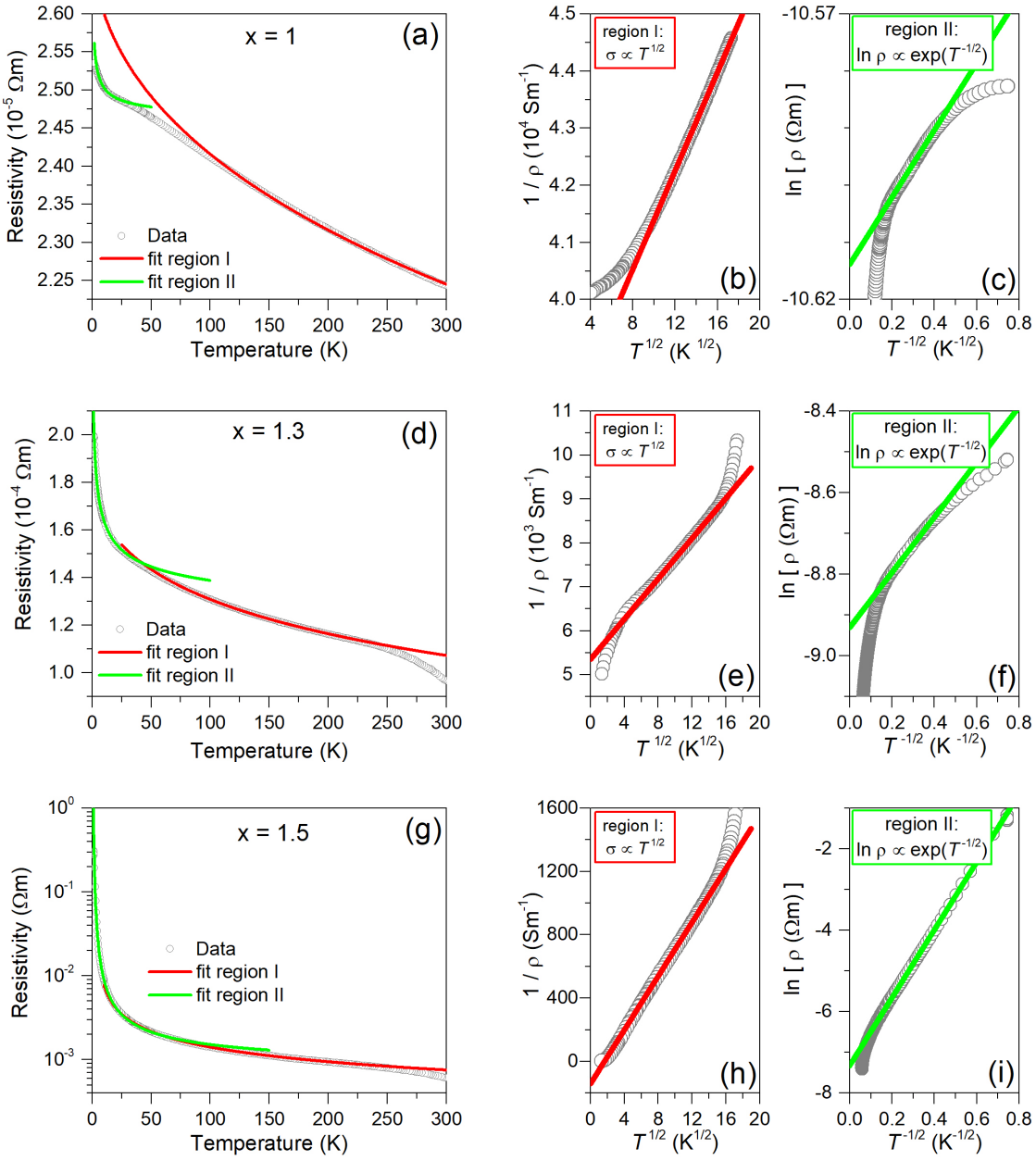

Figure 4.16: Temperature dependence of the resistivity for the TaO_x films with: (a) $x = 1$, (d) $x = 1.3$ and (g) $x = 1.5$. For each line, the pairs of graphs on the right show the linearised plots for the two fitting regions identified in the graphs on the left, for each TaO_x sample, along with the result of the linear least squares fit to the data. The high-temperature regime corresponds to $\sigma = \frac{1}{\rho} \propto T^{1/2}$, while the low-temperature regime corresponds to $\ln \rho \propto T^{-1/2}$

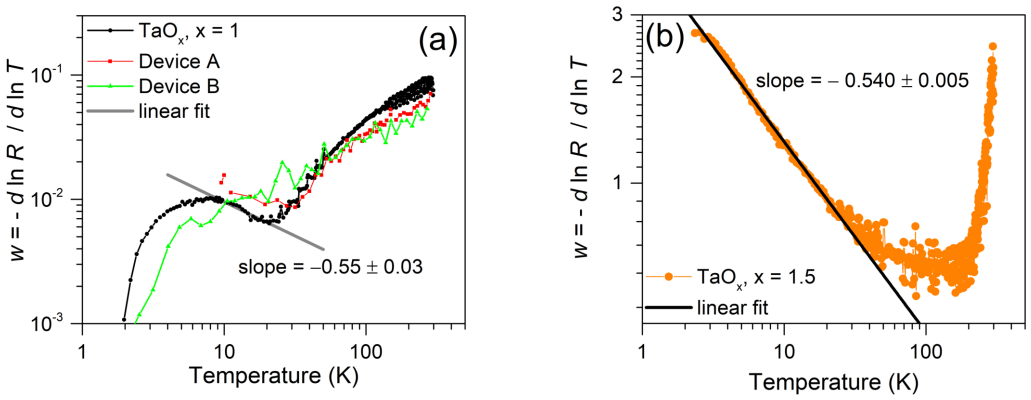

Figure 4.17: Reduced activation energy plots, where the reduced activation energy calculated via equation (4.2) is plotted as a function of the temperature, for: (a) the two ReRAM devices in the LRS shown in Fig. 4.9 and the TaO_x thin film with $x \sim 1$; (b) the TaO_x film with $x \sim 1.5$.

as expected due to the non-observation of the transition in Fig. 4.9(b) already. However, it is clear that down to the lowest measured temperature the samples do not diverge as the temperature decreases to zero, and thus show a behaviour more typical of a metal. On the other hand, the more oxidized TaO_x film with $x = 1.5$, in Fig. 4.17(b), already shows clear differences relatively to the first three and exhibits an insulating behaviour at low temperature. The negative slope is the dominant feature at temperatures up to approximately 50 K, from where the reduced activation energy stabilizes at around 0.6 up to around 250 K.

The observed correlations between the transport in conductive filaments in Ta_2O_5 devices and TaO_x thin films can seem rather strange at first sight, as the dimensionality for transport could be different. However, firstly, the relatively high current measured in the devices indicates a rather thick filament, possibly enabling 3D "bulk"-like transport. Actually, magnetoresistance measurements (see chapter 5) seem to imply that the mean free path of the electrons is quite small in these systems, maybe even below 1 nm, so that even a rather thin filament of a few tens of nm is large enough for the charge carriers to enable 3D transport. This also applies to the TaO_x thin films, where 2D transport was expected, but that due to the very small mean free path also exhibits 3D transport. The origin of the transport mechanisms will be the main concern of the next chapter, which focuses on the TaO_x thin films, especially on the region with $x \sim 1$.

The observed correlations indicate that the material composing the conductive filaments in $Ta/Ta_2O_5/Pt$ ReRAM devices is probably very similar to the deposited films of TaO_x with $x \sim 1$. In order to get a quick verification if such a material makes sense in terms of the resistance values obtained for the ReRAM devices, it is assumed that the filaments have a cylindrical shape, as illustrated in Fig. 4.18. The filaments in such VCM-type systems are normally considered to have a diameter of the order of 10 nm in the simulation models [65]. Considering the thickness of the Ta_2O_5 layer of 5 nm and the measured resistivity for the TaO_x film with $x = 1$, a resistance of approximately 1.5 kΩ is calculated. Higher diameters lead to a lower resistance, such as a value of approximately 620 Ω for a diameter of 20 nm, which is a value quite similar to the ones measured for the LRS. Therefore, this quick calculation

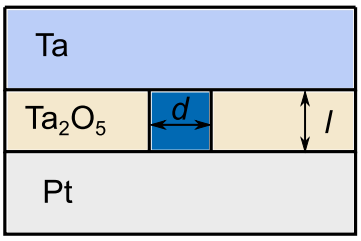

Figure 4.18: Schematic depiction of a simplified filament with a cylindrical geometry used for the resistance calculations based on the resistivity of the TaO_x film with $x = 1$.

further reinforces the assumption of the filament material as being very close to that of the thin films of TaO_x with $x = 1$.

Chapter 5

Understanding the transport in substoichiometric TaO_x thin films

In the previous chapter, a correlation between the electrical transport mechanisms in the conductive filaments inside Ta_2O_5-based ReRAM devices and in substoichiometric TaO_x thin films with $x \sim 1$ was shown. This is a clear indication that the electrical transport is dominated by the same underlying physical processes in both cases. In order to understand the origin of the electrical transport, a detailed study of the TaO_x thin films and also of metallic Ta is presented in this chapter. First, a structural study by means of grazing incidence X-ray diffraction, electron microscopy and other auxiliary techniques is reported. Secondly, the electrical transport was probed by measurements of the resistivity as a function of temperature besides Hall and magnetoresistance measurements. All this information is then used in the development of a model for the electrical transport in the substoichiometric TaO_x thin films. Finally, the impact of this transport model on the conductive filaments in the Ta_2O_5 ReRAM devices is discussed.

The major results and conclusions presented in this chapter were published in: Carlos M. M. Rosário, et al., *Nanoscale* **11**(36): 16978 (2019). `https://doi.org/10.1063/1.5024504`

5.1 Composition and structure of the TaO_x thin films

5.1.1 Composition determination

The sputtering processes used to deposit the TaO_x thin films were obtained by an initial study of the dependence of the density of the thin films with the different process parameters. The final process parameters used for the majority of the studied films are shown in table 3.1 in chapter 3. The film density serves as a relative measure of the composition of the films, because of the different amounts of the tantalum and oxygen chemical elements, which have drastically different atomic masses. The oxide Ta_2O_5 presents the lower density, while the Ta metal presents the higher density. In order to get a quantitative value of the film's composition, RBS measurements were performed in a set of films for which the density was also measured. From the correlation between both quantities, film density measured by XRR and composition (x in TaO_x) measured by RBS, a calibration curve was obtained. All subsequent compositions were calculated based on this initial calibration and XRR data.

X-ray reflectivity

The film density can be obtained from the critical angle for total reflection for X-ray by measuring the XRR. The critical angle is easily spotted in the XRR plot of Fig. 5.1(a), where the intensity first starts decreasing abruptly, an indication that the X-rays are partially transmitted through the sample/air interface. A higher density leads to a higher critical angle. As can be seen in the same plot, the Ta film shows the highest critical angle and the Ta_2O_5 film the lowest. TaO_x with $x = 1$ sits in between the two extremes.

The interference of the X-rays from successive reflections and transmissions in the various interfaces of the layer stack is observed for angles higher than the critical angle. The periodicity of the constructive (destructive) interference maxima (minima) informs of the layer thickness, enabling the experimental determination of the TaO_x films. For later sputtering, the sputter time needed to obtain the desired thickness of the films was calculated from the sputtering rate obtained from calibration processes for which the thickness was determined in this way.

Rutherford backscattering spectrometry

RBS spectra were measured for a set of calibration samples spanning a composition range from $x = 0.97$ up to stoichiometric Ta_2O_5. In order to optimize the oxygen signal from the TaO_x layer, a different stack was used. As the oxygen signal from other oxide layers would superimpose on top of the signal stemming from the TaO_x layer, the 50 nm-thick TaO_x film was deposited on top of a Si substrate with just the native oxide layer (approximately 4 nm in thickness) and a Au capping layer was used instead of the Al_2O_3 used in the rest of the work. Au was preferred in favour of Pt because of the atomic mass and the corresponding superposition of the Pt signal with the signal from Ta that is also critical to capture in order to determine the O/Ta ratio. The inset of Fig. 5.1(d) shows the layer stack used in the RBS measurements, chosen to maximize the relative oxygen signal stemming from the TaO_x layer.

Fig. 5.1(b) and (c) show the RBS spectra for the TaO_x film with $x = 0.97$ and the stoichiometric Ta_2O_5 film, respectively. The oxygen signal is superimposed on the Si signal from the substrate, and is quite weak, but still visible for both samples. It is clear that the amount of oxygen in (c) is higher than in (b) by comparing the relative intensities of the O and the Ta signals for each sample. The quantitative analysis of the composition was performed by fitting the measured spectra using specialized software that also made use of other measurements such as elastic recoil detection analysis (ERDA), which is particularly useful to improve the precision of the oxygen quantification (see details in chapter 3.) According to the data, there is no pronounced O profile along the thickness of the TaO_x film, indicating a homogeneously distribution of the oxygen.

Calibration

Fig. 5.1(d) shows the obtained data of the film density determined by XRR as a function of the x value in TaO_x determined by RBS. The calibration line, shown in red, is a linear fit used to determine the composition of the TaO_x films. The composition in terms of the x index was obtained from RBS measurements performed on a set of calibration samples. Using the same sputtering processes as used for these calibration samples, five samples were deposited for each process and their XRR was measured. The density of the films was extracted from the XRR data. In the graph of Fig. 5.1, the mean density is represented with the error bar

representing the highest deviation from the mean density value. The x index in TaO_x is then calculated from the experimentally obtained density (ρ_V) via the formula:

$$x = \frac{(14.50 \pm 0.34) - \rho_V}{2.96 \pm 0.18} \tag{5.1}$$

The obtained data and linear fit are in agreement with the density vs. composition data from the work of Waterhouse et al., also shown in the plot of Fig. 5.1 [222].

5.1.2 GI-XRD

Grazing incidence X-ray diffraction (GI-XRD) measurements were performed on the TaO_x films to study the dependence of the structural properties with the oxygen content. For comparison, the measurements were also performed for two reference samples at the two extremes of the Ta-O material system, a Ta film and a Ta_2O_5 film, both sputtered in the same deposition tool as the TaO_x films. Fig. 5.2 shows the obtained diffractograms for the two reference samples and three TaO_x films with intermediate oxygen content.

The Ta_2O_5 film shows a broad signal at small angles with no clear peaks from $2\theta = 15°$ to $2\theta = 40°$ and another one at higher angles centred at around $2\theta = 54°$. The absence of clear peaks is characteristic of amorphous materials. Ta_2O_5 typically requires temperatures above 650°C to crystallize, [158, 223] so amorphous Ta_2O_5 is expected from sputtering on top of a SiO_2 substrate at room temperature. The broad features observed are in good agreement with previously published data for amorphous Ta_2O_5 [158, 223].

On the other hand, the sputtered Ta film shows a diffraction pattern characteristic of the crystalline tetragonal β-Ta phase. This phase is commonly observed for magnetron sputtered thin Ta films grown on top of an amorphous oxide [165, 166]. The diffraction pattern shows no evidence of the cubic α-Ta phase, the stable phase of bulk Ta when crystallized under equilibrium conditions [165]. The clearly visible diffraction peaks corresponding to the β-Ta phase are indexed in Fig. 5.2.

For the TaO_x films with compositions between Ta_2O_5 and Ta, the diffraction peaks tend to get broader and eventually disappear with increasing oxygen content. The TaO_x film with $x = 1$ shows a diffraction pattern that is very similar to the one observed for the Ta film, with the difference of exhibiting broader peaks shifted to lower angles. As the oxygen content is further increased to $x = 1.5$, the features observed for the films with $x = 1$ decrease in intensity, and a small-angle broad contribution becomes more prominent. This contribution is most likely associated with amorphous Ta_2O_5, as it appears in the same range of 2θ. However, the diffraction pattern of the TaO_x films cannot be explained solely by a combination of the diffractograms of the pure Ta and Ta_2O_5 samples as they appear in 5.2. The presence of suboxide phases could be one explanation, however, as discussed in section 2.2, the Ta-O system is reported to have only two stable phases: Ta_2O_5 and the Ta(O) solid solution [156]. Indeed, the presence of oxygen in the tantalum seems to play a decisive role. Several works report that the oxygen can occupy interstitial positions in the β-Ta lattice [222, 224]. The incorporation of oxygen should lead to an expansion of the unit cell of the β-Ta lattice, and would thus explain the observed decrease in the Bragg angle of the diffraction peaks for the TaO_x films due to an increase of the interplanar distances. The broadening of the diffraction peaks is probably associated with a decrease of the crystallite size of the Ta grains with increasing oxygen content.

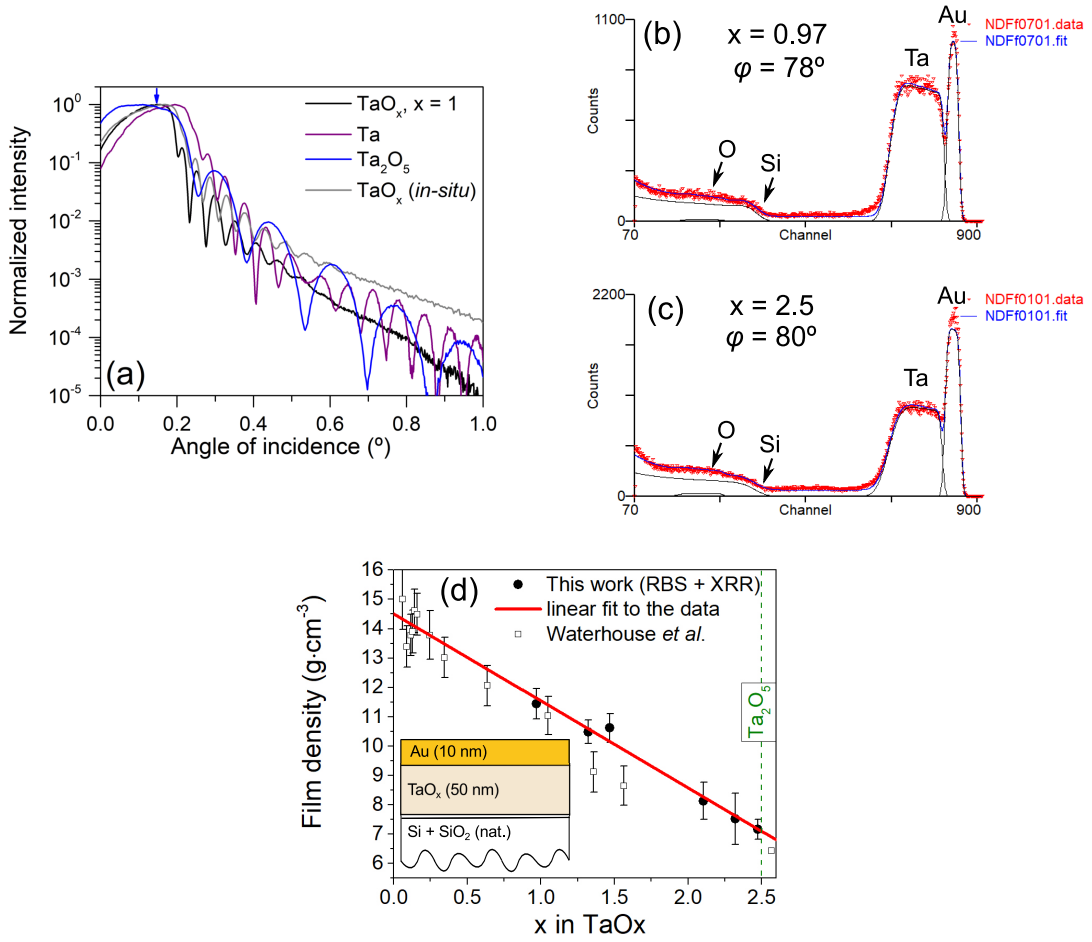

Figure 5.1: (a) X-ray reflectivity data for four samples: Ta, TaO_x with x = 1, TaO_x sputtered for *in-situ* measurements and Ta_2O_5. (b) RBS spectrum for a TaO_x film with x = 0.97 (determined by the RBS experiment) taken at an incident angle of 78°. The blue line represents the total fitting curve, while the black lines represent the individual elemental contributions to the fit. (c) RBS spectrum for a Ta_2O_5 film taken at an incident angle of 80°.(d) TaO_x films' density as determined by the XRR plotted against the x index in TaO_x obtained by RBS. The circle data points represent the mean value of the density, while the error bars indicate the highest deviation from the mean value. The red line is the least squares fit to the experimental data. For comparison, the data published by Waterhouse et al. [222] for films with thicknesses between 140 nm and 620 nm is also included. The inset shows the layer stack used in the samples measured with RBS to determine the composition.

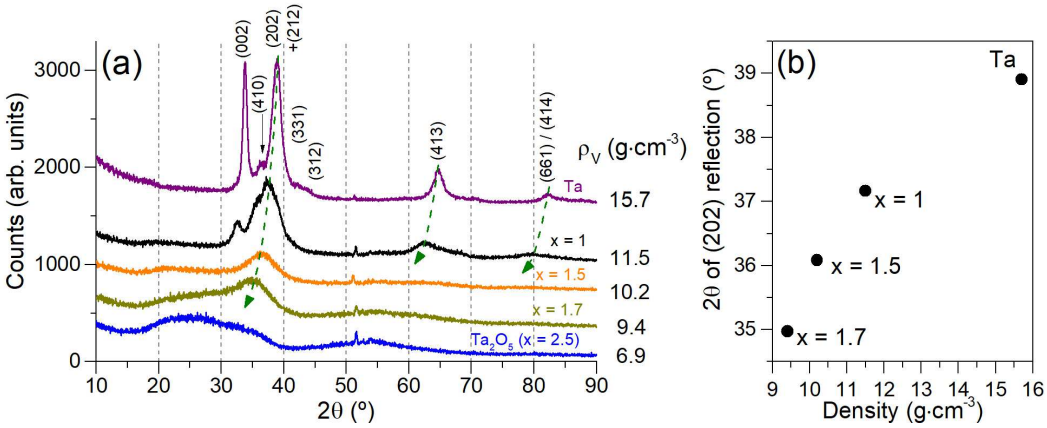

Figure 5.2: (a) X-ray diffractograms of TaO_x samples with different compositions (x), including two reference samples, a sputtered Ta film and a sputtered Ta_2O_5 film. The values on the right side of the plot indicate the film density of the measured samples as determined by XRR measurements. (b) Evolution of the 2θ value of the (202) reflection with the film density (composition).

5.1.3 HAADF-STEM

HAADF STEM Z-contrast imaging was employed to enable the direct observation of a TaO_x film with $x \sim 1.3$. As shown before in the previous chapter, this film exhibits a transport behaviour similar to that of the TaO_x films with $x \sim 1$, namely the transport mechanisms involved. So, it is considered that this film is representative of the structure of TaO_x films in this composition range.

Fig. 5.3 shows an overview micrograph of this TaO_x film sandwiched between SiO_2 and Al_2O_3 layers. The TaO_x film appears brighter than the two other oxide layers due to the presence of the heavy element Ta, as expected with the Z-contrast mechanism. The film exhibits a columnar structure with columns in the growth direction having a width from 2 to 5 nm. To map the elemental distribution along the TaO_x film, EDX spectroscopy mapping was performed in the area shown in the micrograph of Fig. 5.3(b). The general map with the distribution of the elements Ta, O and Al is shown in Fig. 5.3(c), while the individual maps for the elements Ta and O are shown in Fig. 5.3(d) and Fig. 5.3(e), respectively. Tantalum is present in most of the TaO_x film, while oxygen tends to accumulate along the boundaries between the different columns observed in the HAADF micrograph in the less bright areas. However, there seems to be oxygen along the columns as well, albeit with a clearly lower concentration relatively to tantalum in the columnar area. In this scenario, the bright columns visible in Fig. 5.3(a) and (b) should be related to tantalum grains with some oxygen, while the darker intercolumnar space may be related to stoichiometric Ta_2O_5. These findings are consistent with the GI-XRD results that support the existence of both Ta(O) and Ta_2O_5 in the TaO_x films.

The same procedure was also adopted for films of Ta_2O_5 and Ta and the results are displayed in Fig. 5.4 and Fig. 5.5, respectively. The distribution of Ta and O in the Ta_2O_5 layer is much more homogeneous when compared to the TaO_x film discussed above and the film shows no apparent structural inhomogeneities either, further supporting its amorphous character. Contrarily, the Ta film shows evidences of a polycrystalline character with grains

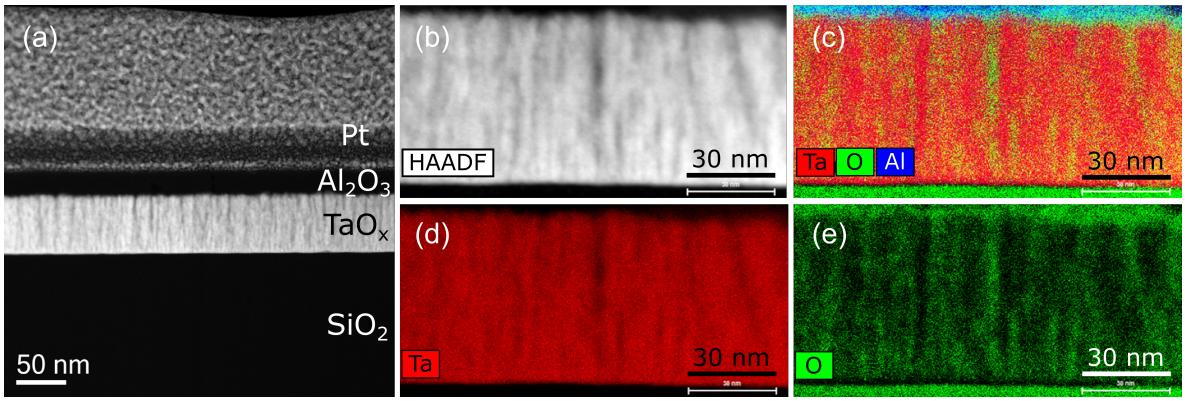

Figure 5.3: (a) HAADF STEM Z-contrast image with an overview of the sample comprising a TaO_x film with $x \sim 1.3$. (b) HAADF STEM Z-contrast image of the TaO_x film with $x \sim 1.3$ showing the area where the EDX mapping was performed. (c) Elemental mapping by EDX showing the distribution of Ta, O and Al in the area shown in (b). (d,e) Individual elemental maps of Ta and O, respectively. The individual mapping of aluminium is not shown because its presence on the TaO_x film is vestigial, and thus it is concluded that aluminium is not incorporated in the TaO_x film.

of approximately 20 nm in width in the cross section, therefore much larger than the columns observed in the TaO_x film. The grains' composition is clearly dominated by Ta, however, once more it is possible to see that O is present in the film and prefers to lodge in the intergranular regions. The existence of oxygen can be one of the reasons to the occurrence of the β-Ta phase in favour of the stable α-Ta phase.

5.1.4 Other auxiliary techniques

XPS

Further experimental evidences of the existence of both Ta and Ta_2O_5 in the TaO_x films were obtained by X-ray photoelectron spectroscopy (XPS). As the TaO_x films' surface is easily oxidized when exposed to air, and XPS measures only the surface of the film, the measurements had to be performed *in-situ*, making it necessary to sputter the films in a different sputtering equipment. The sputtering process was, however, tuned in order to minimize the possible differences in the deposition, and once again the density obtained from the XRR measurements was used to check the composition. *In-situ* XPS measurements were performed on TaO_x samples with $x \sim 1$, grown in conditions similar to the ones studied in terms of the electrical transport. The XRR data in Fig. 5.1(a) enables a comparison between a TaO_x film with $x = 1$ grown normally and the $in-situ$ deposited sample used for the XPS measurements. Although the latter shows a slightly higher density (higher Ta content) the composition is very close to that of TaO_x with $x \sim 1$ and is representative of the films studied in the rest of the work.

The measured Ta4f XPS signal is shown in Fig. 5.6(a). A simulation with contributions from the two stable oxidation states is able to provide a good fit to the experimental data. The data shows a strong contribution from the metallic peak associated with Ta^0, and also a contribution from the Ta^{5+} state, which is associated with the stoichiometric oxide

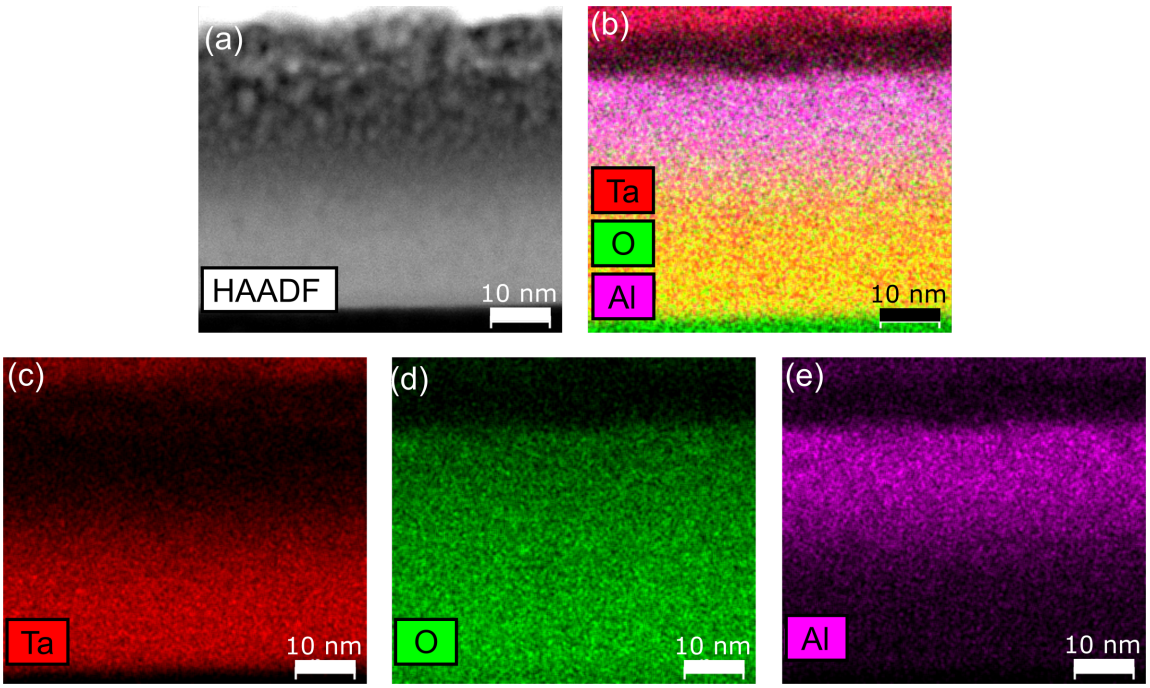

Figure 5.4: (a) HAADF STEM Z-contrast image of a Ta_2O_5 film showing the area where the EDX mapping was performed. (b) Elemental mapping by EDX showing the distribution of Ta, O and Al in the area shown in (a). (c-e) Individual elemental maps of O, Ta and Al, respectively.

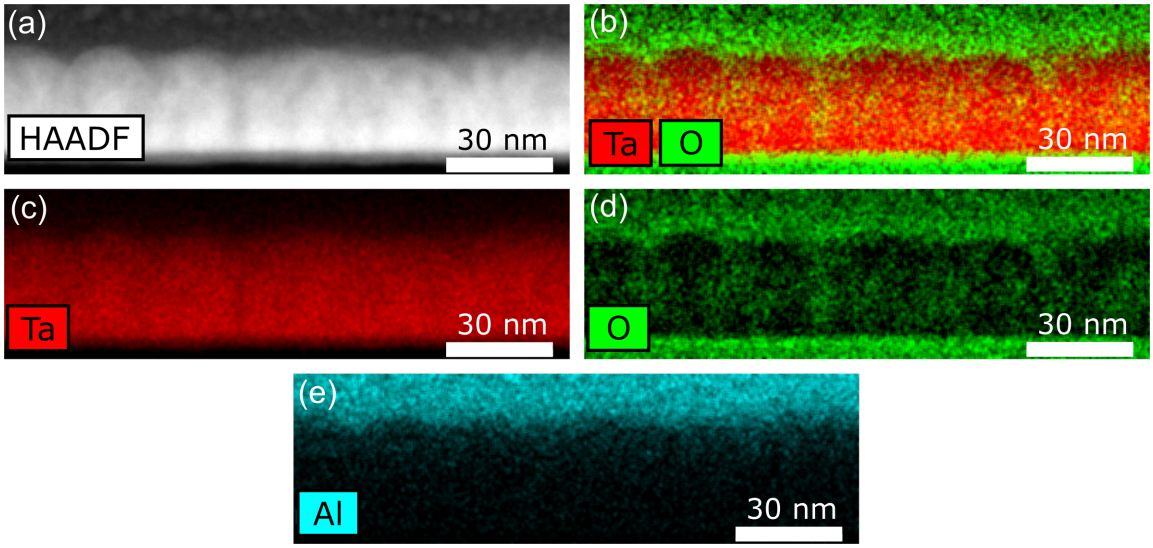

Figure 5.5: (a) HAADF STEM Z-contrast image of a Ta film showing the area where the EDX mapping was performed. (b) Elemental mapping by EDX showing the distribution of Ta and O in the area shown in (a). (c-e) Individual elemental maps of Ta, O and Al, respectively.

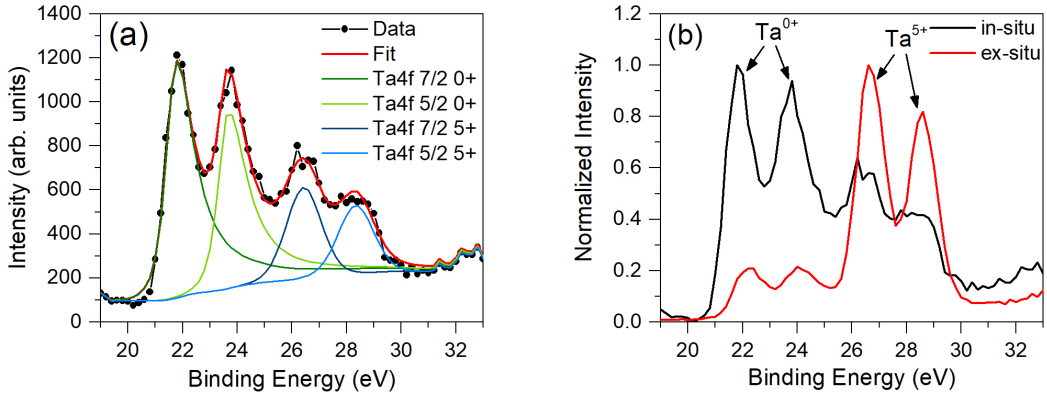

Figure 5.6: (a) XPS data for an *in-situ* sputtered TaO_x film with $x \sim 1$. A fit to the data is shown in red, with the individual fitting contributions from the different valence states shown in green and orange. (b) Comparison of the XPS measurement performed on an *in-situ* sample and an *ex-situ* sample (grown in the same conditions as the main samples described in the text).

Ta_2O_5. During the fitting procedure, the Ta^0 peaks were chosen to be asymmetrical because transition metal XPS spectra are normally considered to have an asymmetry [225]. The Ta metallic peaks are thus also normally fitted to asymmetrical curves [226]. The asymmetrical contribution provides a good fit to the XPS data. A good fit is also obtained when the Ta^0 contribution is considered symmetrical, but there is the need to consider an additional oxidation state, Ta^{2+}. The Ta^{2+} contribution could arise because of a suboxide TaO phase. However, it does not necessarily indicate the presence of this suboxide phase, because the contribution could arise from the interfaces between Ta and Ta_2O_5. At these interfaces, the bonding differs from that in pure Ta and Ta_2O_5 clusters. However, the main contributions are clearly from the Ta^0 and Ta^{5+} states. Therefore, the XPS data indicate the existence of both Ta and Ta_2O_5 inside the TaO_x films with $x \sim 1$.

A comparison between the *in-situ* measurements and *ex-situ* data obtained on a sample grown in the same conditions as the samples studied for the electrical transport is displayed in Fig. 5.6(b). It is possible to conclude that the oxidation on the surface is responsible for the increase in the relative contribution of the signal arising from the Ta^{5+} oxidation state. Nevertheless, it is still possible to observe the contribution from the Ta^0 oxidation state in the *ex-situ* sample, corroborating the existence of Ta and Ta_2O_5 concluded from the analysis of the XPS performed on the *in-situ* sample.

LC-AFM

The two stable phases in the Ta-O material system, Ta_2O_5 and the Ta(O) solid solution should be easily distinguishable in terms of conductivity. While the former is an insulator, the latter should exhibit a metallic behaviour. As shown before, the TaO_x thin films appear to be composed of a mixture of these two phases. Therefore, by using an AFM with a conductive tip, it should be possible to see this phase segregation. As the TaO_x films' surface is easily oxidized when exposed air, the measurements had to be performed *in-situ*, just as in the case of the XPS measurements.

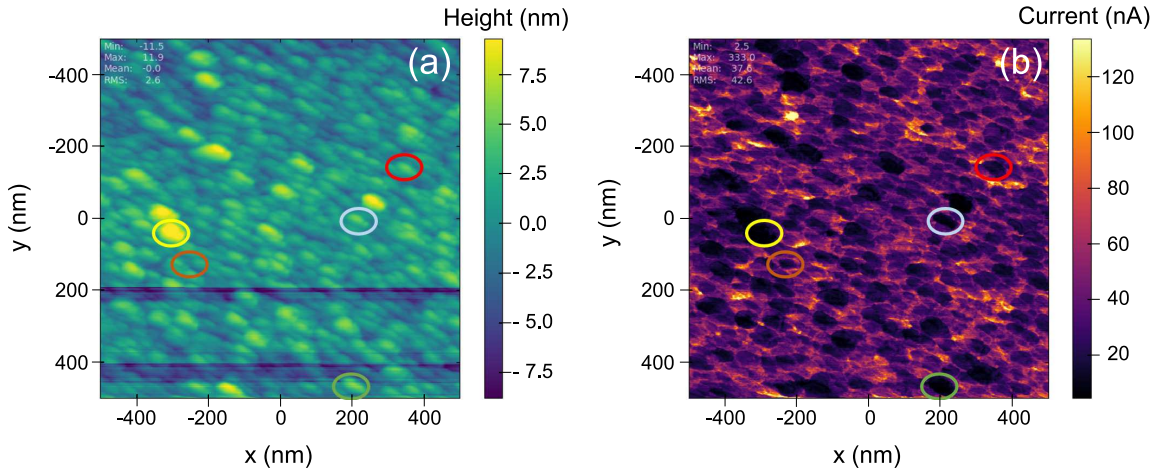

Figure 5.7: AFM topography image (a) and the correspondent current map measured by LCAFM (b) for an *in-situ* sputtered sample with $x \sim 1$. For the current map, a voltage of 8 V relative to the grounded sample holder was used to measure the current through the sample.

Fig. 5.7 shows a topography image of the surface of a film with $x \sim 1$ and the corresponding current map. This film was deposited on top of a SiO_2/Si substrate with 430 nm of oxide. The topography image shows a granular structure with grains with an approximate diameter of 50 nm. The current map shows the existence of dark regions with low current embedded in a purple and yellow matrix where the current is higher. There is no direct correlation between the topography and current maps, as can be seen by comparing the same regions in both images (shown as coloured marked circumferences). In some cases the regions with low current correspond to the highest grains, while in others, the contrary is observed.

Optical absorption spectroscopy

Optical absorption spectroscopy also reveals the existence of a component with high absorption in the TaO_x films. Fig. 5.8(a) shows the experimental results of the absorption measurements in terms of absorbance as a function of the wavelength of the light. The reduction of the oxygen content increases the absorbance and promotes the appearance of an Urbach's tail. For the Ta_2O_5 sample, the existence of a bandgap is clearly visible, evidenced by the sudden increase of the absorbance below 300 nm. The graphical representation shown in Fig. 5.8(b) indicates an indirect bandgap of approximately 4.3 eV for the Ta_2O_5 film, while a direct bandgap would have a value of 4.9 eV (respective plot not shown). This value is in good agreement with the literature, where amorphous Ta_2O_5 is said to have a bandgap value of 4.3 that decreases to 4.0 for substoichiometric oxide [227, 228], among other studies where its value is higher and in the range from 4.4 to 4.9 [228–230]. As can be seen in Fig. 5.8(b), the thin films studied in this work also exhibit a monotonically decreasing bandgap with decreasing oxygen content, until it disappears completely due to the high absorption of the samples with lower oxygen concentration. This is another indication of the presence of the metallic granules in the samples with less oxygen.

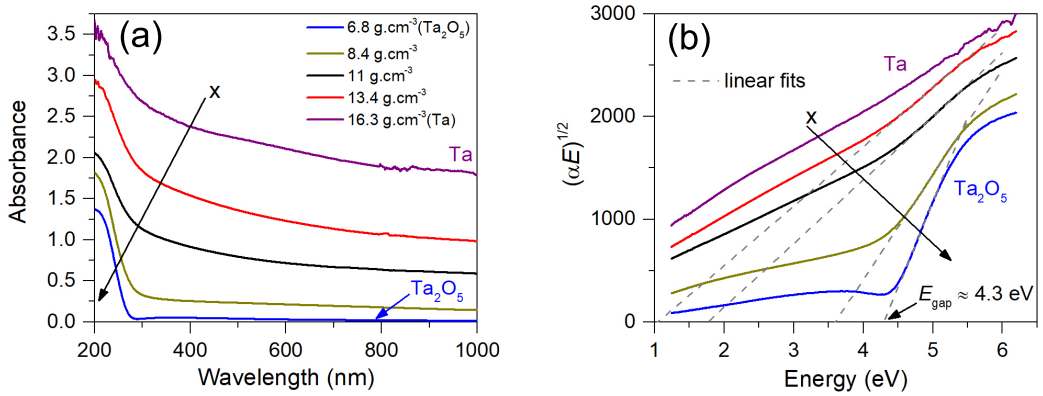

Figure 5.8: (a) Optical absorption spectra, *i.e.*, absorbance as a function of the wavelength of the light for the TaO_x thin films with different densities, and thus, oxygen content. (b) Indirect bandgap test plot, used to visualize the indirect bandgap, with the data from the TaO_x films shown in (a). α represents the absorption coefficient, obtained from the absorbance (A) and the sample thickness (t) by: $\alpha = \frac{1}{t} \ln\left(10^A\right)$. The dashed lines are linear fits to the linear portion of the data, indicating the indirect bandgap of the samples where the fit line intersects the energy axis.

5.1.5 Discussion

The measured XRD patterns of the TaO_x films indicate the presence of the β-Ta phase with oxygen interstitials and amorphous Ta_2O_5. Different mixtures of these two phases lead to different overall oxygen concentrations in the TaO_x films, as measured by X-ray reflectometry and Rutherford backscattering spectrometry, which provide an average over a relatively large sample area compared to the size of possible inhomogeneities. Considering this, it is more likely that the TaO_x films are composed of a mixture of Ta with oxygen interstitials and Ta_2O_5. The columnar structures observed in the HAADF STEM Z-contrast micrographs are associated with the β-Ta phase, while a higher concentration of oxygen between columns indicates accumulation of Ta_2O_5 between the metallic columns. Besides these experimental evidences, also the other experimental data shown in the preceding sections corroborate the phase seggregation in the TaO_x thin films, with the appearance of a metallic Ta(O) phase and an insulating Ta_2O_5 phase. This is perfectly in line with the Ta-O material system presented before in chapter 2. The phase diagram of the Ta-O system only has the mentioned two stable phases: a Ta(O) solid solution and the fully oxidized Ta_2O_5 [156]. So the presence of suboxides are not foreseen in thermodynamic equilibrium, even though some works do report the obsevance of some of the metastable suboxide phases, mostly obtained at high temperature either during deposition or through post-deposition annealing [40, 175–177]. The room temperature processing used for the deposition of the TaO_x films should impede the formation of these suboxide phases.

The experimental results obtained are further supported by a first-principles study using molecular dynamics to investigate amorphous TaO_x in a wide composition range of $0.75 \leq x \leq 2.85$ performed by Xiao and Watanabe [231]. This study has shown that as the oxygen concentration in TaO_x is decreased, the Ta atoms tend to coalesce together and form Ta clusters where Ta-Ta bonds prevail [231]. For $x = 2.25$, the Ta clusters are isolated and, thus,

do not form a continuous conduction path. In this case, the transport is mainly carried out by hopping between the localized electrons at the metallic clusters. For a lower oxygen content such as in the case with $x = 0.75$, the number of Ta-Ta bonds is high enough to enable a continuous metallic conduction path with delocalized electrons.

The XRD of the Ta film indicates that the dominating structure is the one from the β-Ta phase, with no evidences of the α-Ta phase. The appearance of the β phase instead of the more thermodynamically stable α phase can be explained by the more favourable growth of the β phase on amorphous oxide substrates [165, 168]. The base pressure in the sputtering chamber was also not lower than 10^{-6} mbar prior to the sputtering, probably leaving enough oxygen to promote the formation of β-Ta, as according to the literature the presence of oxygen during the deposition can be one of the causes for the formation of β-Ta instead of the α phase [167].

It is important to emphasize that the increase in the oxygen content is not only reflected in the appearance of the amorphous Ta_2O_5 phase, but also in the increase of the amount of oxygen interstitials in the Ta granules. The presence of oxygen along the grains observed in the EDX maps corroborates the existence of oxygen in the β-Ta lattice. This is also concluded from the shift of the diffraction peaks observed in the XRD data, caused by a change in the lattice parameter of the Ta granules induced by the presence of interstitial oxygen atoms and the respective expansion of the unit cell. The shift increases with increasing x index of the TaO_x films, showing that the solubility limit of the oxygen in the β-Ta grains may not yet be reached in the films with oxygen content around $x \sim 1.5$. Waterhouse et al. [222] report a 10% increase of the (202) interplanar distances for an oxygen content of approximately 60%. Cheng et al. [224] report a 5.4 $Å^3$ volume expansion of the unit cell after annealing β-Ta films at 400°C in air, and also attribute this expansion to the presence of interstitial oxygen. The simultaneous occurrence of Ta and Ta_2O_5 in the TaO_x films is crucial for the understanding of the electrical transport in the TaO_x thin films.

5.2 Temperature dependence of the resistivity

The structural analysis revealed the existence of Ta clusters in the substoichiometric TaO_x thin films. Therefore, in order to gain more insight into the transport properties of the TaO_x films, the transport in Ta films was also measured and compared to the former. As for Ta_2O_5, no transport measurements were possible in the configuration used, due to the very high resistivity. This was also the case for samples with $x > 1.5$, which proved too resistive as well.

Resistivity measurements using the vdP configuration were performed on the TaO_x thin films with different oxygen contents and on the Ta film. The temperature dependence of the resistivity of the TaO_x films is replotted in Fig. 5.9(a), now with the inclusion of the data measured for the Ta film. The Ta film has a resistivity that is one order of magnitude lower than the one from the TaO_x film with $x = 1$. A close inspection of the temperature dependence of the resistivity of the Ta film reveals that for most of the temperature range the overall behaviour is very similar to the one exhibited by the TaO_x film with $x = 1$. The plot in Fig. 5.9(b) reflects exactly this similarity in a qualitative way (note that the resistivity scale is different for each sample). This also shared with the ReRAM devices in the LRS with a negative TCR, as it was previously highlighted in the preceding chapter and can also be seen in the same plot. The similarity is further reinforced when the conductivity is plotted

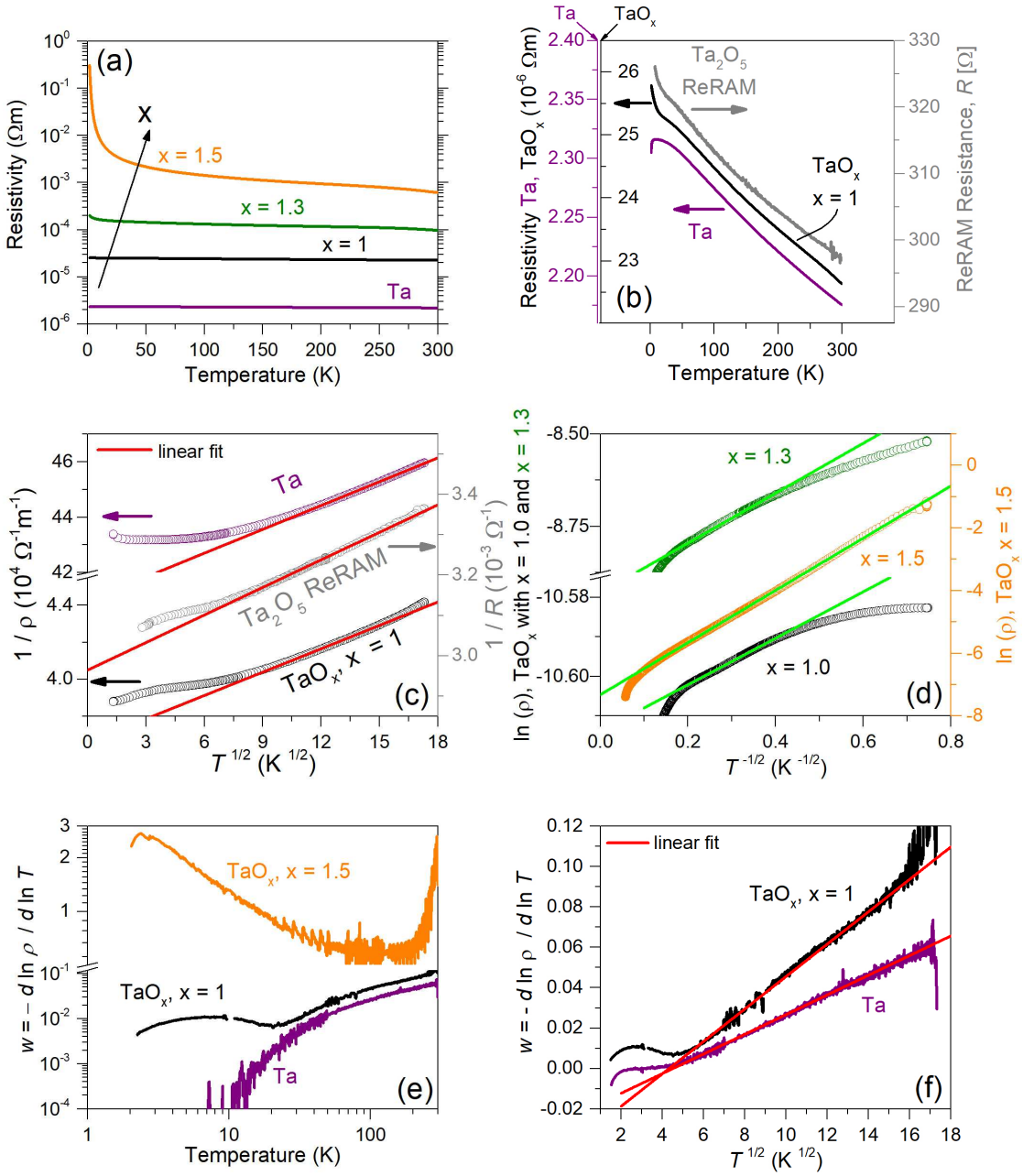

Figure 5.9: (a) Resistivity vs. temperature for three thin TaO_x films with $x = 1.0$, 1.3 and 1.5 and the Ta film. (b) Comparison of the temperature dependence of the resistivity of the TaO_x film with $x = 1$ and of the Ta film. Data for a $Ta/Ta_2O_5/Pt$ device in the LRS is also plotted. (c) Conductivity plotted as a function of $T^{1/2}$ showing linear fits for both films and the device in the LRS in the high-temperature region. (d) Logarithm of the resistivity as a function of $T^{-1/2}$ for the three TaO_x films, to evidence the Efros-Schlovskii-like hopping mechanism at the lowest temperatures. (e) Zabrodskii plot, with the reduced activation energy plotted against the temperature on the double logarithmic scale, for the Ta film and the TaO_x films with x = 1.0 and 1.5. (f) Plot of the reduced activation energy exhibiting a linear dependence on $T^{1/2}$ for both the Ta and the TaO_x film with $x = 1$, thus evidencing a power-law behaviour of the conductivity.

as a function of $\sqrt{T}$ for these three cases in Fig. 5.9(c). All of them show this dependence in a wide temperature range from room temperature down to approximately 50 K. Below this temperature, the TaO_x films can be reasonably fitted by using an Efros-Schlovskii-like hopping mechanism, where $\ln(\rho) \propto T^{-1/2}$. The best fit is obtained for the film with $x = 1.5$, while both the film with x = 1 and the one with x = 1.3 show clear deviations from this behaviour at the lowest temperatures. On the other hand, this mechanism cannot explain the Ta data below 50 K.

The reduced activation energy plot of Fig. 5.9(e) also shows the same behaviour for the Ta and TaO_x film with $x = 1$ and enables a better determination of the temperature where the behaviour of the samples start to diverge, which happens at approximately 25 K. The more oxidized film with $x = 1.5$ already shows noticeable differences in the temperature dependence, even though its resistivity can also be explained by the same transport mechanisms. The sign of the slope in the w vs. T plots is an important parameter in selecting the conduction mechanisms eligible to explain the observed temperature dependence. An activated process, such as hopping, normally described in the form $\sigma = \sigma_0 \exp[(T_0/T)^{\alpha}]$, has a reduced activation energy given by:

$$w = (T_0/T)^{\alpha}\,. \tag{5.2}$$

This means that w should decrease with increasing temperature, which is observed at $T < 25$ K in the TaO_x films. For $x = 1$, this trend is again interrupted at $T < 10$ K, where w starts decreasing again with decreasing temperature. However, for $x = 1.5$, which shows a more pronounced activated part, the trend lasts down to the lowest measured temperatures. On the other hand, a positive slope in the w vs. T plot, with w increasing with rising temperature, is typical of metallic systems, where the conductivity is dominated by a power law of the kind $\sigma = a + bT^p$ [221], for which:

$$w = \frac{pbT^p}{a + bT^p}. \tag{5.3}$$

The plot of w vs. $T^{1/2}$ in Fig. 5.9(f) shows a linear behaviour of the data, thus $p = 1/2$ is a good exponent for the power-law temperature dependence of the conductivity for Ta and the TaO_x film with $x = 1$. This agrees well with the $\sqrt{T}$ behaviour of the resistivity observed at $T > 50$ K. For the TaO_x film with $x = 1.5$, also shown in Fig. 5.9(e), w has a constant value of approximately 0.58 from 50 K almost up to room temperature. This should be expected for a power-law dependence when $a \gg bT^p$, which gives $w \approx p$. So, the TaO_x film with $x = 1.5$ also demonstrates the presence of a power-law dependence with an exponent close to 1/2. All this analysis clearly links the transport in the TaO_x films with $x \sim 1$ with the transport in the metallic Ta film.

Interestingly, the Ta film does not show the typical positive TCR observed for ordinary metals, indeed showing a negative TCR. However, as shown before in Fig. 4.11(a), a 15 nm-thick Ta film sputtered on top of a 5 nm-thick Ta_2O_5 layer does show a positive TCR. Indeed, the sign of the TCR as well as the resistivity value is highly dependent on the substrate material and the thickness of the Ta film. A more detailed study of the dependence of the resistivity and the TCR of the Ta films with different thickness on top of Ta_2O_5 and SiO_2 is presented in appendix C.

As mentioned in the preceding chapter, the temperature dependence of the resistivity of the TaO_x films can be divided into two regions. For the high temperature region (region I), a very good fit of the data is obtained with a $\sqrt{T}$ dependence of the conductivity, while for the low temperature region (region II), an exponential behaviour of the kind $\rho \propto \exp\left(1/\sqrt{T}\right)$

Table 5.1: Summary of the important parameters associated with the fits shown in Fig. 5.9.

Film	Region I slope ($Sm^{-1}K^{1/2}$)	Region II slope (dimensionless)
Ta	1955 ± 2	—
$TaO_{x=1}$	431.1 ± 0.5	0.05874 ± 0.00007
$TaO_{x=1.3}$	243.3 ± 0.2	0.677 ± 0.002
$TaO_{x=1.5}$	84.88 ± 0.03	8.321 ± 0.007

enables a good fit of the measured data. These two functions allow a good fitting of the data for all three TaO_x films. For the Ta film, only the high temperature regime is observed. The slope of the linear fit for region I decreases as x increases, *i.e.*, with increasing oxygen concentration in the films. Table 5.1 lists the slopes obtained from the linear fits in both regions, obtained for the different TaO_x films measured and also Ta, showing the evolution of the slope with the oxygen concentration. With the increase of the oxygen concentration, the slope from region I decreases, while the slope from region II increases. Among all the samples, the highest slope for region I is obtained for the Ta film, which is the sample with the lowest oxygen concentration, further confirming the trend.

However, there is one clear difference between Ta and TaO_x films, which is the behaviour at the lowest temperatures measured. While for the TaO_x films the resistivity keeps increasing at the lowest temperatures, for the Ta film the resistivity has a pronounced downturn below 10 K, as can be observed in Fig. 5.9(b). This downturn is a typical signature of weak antilocalization, one of the quantum interference effects presented in chapter 2. To confirm the existence of this effect, a magnetic filed can be applied to modulate the interference and eventually destroy it, for a sufficiently high magnetic field. By decreasing the strength of the weak antilocalization, the resistivity of the sample should increase. Fig. 5.10(a) shows the temperature dependence of the resistivity for the Ta film for $T < 50$ K for different magnitudes of an externally applied magnetic field up to 9 T. It is clearly visible that the application of the magnetic field leads to the disappearance of the resistivity downturn at the lowest temperatures. This magnetoresistance effect will be further explored in a subsequent section. The same magnetic field test was applied to the TaO_x film with $x \sim 1$, with the results shown in Fig. 5.10(b). Again, the application of the magnetic field leads to an increase in the resistivity in the same fashion as for the Ta. This establishes another link between the transport in TaO_x films and the transport in Ta and reveals that weak antilocalization can also be occurring in the TaO_x films, although no clear characteristic downturn of the resistivity is observed.

As the magnetic field is increased, the temperature dependence of the Ta and TaO_x films below 25 K changes significantly. For TaO_x, the resistivity data approaches the characteristic temperature dependence associated with VRH, when $\ln(\rho) \propto T^{1/4}$, as can be seen for the higher magnetic field values in Fig. 5.10(d). The same is not observed for the Ta film in Fig. 5.10(c), where at 9 T there is no linearity of the data in the same set of axes.

5.3 Hall measurements

The use of the van der Pauw geometry for the study of the thin films of substoichiometric TaO_x enables further measurements of the transport properties that are not possible to perform on the conductive filaments inside the ReRAM devices. A particular example is the Hall

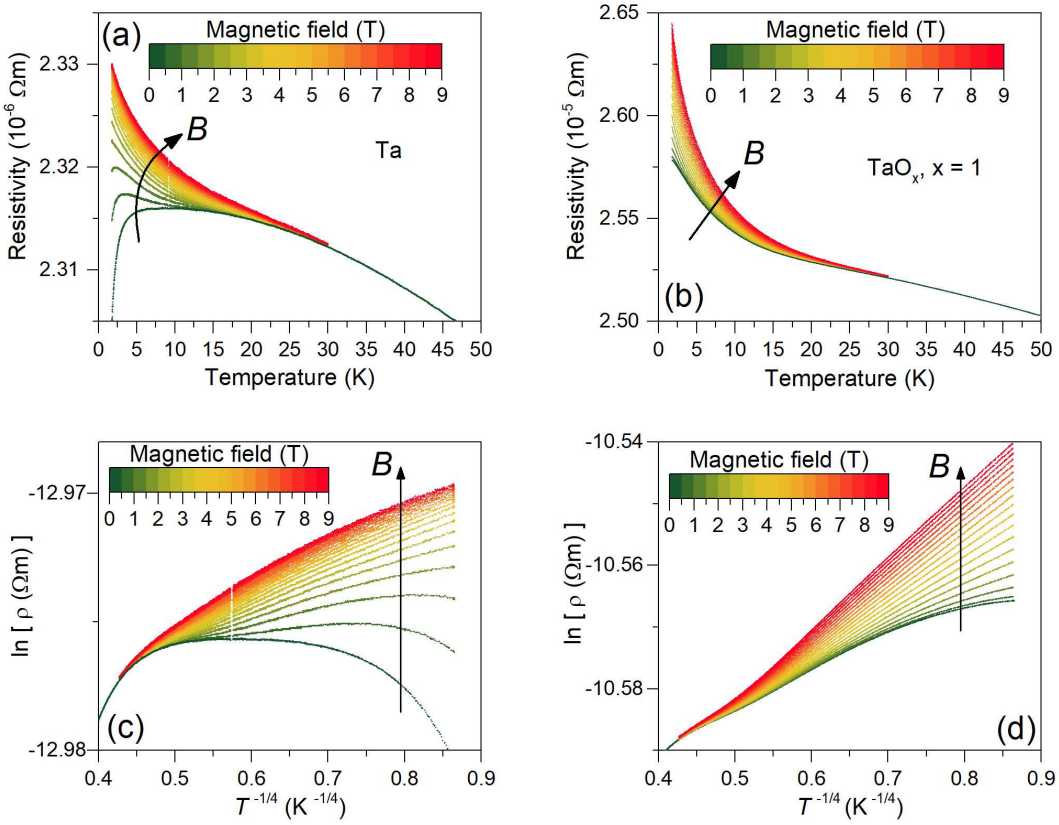

Figure 5.10: Temperature dependence of the resistivity for different applied magnetic fields up to 9 T for: (a) TaO_x film with $x = 1.0$; (b) Ta film. The magnetic field step between every ρ vs. T data set is 0.5 T. (c) and (d) show the same data as (a) and (b) but in a VRH plot, where the $\ln(\rho)$ is plotted against $T^{-1/4}$.

effect, which was performed in the temperature range from 1.8 K up to 300 K. In the next sections, the TaO_x film with $x = 1$ is highlighted because it shows the biggest correlations with the transport in the conductive filaments of the Ta_2O_5 resistive switching devices and also with the transport in the Ta films.

For each temperature, the magnetic field was swept starting from 0 T, going up to +9 T and then down to −9 T before finishing back at 0 T, with a small step of 10 mT and a slow sweeping rate. This allowed the measurement of the Hall resistance, *i.e.* the ratio between the Hall voltage and the applied current (measured in the correct vdP configuration), for a broad range of the magnetic field. The Hall carrier concentration was then calculated from the slope of the linear dependence of the resistance as a function of the magnetic field. The MR contribution had to be subtracted in order to observe the linear dependence of the Hall resistance. The magnetic field dependence of the Hall resistance measured for the Ta film and for the TaO_x film with $x = 1$ at $T = 1.8$ K is shown in Fig. 5.11(a). As can be seen, there is no big change in the slope between the two samples, indicating similar carrier concentrations.

The measurement of the Hall resistance as a function of magnetic field also enabled the observation of an abnormal behaviour for temperatures around $T = 22$ K in the TaO_x films.

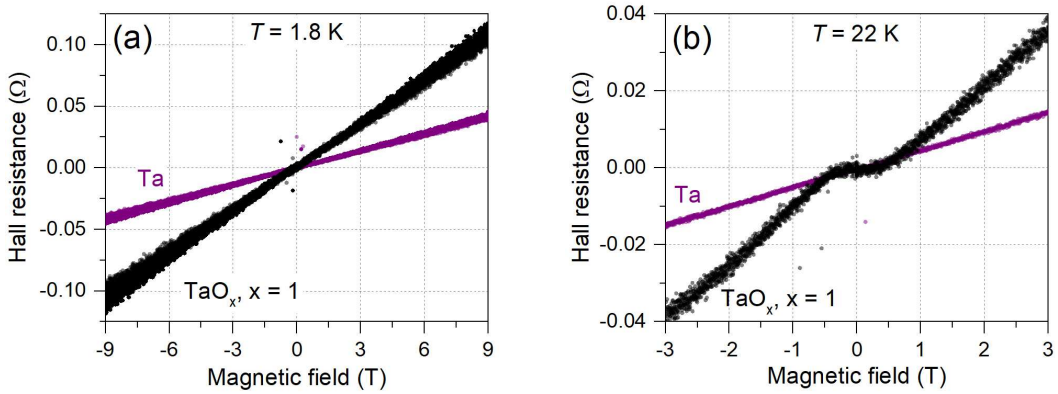

Figure 5.11: (a) Hall resistance (Hall voltage divided by the applied current) as a function of the magnetic field for the Ta film and the TaO_x film with $x = 1$ at $T = 1.8$ K (coloured symbols) and $T = 300$ K (light coloured symbols). (b) Same as in (a) but at $T = 22$ K and for a smaller magnetic field range, evidencing an abnormal behaviour of the Hall resistance (Hall voltage) at this temperature.

When subtracting the MR contribution from the Hall resistance and a voltage offset (probably due to small asymmetries in the vdP structure), the resistance depends linearly on the magnetic field, as expected. However, for temperatures around $T = 22$ K, and only around this temperature, a different dependence is observed for the lower magnetic fields, as can be seen in Fig. 5.11(b). The Hall resistance barely changes for $|B| < 0.3$ T. This observation suggests the critical nature of this temperature, indicating a possible transition between conduction mechanisms. This coincides with the temperature range where the transition in the temperature dependence of the resistivity observed in the resistivity data occurs. This abnormal behaviour of the Hall resistance is not observed, however, for the Ta film, as can also be seen in Fig. 5.11(b) showing a clear difference between the metallic film and the TaO_x films. This seems to corroborate the non-observance of the low temperature region dependence in the Ta films.

From the Hall resistance dependence with the magnetic field the values of the Hall carrier concentration and the Hall mobility were obtained. It is considered that only one type of charge carriers is responsible for the electrical transport, namely electrons, as concluded from the signal of the measured Hall voltage and as expected for the metal. The Hall mobility is calculated from the carrier concentration and the resistivity by:

$$\mu_{\text{Hall}} = \frac{1}{n_{\text{Hall}} e \rho}, \tag{5.4}$$

with e the elementary charge. Fig. 5.12(a) shows the two quantities as a function of the temperature for the Ta film. It shows a carrier concentration of around 6×10^{22} cm^{-3}, in relative good agreement with literature values of 5.2×10^{22} [232]. The Hall mobility is, however, rather low for a metallic sample. The temperature dependence of both the carrier concentration and the mobility is very weak, being slightly more visible in the carrier concentration, which increases for most of the temperature range from 1.8 K up to 300 K. The mobility seems to exhibit an increase as the temperature decreases from 25 K down to 1.8 K, but remains constant for the rest of the temperature range. Fig. 5.12(b) shows the

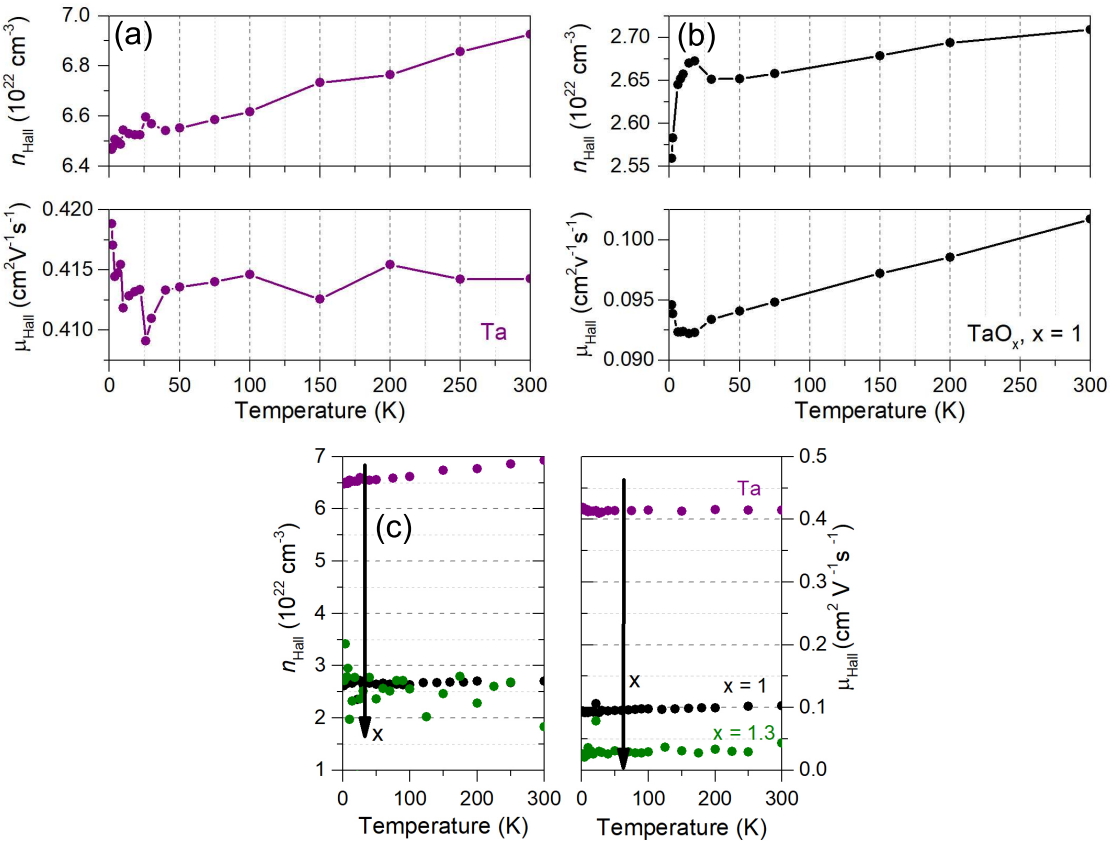

Figure 5.12: (a) Temperature dependence of the carrier concentration and mobility obtained from the Hall measurements performed on the Ta film. The lines are visual guides connecting the experimental data points. (b) Temperature dependence of the carrier concentration and mobility obtained from the Hall measurements performed on the TaO_x film with $x = 1$. (c) Comparison of the Hall results obtained for the TaO_x films with $x = 1$, $x = 1.3$ and the Ta film.

temperature dependence of the carrier concentration and Hall mobility for the TaO_x film with $x = 1$. The Hall measurements show again a very high carrier concentration of around 2.6×10^{22} cm^{-3} with a weak temperature dependence in the measured range. The temperature dependence is stronger for $T < 25$ K, which coincides with the change of the temperature dependence of the resistivity shown in the preceding section. The mobility does not show a strong dependence on temperature either, increasing slightly as the temperature is increased and similarly to the Ta case, increasing also with decreasing temperature for $T < 25$ K.

The comparison of the data between the two samples, Ta and TaO_x, clearly evidences the similarities. Both show a similar carrier concentration of the order of 10^{22} cm^{-3} and a weak temperature dependence of the carrier concentration and mobility. For a better comparison, the data are replotted in Fig. 5.12(c) and joined by a third set of data corresponding to a TaO_x film with $x = 1.3$. The latter shows similar values of the carrier concentration and mobility relatively to the film with $x = 1$, although a smaller mobility is clearly measured. This indicates that with increasing oxygen content both the carrier concentration as well as the mobility decrease, which corresponds to the increase in the resistivity presented before. For the TaO_x films with higher oxygen content the data was too noisy to retrieve the Hall carrier concentration and mobility.

5.4 Magnetoresistance

The MR as a function of the applied magnetic field for the Ta film as well as for the TaO_x film with $x = 1$ is shown at different temperatures in Fig. 5.13(a) and (b), respectively. The MR is calculated through the expression:

$$\mathrm{MR} = \frac{R_B - R_{B=0}}{R_{B=0}}, \tag{5.5}$$

with R_B the resistance with an external magnetic field B applied and $R_{B=0}$ the resistance measured with no externally applied magnetic field. The measured MR is positive, *i.e.* the resistance increases when a magnetic field is applied. The MR is only measurable for temperatures below approximately 30 K, because for $T > 30$ K the MR is lower than the noise level. For a fixed magnetic field, the MR decays exponentially with the increase of temperature as can be seen in Fig. 5.13(d), with the MR at $T = 25$ K decaying to less than 1 % of the initial value at 1.8 K. The temperature for which the MR becomes too small to measure, coincides with the transition temperature between the two transport mechanisms in the TaO_x films.

The two films show a very similar MR behaviour. Noticeable differences are the shape of the MR, which exhibits a steeper increase of the MR for low fields compared to the TaO_x film. The plots in Fig. 5.13(e) and (f), where the MR was normalized for each temperature, enable a better view of the evolution of the MR dependence with the magnetic field as the temperature is changed. Interestingly, the normalized MR of the Ta film at temperatures around 10 K has an almost identical shape to the one measured for the TaO_x film at 1.8 K, although having a clearly different magnitude of the effect. This is another qualitative indication that the underlying physical mechanism responsible for the MR is the same in both cases. Another visible feature is the broadening of the field dependence of the MR as the temperature increases, which in both cases, evolves from a cusp-like shape into a parabolic dependence.

Additional evidences for the evolution of the MR as the oxygen content increases is provided by the comparison plot of Fig. 5.14, where the data for the aforementioned samples

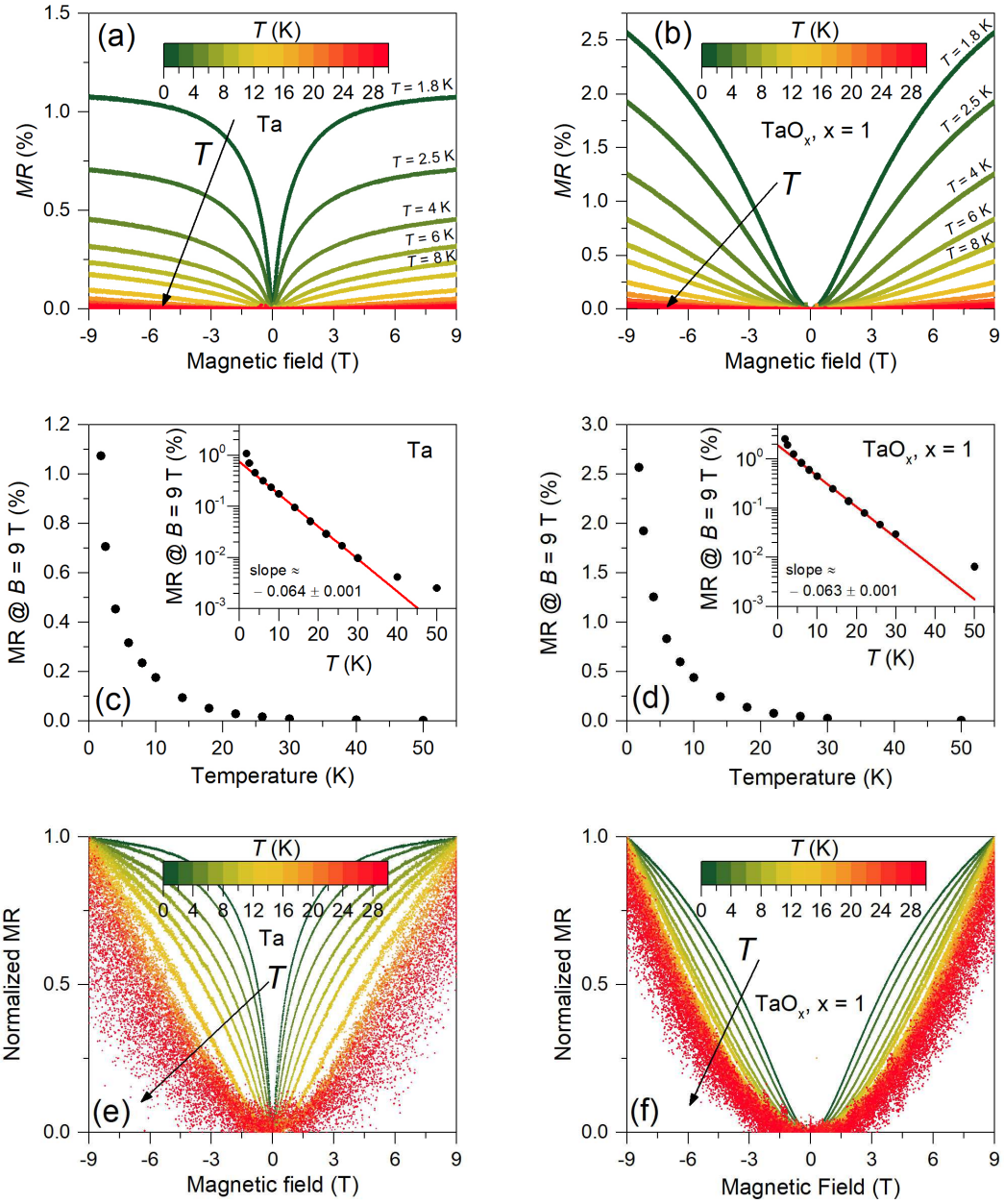

Figure 5.13: (a) MR of the Ta film as a function of the applied magnetic field at various temperatures from 1.8 K to 30 K (b) Magnetoresistance (MR) of the TaO_x film with $x = 1$ as a function of the applied external magnetic field at different temperatures ranging from 1.8 K to 30 K. (c) Decay with temperature of the MR at B = 9 T of the Ta film. The inset shows the same data but on a logarithmic y-axis evidencing an exponential decay, at least in some range, as shown by the linear fit (red line). (d) Same as in (c) but for the TaO_x film with $x = 1$. (e) Normalized MR as a function of the magnetic field for the Ta film, where the normalization was performed for each individual temperature, enabling a comparison of the field dependence of the MR at the different temperatures. (f) Same as in (e) for the TaO_x film with $x = 1$.

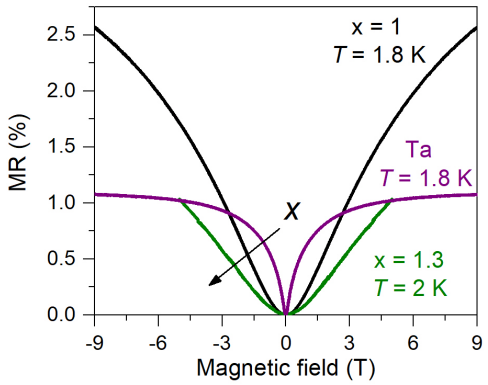

Figure 5.14: MR as a function of the magnetic field at $T = 1.8$ K for the TaO_x film with $x = 1.0$ and for the Ta film, and at $T = 2$ K for the TaO_x film with $x = 1.3$.

at $T = 1.8$ K is accompanied by the MR of a TaO_x film with $x = 1.3$ at $T = 2$ K. As the oxygen concentration in the film increases, the MR decreases for the same magnetic field amplitude, *i.e.* the effect causing the MR tends to get weaker. Besides that, the shape of the MR vs. B curve also changes, with the effect becoming progressively broader as the oxygen concentration is increased.

With the positive cusp-like shaped MR just presented, and the decrease of the resistivity at the lower temperatures that is destroyed with the application of an external magnetic field, as shown before in Fig. 5.10, the samples show two distinctive fingerprints of weak antilocalization (WAL). WAL arises from a quantum correction to the classical metal conductivity obtained from the Boltzmann transport equation, and is directly linked to the manifestation of the wave properties of the charge carriers when they scatter elastically from static disorder [135]. The occurrence of WAL, and not weak localization, is explained by the high spin-orbit coupling of the heavy Ta atoms ($Z = 73$). The change in the conductivity due to the localization phenomena is mathematically described by the Hikami-Larkin-Nagaoka (HLN) formalism (Eq. 2.21), which can be used to fit the magnetoconductance data [139]. The mathematical formula of the HLN formalism were presented in chapter 2. However, this formula was originally developed for a 2D case. The dimensionality of the effect is determined by the phase breaking length (PBL) and the thickness of the film. When the PBL is considerably higher than the film thickness, the WAL is then described by the 2D formula developed by HLN (Eq. 2.21). For the case the effect takes place in 3D, the 3D formula is better suited to describe the data (Eq. 2.25). In the case that the PBL is much higher than the spin-orbit scattering length and the mean free path, the HLN formalism in 2D can be simplified to depend only on the PBL (Eq. 2.22).

The data measured in the Ta film is accurately described with the simplified 2D formula of Eq. 2.22 for $T < 10$ K, as can be verified in Fig. 5.15(a). The obtained PBL is considerably higher than the film thickness, validating the used formula. The original HLN formula of Eq. 2.21 was initially used to fit the data, but the best fits were always achieved when only the component associated with the PBL was considered, which indicated that the assumptions leading to the simplified Eq. 2.22 are reasonable. For $T > 10$ K, the 3D formula is used with success, as can be seen in Fig. 5.15(b), because the PBL becomes smaller than the thickness

of the Ta film. As for the TaO_x thin film with $x = 1$, the data is best described by the 3D expression from Eq. 2.25 for all temperatures from 1.8 K up to 26 K, as can be seen in Fig. 5.15(c). This is justified by the obtained PBL, which is smaller than the film thickness of 20 nm for the whole temperature range.

The sound fit of the WAL formalism to the experimental data both for Ta and the TaO_x establishes a clear link between the MR behaviour of the two films. The major difference is the magnitude of the PBL, which not only affects the dimensionality but also the shape of the MR vs B curve. At $T = 1.8$ K, the Ta film has a PBL of 95 nm, while for the TaO_x film with $x = 1.0$ the value is reduced to 19 nm, *i.e.*, five times smaller. The higher PBL in the Ta film indicates that the charge carriers can keep their phase over a longer spatial distance, which promotes WAL. In the TaO_x film, as the PBL is smaller, the inelastic scattering events, like electron-electron or electron-phonon collisions, occur more frequently, leading to the loss of the phase and weaker interference. The PBL values obtained at different temperatures from the fitting procedure are displayed in Fig. 5.15d for both samples. The PBL follows a power-law decay with increasing temperature with an exponent of -0.55 ± 0.02 and -0.76 ± 0.02 for the TaO_x and Ta films, respectively. For the Ta film and at temperatures above 10 K, the exponent seems to decrease to -1.1 ± 0.2.

The remaining parameters obtained from the fits can be seen in Fig. 5.15(e) and (f). The simplified formula of Eq. 2.22 includes a quadratic component b that relates not only with the classic cyclotronic term but also with the simplified components of the spin-orbit and elastic terms of the general Hikami-Larkin-Nagaoka model, giving $b = b_c + b_q$, with b_c and b_q being the classical and quantum terms, respectively. The classical term arising from the cyclotronic MR is given by [140]:

$$b_c = -\mu_{\mathrm{MR}}^2 G_0, \tag{5.6}$$

where μ_{MR} is the MR mobility that can be approximated by the Hall mobility [140], and $G_0 = (2e^2)/h$ is the conductance quantum. On the other hand, the quantum term is given by:

$$b_q = -\frac{e^2}{24\pi h}\left(\frac{1}{B_{\mathrm{SO}} + B_e}\right)^2 + \frac{3e^2}{48\pi h}\left(\frac{1}{\frac{4}{3}B_{\mathrm{SO}} + B_\phi}\right)^2. \tag{5.7}$$

Considering the measured Hall mobility for the Ta film, the classical term b is much lower than the parameter b obtained from the fits, therefore the quantum term is the dominating one, and $b \approx b_q$. Considering also that the mean free path L_e is much smaller than L_{SO}, the expression relating $B_{\mathrm{SO}} = \frac{\hbar}{4eL_{\mathrm{SO}}^2}$ with the fitting parameters $B_\phi = \frac{\hbar}{4eL_\phi^2}$ and b can be derived, giving:

$$B_{\mathrm{SO}} \approx \frac{3}{8}\left[\left(B_\phi^2 - 4B_\phi + \frac{e^2}{4\pi hb}\right)^{1/2} - B_\phi\right]. \tag{5.8}$$

The fit parameter L_ϕ is already shown in Fig. 5.15(d). The parameters α and L_{SO} resulting from the fit of the 3D WAL formalisms to the data measured on the Ta film and on the TaO_x film with $x = 1$ are shown in Fig. 5.15(e) and (f), respectively. For the 2D case, the L_{SO} was determined from the fitting parameter b using Eq. 5.8 and added to the plot of Fig. 5.15(e). As can also be seen in the plot, the change of the fitting formula (from 2D to 3D) did not create big discontinuities in the temperature dependence of both the α and L_{SO} parameters.

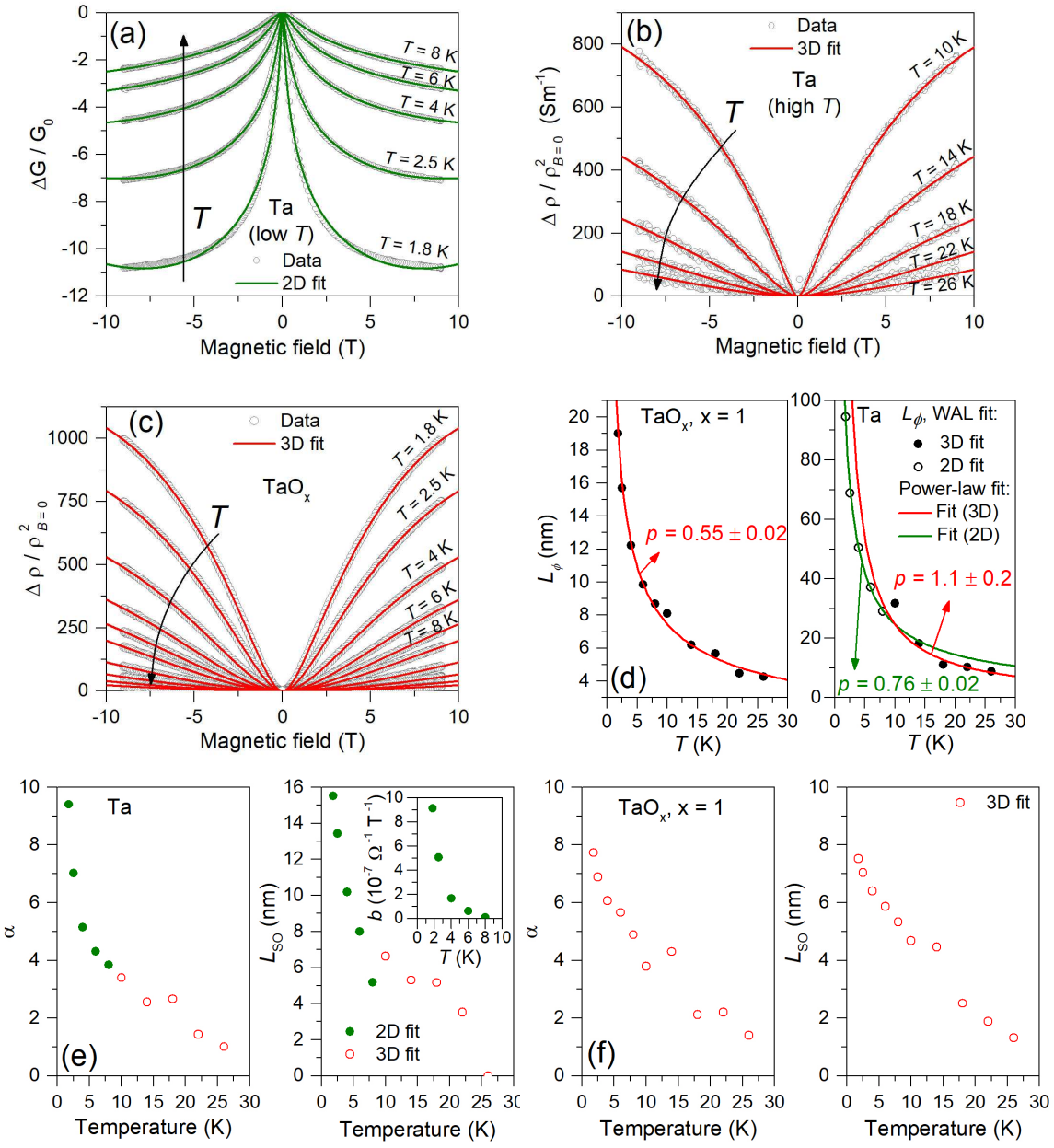

Figure 5.15: (a) Change in conductance (normalized by $G_0 = 2e^2/h$, the conductance quantum) as a function of the applied magnetic field at 1.8 K $\leq T \leq$ 8 K for the Ta film. The lines show the least-squares fit to the simplified 2D Hikami-Larkin-Nagaoka formula shown in Eq. 2.22. (b) Change in resistivity as a function of the applied magnetic field at 10 K $\leq T \leq$ 26 K for the Ta film. The lines show the least-squares fit to the 3D weak antilocalization formula shown in Eq. 2.25. (c) Same as (b) for the TaO_x film with x = 1.0 for $T \leq$ 26 K. (d) Decay of the PBL (L_ϕ) obtained from the fits shown in (a)-(c) for all temperatures. The lines show a power-law fit to the full data points, with the indicated exponent p. For the Ta sample (on the right), two fits were performed, with the data divided in two ranges: $T \leq$ 8 K and $T \geq$ 10 K. (e-f) Remaining parameters α and L_{SO} resultant from the fits using the weak antilocalization formulas for Ta and TaO_x with x = 1, respectively. The parameter b in the inset of (e) is the true fitting parameter from which L_{SO} is calculated.

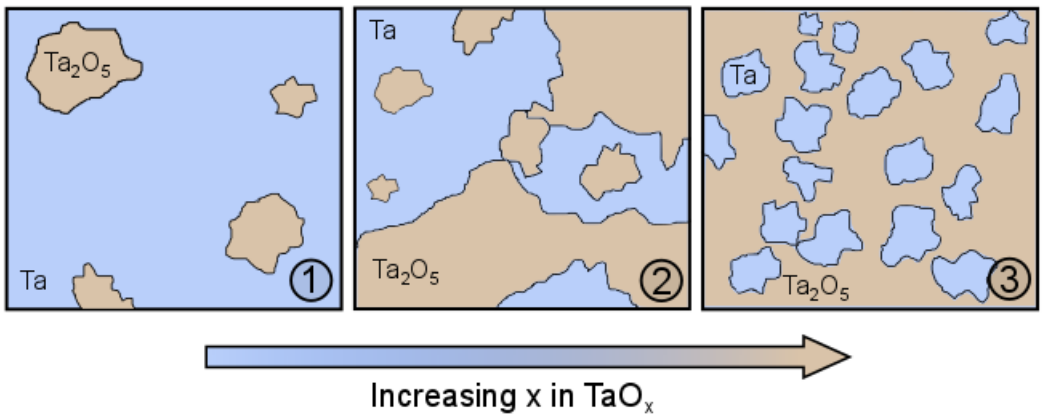

Figure 5.16: Schematic model (as it would be seen from the top view of the film's surface area) of the microstructure evolution in the TaO_x films with increasing oxygen concentration x. The blue region represents Ta(O), while the beige fields represent Ta_2O_5. The increasing oxygen concentration leads to a higher Ta_2O_5 content, eventually breaking the percolation of Ta granules and thus, inhibiting the metallic behaviour.

5.5 Discussion of a possible model for the transport in the TaO_x thin films

5.5.1 Structure model for the transport

The temperature dependent data of the resistivity of the Ta and TaO_x films revealed the same transport mechanisms, especially at temperatures above 25 K. Nevertheless, the resistivity of the TaO_x films with $x = 1$ is one order of magnitude higher than the resistivity of the Ta films. Hall measurements revealed a high carrier concentration in the TaO_x films with $x = 1.0$ and $x = 1.3$, only approximately 2.7 times lower than the that measured in the Ta film. And finally, the MR observed in the TaO_x films with $x = 1$ at low temperatures is accurately described by the same quantum interference effect as that observed in the Ta film. These three experiments add to the structural analysis discussed before in favour of the decisive role of metallic Ta in defining the electrical transport in the TaO_x thin films.

Given a sufficient metal concentration in the films, provided by the Ta(O) phase, it is possible to form a percolation path for transport consisting of metallic Ta granules. This seems to be the case for TaO_x films with $x \leq 1.5$, as the films with higher oxygen content proved too resistive for the methodology implemented in this work. A schematic model of the evolution of the structure of the TaO_x films with increasing x is shown in Fig. 5.16. At stages 1 and 2 of the schematics, representing the situation for lower x values, it is still possible to have a continuous conduction path through the Ta granules. Considering this percolation model, it is also understandable why the resistance of the samples with $x > 1.5$ is so high that we could not measure it with the used setup. Most probably, the amount of oxygen was high enough to form a sufficient quantity of the oxide phase to impede a percolation path, as schematically depicted in the third stage of the schematics in Fig. 5.16. As the resistivity of Ta_2O_5 is very high, the resistance of such a film would be dramatically higher than the one obtained in films where the metallic percolation is achieved.

5.5.2 Transport mechanisms

High temperature regime

The behaviour observed in the Ta and TaO_x films, with the negative TCR and the power-law temperature dependence of the conductivity with an exponent of 1/2, is typical of disordered metals [138, 144], also known as dirty metals. An example of this is the transport of the metal alloys studied by Mooij. The same is also observed in other disordered systems, such as n-type nanocrystalline silicon with electron density above 10^{19} cm^{-3} [233]. The temperature dependence of the conductivity in these metals, where disorder dominates the transport behaviour, is related to electron-electron interactions and weak localization [138]. These effects are not considered when solving the Boltzmann transport equation for typical metals. However, they become important when the disorder is high, *i.e.*, when the Ioffe-Regel criterion is not fulfilled. The criterion is based on the calculation of the quantity $k_F \cdot L_e$, where k_F is the Fermi wave vector. $k_F \cdot L_e$ can be estimated based on the experimentally determined charge carrier concentration and resistivity. For that an approximation to the Drude model and a spherical Fermi surface is considered, which returns [135]:

$$k_F \cdot L_e = \left(3\pi^2\right)^{2/3} \frac{\hbar}{e^2} \frac{n^{-1/3}}{\rho}. \tag{5.9}$$

Based on the experimental results, $k_F \cdot L_e$ is 4.4, for the Ta film, while for the TaO_x film with $x = 1$, it is approximately 0.58. As expected, the value is greater in the Ta film, indicating a smaller degree of disorder relatively to the TaO_x films. With these values, the Ioffe-Regel criterion $k_F \cdot L_e \gg 1$ is not fulfilled, and the Boltzmann transport equation cannot be applied without significant prediction error. Thus, the quantum corrections to the conductivity play a decisive role in determining the electrical transport.

From the quantum corrections presented in chapter 2 there is one that stands out due to the explicit dependence on $\sqrt{T}$: the electron-electron interference. This effect leads to a correction to the metal conductivity known as the Aronov-Alt'shuler effect [143], which for 3D-transport is mathematically described by [138]:

$$\Delta\sigma = \frac{1.3}{\sqrt{2}} \frac{e^2}{4\pi^2\hbar} \left(\frac{4}{3} - \frac{3}{2}\widetilde{F}_\sigma\right) \sqrt{\frac{T}{D}}, \tag{5.10}$$

where $\widetilde{F}_\sigma = -\frac{32}{3}F\left[1 + \frac{3}{4}F - \left(1 + \frac{F}{2}\right)^{\frac{3}{2}}\right]$, F is the Hartree term that quantifies the strength of the screening between electrons, and D is the electron diffusion constant. This correction fits very well to the measured transport temperature dependence for the Ta and TaO_x thin films at $T > 25$ K. Furthermore, the analysis of the MR data suggests that the mean free path is very small, very probably smaller than units of nm, enabling 3D transport in the 20 nm-thick films. Despite this good framework to understand the transport in the TaO_x films, it is observed that, from sample to sample, the slope in the σ vs $\sqrt{T}$ plots (Fig. 5.9) changes considerably. Considering Eq. 5.10, the only parameters that can change with the sample are F and D. The linear fits indicate a decrease of the slope by a factor of 4.6 from Ta to TaO_x. The F term should take a value close to 0.44 for Ta, as reported in the literature [232], and it should decrease going from Ta to TaO_x. However, going to higher oxygen concentration, the slope decreases further. This makes it problematic to explain the data solely in this framework

because the screening term F should not vary by orders of magnitude, unless there is a big change in the carrier concentration [232], which is definitely not the case.

Electron-electron interference is also commonly observed in granular metals, where metallic granules are surrounded by insulating domains [147, 150, 155]. For the TaO_x films, considering the proposed model (Fig. 5.16), the increasing oxygen concentration leads to the formation of the insulating oxide. Therefore, the granular-metal scenario in the metallic regime could provide a better framework to explain the transport data. In this case, the correction due to the electron-electron interference preserves the $\sqrt{T}$ dependence for 3D transport but would be directly proportional to the size of the granules a through the expression (calculated from Ref. [150]):

$$\frac{\Delta\sigma}{\sigma_0} = \frac{\alpha}{12\pi^2 g} a \sqrt{\frac{T}{D_{\text{eff}}}}, \tag{5.11}$$

where $\alpha = 1.83$ is a numerical constant, g is the tunnelling conductance between granules, and D_{eff} is an effective diffusion constant related to the transport on scales much larger than the granule size. Therefore, the decrease in the granule size with increasing oxygen concentration can explain the decreasing slope. It should be noted, nevertheless, that the ascription of the electron-electron interactions to the observed dependence up to room temperature is still a controversial topic in literature, and thus still lacking a more consensual explanation.

Low temperature regime

The experimental resistivity data for the TaO_x films show that the $\sqrt{T}$ behaviour breaks at low temperatures, especially below 25 K. Another mechanism should then be responsible for the observed temperature dependence. The fits were fairly good with the Efros-Schlovskii hopping mechanism.

It is also reasonable to think that in the granular metal scenario, the Ta granules are sometimes separated by a region of insulating Ta_2O_5, so that the electrons could have to overcome or tunnel through a potential barrier during inter-granular transport. In fact, Eq. 5.11 already includes g, the tunnelling conductance between granules. This inter-granular transport could, very probably, become the bottleneck for the transport below a critical temperature. The situation is very similar to the case of a granular metal in the insulating regime, where the granules are separated in space and no percolation is possible. In the insulating regime, the transport is characterized by a temperature dependence with the exact same form of the Efros-Schlosvkii hopping mechanism. Therefore, this offers a decent explanation for the low temperature regime, especially for the film with $x = 1.5$. The application of a magnetic field changes the behaviour for the TaO_x film with $x = 1$, leading to a shift from the $\ln(\rho) \propto T^{-1/2}$ dependence to a $\ln(\rho) \propto T^{-1/4}$ dependence, which is characteristic of Mott's VRH. This could mean that the carriers become strongly localized at low temperature under the effect of the magnetic field, thus breaking the metallic transport observed for higher temperatures. However, the reduced activation energy plot does not clearly classify this particular sample as insulating, because there is no obvious divergence to high resistivity down to 1.8 K. Although a similar trend with the application of a magnetic field is observed also for Ta, the VRH regime is not yet obtained at 9 T, and does not seem to evolve further, as the MR is already saturated for this value of the magnetic field. Probably, the reason for this difference comes from the lower amount of oxygen in the Ta film, which is not sufficient to break the continuous path of Ta throughout the sample.

Other possibility for the deviation from the $\sqrt{T}$ behaviour was reported for other material systems, such as Fe-SiO_2 nanocomposite films behaving like a granular metal [147]. The authors explain the deviation at low temperature with an emergence of quantum size effects. These occur due to the small contact volume between neighbouring granules that create nano-sized constrictions. However, this transition is accompanied by a decrease of the carrier concentration of one order of magnitude. This does not seem to be the case for the measured TaO_x films, although a slightly stronger change of the carrier concentration is observed below the transition temperature.

5.5.3 Magnetoresistance

The observed decrease of the PBL from the Ta to the TaO_x films should be associated with the increase of the oxygen concentration in the films. This increase is translated into an increase of the interstitial oxygen concentration in the Ta granules, as well as into a reduction of the size of the Ta granules due to the formation of Ta_2O_5. Both lead to an increase of the inelastic scattering probability, thus reducing the PBL.

The decay exponent of the PBL with temperature provides information on the dominating dephasing mechanisms involved. According to Assaf et al. and references therein [140, 234, 235], the exponents -0.5 and -0.75 are associated with inelastic electron-electron collisions in 2D and 3D, respectively. Electron-phonon collisions result in a faster decay with an exponent of at least -1. For the TaO_x film, the fitted exponent of -0.55 ± 0.02 indicates that the dominating dephasing mechanism involves 2D electron-electron collisions. For the Ta film, at lower temperatures the exponent of -0.76 ± 0.02 indicates that the scattering is dominated by 3D electron-electron collisions, while at higher temperatures, electron-phonon collisions become the dominant scattering mechanism giving an exponent of -1.1 ± 0.2.

5.6 Insight into the conductive filaments of ReRAM devices

Transport model for the filament

Chapter 4 presented a correlation between the transport mechanisms in the substoichiometric TaO_x films with $x \sim 1$ and in the Ta_2O_5-based RS devices in the LRS. The experimental evidences presented in this chapter enabled the understanding of the physical origin of the transport properties of the TaO_x thin films. Piecing these two parts of the puzzle together reveals some insight into the physical properties of the conductive filaments inside the Ta_2O_5 ReRAM devices. The overall conclusion is that the transport in the conductive filaments is also dominated by the metallic Ta(O) phase. There should indeed be a Ta percolation path in the filament that is responsible for the transport behaviour. This is schematically depicted in Fig. 5.17, where the filament body includes Ta clusters that enable metallic transport between the two electrodes in the LRS.

This model describes well the Ta_2O_5-based ReRAM devices where the LRS shows a low resistance, up to units of kΩ, and an ohmic $I - V$ characteristic. However, it could fail for devices where the resistance in the LRS is of the order of 10 kΩ, where potential barriers at the Pt/Ta_2O_5 interface could play a key role [65, 80]. Considering our conductivity data, a cylindrical filament of TaO_x with $x = 1$ and a length of 5 nm returns a resistance of 1.5 kΩ and 5.8 kΩ for diameters of 10 and 5 nm, respectively. These values should indicate an upper

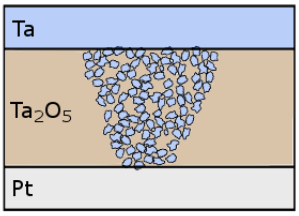

Figure 5.17: Schematic model of the conductive filament in Ta_2O_5-based ReRAM devices, showing its structure, composed of granules of metallic Ta in an insulating Ta_2O_5 matrix. The blue region represents Ta, while the beige region represents Ta_2O_5.

limit of the resistance for the validity of the proposed model. In our case, devices with an LRS of 3.5 kΩ still exhibit metallic behaviour.

Besides LRSs exhibiting negative TCR, there are also LRSs which show a positive TCR. This is actually in agreement with other previously published works [90, 96, 236]. The positive TCR in the LRS was observed in RS devices where a higher current (typically above 2 mA) was allowed through the conductive filaments. The positive TCR could be related with a structural change of the Ta phase in the filament. Indeed, the TCR is normally used to distinguish the two phases of Ta. While the bulk α-Ta phase exhibits a positive TCR, the disordered β-Ta phase is known to exhibit a negative TCR [171, 174]. Additionally, for a sufficient quantity of the α phase, a mixture of both phases can also lead to a positive TCR [174]. For thin films, the β-Ta to α-Ta transformation is achieved via thermal annealing in vacuum of the as-grown films at temperatures in the range from $400 - 650$°C [165]. On the other hand, it is widely understood that operation of the RS devices induces very high local temperatures that can surpass 1000 K due to Joule heating in the conductive filaments [27, 66–70]. Therefore, it is possible that during electroforming and during SET (switching from the high-resistance state to the LRS) at a high current level, the local temperature in the conductive filament is high enough to induce the structural change of the Ta granules from the β- to the α-phase. The mixture of α-Ta and β-Ta would then enable the positive TCR observed. Crystalline α-Ta and β-Ta phases have been observed in conductive filaments in $Ta/TaO_x/Pt$ devices by means of electron diffraction, along with a positive TCR in the LRS [236]. When the current through the filament is limited to lower values, the structural transformation can be impeded, at least to a certain extent, and a negative TCR is obtained. Another important thing to consider in the phase transformation is the amount of oxygen in the Ta granules. The disordered β-Ta phase appears to be able to accommodate much more oxygen than α-Ta. Structural studies of sputtered Ta films in a chamber with controlled oxygen content reveal the phase transformation from α to β as soon as 4% of oxygen is used, with the α-Ta disappearing completely after 10% of oxygen [222]. Based on this, the movement of oxygen in and out of the conductive filaments during the RESET and SET could, thus, also play a role in the β to α transition and vice-versa. The increase in current through the conductive filaments is commonly perceived also as an increase in the filament's diameter. Other molecular dynamics studies show that the phase stability is dependent on the size of the Ta clusters. The beta phase is more stable for smaller clusters (smaller than 200 atoms), while the α phase is more stable for bigger clusters [237]. It is not possible, nevertheless,

to completely disregard the parasitic effects at play when discussing the positive TCR, as discussed in chapter 4. Although the measurements performed in the breakdown devices, which show a significantly lower resistance, increase the confidence in that the positive TCR effect stems from the conductive filament.

Model in the framework of the literature

The metallic Ta-rich filament model is supported by first-principles studies reported by Xiao and Watanabe [231]. The authors suggest that the Ta-Ta bonds are the main contributors to the formation of the conductive filaments in TaO_x-based RS devices, instead of oxygen vacancies. This theoretical study also reports that above 1400 K the Ta atoms tend to arrange in a layered structure, crystallizing in the α-Ta phase with interstitial O atoms. This last statement supports the β to α evolution obtained at higher currents.

Experimentally, Ta-rich conductive filaments have been observed in RS devices by means of different techniques. However, the authors sometimes refrain from claiming the metallic nature of such Ta-rich filaments. Strachan et al. imaged the conductive filaments in $Ta/Ta_2O_5/Pt$ devices with X-ray spectromicroscopy, which revealed a localized region less than 150 nm in diameter with a Ta-rich composition sorrounded by nano-crystalline Ta_2O_5 [45]. These results highlight the role a material change in the insulating Ta_2O_5 to the resistive switching phenomenon in TaO_x-based ReRAM devices. High-resolution TEM and related techniques have also been instrumental in revealing the Ta-richness of the conductive filaments. Park et al. verified in-situ the formation and annihilation of conducting channels in a more complicated TaO_x-based structure with the $Pt/SiO_2/Ta_2O_{5-x}/TaO_{2-x}/Pt$ layer stack [91]. But the results also support internal atomic rearrangements that lead to the formation of Ta-rich regions, with the authors reporting a probable composition of TaO_{1-x} inside the conducting channels that form in the SiO_2 layer, while Ta-rich clusters form a percolation path in the Ta_2O_{5-x} layer. More recently, the Skowronski group published two papers revealing the atomic composition of the conductive filaments in $TiN/TaO_{2.0}/TiN$ structures by HAADF STEM coupled with EDX and electron energy loss spectroscopy [48, 49]. They show that the composition of the filaments can reach $TaO_{0.4}$, a very high degree of oxygen deficiency. The authors argue that the lateral motion of Ta and O driven by temperature gradients (Soret effect) is a particularly important driving force for the re-distribution of these two elements in the switching region. The conduction model put forth in this thesis introduces a possible physical transport mechanism that is compatible with the metallic filament picture supported by the experimental works mentioned. This picture is not compatible with commonly reported oxygen vacancy-based transport mechanisms.

Conclusions and outlook

Summary of the conclusions

This work started with the objective of performing a detailed study of the electrical transport in conductive filaments of valence change mechanism-based ReRAM devices. Ta_2O_5 was chosen as the insulator material for being a popular choice among the resistive switching community, due to its resistive switching performance. Starting with the study of transport in the Ta_2O_5 ReRAM devices, the work evolved in parallel to the structural and electrical transport characterization of substoichiometric TaO_x thin films, to recreate in a better geometry (for research purposes) the material of the filaments.

The ohmic behaviour of the $I-V$ characteristics in the low-resistance state (LRS), and the weak temperature dependence of the resistance in the temperature range from 2 K up to 300 K indicate that the conduction in this state is mainly determined by the conductive filament. This precludes a strong influence from the interfacial effects. The weak temperature dependence is accompanied by a negative temperature coefficient of the resistance (TCR), typically observed in insulators. However, the small value for the TCR is more common in metals and the resistance does not diverge strongly at the lowest temperature, which is one of the conditions for being an insulator. On the other hand, in the high-resistance state (HRS) $I-V$ characteristics do show a more pronounced non-linearity, impeding the analysis employed for the LRS. Interestingly, different HRSs show evidence for the occurrence of random telegraph noise (RTN). Transport measurements in the substoichiometric TaO_x thin films show that resistivity evolves similarly with temperature for $x = 1 - 1.5$. Moreover, a clear correlation between the electrical transport mechanisms in conductive filaments in Ta_2O_5-based ReRAM devices in the LRS and the in-plane transport in substoichiometric TaO_x thin films with $x \sim 1$ was shown. At $T > 50$ K, the conductivity follows a $\sqrt{T}$ dependence for both cases. This also indicates that the dimensionality of conduction is similar in both systems. The correlations provide strong evidence that both systems share common material properties at microscopic level. This finding motivated further detailed analytical studies on substoichiometric TaO_x films, as they may provide a much needed insight into the composition and structure of the conductive filaments in Ta_2O_5 ReRAM devices.

In order to clarify the origin of the observed electrical transport in the TaO_x thin films, the study was extended also to metallic Ta and Ta_2O_5, the two known stable phases of the Ta-O material system. Grazing incidence X-ray diffraction (GIXRD) of the TaO_x films reveals a mixture of the disordered β-Ta phase and amorphous Ta_2O_5. The change of the lattice parameters relatively to the metallic Ta film evidences the existence of oxygen interstitials, responsible for the expansion of the unit cell. The relative contributions from the β-Ta and the amorphous Ta_2O_5 change with increasing x in TaO_x, where the metallic peaks decrease in intensity relatively to the broad features of the oxide phase. These findings agree well

with the columnar structure and elemental distribution observed by scanning transmission electron microscopy (STEM) using Z-contrast coupled with EDX. The microscopy experiments also showed that there is an accumulation of oxygen in the space between the Ta-rich columns. The temperature dependence of the conductivity in the TaO_x films with $x \sim 1$ is dominated by disorder-induced effects that lead to a power-law temperature dependence with an exponent of 1/2. The same dependence was observed in sputtered β-Ta films. This behaviour probably originates from electron-electron interactions. The Hall data shows a very high carrier concentration of approximately 2.6×10^{22} cm^{-3} and a rather low mobility on the order of 0.1 cm^2 V^{-1}s^{-1} for the films with $1 \leq x \leq 1.3$. This carrier concentration is only half that which was measured in the Ta film. Magnetoresistance measurements on the TaO_x films indicate weak antilocalization at temperatures below 30 K. Once again, the Hall and MR results establish a clear link between the TaO_x films and the β-Ta film, which shows the same characteristic magnetotransport behaviour. Therefore, the transport in TaO_x films is understood as conduction through a percolation path formed by disordered Ta granules.

Based on the correlations between the transport mechanisms in conductive filaments in Ta_2O_5-based ReRAM devices and in substoichiometric TaO_x thin films with $x \sim 1$, it is possible to infer that the transport in the conductive filaments also occurs by percolation through metallic Ta granules. This agrees with previous literature results where metallic Ta or a very Ta-rich material has been observed in the filaments. This understanding allows for a more correct interpretation of the electrical transport in the scenario of a filament composed of very O-poor TaO_x, compared to the oxygen vacancy-based transport models. The transport in the filaments is also dominated by disorder-induced effects that lead to a negative TCR However, for sufficiently high currents, the conductive filaments show a positive TCR that could be associated with an ordering of the disordered Ta phase to α-Ta.

These conclusions could possibly be applied to other material systems where similar filamentary resistive switching is observed, such as HfO_2.

Future work

This thesis clarified some aspects regarding the filamentary conduction in Ta_2O_5-based ReRAM devices. However, it also opens various different roads for possible future work.

Although technically challenging to pursue, the direct observation of the conductive filaments in operating ReRAM devices has been achieved by other research groups, mainly through transmission electron microscopy and other microscopy techniques. Some recent studies on Ta_2O_5-based devices point to the very Ta-rich conductive filaments, corroborating the transport studies carried out in this work. Applying this kind of techniques to the same samples used for the transport study could strengthen and reinforce these conclusions.

While the transport in the LRS was clarified in detail in this thesis, the transport in the HRS still requires further investigation. It is clear that the emergence of the non-linearity of the HRS is related to the atomic reconfigurations that cause the resistive switching. However, these reconfigurations could occur in the filament, close to the active electrode interface, at the interface itself or even at all these locations. A detailed study to uncover the origin of the differences in transport between the LRS and the HRS could provide a much needed insight into this topic. Towards this goal, a more systematic study of the random telegraph noise effect, observed during this work, could also be useful.

With the objective of turning the input from this thesis into more significant information

for the ReRAM community and industry, it is important to discuss the impact of the findings on the state of the art models of the valence change mechanism. The metallic nature of the filament could impose significant changes in the switching dynamics, mobility of the mobile species, among other important electrochemistry and materials aspects. This could lead to better physics-based dynamic models and compact models that can more accurately describe the behaviour of the ReRAM devices and provide better device design rules.

This work also uncovered interesting questions of a more fundamental physics nature. One such example is the obtained magnetoresistance results in the measured Ta and TaO_x samples. The main variable in the study was the oxygen concentration in the sample, and the magnetoresistance showed considerable differences between the samples. However, the physical origin of the changes in magnetoresistance with increasing oxygen concentration was not completely clarified. A more systematic and detailed study could provide an answer to this question. This should comprise not only the relevant transport and magnetotransport measurements but also structural characterisation and theoretical simulations. This last point is particularly relevant in evaluating the possible impact of the increase in oxygen on the electrical transport.

Appendices

Appendix A

On the representativeness of the samples

To simplify the discussion in the main text of the thesis, only a few representative samples were chosen to show the overall trend and results of the experimental work. In this appendix, additional data is presented in order to clarify the representativeness of the samples highlighted throughout the thesis.

A.1 Transport in Ta_2O_5 ReRAM devices in the LRS

As it was shown in chapter 4, the temperature dependence of the resistance of the LRS of the studied Ta_2O_5 ReRAM devices shows a clear linear relationship of the conductance with $\sqrt{T}$ (identified as region I in the main text). As can also be seen in the same chapter, in Fig. 4.7, sometimes the resistance clearly shows a transition at around 50 K. However, this transition is not observed in other devices, where the temperature dependence of region I is maintained until a lower temperature. Region I, however, always appears for the devices where the LRS shows a negative TCR. Fig. A.1 shows additional data, evidencing the linear relationship typical of region I also for the devices shown in Fig. 4.7(c) and (d).

A.2 Transport in substoichiometric TaO_x thin films

For the case of the electrical transport in the sputtered substoichiometric TaO_x thin films, the same behaviour as a function of the temperature was observed. Fig. A.2 shows additional data to support this. In Fig. A.2(a) resistivity data for a TaO_x film with $x \sim 1$ with a thickness of approximately 100 nm. The data shows the same behaviour that was observed for the samples shown in the main text for the same oxygen content. Again, the data can be divided in the same two regions, where the two characteristic temperature dependencies are clearly seen. The absolute value of the resistivity is, however, slightly different when compared to the value obtained for the film with a thickness of 20 nm shown in the main text. But the overall trend and behaviour with temperature is exactly the same.

In Fig. A.2(b) and (e), additional data for TaO_x films obtained with the same sputtering process as the film with $x \sim 1$ shown in the main text at different times (in a period spanning 2 to 3 years). Again, the same behaviour is observed, with the resistivity exhibiting the same characteristic temperature dependence of the two regions mentioned above, as can

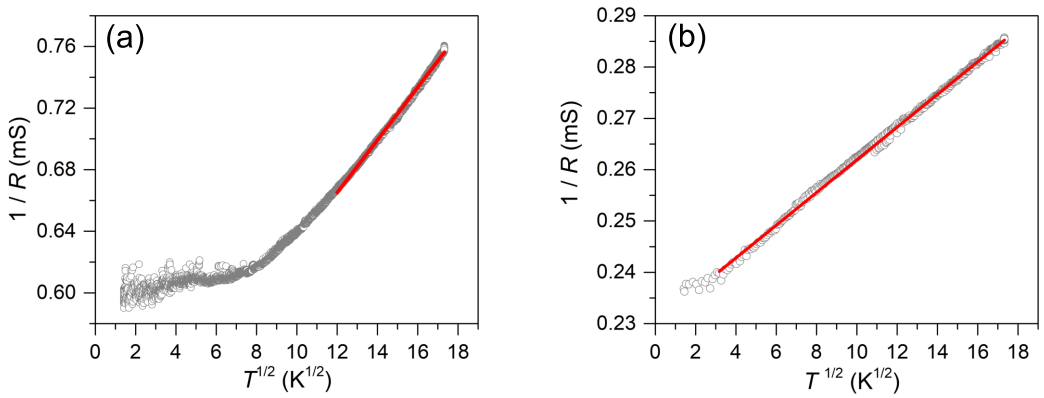

Figure A.1: Temperature dependence of the resistance in the LRS for the devices with the switching shown in Fig. 4.2(c) and (d), respectively in (a) and (b). The data is shown in the linearized plot to observe the linear behaviour of the conductance with $\sqrt{T}$. The red lines show a linear fit to the data.

be seen in the linearized plots shown in Fig. A.2(c-d) and (f-g). The difference in the absolute values of the resistivity can stem from small variations of the exact composition of the films. This is probably due to the not exact repeatability of the sputtering processes at room temperature. This clearly shows that the electrical transport properties of the TaO_x samples with $x \sim 1$ shown in the main text is representative of the behaviour of different samples with approximately the same composition.

In terms of magnetoresistance and Hall data, the trend is similar to the one observed for the resistivity. All the sputtered TaO_x samples with $x \sim 1$ show the same characteristic magnetotransport, with positive magnetoresistance that can be explained by weak antilocalization, and the high values of the Hall carrier concentration. As an example, Fig. A.3 shows the magnetoresistance and Hall data for the sample with the resistivity shown in Fig. A.2(b). Once more, the absolute values, in this case of the MR and the Hall data, show a deviation from the ones obtained for the sample highlighted in the main text. This variation is probably due to the same reasons discussed above for the case of the resistivity.

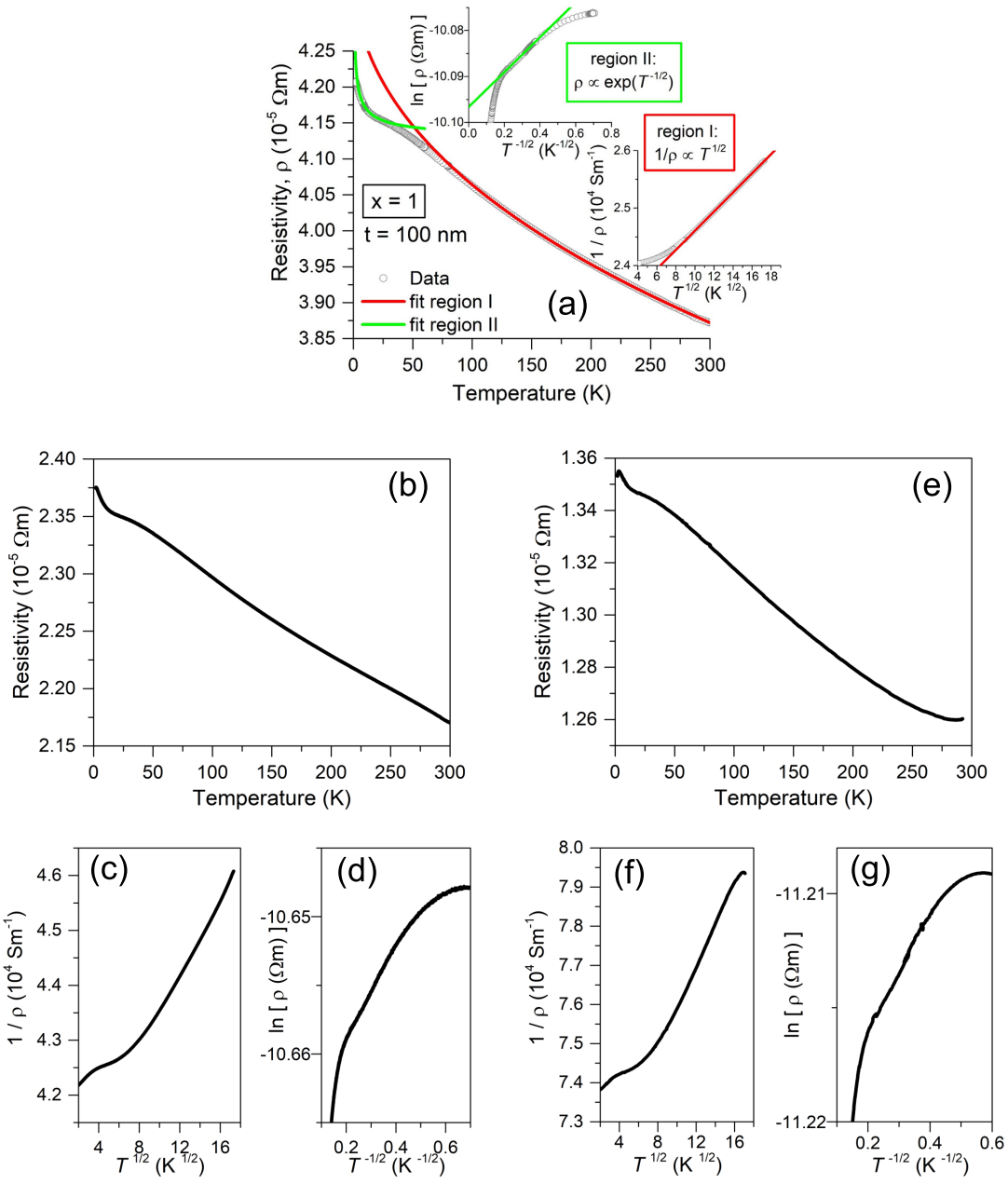

Figure A.2: (a) Temperature dependence of the resistivity for a TaOx film with $x \sim 1$ and a thickness of 100 nm. The insets show the fitting to the two regions mentioned in the main text. (b) and (e) show the temperature dependence of the resistivity for different TaO_x vdP structures obtained with the process for $x \sim 1$, deposited at different times and with different thicknesses (approximately 50 nm for (b) and 20 nm for (e)). (c-d) and (f-g) show plots of the data in the axis used for the fitting procedures mentioned in the text.

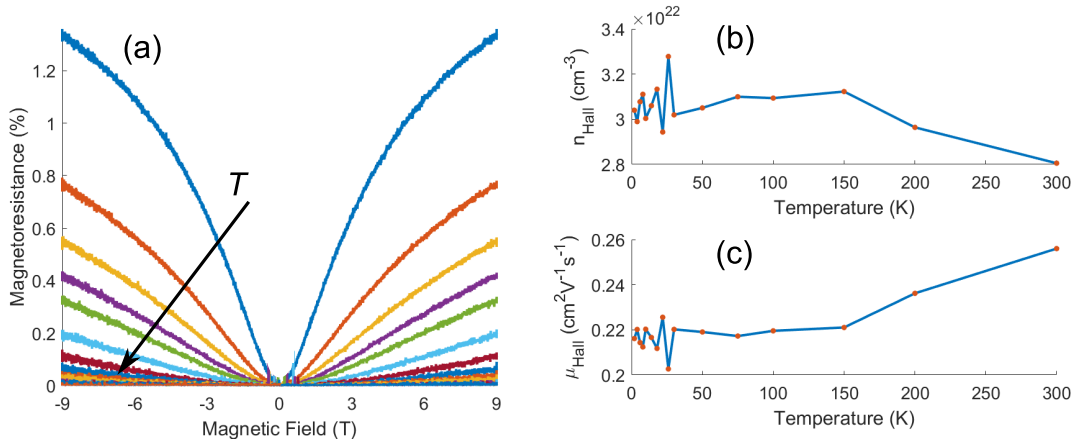

Figure A.3: Magnetoresistance and Hall data for the sample with the resistivity shown in Fig. A.2(b): (a) Magnetoresistance as a function of the externally applied magnetic field for different temperatures from 1.8 K up to 30 K. (b) Hall carrier concentration as a function of the temperature. (c) Hall mobility as a function of the temperature.

Appendix B

Numerical method to calculate the reduced activation energy

The reduced activation energy is defined as [220]:

$$w = \frac{d \ln \sigma}{d \ln T} = -\frac{d \ln \rho}{d \ln T} \tag{B.1}$$

The numerical differentiation needed to calculate w from the measured temperature dependence resistivity data enhances the noise of the measurement, and thus can be problematic. To minimize this problem, a centred moving average with an odd number of points n was applied to the resistivity data, and then the reduced activation energy was obtained by calculating the divided differences between adjacent points after the averaging procedure. n varied between 10 and 15 for the used data. An additional moving average filtering was used after the numerical differentiation, while keeping the same temperature dependence observed prior to the smoothing procedure in order to make the dependence clearer. An example of the effect of the smoothing procedure is shown in Fig. B.1, where the smoothed results are compared with the raw numerical differentiation data.

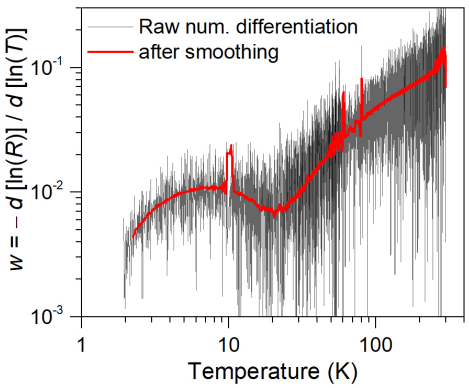

Figure B.1: Reduced activation energy for a TaO_x thin film with $x = 1$, exemplifying the need for a smoothing procedure to make the numerical differentiation results clearer.

Appendix C

Transport in Ta thin films: effect of film thickness and substrate

The different electrical properties, namely the temperature coefficient of the resistance (TCR), of the Ta thin films on top of SiO_2 and Ta_2O_5, motivated further studies. Therefore, Ta layers of different thickness were deposited on top of an insulating SiO_2/Si substrate and, simultaneously, Ta layers with the same thickness values were also deposited on top of 5 nm-thick Ta_2O_5 layer (itself deposited on top of the same insulating SiO_2/Si substrate mentioned before). The samples were structured in a Hall bar configuration, where for each 1 inch substrate, there were two Hall bars, one with the Ta_2O_5 additional layer, and one without, as can be seen in Fig. C.2. Through this method, the Ta layer is deposited at the same time for both cases, therefore allowing for a better comparison. All layers were capped by a 20 nm-thick Al_2O_3, to avoid oxidation of the Ta from the atmospheric exposure. For each sample, the resistance was measured in the temperature range between 230 K and 300 K. This allowed for the calculation of the resistivity and TCR for each sample. The thickness of the Ta films varied from 2 nm up to 100 nm, while the focus was on films with a lower thickness, closer to the thickness values employed in the ReRAM devices shown in this work. A calibration was routinely performed in order to tune the deposition parameters to achieve a desired thickness. Just like described before, in chapter 3, this calibration was achieved through XRR measurements to determine the deposition rate.

The experimental data for the resistivity and TCR of the Ta thin films is summarized in Fig. C.1. The room temperature resistivity decreases with increasing thickness up to approximately 20 nm, where it stabilizes and does not show significant changes for higher thickness values. This is observed for both substrates. However, by comparing the resistivity as a function of the film thickness for the two substrates, it can be seen that the rate of change is different. There is even a crossing at around 6 nm. Below that thickness the Ta films deposited on top of Ta_2O_5 show a higher resistivity, while for a higher thickness, the Ta films deposited directly on top of SiO_2 present a higher resistivity. Interestingly, the TCR shows a similar crossing at around the same thickness value of 4 nm. But the real difference is that the TCR for the films on top of SiO_2 is always negative, while for the case of the Ta_2O_5 substrate it starts being negative for lower thickness values but changes at around 7 nm to positive. After peaking at around 20 nm, the TCR starts dropping again as the thickness increases, even reaching a small negative value for a thickness of 100 nm. However, there is always a quite distinct value of the TCR between the two substrates after the crossing

thickness. This shows more clearly the differences in the TCR sign observed in chapters 4 and 5 for the Ta films deposited on SiO_2 and the ones deposited on top of Ta_2O_5/SiO_2.

Plotting the TCR as a function of the resistivity at $T = 293$ K in Fig. C.1(c), it is visible that there seems to be a correlation between the two values. As the resistivity increases, the TCR decreases, even changing sign. The resistivity value for which the TCR changes from negative to positive values is of approximately 150 $\mu\Omega$cm. As seen in chapter 2, this corresponds to the resistivity value defined by Mooij for the change of the TCR sign in disordered metallic alloys [136]. This is another indication that the transport in the deposited Ta thin films is strikingly similar to the one observed in disordered metals.

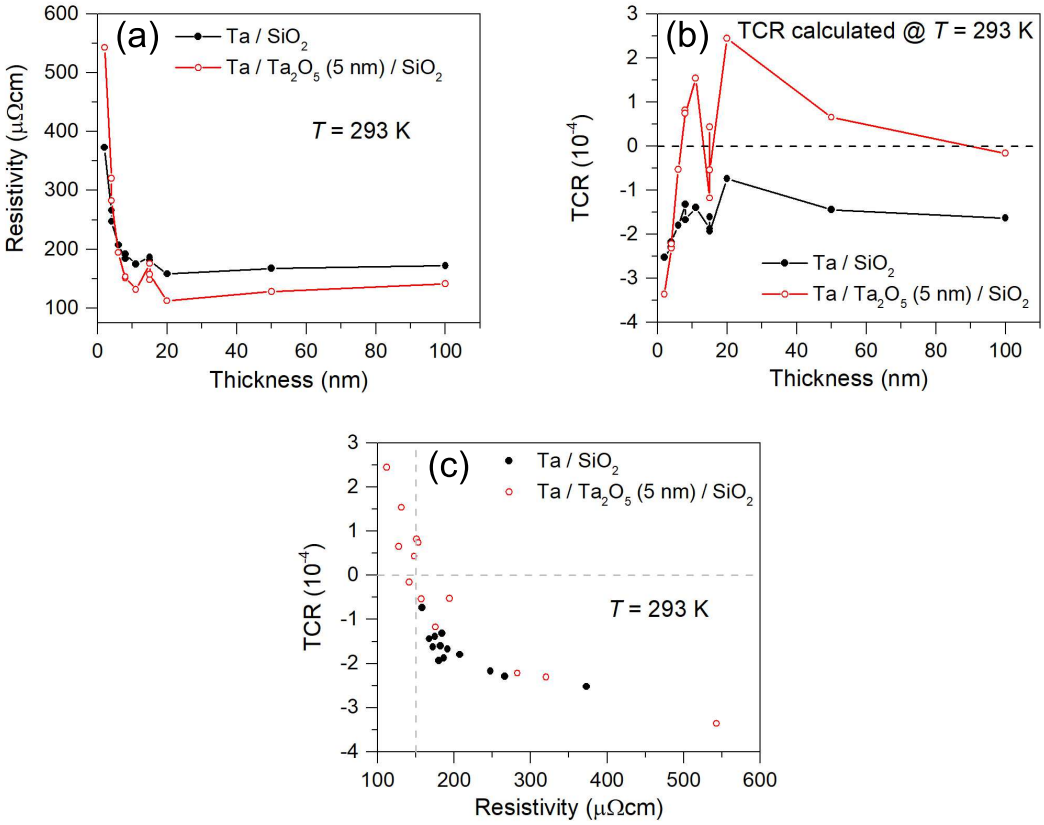

Figure C.1: (a) Resistivity of the Ta thin films as a function of the film thickness. The black symbols indicate the data for the Ta films grown on top of the SiO_2 substrate, while the red symbols represent the data obtained for the Ta films grown on top of the 5 nm-thick Ta_2O_5 layer. The lines are connecting the experimental data points and serve as a visual guide of the data trend. (b) Temperature coefficient of the resistance (TCR) of the Ta films as a function of the film thickness. (c) TCR as a function of the resistivity for the data shown in (a) and (b). The horizontal dashed line indicates the zero TCR value, while the vertical dashed line indicates the limit of the Mooijs rule of 150 $\mu\Omega$cm.

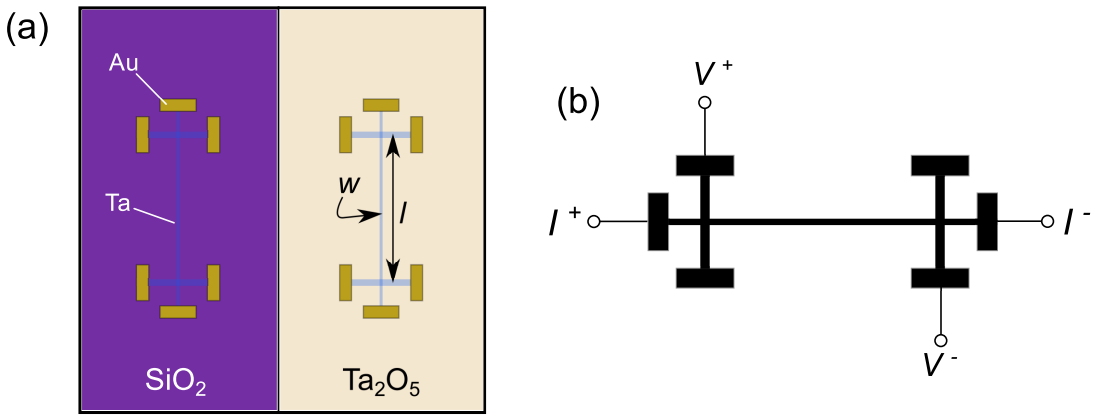

Figure C.2: (a) Illustration of the sample layout, with the sample divided in two areas, one where there is only the SiO_2 layer underneath the Hall bar structure, and another where there is an additional Ta_2O_5 layer on top of SiO_2. The Ta is represented in light blue, while the electrodes are composed of Au. (b) Scheme of the Hall bar with the indication of the electrical contacting configuration, where four electrical contacts were used. The current is sourced and the voltage is measured.

Bibliography

[1] R. Waser and M. Aono. "Nanoionics-based resistive switching memories". *Nature Materials* **6**(11): 833–40, 2007.

[2] R. Waser, R. Bruchhaus, and S. Menzel. "Redox-based resistive switching memories". *Nanoelectronics and Information Technology*. Ed. by R. Waser. 3rd ed. Weinheim: Wiley-VCH, 2012. Chap. 30, pp. 685–710.

[3] E. Linn, R. Rosezin, C. Kügeler, and R. Waser. "Complementary resistive switches for passive nanocrossbar memories". *Nature materials* **9**(5): 403–406, 2010.

[4] F. Nardi, S. Balatti, S. Larentis, and D. Ielmini. "Complementary switching in metal oxides: Toward diode-less crossbar RRAMs". *2011 IEEE International Electron Devices Meeting (IEDM) Technical Digest*, 709–712, 2011.

[5] F. Nardi, S. Balatti, S. Larentis, D. C. Gilmer, and D. Ielmini. "Complementary switching in oxide-based bipolar resistive-switching random memory". *IEEE Transactions on Electron Devices* **60**(1): 70–77, 2013.

[6] R. Waser, D. Ielmini, H. Akinaga, H. Shima, H.-S. Phillip Wong, J. J. Yang, and S. Yu. "Introduction to Nanoionic Elements for Information Technology". *Resistive Switching*. Ed. by D. Ielmini and R. Waser. Weinheim: Wiley-VCH Verlag, 2016. Chap. 1, pp. 1–29.

[7] T. W. Hickmott. "Low Frequency Negative Resistance in Thin Anodic Oxide Films". *Journal of Applied Physics* **33**(9): 2669–2682, 1962.

[8] N. M. Bashara and P. H. Nielsen. "Memory effects in thin film negative resistance structures". *Annual Report 1963 Conference on Electrical Insulation*. White Sulphur Springs, WV, 1963, pp. 29–32.

[9] P. Nielsen and N. Bashara. "The reversible voltage-induced initial resistance in the negative resistance sandwich structure". *IEEE Transactions on Electron Devices* **11**(5): 243–244, 1964.

[10] J. Gibbons and W. Beadle. "Switching properties of thin Nio films". *Solid-State Electronics* **7**(11): 785–790, 1964.

[11] J. Simmons and R. Verderber. "New thin-film resistive memory". *Radio and Electronic Engineer* **34**(2): 81–89, 1967.

[12] A. Asamitsu, Y. Tomioka, H. Kuwahara, and Y. Tokura. "Current switching of resistive states in magnetoresistive manganites". *Nature* **388**(6637): 50–52, 1997.

[13] A. Beck, J. G. Bednorz, C. Gerber, C. Rossel, and D. Widmer. "Reproducible switching effect in thin oxide films for memory applications". *Applied Physics Letters* **77**(1): 139–141, 2000.

[14] W. Zhuang, W. Pan, B. Ulrich, J. Lee, L. Stecker, A. Burmaster, D. Evans, S. Hsu, M. Tajiri, A. Shimaoka, K. Inoue, T. Naka, N. Awaya, A. Sakiyama, Y. Wang, S. Liu, N. Wu, and A. Ignatiev. "Novel colossal magnetoresistive thin film nonvolatile resistance random access memory (RRAM)". *2002 IEEE International Electron Devices Meeting (IEDM) Technical Digest*, 193–196, 2002.

[15] I. Baek, M. Lee, S. Sco, M. Lee, D. Seo, D.-S. Suh, J. Park, S. Park, H. Kim, I. Yoo, U.-I. Chung, and J. Moon. "Highly scalable non-volatile resistive memory using simple binary oxide driven by asymmetric unipolar voltage pulses". *2004 IEEE International Electron Devices Meeting (IEDM) Technical Digest*, 587–590, 2004.

[16] D. B. Strukov, G. S. Snider, D. R. Stewart, and R. S. Williams. "The missing memristor found". *Nature* **453**(7191): 80–83, 2008.

[17] L. Chua. "Memristor - The missing circuit element". *IEEE Transactions on Circuit Theory* **CT-18**(5): 507–519, 1971.

[18] M. Di Ventra, Y. V. Pershin, and L. O. Chua. "Circuit Elements With Memory : Memristors, Memcapacitors and Meminductors". *Proceedings of the IEEE* **97**(10): 1717–1724, 2009.

[19] L. O. Chua and S. M. Kang. "Memristive Devices and Systems". *Proceedings of the IEEE* **64**(2): 209–223, 1976.

[20] L. Chua. "Resistance switching memories are memristors". *Applied Physics A* **102**(4): 765–783, 2011.

[21] D. S. Jeong, R. Thomas, R. S. Katiyar, J. F. Scott, H. Kohlstedt, A. Petraru, and C. S. Hwang. "Emerging memories: resistive switching mechanisms and current status". *Reports on Progress in Physics* **75**(7): 076502, 2012.

[22] S. Vongehr and X. Meng. "The missing memristor has not been found". *Scientific Reports* **5**, 11657, 2015.

[23] D. S. Shang, Y. S. Chai, Z. X. Cao, J. Lu, and Y. Sun. "Toward the complete relational graph of fundamental circuit elements". *Chinese Physics B* **24**(6): 068402, 2015.

[24] J. Shen, J. Cong, Y. Chai, D. Shang, S. Shen, K. Zhai, Y. Tian, and Y. Sun. "Nonvolatile Memory Based on Nonlinear Magnetoelectric Effects". *Physical Review Applied* **6**(2): 021001, 2016.

[25] F. Corinto, P. P. Civalleri, and L. O. Chua. "A complete classification of memristor devices". *2015 European Conference on Circuit Theory and Design (ECCTD 2015)*. Trondheim: IEEE, 2015.

[26] R. Waser, R. Dittmann, S. Menzel, and T. Noll. "Introduction to new memory paradigms: Memristive phenomena and neuromorphic applications". *Faraday Discussions* **213**, 11–27, 2019.

[27] S. Menzel, M. Waters, A. Marchewka, U. Böttger, R. Dittmann, and R. Waser. "Origin of the Ultra-nonlinear Switching Kinetics in Oxide-Based Resistive Switches". *Advanced Functional Materials* **21**(23): 4487–4492, 2011.

[28] R. Waser, R. Dittmann, G. Staikov, and K. Szot. "Redox-Based Resistive Switching Memories - Nanoionic Mechanisms, Prospects, and Challenges". *Advanced Materials* **21**(25-26): 2632–2663, 2009.

[29] A. Chen. “Electronic Effect Resistive Switching Memories”. *Emerging Nanoelectronic Devices*. Ed. by A. Chen, J. Hutchby, V. Zhirnov, and G. Bourianoff. Chichester, West Sussex: John Wiley & Sons, Ltd, 2015. Chap. 9, pp. 162–180.

[30] A. B. Chen, S. G. Kim, Y. Wang, W. S. Tung, and I. W. Chen. “A size-dependent nanoscale metal-insulator transition in random materials”. *Nature Nanotechnology* **6**(4): 237–241, 2011.

[31] B. J. Choi, A. B. Chen, X. Yang, and I. W. Chen. “Purely electronic switching with high uniformity, resistance tunability, and good retention in Pt-dispersed SiO2 thin films for ReRAM”. *Advanced Materials* **23**(33): 3847–3852, 2011.

[32] Y. Lu, A. Alvarez, C.-H. Kao, J.-S. Bow, S.-Y. Chen, and I.-W. Chen. “An electronic silicon-based memristor with a high switching uniformity”. *Nature Electronics* **2**(February): 66–74, 2019.

[33] J. A. Rupp, M. Querré, A. Kindsmüller, M. P. Besland, E. Janod, R. Dittmann, R. Waser, and D. J. Wouters. “Different threshold and bipolar resistive switching mechanisms in reactively sputtered amorphous undoped and Cr-doped vanadium oxide thin films”. *Journal of Applied Physics* **123**(4): 044502, 2018.

[34] S. Kumar, J. P. Strachan, and R. S. Williams. “Chaotic dynamics in nanoscale NbO2 Mott memristors for analogue computing”. *Nature* **548**(7667): 318–321, 2017.

[35] D. Ielmini, R. Bruchhaus, and R. Waser. “Thermochemical resistive switching: materials, mechanisms, and scaling projections”. *Phase Transitions* **84**(7): 570–602, 2011.

[36] D. J. Wouters, R. Waser, and M. Wuttig. “Phase-Change and Redox-Based Resistive Switching Memories”. *Proceedings of the IEEE* **103**(8): 1274–1288, 2015.

[37] S. Menzel, E. Linn, and R. Waser. “Redox-based Resistive Memory”. *Emerging Nanoelectronic Devices*. Ed. by A. Chen, J. Hutchby, V. Zhirnov, and G. Bourianoff. Chichester, West Sussex: Wiley, 2015. Chap. 8, pp. 137–161.

[38] D.-H. Kwon, K. M. Kim, J. H. Jang, J. M. Jeon, M. H. Lee, G. H. Kim, X.-S. Li, G.-S. Park, B. Lee, S. Han, M. Kim, and C. S. Hwang. “Atomic structure of conducting nanofilaments in TiO_2 resistive switching memory”. *Nature Nanotechnology* **5**, 148–153, 2010.

[39] I. Valov, R. Waser, J. R. Jameson, and M. N. Kozicki. “Electrochemical metallization memories - fundamentals, applications, prospects”. *Nanotechnology* **22**(25): 254003, 2011.

[40] A. Wedig, M. Luebben, D. Y. Cho, M. Moors, K. Skaja, V. Rana, T. Hasegawa, K. K. Adepalli, B. Yildiz, R. Waser, and I. Valov. “Nanoscale cation motion in TaO_x, HfO_x and TiO_x memristive systems”. *Nature Nanotechnology* **11**(1): 67–74, 2016.

[41] D. M. Smyth. *The defect chemistry of metal oxides*. New York: Oxford University Press, 2000.

[42] G. I. Meijer, U. Staub, M. Janousch, S. L. Johnson, B. Delley, and T. Neisius. “Valence states of Cr and the insulator-to-metal transition in Cr-doped $SrTiO_3$”. *Physical Review B* **72**(15): 155102, 2005.

[43] C. Baeumer, C. Schmitz, A. H. Ramadan, H. Du, K. Skaja, V. Feyer, P. Muller, B. Arndt, C. L. Jia, J. Mayer, R. A. De Souza, C. Michael Schneider, R. Waser, and R. Dittmann. "Spectromicroscopic insights for rational design of redox-based memristive devices". *Nature Communications* **6**, 8610, 2015.

[44] K. Skaja, C. Bäumer, O. Peters, S. Menzel, M. Moors, H. Du, M. Bornhöfft, C. Schmitz, V. Feyer, C. L. Jia, C. M. Schneider, J. Mayer, R. Waser, and R. Dittmann. "Avalanche-Discharge-Induced Electrical Forming in Tantalum Oxide-Based Metal-Insulator-Metal Structures". *Advanced Functional Materials* **25**(46): 7154–7162, 2015.

[45] J. P. Strachan, G. Medeiros-Ribeiro, J. J. Yang, M. X. Zhang, F. Miao, I. Goldfarb, M. Holt, V. Rose, and R. S. Williams. "Spectromicroscopy of tantalum oxide memristors". *Applied Physics Letters* **98**(24): 242114, 2011.

[46] F. Miao, J. P. Strachan, J. J. Yang, M.-X. Zhang, I. Goldfarb, A. C. Torrezan, P. Eschbach, R. D. Kelley, G. Medeiros-Ribeiro, and R. S. Williams. "Anatomy of a nanoscale conduction channel reveals the mechanism of a high-performance memristor." *Advanced Materials* **23**(47): 5633–40, 2011.

[47] U. Celano, L. Goux, R. Degraeve, A. Fantini, O. Richard, H. Bender, M. Jurczak, and W. Vandervorst. "Imaging the three-dimensional conductive channel in filamentary-based oxide resistive switching memory". *Nano Letters* **15**(12): 7970–7975, 2015.

[48] Y. Ma, D. Li, A. A. Herzing, D. A. Cullen, B. T. Sneed, K. L. More, N. T. Nuhfer, J. A. Bain, and M. Skowronski. "Formation of the Conducting Filament in TaO_x-Resistive Switching Devices by Thermal-Gradient-Induced Cation Accumulation". *ACS Applied Materials & Interfaces* **10**(27): 23187–23197, 2018.

[49] Y. Ma, J. M. Goodwill, D. Li, D. A. Cullen, J. D. Poplawsky, K. L. More, J. A. Bain, and M. Skowronski. "Stable Metallic Enrichment in Conductive Filaments in TaO_x-Based Resistive Switches Arising from Competing Diffusive Fluxes". *Advanced Electronic Materials* **5**(7): 1800954, 2019.

[50] A. Sawa. "Resistive switching in transition metal oxides". *Materials Today* **11**(6): 28–36, 2008.

[51] A. Sawa, T. Fujii, M. Kawasaki, and Y. Tokura. "Interface resistance switching at a few nanometer thick perovskite manganite active layers". *Applied Physics Letters* **88**(23): 232112, 2006.

[52] C. Baeumer, T. Heisig, B. Arndt, K. Skaja, F. Borgatti, F. Offi, F. Motti, G. Panaccione, R. Waser, S. Menzel, and R. Dittmann. "Spectroscopic elucidation of ionic motion processes in tunnel oxide-based memristive devices". *Faraday Discussions* **213**, 215–230, 2019.

[53] R. Muenstermann, T. Menke, R. Dittmann, and R. Waser. "Coexistence of Filamentary and Homogeneous Resistive Switching in Fe-Doped $SrTiO_3$ Thin-Film Memristive Devices". *Advanced Materials* **22**(43): 4819–4822, 2010.

[54] K. Shibuya, R. Dittmann, S. Mi, and R. Waser. "Impact of Defect Distribution on Resistive Switching Characteristics of Sr_2TiO_4 Thin Films". *Advanced Materials* **22**(3): 411–414, 2010.

[55] A. Schoenhals, C. M. M. Rosário, S. Hoffmann-Eifert, R. Waser, S. Menzel, and D. J. Wouters. "Role of the Electrode Material on the RESET Limitation in Oxide ReRAM Devices". *Advanced Electronic Materials* **4**(2): 1700243, 2018.

[56] J. J. Yang, J. Borghetti, D. Murphy, D. R. Stewart, and R. S. Williams. "A Family of Electronically Reconfigurable Nanodevices". *Advanced Materials* **21**(37): 3754–3758, 2009.

[57] S. Stille, C. Lenser, R. Dittmann, A. Koehl, I. Krug, R. Muenstermann, J. Perlich, C. M. Schneider, U. Klemradt, and R. Waser. "Detection of filament formation in forming-free resistive switching $SrTiO_3$ devices with Ti top electrodes". *Applied Physics Letters* **100**(22): 223503, 2012.

[58] H. Zhang, S. Yoo, S. Menzel, C. Funck, F. Cueppers, D. J. Wouters, C. Seong Hwang, R. Waser, and S. Hoffmann-Eifert. "Understanding the Coexistence of Two Bipolar Resistive Switching Modes with Opposite Polarity in $Pt/TiO_2/Ti/Pt$ Nanosized ReRAM Devices". *ACS Applied Materials & Interfaces* **10**(35): 29766–29778, 2018.

[59] A. R. Genreith-Schriever and R. A. De Souza. "Field-enhanced ion transport in solids: Reexamination with molecular dynamics simulations". *Physical Review B* **94**(22): 224304, 2016.

[60] I. Valov. "Redox-Based Resistive Switching Memories (ReRAMs): Electrochemical Systems at the Atomic Scale". *ChemElectroChem* **1**(1): 26–36, 2014.

[61] K. Szot, M. Rogala, W. Speier, Z. Klusek, A. Besmehn, and R. Waser. "TiO_2–a prototypical memristive material". *Nanotechnology* **22**(25): 254001, 2011.

[62] K. Szot, W. Speier, G. Bihlmayer, and R. Waser. "Switching the electrical resistance of individual dislocations in single-crystalline $SrTiO_3$". *Nature Materials* **5**(4): 312–20, 2006.

[63] J. J. Yang, J. P. Strachan, F. Miao, M.-X. Zhang, M. D. Pickett, W. Yi, D. A. A. Ohlberg, G. Medeiros-Ribeiro, and R. S. Williams. "$Metal/TiO_2$ interfaces for memristive switches". *Applied Physics A* **102**(4): 785–789, 2011.

[64] A. Marchewka, R. Waser, and S. Menzel. "Physical simulation of dynamic resistive switching in metal oxides using a Schottky contact barrier model". *2015 International Conference on Simulation of Semiconductor Processes and Devices (SISPAD)*. Washington, D.C., 2015, pp. 297–300.

[65] A. Marchewka, B. Roesgen, K. Skaja, H. Du, C. L. Jia, J. Mayer, V. Rana, R. Waser, and S. Menzel. "Nanoionic Resistive Switching Memories: On the Physical Nature of the Dynamic Reset Process". *Advanced Electronic Materials* **2**(1): 1500233, 2016.

[66] E. Yalon, A. Gavrilov, S. Cohen, D. Mistele, B. Meyler, J. Salzman, and D. Ritter. "Resistive Switching in HfO_2 Probed by a Metal - Insulator - Semiconductor Bipolar Transistor". *IEEE Electron Device Letters* **33**(1): 11–13, 2012.

[67] E. Yalon, I. Riess, and D. Ritter. "Heat Dissipation in Resistive Switching Devices: Comparison of Thermal Simulations and Experimental Results". *IEEE Transactions on Electron Devices* **61**(4): 1137–1144, 2014.

[68] E. Yalon, A. A. Sharma, M. Skowronski, J. A. Bain, D. Ritter, and I. V. Karpov. "Thermometry of Filamentary RRAM Devices". *IEEE Transactions on Electron Devices* **62**(9): 2972–2977, 2015.

[69] J. Kwon, A. A. Sharma, C. Y. Chen, A. Fantini, M. Jurczak, A. A. Herzing, J. A. Bain, Y. N. Picard, and M. Skowronski. "Transient Thermometry and High-Resolution Transmission Electron Microscopy Analysis of Filamentary Resistive Switches". *ACS Applied Materials & Interfaces* **8**(31): 20176–20184, 2016.

[70] M. von Witzleben, K. Fleck, C. Funck, B. Baumkötter, M. Zuric, A. Idt, T. Breuer, R. Waser, U. Böttger, and S. Menzel. "Investigation of the Impact of High Temperatures on the Switching Kinetics of Redox-Based Resistive Switching Cells using a High-Speed Nanoheater". *Advanced Electronic Materials* **3**(12): 1700294, 2017.

[71] H. Schroeder, R. Pandian, and J. Miao. "Resistive switching and changes in microstructure". *Physica Status Solidi (a)* **208**(2): 300–316, 2011.

[72] C. Nauenheim, C. Kuegeler, A. Ruediger, and R. Waser. "Investigation of the electroforming process in resistively switching TiO_2 nanocrosspoint junctions". *Applied Physics Letters* **96**(12): 122902, 2010.

[73] W. Kim, S. Menzel, D. J. Wouter, Y. Guo, J. Robertson, B. Roesgen, R. Waser, and V. Rana. "Impact of oxygen exchange reaction at the ohmic interface in Ta_2O_5-based ReRAM devices". *Nanoscale* **8**(41): 17774–17781, 2016.

[74] J. P. Strachan, J. J. Yang, L. A. Montoro, C. A. Ospina, A. J. Ramirez, A. L. D. Kilcoyne, G. Medeiros-Ribeiro, and R. S. Williams. "Characterization of electroforming-free titanium dioxide memristors". *Beilstein Journal of Nanotechnology* **4**(1): 467–473, 2013.

[75] B. Govoreanu, G. S. Kar, Y. Y. Chen, V. Paraschiv, S. Kubicek, A. Fantini, I. P. Radu, L. Goux, S. Clima, R. Degraeve, N. Jossart, O. Richard, T. Vandeweyer, K. Seo, P. Hendrickx, G. Pourtois, H. Bender, L. Altimime, D. J. Wouters, J. A. Kittl, and M. Jurczak. "10x10 nm^2 Hf/HfO_x crossbar resistive RAM with excellent performance, reliability and low-energy operation". *2011 IEEE International Electron Devices Meeting (IEDM) Technical Digest*, 729–732, 2011.

[76] W. Kim, A. Hardtdegen, C. Rodenbuecher, S. Menzel, D. J. Wouters, S. Hoffmann-Eifert, D. Buca, R. Waser, and V. Rana. "Forming-free metal-oxide ReRAM by oxygen ion implantation process". *2017 IEEE International Electron Devices Meeting (IEDM) Technical Digest* **5**, 91–94, 2017.

[77] J. L. Pacheco, D. L. Perry, D. R. Hughart, M. Marinella, and E. Bielejec. "Electroforming-free TaO_x memristors using focused ion beam irradiations". *Applied Physics A* **124**(9): 626, 2018.

[78] J. J. Yang, M.-X. Zhang, J. P. Strachan, F. Miao, M. D. Pickett, R. D. Kelley, G. Medeiros-Ribeiro, and R. S. Williams. "High switching endurance in TaO_x memristive devices". *Applied Physics Letters* **97**(23): 232102, 2010.

[79] I. Goldfarb, F. Miao, J. J. Yang, W. Yi, J. P. Strachan, M. X. Zhang, M. D. Pickett, G. Medeiros-Ribeiro, and R. S. Williams. "Electronic structure and transport measurements of amorphous transition-metal oxides: Observation of Fermi glass behavior". *Applied Physics A: Materials Science and Processing* **107**(1): 1–11, 2012.

[80] Z. Wei, Y. Kanzawa, K. Arita, Y. Katoh, K. Kawai, S. Muraoka, S. Mitani, S. Fujii, K. Katayama, M. Iijima, T. Mikawa, T. Ninomiya, R. Miyanaga, Y. Kawashima, K. Tsuji, A. Himeno, T. Okada, R. Azuma, K. Shimakawa, H. Sugaya, T. Takagi, R. Yasuhara, K. Horiba, H. Kumigashira, and M. Oshima. "Highly reliable TaO_x ReRAM and direct evidence of redox reaction mechanism". *2008 IEEE International Electron Devices Meeting (IEDM) Technical Digest*, 293–296, 2008.

[81] M.-J. Lee, C. B. Lee, D. Lee, S. R. Lee, M. Chang, J. H. Hur, Y.-B. Kim, C.-J. Kim, D. H. Seo, S. Seo, U.-I. Chung, I.-K. Yoo, and K. Kim. "A fast, high-endurance and scalable non-volatile memory device made from asymmetric Ta_2O_{5-x}/TaO_{2-x} bilayer structures". *Nature Materials* **10**(8): 625–630, 2011.

[82] Y. Guo and J. Robertson. "Materials selection for oxide-based resistive random access memories". *Applied Physics Letters* **105**(22): 223516, 2014.

[83] A. C. Torrezan, J. P. Strachan, G. Medeiros-Ribeiro, and R. S. Williams. "Sub-nanosecond switching of a tantalum oxide memristor". *Nanotechnology* **22**(48): 485203, 2011.

[84] *Panasonic Starts World's First Mass Production of ReRAM Mounted Microcomputers*. 2013. URL: `http://news.panasonic.com/press/news/official.data/data.dir/2013/07/en130730-2/en130730-2.html` (visited on 06/15/2015).

[85] A. Kawahara, R. Azuma, Y. Ikeda, K. Kawai, Y. Katoh, Y. Hayakawa, K. Tsuji, S. Yoneda, A. Himeno, K. Shimakawa, T. Takagi, and T. Mikawa. "An 8 Mb Multi-Layered Cross-Point ReRAM Macro With 443 MB / s Write Throughput". *IEEE Journal of Solid-State Circuits* **48**(1): 178–185, 2013.

[86] Y. Wang, Y. Yan, C. Wang, Y. Chen, J. Li, J. Zhao, and C. S. Hwang. "Controlling the thin interfacial buffer layer for improving the reliability of the $Ta/Ta_2O_5/Pt$ resistive switching memory". *Applied Physics Letters* **113**(7): 072902, 2018.

[87] N. Sedghi, H. Li, I. F. Brunell, K. Dawson, R. J. Potter, Y. Guo, J. T. Gibbon, V. R. Dhanak, W. D. Zhang, J. F. Zhang, J. Robertson, S. Hall, and P. R. Chalker. "The role of nitrogen doping in ALD Ta_2O_5 and its influence on multilevel cell switching in RRAM". *Applied Physics Letters* **110**(10): 102902, 2017.

[88] L. Goux, A. Fantini, Y. Y. Chen, A. Redolfi, R. Degraeve, and M. Jurczak. "Evidences of Electrode-Controlled Retention Properties in Ta_2O_5-Based Resistive-Switching Memory Cells". *ECS Solid State Letters* **3**(11): Q79–Q81, 2014.

[89] A. Schönhals, D. Wouters, A. Marchewka, T. Breuer, K. Skaja, V. Rana, S. Menzel, and R. Waser. "Critical ReRAM Stack Parameters Controlling Complimentary versus Bipolar Resistive Switching". *2015 IEEE 7th International Memory Workshop (IMW)*. Monterey, CA, 2015, pp. 1–4.

[90] F. Miao, W. Yi, I. Goldfarb, J. J. Yang, M. X. Zhang, M. D. Pickett, J. P. Strachan, G. Medeiros-Ribeiro, and R. S. Williams. "Continuous electrical tuning of the chemical composition of TaO_x-based memristors". *ACS Nano* **6**(3): 2312–2318, 2012.

[91] G. S. Park, Y. B. Kim, S. Y. Park, X. S. Li, S. Heo, M. J. Lee, M. Chang, J. H. Kwon, M. Kim, U. I. Chung, R. Dittmann, R. Waser, and K. Kim. "In situ observation of filamentary conducting channels in an asymmetric Ta_2O_{5-x}/TaO_{2-x} bilayer structure". *Nature Communications* **4**, 2382, 2013.

[92] S. Kim, S. Choi, and W. Lu. "Comprehensive physical model of dynamic resistive switching in an oxide memristor". *ACS Nano* **8**(3): 2369–2376, 2014.

[93] S. U. Sharath, M. J. Joseph, S. Vogel, E. Hildebrandt, P. Komissinskiy, J. Kurian, T. Schroeder, and L. Alff. "Impact of oxygen stoichiometry on electroforming and multiple switching modes in TiN/TaO_x/Pt based ReRAM". *Applied Physics Letters* **109**(17): 173503, 2016.

[94] C. E. Graves, N. Dávila, E. J. Merced-Grafals, S. T. Lam, J. P. Strachan, and R. S. Williams. "Temperature and field-dependent transport measurements in continuously tunable tantalum oxide memristors expose the dominant state variable". *Applied - Physics Letters* **110**(12): 123501, 2017.

[95] P. R. Mickel, A. J. Lohn, B. Joon Choi, J. Joshua Yang, M.-X. Zhang, M. J. Marinella, C. D. James, and R. Stanley Williams. "A physical model of switching dynamics in tantalum oxide memristive devices". *Applied Physics Letters* **102**(22): 223502, 2013.

[96] Y. Zhang, N. Deng, H. Wu, Z. Yu, J. Zhang, and H. Qian. "Metallic to hopping conduction transition in Ta_2O_{5-x}/TaO_y resistive switching device". *Applied Physics Letters* **105**(2014): 063508, 2014.

[97] R. M. Fleming, D. V. Lang, C. D. Jones, M. L. Steigerwald, D. W. Murphy, G. B. Alers, Y. H. Wong, R. B. Van Dover, J. R. Kwo, and A. M. Sergent. "Defect dominated charge transport in amorphous Ta_2O_5 thin films". *Journal of Applied Physics* **88**(2): 850–862, 2000.

[98] V. A. Gritsenko, T. V. Perevalov, V. A. Voronkovskii, A. A. Gismatulin, V. N. Kruchinin, V. S. Aliev, V. A. Pustovarov, I. P. Prosvirin, and Y. Roizin. "Charge Transport and the Nature of Traps in Oxygen Deficient Tantalum Oxide". *ACS Applied Materials and Interfaces* **10**(4): 3769–3775, 2018.

[99] T. Perevalov, V. Gritsenko, A. Gismatulin, V. Voronkovskii, A. Gerasimova, V. Aliev, and I. Prosvirin. "Electronic structure and charge transport in nonstoichiometric tantalum oxide". *Nanotechnology* **29**(26): 264001, 2018.

[100] I. Goldfarb and R. S. Williams. "Conduction centers in a Ta_2O_5-δ Fermi glass". *Applied Physics A* **114**(2): 287–289, 2014.

[101] G. E. Moore. "Cramming More Components onto Integrated Circuits". *Proceedings of the IEEE* **86**(1): 82–85, 1998.

[102] M. M. Waldrop. "More than moore". *Nature* **530**, 144–147, 2016.

[103] R. H. Dennard, F. H. Gaensslen, V. L. Rideout, E. Bassous, and A. R. LeBlanc. "Design of ion-implanted MOSFET's with very small physical dimensions". *IEEE Journal of Solid-State Circuits* **9**(5): 256–268, 1974.

[104] I. L. Markov. "Limits on fundamental limits to computation". *Nature* **512**(7513): 147–154, 2014.

[105] S. Adee. *Memristor Inside: HP partners with Hynix to commercialize memristors in an all-purpose memory.* 2010. URL: `http://spectrum.ieee.org/semiconductors/devices/memristor-inside` (visited on 08/29/2019).

[106] R. Waser. "Redox-Based Resistive Switching Memories". *Journal of Nanoscience and Nanotechnology* **12**(10): 7628–7640, 2012.

[107] D. Ielmini. “Resistive switching memories based on metal oxides: mechanisms, reliability and scaling”. *Semiconductor Science and Technology* **31**(6): 63002, 2016.

[108] C. Monzio Compagnoni, A. Goda, A. S. Spinelli, P. Feeley, A. L. Lacaita, and A. Visconti. “Reviewing the Evolution of the NAND Flash Technology”. *Proceedings of the IEEE* **105**(9): 1609–1633, 2017.

[109] G. W. Burr, B. N. Kurdi, J. C. Scott, C. H. Lam, K. Gopalakrishnan, and R. S. Shenoy. “Overview of candidate device technologies for storage-class memory”. *IBM Journal of Research and Development* **52**(4/5): 449–464, 2008.

[110] R. Carboni and D. Ielmini. “Stochastic Memory Devices for Security and Computing”. *Advanced Electronic Materials* **5**(9): 1900198, 2019.

[111] M. J. Miller. *Storage Class Memory: The Coming Revolution*. 2016. URL: `https://forwardthinking.pcmag.com/hard-drives/346999-storage-class-memory-the-coming-revolution` (visited on 05/23/2019).

[112] Intel Corporation. *Intel Optane Technology*. 2017. URL: `https://www.intel.com/content/www/us/en/architecture-and-technology/intel-optane-technology.html` (visited on 08/29/2019).

[113] M. Technology. *3D XPoint Technology*. URL: `https://www.micron.com/products/advanced-solutions/3d-xpoint-technology` (visited on 08/29/2019).

[114] J. J. Yang, D. B. Strukov, and D. R. Stewart. “Memristive devices for computing.” *Nature Nanotechnology* **8**(1): 13–24, 2013.

[115] W.-S. Khwa, D. Lu, C.-M. Dou, and M.-F. Chang. “Emerging NVM Circuit Techniques and Implementations for Energy-Efficient Systems”. *Beyond-CMOS Technologies for Next Generation Computer Design*. Ed. by R. O. Topaloglu and H.-S. Philip Wong. Cham: Springer, 2019. Chap. 4, pp. 85–132.

[116] S. Tanakamaru and K. Takeuchi. “A 0.5 V Operation V_{TH} Loss Compensated DRAM Word-Line Booster Circuit for Ultra-Low Power VLSI Systems”. *IEEE Journal of Solid-State Circuits* **46**(10): 2406–2415, 2011.

[117] J. S. Meena, S. M. Sze, U. Chand, and T.-Y. Tseng. “Overview of emerging nonvolatile memory technologies”. *Nanoscale Research Letters* **9**, 526, 2014.

[118] J. von Neumann. “First draft of a report on the EDVAC”. *IEEE Annals of the History of Computing* **15**(4): 27–75, 1993.

[119] D. S. Jeong, K. M. Kim, S. Kim, B. J. Choi, and C. S. Hwang. “Memristors for Energy-Efficient New Computing Paradigms”. *Advanced Electronic Materials* **2**(9): 1600090, 2016.

[120] D. Ferrucci, E. Brown, J. Chu-Carroll, J. Fan, D. Gondek, A. A. Kalyanpur, A. Lally, J. W. Murdock, E. Nyberg, J. Prager, N. Schlaefer, and C. Welty. “Building watson: An overview of the deepQA project”. *AI Magazine* **31**(3): 59–79, 2011.

[121] D. Ferrucci, A. Levas, S. Bagchi, D. Gondek, and E. T. Mueller. “Watson: Beyond jeopardy!” *Artificial Intelligence* **199-200**, 93–105, 2013.

[122] D. Silver, A. Huang, C. J. Maddison, A. Guez, L. Sifre, G. van den Driessche, J. Schrittwieser, I. Antonoglou, V. Panneershelvam, M. Lanctot, S. Dieleman, D. Grewe, J. Nham, N. Kalchbrenner, I. Sutskever, T. Lillicrap, M. Leach, K. Kavukcuoglu, T. Graepel, and D. Hassabis. "Mastering the game of Go with deep neural networks and tree search". *Nature* **529**, 484–489, 2016.

[123] D. Silver, J. Schrittwieser, K. Simonyan, I. Antonoglou, A. Huang, A. Guez, T. Hubert, L. Baker, M. Lai, A. Bolton, Y. Chen, T. Lillicrap, F. Hui, L. Sifre, G. van den Driessche, T. Graepel, and D. Hassabis. "Mastering the game of Go without human knowledge". *Nature* **550**(7676): 354–359, 2017.

[124] S. H. Jo, T. Chang, I. Ebong, B. B. Bhadviya, P. Mazumder, and W. Lu. "Nanoscale memristor device as synapse in neuromorphic systems". *Nano Letters* **10**(4): 1297–1301, 2010.

[125] N. K. Upadhyay, H. Jiang, Z. Wang, S. Asapu, Q. Xia, and J. J. Yang. "Emerging Memory Devices for Neuromorphic Computing". *Advanced Materials Technologies* **4**(4): 1800589, 2019.

[126] Y. Kim, W. H. Jeong, S. B. Tran, H. C. Woo, J. Kim, C. S. Hwang, K.-S. Min, and B. J. Choi. "Memristor crossbar array for binarized neural networks". *AIP Advances* **9**(4): 045131, 2019.

[127] G. W. Burr, R. M. Shelby, A. Sebastian, S. Kim, S. Kim, S. Sidler, K. Virwani, M. Ishii, P. Narayanan, A. Fumarola, L. L. Sanches, I. Boybat, M. Le Gallo, K. Moon, J. Woo, H. Hwang, and Y. Leblebici. "Neuromorphic computing using non-volatile memory". *Advances in Physics: X* **2**(1): 89–124, 2017.

[128] Q. Xia and J. J. Yang. "Memristive crossbar arrays for brain-inspired computing". *Nature Materials* **18**(April): 309–323, 2019.

[129] A. Siemon, T. Breuer, N. Aslam, S. Ferch, W. Kim, J. Van Den Hurk, V. Rana, S. Hoffmann-Eifert, R. Waser, S. Menzel, and E. Linn. "Realization of Boolean Logic Functionality Using Redox-Based Memristive Devices". *Advanced Functional Materials* **25**(40): 6414–6423, 2015.

[130] W. Kim, A. Chattopadhyay, A. Siemon, E. Linn, R. Waser, and V. Rana. "Multistate Memristive Tantalum Oxide Devices for Ternary Arithmetic". *Scientific Reports* **6**, 36652, 2016.

[131] S. Pi, M. Ghadiri-Sadrabadi, J. C. Bardin, and Q. Xia. "Nanoscale memristive radiofrequency switches". *Nature Communications* **6**(May): 7519, 2015.

[132] N. Wainstein and S. Kvatinsky. "A Lumped RF Model for Nanoscale Memristive Devices and Nonvolatile Single-Pole Double-Throw Switches". *IEEE Transactions on Nanotechnology* **17**(5): 873–883, 2018.

[133] M. Wuttig. "Electron Transport: Disorder and Correlations". *Memristive Phenomena - From Fundamental Physics to Neuromorphic Computing (Lecture Notes of the 47th IFF Spring School 2016)*. Ed. by R. Waser and M. Wuttig. Jülich: Forschungszentrum Jülich GmbH, 2016. Chap. A7, pp. 209–253.

[134] H. Ibach and H. Lüth. *Solid-State Physics: An introduction to Principles of Materials Science*. 2nd ed. Berlin Heidelberg: Springer-Verlag, 1995.

[135] V. F. Gantmakher. *Electrons and Disorder in Solids*. 1st ed. New York: Oxford University Press, 2005.

[136] J. H. Mooij. "Electrical conduction in concentrated disordered transition metal alloys". *Physica Status Solidi (a)* **17**(2): 521–530, 1973.

[137] G. Bergmann. "Physical interpretation of weak localization: A time-of-flight experiment with conduction electrons". *Physical Review B* **28**(6): 2914–2920, 1983.

[138] P. A. Lee and T. V. Ramakrishnan. "Disordered electronic systems". *Reviews of Modern Physics* **57**, 287–337, 1985.

[139] S. Hikami, A. I. Larkin, and Y. Nagaoka. "Spin-Orbit Interaction and Magnetoresistance in the Two Dimensional Random System". *Progress of Theoretical Physics* **63**(2): 707–710, 1980.

[140] B. A. Assaf, T. Cardinal, P. Wei, F. Katmis, J. S. Moodera, and D. Heiman. "Linear magnetoresistance in topological insulator thin films: Quantum phase coherence effects at high temperatures". *Applied Physics Letters* **102**(1): 012102, 2013.

[141] D. K. Schroder. *Semiconductor Material and Device Characterization*. Hoboken, New Jersey: John Wiley & Sons, 2006.

[142] J. C. Ousset, S. Askenazy, H. Rakoto, and J. M. Broto. "Analytic expressions of the magnetoresistance due to localization and electron-electron interaction effects. Application to the amorphous alloys La_3Al and La_3Ga". *Journal de Physique* **46**(12): 2145–2149, 1985.

[143] B. L. Altshuler and A. G. Aronov. "Zero bias anomaly in tunnel resistance and electron-electron interaction". *Solid State Communications* **30**, 115–117, 1979.

[144] M. A. Howson. "Incipient localisation and electron-electron correlation effects in metallic glass alloys". *Journal of Physics F: Metal Physics* **14**(3): L25–L31, 1984.

[145] M. A. Howson and D. Greig. "Temperature dependence of conductivity arising from electron-electron interaction effects in amorphous metals". *Physical Review B* **30**(8): 4805–4806, 1984.

[146] M. A. Howson and D. Greig. "Localisation and interaction effects in the temperature and magnetic field dependence of the resistivity of metallic glasses". *Journal of Physics F: Metal Physics* **16**, 989–1004, 1986.

[147] B. Raquet, M. Goiran, N. Nègre, J. Léotin, B. Aronzon, V. Rylkov, and E. Meilikhov. "Quantum size effect transition in percolating nanocomposite films". *Physical Review B* **62**(24): 17144–17150, 2000.

[148] N.F.Mott and E.A. Davis. *Electronic Processes in Non-Crystalline Materials*. 2nd. New York: Oxford University Press, 1979.

[149] A. L. Efros and B. I. Shklovskii. "Coulomb gap and low temperature conductivity of disordered systems". *Journal of Physics C: Solid State Physics* **8**, L49–L51, 1975.

[150] I. S. Beloborodov, A. V. Lopatin, V. M. Vinokur, and K. B. Efetov. "Granular electronic systems". *Reviews of Modern Physics* **79**(2): 469–518, 2007.

[151] S. Kirkpatrick. "Percolation and Conduction". *Reviews of Modern Physics* **45**(4): 574–588, 1973.

[152] B. A. Aronzon, S. V. Kapelnitsky, and A. S. Lagutin. “Transport and Magnetic Properties of Nanogranular Metals”. *Physico-Chemical Phenomena in Thin Films and at Solid Surfaces - Thin Films and Nanostructures vol. 34*. Ed. by L. I. Trakhtenberg, S. H. Lin, and O. J. Ilegbusi. Amsterdam: 10.1016/S1079-4050(06)34011-2, 2007. Chap. 11, pp. 581–637.

[153] M. Huth, D. Klingenberger, C. Grimm, F. Porrati, and R. Sachser. “Conductance regimes of W-based granular metals prepared by electron beam induced deposition”. *New Journal of Physics* **11**, 033032, 2009.

[154] M. V. Feigel’man and A. S. Ioselevich. “Variable-range cotunneling and conductivity of a granular metal”. *Journal of Experimental and Theoretical Physics Letters* **81**(6): 277–283, 2005.

[155] A. Carl, G. Dumpich, and E. F. Wassermann. “Significance of quantum size effects in the conductivity of granular PdxC1-x films”. *Physical Review B* **50**(7): 4802–4810, 1994.

[156] S. P. Garg, N. Krishnamurthy, A. Awasthi, and M. Venkatraman. “The O-Ta (Oxygen-Tantalum) system”. *Journal of Phase Equilibria* **17**(1): 63–77, 1996.

[157] C. Chaneliere, J. L. Autran, R. A. Devine, and B. Balland. “Tantalum pentoxide (Ta_2O_5) thin films for advanced dielectric applications”. *Materials Science and Engineering R: Reports* **22**(6): 269–322, 1998.

[158] R. Hollerweger, D. Holec, J. Paulitsch, M. Bartosik, R. Daniel, R. Rachbauer, P. Polcik, J. Keckes, C. Krywka, H. Euchner, and P. H. Mayrhofer. “Complementary ab initio and X-ray nanodiffraction studies of Ta_2O_5”. *Acta Materialia* **83**, 276–284, 2015.

[159] C. Joseph, P. Bourson, and M. D. Fontana. “Amorphous to crystalline transformation in Ta_2O_5 studied by Raman spectroscopy”. *Journal of Raman Spectroscopy* **43**(8): 1146–1150, 2012.

[160] S. Ezhilvalavan and T. Y. Tseng. “Preparation and properties of Ta_2O_5 thin films for ultra large scale integrated circuits”. *Journal of Materials Science: Materials in Electronics* **10**, 9–31, 1999.

[161] V. A. Shvets, V. S. Aliev, D. V. Gritsenko, S. S. Shaimeev, E. V. Fedosenko, S. V. Rykhlitski, V. V. Atuchin, V. A. Gritsenko, V. M. Tapilin, and H. Wong. “Electronic structure and charge transport properties of amorphous Ta_2O_5 films”. *Journal of Non-Crystalline Solids* **354**(26): 3025–3033, 2008.

[162] G. Gregori. “Defect Structure of Metal Oxides”. *Resistive Switching*. Ed. by D. Ielmini and R. Waser. Weinheim: Wiley-VCH, 2016. Chap. 4, pp. 95–124.

[163] K. Skaja. “Redox processes and ionic transport in resistive switching binary metal oxides”. PhD thesis. RWTH Aachen University, 2016.

[164] U. N. Gries, H. Schraknepper, K. Skaja, and F. Gunkel. “A SIMS study of cation and anion diffusion in tantalum oxide”. *Physical Chemistry Chemical Physics* **20**, 989–996, 2018.

[165] J. J. Colin, G. Abadias, A. Michel, and C. Jaouen. “On the origin of the metastable β-Ta phase stabilization in tantalum sputtered thin films”. *Acta Materialia* **126**, 481–493, 2017.

[166] W. D. Westwood and N. Waterhouse. “Structural and electrical properties of tantalum films sputtered in oxygen-argon mixtures”. *Journal of Applied Physics* **42**(7): 2946–2952, 1971.

[167] C. F. Almeida Alves, C. Mansilla, L. Pereira, F. Paumier, T. Girardeau, and S. Carvalho. “Influence of magnetron sputtering conditions on the chemical bonding, structural, morphological and optical behavior of $Ta_{1-x}O_x$ coatings”. *Surface and Coatings Technology* **334**, 105–115, 2018.

[168] L. G. Feinstein and R. D. Huttemann. “Factors controlling the structure of sputtered Ta films”. *Thin Solid Films* **16**(2): 129–145, 1973.

[169] A. Javed and J. B. Sun. “An investigation of structural phase transformation and electrical resistivity in Ta films”. *Applied Surface Science* **257**(4): 1211–1215, 2010.

[170] D. Bernoulli, U. Mueller, M. Schwarzenberger, R. Hauert, and R. Spolenak. “Magnetron sputter deposited tantalum and tantalum nitride thin films: An analysis of phase, hardness and composition”. *Thin Solid Films* **548**, 157–161, 2013.

[171] M. Grosser and U. Schmid. “The impact of sputter conditions on the microstructure and on the resistivity of tantalum thin films”. *Thin Solid Films* **517**(16): 4493–4496, 2009.

[172] R. Knepper, B. Stevens, and S. P. Baker. “Effect of oxygen on the thermomechanical behavior of tantalum thin films during the β-α Phase transformation”. *Journal of Applied Physics* **100**(12): 123508, 2006.

[173] A. Arakcheeva, G. Chapuis, and V. Grinevitch. “The self-hosting structure of β-Ta”. *Acta Crystallographica Section B* **B58**, 1–7, 2002.

[174] N. Schwartz, W. A. Reed, P. Polash, and M. H. Read. “Temperature coefficient of resistance of beta-tantalum films and mixtures with b.c.c.-tantalum”. *Thin Solid Films* **14**(2): 333–346, 1972.

[175] S. Gnanarajan, S. K. H. Lam, and C. P. Foley. “Optically transparent and electrically conducting epitaxial Ta2O films”. *Journal of Applied Physics* **101**(6): 063535, 2007.

[176] O. K. Donaldson, K. Hattar, J. R. Trelewicz, and E. I. Johnson. “Metastable Tantalum Oxide Formation During the Devitrification of Amorphous Tantalum Thin Films”. *Journal of the American Ceramic Society* **99**(11): 3775–3783, 2016.

[177] R. Chandrasekharan, I. Park, R. I. Masel, and M. A. Shannon. “Thermal oxidation of tantalum films at various oxidation states from 300 to 700 °C”. *Journal of Applied Physics* **98**(11): 114908, 2005.

[178] D. M. Mattox. *Handbook of Physical Vapor Deposition (PVD) Processing*. New Jersey: Noyes Publications, 1998.

[179] S. Rossnagel. “Sputtering and Sputter Deposition”. *Handbook of Thin Film Deposition: Processes and Technologies*. Ed. by K. Seshan. 2nd ed. Norwich, New York: Noyes Publications, 2002. Chap. 8.

[180] S. Franssila. *Introduction to Microfabrication*. Chichester, West Sussex: John Wiley & Sons, Ltd, 2004.

[181] C. Hammond. *The Basics of Crystallography and Diffraction*. 3rd ed. Oxford: Oxford University Press, 2009.

[182] G. Renaud and A. Barbier. “Atomic structure of oxide surfaces by surface X-ray scattering”. *Oxide Surfaces - Chemical Physics of Solid Surfaces vol. 9*. Ed. by D. Woodruff. Amsterdam: Elsevier Science B.V., 2001. Chap. 6, pp. 256–300.

[183] T. Ryan. “The development of instrumentation for thin-film X-ray diffraction”. *Journal of Chemical Education* **78**(5): 613–616, 2001.

[184] K. N. Stoev and K. Sakurai. “Review on grazing incidence X-ray spectrometry and reflectometry”. *Spectrochimica acta, Part B: Atomic spectroscopy* **54**(1): 41–82, 1999.

[185] S. A. Veldhuis, P. Brinks, T. M. Stawski, O. F. Göbel, and J. E. Ten Elshof. “A facile method for the density determination of ceramic thin films using X-ray reflectivity”. *Journal of Sol-Gel Science and Technology* **71**(1): 118–128, 2014.

[186] M. Mayer. *Rutherford backscattering spectrometry (RBS)*. Tech. rep. The Abdus Salam International Centre for Theoretical Physics, 2003, pp. 59–80.

[187] N. P. Barradas, C. Jeynes, R. P. Webb, U. Kreissig, and R. Grötzschel. “Unambiguous automatic evaluation of multiple Ion Beam Analysis data with Simulated Annealing”. *Nuclear Instruments and Methods in Physics Research, Section B: Beam Interactions with Materials and Atoms* **149**(1-2): 233–237, 1999.

[188] N. P. Barradas and C. Pascual-Izarra. “Double scattering in RBS analysis of PtSi thin films on Si”. *Nuclear Instruments and Methods in Physics Research, Section B: Beam Interactions with Materials and Atoms* **228**(1-4 SPEC. ISS.): 378–382, 2005.

[189] N. P. Barradas and M. A. Reis. “Accurate calculation of pileup effects in PIXE spectra from first principles”. *X-Ray Spectrometry* **35**, 232–237, 2006.

[190] *RUMP: RBS Analysis and Plotting*. URL: `http://www.genplot.com/doc/rump.htm` (visited on 12/20/2019).

[191] D. B. Williams and C. B. Carter. *Transmission Electron Microscopy*. 2nd ed. New York, NY: Springer, 2009.

[192] R. M. Brydson and C. Hammond. “Generic methodologies for nanotechnology: characterization”. *Nanoscale Science and Technology*. Ed. by R. W. Kelsall, I. W. Hamley, and M. Geoghegan. Chichester: John Wiley & Sons, Ltd, 2005. Chap. 2.

[193] A. Kovács, R. Schierholz, and K. Tillmann. “FEI Titan G2 80-200 CREWLEY”. *Journal of large-scale research facilities* **2**, A43, 2016.

[194] L. J. van der Pauw. “A method of measuring the resistivity and Hall coefficient on lamellae of arbitrary shape”. *Philips Technical Review* **20**, 220–224, 1958.

[195] N. Apsley, D. A. Anderson, and J. B. Morrison. “The Hall scattering factor in InP”. *Semiconductor Science and Technology* **2**(1): 44–49, 1987.

[196] N. P. Breznay, H. Volker, A. Palevski, R. Mazzarello, A. Kapitulnik, and M. Wuttig. “Weak antilocalization and disorder-enhanced electron interactions in annealed films of the phase-change compound GeSb2Te4”. *Physical Review B* **86**(20): 205302, 2012.

[197] J. M. Hollas. “Photoelectron and Related spectroscopies”. *Modern Spectroscopy*. 4th ed. Chichester, West Sussex: John Wiley & Sons, Ltd, 2004. Chap. 8, pp. 289–336.

[198] C. Wiemann, M. Patt, I. P. Krug, N. B. Weber, M. Escher, M. Merkel, and C. M. Schneider. “A new nanospectroscopy tool with synchrotron radiation: NanoESCA@Elettra”. *e-Journal of Surface Science and Nanotechnology* **9**, 395–399, 2011.

[199] A. Avila and B. Bhushan. “Electrical measurement techniques in atomic force microscopy”. *Critical Reviews in Solid State and Materials Sciences* **35**(1): 38–51, 2010.

[200] M. P. Murrell, M. E. Welland, S. J. O’Shea, T. M. H. Wong, J. R. Barnes, A. W. McKinnon, M. Heyns, and S. Verhaverbeke. “Spatially resolved electrical measurements of SiO2 gate oxides using atomic force microscopy”. *Applied Physics Letters* **62**(7): 786–788, 1993.

[201] M. Lanza. “A review on resistive switching in high-k dielectrics: A nanoscale point of view using conductive atomic force microscope”. *Materials* **7**(3): 2155–2182, 2014.

[202] S. Brivio, J. Frascaroli, and M. H. Lee. “Electrical AFM for the analysis of resistive switching”. *Electrical Atomic Force Microscopy for Nanoelectronics - NanoScience and Technology*. Ed. by U. Celano. Springer, Cham, 2019. Chap. 7, pp. 205–229.

[203] J. M. Hollas. “Electromagnetic Radiation and its Interaction with Atoms and Molecules”. *Modern Spectroscopy*. 4th ed. Chichester, West Sussex: John Wiley & Sons, Ltd, 2004. Chap. 2, pp. 27–39.

[204] R. Nakamura, T. Toda, S. Tsukui, M. Tane, M. Ishimaru, T. Suzuki, and H. Nakajima. “Diffusion of oxygen in amorphous Al2O3, Ta2O5, and Nb2O5”. *Journal of Applied Physics* **116**(3): 033504, 2014.

[205] A. Schoenhals. “Non-Standard Switching Phenomena and Interface Effects in Resistive Switching Devices”. PhD thesis. RWTH Aachen University, 2018.

[206] Y.-S. Fan, L. Zhang, D. Crotti, T. Witters, M. Jurczak, and B. Govoreanu. “Direct Evidence of the Overshoot Suppression in Ta2O5-Based Resistive Switching Memory With an Integrated Access Resistor”. *IEEE Electron Device Letters* **36**(10): 1027–1029, 2015.

[207] H. J. Wan, P. Zhou, L. Ye, Y. Y. Lin, T. A. Tang, H. M. Wu, and M. H. Chi. “In situ observation of compliance-current overshoot and its effect on resistive switching”. *IEEE Electron Device Letters* **31**(3): 246–248, 2010.

[208] P. Shrestha, D. Nminibapiel, J. P. Campbell, K. P. Cheung, H. Baumgart, S. Deora, and G. Beruker. “Dependence of Maximum RESET Current on the Duration of Current Overshoot”. *2013 IEEE International Integrated Reliability Workshop*. 2013, pp. 55–58.

[209] S. Ambrogio, V. Milo, Z. Q. Wang, S. Balatti, and D. Ielmini. “Analytical Modeling of Current Overshoot in Oxide-Based Resistive Switching Memory (RRAM)”. *IEEE Electron Device Letters* **37**(10): 1268–1271, 2016.

[210] D. Cooper, C. Baeumer, N. Bernier, A. Marchewka, C. La Torre, R. E. Dunin-Borkowski, S. Menzel, R. Waser, and R. Dittmann. “Anomalous Resistance Hysteresis in Oxide ReRAM: Oxygen Evolution and Reincorporation Revealed by In Situ TEM”. *Advanced Materials* **29**(23): 1700212, 2017.

[211] A. Fantini, D. J. Wouters, R. Degraeve, L. Goux, L. Pantisano, G. Kar, Y. Y. Chen, B. Govoreanu, J. A. Kittl, L. Altimime, and M. Jurczak. “Intrinsic switching behavior in HfO 2 RRAM by fast electrical measurements on novel 2R test structures”. *2012 4th IEEE International Memory Workshop (IMW)*. Milan, 2012, pp. 1–4.

[212] D. J. Wouters, S. Menzel, J. A. Rupp, T. Hennen, and R. Waser. "On the universality of I-V switching characteristics in non-volatile and volatile resistive switching oxides". *Faraday Discussions* **213**, 183–196, 2018.

[213] R. Bassiri, F. Liou, M. R. Abernathy, A. C. Lin, N. Kim, A. Mehta, B. Shyam, R. L. Byer, E. K. Gustafson, M. Hart, I. Maclaren, I. W. Martin, R. K. Route, S. Rowan, J. F. Stebbins, and M. M. Fejer. "Order within disorder: The atomic structure of ion-beam sputtered amorphous tantala (a-Ta_2O_5)". *APL Materials* **3**(3): 036103, 2015.

[214] Y. Lu and I.-W. Chen. "Probing material conductivity in two-terminal devices by resistance difference". *Applied Physics Letters* **111**(8): 083501, 2017.

[215] M. Wang, C. Bi, L. Li, S. Long, Q. Liu, H. Lv, N. Lu, P. Sun, and M. Liu. "Thermoelectric seebeck effect in oxide-based resistive switching memory". *Nature Communications* **5**, 4598, 2014.

[216] F. M. Puglisi, P. Pavan, A. Padovani, and L. Larcher. "A study on HfO_2 RRAM in HRS based on I-V and RTN analysis". *Solid-State Electronics* **102**, 69–75, 2014.

[217] N. Raghavan, R. Degraeve, A. Fantini, L. Goux, S. Strangio, B. Govoreanu, D. J. Wouters, G. Groeseneken, and M. Jurczak. "Microscopic origin of random telegraph noise fluctuations in aggressively scaled RRAM and its impact on read disturb variability". *2013 IEEE International Reliability Physics Symposium Proceedings (IRPS)*. Anaheim, CA, 2013, 5E.3.1–5E.3.7.

[218] R. Degraeve, A. Fantini, N. Raghavan, L. Goux, S. Clima, Y. Chen, A. Belmonte, S. Cosemans, B. Govoreanu, D. Wouters, P. Roussel, G. Kar, G. Groeseneken, and M. Jurczak. "Hourglass concept for RRAM: a dynamic and statistical device model". *Proceedings of the 21th International Symposium on the Physical and Failure Analysis of Integrated Circuits (IPFA)*. Marina Bay Sands, Singapore, 2014, pp. 245–249.

[219] P. N. Baker. "Preparation and properties of tantalum thin films". *Thin Solid Films* **14**(1): 3–25, 1972.

[220] A. G. Zabrodskii and K. N. Zinov'eva. "Low-temperature conductivity and metal-insulator transition in compensate n-Ge". *Sov. Phys. JETP* **59**(July 1983): 425–433, 1984.

[221] A. Moebius, C. Frenzel, and R. Thielsch. "Metal-insulator transition in amorphous $Si_{1-x}Ni_x$: Evidence for Mott's minimum metallic conductivity". *Physical Review B* **60**(20): 18–22, 1999.

[222] N. Waterhouse, P. S. Wilcox, and D. J. Willmott. "Effect of oxygen on the electrical and structural properties of triode-sputtered tantalum films". *Journal of Applied Physics* **42**(13): 5649–5653, 1971.

[223] S. Sathasivam, B. A. D. Williamson, A. Kafizas, S. A. Althabaiti, A. Y. Obaid, S. N. Basahel, D. O. Scanlon, C. J. Carmalt, and I. P. Parkin. "Computational and Experimental Study of Ta_2O_5 Thin Films". *The Journal of Physical Chemistry C* **121**(1): 202–210, 2017.

[224] M. H. Cheng, T. C. Cheng, W. J. Huang, M. N. Chang, and M. K. Chung. "Influence of oxygen diffusion on residual stress for tantalum thin films". *Journal of Vacuum Science & Technology B* **25**(1): 147, 2007.

[225] E. Sacher. "Asymmetries in transition metal XPS spectra: Metal nanoparticle structure, and interaction with the graphene-structured substrate surface". *Langmuir* **26**(6): 3807–3814, 2010.

[226] O. Kerrec, D. Devilliers, H. Groult, and P. Marcus. "Study of dry and electrogenerated Ta_2O_5 and $Ta/Ta_2O_5/Pt$ structures by XPS". *Materials Science and Engineering B* **55**, 134–142, 1998.

[227] M. Cevro and G. Carter. "Ion-beam and dual-ion-beam sputter deposition of tantalum oxide films". *Optical Engineering* **34**(2): 596–606, 1995.

[228] E. Franke, M. Schubert, C. L. Trimble, M. J. DeVries, and J. A. Woollam. "Optical properties of amorphous and polycrystalline tantalum oxide thin films measured by spectroscopic ellipsometry from 0.03 to 8.5 eV". *Thin Solid Films* **388**(1-2): 283–289, 2001.

[229] J. H. Thomas. "Defect photoconductivity of anodic Ta_2O_5 films". *Applied Physics Letters* **22**(8): 406–408, 1973.

[230] E. Franke, C. L. Trimble, M. J. DeVries, J. A. Woollam, M. Schubert, and F. Frost. "Dielectric function of amorphous tantalum oxide from the far infrared to the deep ultraviolet spectral region measured by spectroscopic ellipsometry". *Journal of Applied Physics* **88**(9): 5166–5174, 2000.

[231] B. Xiao and S. Watanabe. "Oxygen vacancy effects on an amorphous-TaO_x -based resistance switch: a first principles study". *Nanoscale* **6**(17): 10169, 2014.

[232] R. Rosenbaum, M. Ben-Shlomo, S. Goldsmith, and R. L. Boxman. "Low-temperature electronic transport properties of W, Mo, Ta, and Zr thin films". *Physical Review B* **39**(14): 10009–10019, 1989.

[233] M. Taguchi, Y. Tsutsumi, R. N. Bhatt, and S. Wagner. "Nanocrystalline silicon - from disordered insulator to dirty metal". *Journal of Non-Crystalline Solids* **198-200**, 899–902, 1996.

[234] B. L. Altshuler, A. G. Aronov, and D. E. Khmelnitsky. "Effects of electron-electron collisions with small energy transfers on quantum localisation". *Journal of Physics C: Solid State Physics* **15**(36): 7367–7386, 1982.

[235] G. Bergmann. "Weak localization in thin films". *Physics Reports* **107**(1): 1–58, 1984.

[236] M. K. Yang, H. Ju, G. H. Kim, J. K. Lee, and H. C. Ryu. "Direct evidence on Ta-metal phases igniting resistive switching in TaO_x thin film". *Scientific Reports* **5**(September): 14053, 2015.

[237] A. Jiang, T. A. Tyson, and L. Axe. "The stability of the β-phase of tantalum: A molecular dynamics study". *Journal of Physics Condensed Matter* **17**(12): 1841–1850, 2005.